

UNIVERSIDADE DE SANTIAGO
DE COMPOSTELA

FACULTAD DE FÍSICA

Departamento de Física de Partículas



**On the Multiwire Drift Chambers
alignment of the HADES
dilepton spectrometer**

Memoria presentada para
optar al Grado de Doctor
en Ciencias Físicas por:

Héctor Alvarez Pol

Octubre 2002

Ignacio Durán Escribano, Profesor Titular
de la **Universidad de Santiago de Compostela**,

CERTIFICO: que la memoria titulada “**On the Multiwire Drift Chambers alignment of the HADES dilepton spectrometer**”, ha sido realizada por **Héctor Alvarez Pol** bajo mi dirección en el **Departamento de Física de Partículas** de esta Universidad, y constituye la Tesis que presenta para optar al grado de **Doctor en Ciencias Físicas**.

Santiago de Compostela, Octubre de 2002

Prof. Ignacio Durán Escribano **Héctor Alvarez Pol**

In memoriam

Carmen Fernández Cambronero

A Loly y Ari, con mi amor.

Acknowledgements

Agradecimientos

I would like to thank Prof. Helmut Bokemeyer and Dr. Wolfgang Koenig for their support during my stay at GSI, as well as the KP1 department staff. Special gratitude to Mrs. Bush, for her constant attention. I would like to thank the support and friendship of the MDC team: Dr. Joachim Stroth and Dr. Christian Müntz. The long and cold times at GSI were more pleasant staying close to my friends and old room mates: Jaroslav Bielcik, Jochen Market, Jörn Wustefeld and Peter Zumbruch. Thanks also to Dr. Deni Bertini and Dr. Ilse Koenig for the interesting discussions. I would like to thank Ulrich Kopf and the GSI Konstruktionsbüro and Mechanische Werkstatt staff for their help.

The use of the RASNIK devices has been possible thanks to the help of their developers. I am indebted to Dr. Harry van der Graaf, Henk Groenstege and Robert Hart for their continuous support and friendly advise. Thanks also to Dr. Vicente Moreno, for inviting me to test the devices in the optical bench at the Optics laboratory.

Mis agradecimientos para los profesores Ignacio Durán y Juan Antonio Garzón, que me han ofrecido la oportunidad de realizar este trabajo y de aprender de sus experiencias. A Rosalino Lorenzo por las largas discusiones sobre estadística y otras artes.

Mis amigos y compañeros de carrera estuvieron a mi lado en este tiempo: David, Oswaldo, JJ, Miguel, Belén y en especial a Bea, que puso más de una huella sobre el trabajo. Gracias a mis amigos que trabajaron codo con codo en HADES, Manuel, Antonio y recientemente Diego y Teresa; y a Miguel Rozas, por su paciencia.

Siempre conmigo estuvo mi familia, mis padres y mis hermanos. No solo mis gracias, sino mi amor es para ellos. A Loly y Ari, que lo aguantaron todo, la calma y la tormenta, y aún no se quejan.

Foreword

The HADES experiment involves the participation of multiple branches of our knowledge: Mechanical Engineering, Electronics, Computing and several Physics flavors (in case you did not find Physics in the previous points!). A large effort and the proficiency of the engaged people links the tasks in order to build a senseful device.

The alignment of the detectors, even though to be just a small part in the play, is essential for the accurate dilepton analysis, and it has also involved a few topics, some of them quite new for me. My work, as probably should be a job like this, has resembled more a straggling discovery than a demonstration of skillfulness. The harder the way, the better the feeling (at the end).

I have divided the work in three parts, the first devoted to the introduction to the HADES experiment, and the other two to the alignment methods, hardware and software. To improve the readability and continuity of the text, several explanatory or supplementary sections are included as appendices, at the end.

The introduction of the work first contains those topics concerning the physical motivation of the experiment, followed by a section where the spectrometer components are carefully described. The main actor in the story, the drift chambers, are described in their own chapter.

The second part is introduced by the effects that misalignment (the lack of alignment) produces on the most relevant magnitudes. An structural view of the spectrometer is required for the explanation of the proposed and implemented hardware solutions. In the next chapter, the optical components (RASNIK) we have selected to perform the monitoring are presented. Their implementation required the design of new support parts as well as the calculations of transformation matrices and relations between the spectrometer detectors and the alignment devices. Before the final implementation in the HADES spectrometer, a test on the optical bench is described. Finally, the setup calibration and the monitoring and control software explanation is reported, to end with the results and measurements

on the spectrometer.

The third part includes the tracking-based approximations to the alignment problem. The theoretical machinery is first presented and evaluated in a realistic simulation. Next, the results of the analysis of data from the experiment are shown, and their accuracy is discussed.

Taken this as a work, I have enjoyed the discoveries and the surprises (do you know the feeling when you have in your hands a real piece that you have designed!?). No doubt, it is more than a work, it is quite personal, and inside there is a lot from the people I have meet during this time.

Just my personal two cents...

Héctor Alvarez Pol
Santiago de Compostela,
October 2002

Contents

Acknowledgements	i
Foreword	iii
Resumen (en castellano)	I
El espectrómetro HADES	I
Los métodos de alineamiento de las MDCs	VI
Alineamiento mediante RASNIK	VII
Alineamiento por medio del estudio de trazas	XI
I INTRODUCTION TO THE HADES EXPERIMENT	1
1 The HADES experiment	3
1.1 Introduction to the HADES Physics	3
1.2 The HADES spectrometer	6
1.3 Commissioning and planned studies	23
Bibliography	25
2 The HADES multiwire drift chambers	27
2.1 Introduction to the drift chambers	27
2.2 The HADES drift chambers	33
Bibliography	41
II HARDWARE ALIGNMENT	43
3 Introduction to the alignment methods	45
3.1 Simulation of misalignment effects	45
3.2 Hardware and software solutions	53
Bibliography	59

4	The MDC RASNIK System	61
4.1	RASNIK: a relative alignment device	62
4.2	RASNIK description	64
4.3	Mechanical construction	72
4.4	Bench test of angle and aperture dependence	77
4.5	Integration in the spectrometer	85
4.6	On-bench calibration	90
4.7	On-line monitoring: RAHAD and EPICS	100
4.8	In situ experimental results	105
	Bibliography	124
III	SOFTWARE ALIGNMENT	125
5	Relative Alignment Methods	127
5.1	Introduction	127
5.2	The Target Finder algorithm	130
5.3	Relative alignment for 2 MDCs	141
5.4	Relative alignment for 3 MDCs	170
	Bibliography	183
6	Relative Alignment Results	185
6.1	Module resolution and tracking features	185
6.2	Target Finder Results	186
6.3	Alignment of sectors with two modules	190
6.4	Alignment of sectors with three modules	197
6.5	Beam line reconstruction	204
	Conclusions	209
A	Theoretical frame of the HADES Physics	211
A.1	The vector mesons	211
A.2	The chiral symmetry and the quark mass	213
	Bibliography	215
B	Previous dilepton studies	217
B.1	The DLS results	217
B.2	CERES results	219
	Bibliography	221
C	Limits to the drift chamber resolution	223
	Bibliography	227

D	The MDC tracking software	229
D.1	Data levels	229
D.2	The Dubna Hit finder and fitting	231
D.3	The Santiago Hit finder and fitting	232
D.4	Slope correction to the tracking software	233
	Bibliography	235
E	Euler transformations	237
	Bibliography	239
F	Coordinate system transformation using the Euler angles	241
G	Geometry of the mask support pieces	247
H	Geometrical solution to the “out of plane” rotation	253
I	Technical drawings	259
	Conclusiones (en castellano)	273

Resumen

El experimento HADES implica a múltiples ramas del conocimiento: Ingeniería Mecánica, Electrónica, Informática... Sólo un esfuerzo combinado de gente experimentada puede unir estas tareas y construir un dispositivo coherente.

El presente trabajo de Tesis está concebido como un estudio y aplicación de los métodos de alineamiento en el campo de los detectores de Física de Partículas y, en particular, en los detectores denominados Multiwire Drift Chambers (MDCs o cámaras de deriva multihilo) del espectrómetro HADES.

El alineamiento de los detectores es sólo una pequeña parte del juego, si bien hay que considerarla como fundamental en el análisis de los datos del espectrómetro. Pero aún dentro de esta pequeña parte, se han barajado un buen número de disciplinas hasta lograr el objetivo. El conseguir que estas disciplinas se integren, formando algo útil es, también, el propósito de este trabajo.

El espectrómetro HADES

El espectrómetro HADES (High Acceptance Di-Electron Spectrometer, o espectrómetro de di-electrones de alta aceptación) está instalado en el área experimental del GSI (Gesellschaft für Schwerionenforschung, Sociedad para la investigación de iones pesados) en la ciudad alemana de Darmstadt. El principal dispositivo del GSI es un acelerador de iones pesados de energías intermedias (de hasta 2 AGeV), que está clasificado como una European Large Facility por la Union Europea.

HADES pretende detectar y estudiar los pares electrón-positrón que provienen de la zona densa y caliente que se forma en las colisiones de iones pesados. Después de la colisión de los iones, durante un tiempo muy corto ($10 - 100 \text{ fm}/c$), se produce un estado donde los nucleones interactúan entre sí, excitándose y emitiendo gran cantidad de piones y η .

La expansión del sistema frena las interacciones hasta un punto en el que las colisiones inelásticas dejan de producirse y la composición del sistema final queda fijada (hadronización). Los dileptones producidos no interactúan fuertemente y, por tanto, calculando la masa invariante del par se reconstruye la información acerca de las masas de las partículas de las que proviene: en particular, resultan de gran interés las desintegraciones en pares e^+e^- de los denominados mesones vectoriales, ρ , ω y ϕ . Estos mesones vectoriales tienen vidas medias cortas, del orden del tiempo que dura el condensado de alta densidad, o incluso menor en el caso del ρ , una ancha resonancia. Identificando y reconstruyendo la masa invariante de los dileptones que provienen de los mesones vectoriales se pueden contrastar las predicciones teóricas sobre la dependencia de las propiedades básicas (masa, anchura) de las resonancias con la densidad del medio. Esta dependencia con la densidad está implícita en modelos básicos que describen la interacción fuerte y se relaciona directamente con la restauración de la simetría quiral del Lagrangiano de QCD, simetría que está espontáneamente rota en el estado fundamental (solución de menor energía).

La tarea de encontrar los pares e^+e^- se ve tremendamente dificultada por la bajísima probabilidad de desintegración de los mesones vectoriales en pares, del orden de sólo unas decenas por millón de desintegraciones. Por otro lado, existen diversas fuentes de pares e^+e^- de mayor o comparable intensidad que podrían ocultar la información relevante si no se identifica claramente su origen: por ejemplo, pares provenientes de la conversión de un fotón o aquellos que surgen de las desintegraciones de tipo Dalitz (un par de leptones más un fotón, que no se detecta). De igual modo, se pretende reducir al máximo la identificación equivocada de una desintegración a partir de un electrón y un positrón que provengan en realidad de diferentes fuentes, que no fueron debidamente identificadas, lo que se denomina fondo combinatorial.

El espectrómetro HADES está diseñado siguiendo unas especificaciones que lo capacitan para la identificación y medida de las propiedades de los pares e^+e^- y de las partículas cargadas que los acompañan, que caracterizan la reacción. En concreto, se requiere: una **amplia aceptación** de los pares generados por la reacción, la **capacidad de adquirir grandes tasas de interacción** producida por grandes intensidades en el haz, **soportar grandes multiplicidades** generadas en las colisiones centrales e **identificar las señales de fuentes hadrónicas y electromagnéticas** que complican la medida. El objetivo es la **completa caracterización del evento**, junto con la reconstrucción de la masa invariante de los pares con una **resolución en masa en torno al 1% en la zona del ω** , del

orden de su anchura, permitiendo estudiar efectos de interferencia con el ρ . El espectrómetro debe tener una **aceptancia prácticamente plana en masa y momento transverso**, y debe estar construido con **materiales de baja densidad y número atómico**, para minimizar los efectos de la dispersión múltiple.

El espectrómetro está compuesto por los siguientes detectores:

- **RICH (Ring Imaging CHerenkov o detector de anillos de luz Cherenkov)**, basado en la detección de los anillos de luz que se producen en un gas denominado radiador (C_4F_{10}), cuando lo atraviesan partículas cargadas a velocidades mayores que la de la luz en el medio. Los fotones generados se reflejan en un espejo esférico de sólo 2 mm de grosor de carbono aluminizado y, tras atravesar una ventana de CaF_2 , alcanzan un fotoconvertidor de CsI que emite electrones, para su detección en una cámara proporcional multihilo llena de CH_4 puro. El detector RICH actúa como un detector de umbral, resultando completamente ciego a los hadrones (incluso a piones de hasta 3 GeV), con lo que la producción de anillos identifica unívocamente a los leptones.
- **MDC (Multiwire Drift Chambers o cámaras de deriva multihilo)**, consistente en cuatro planos de cámaras colocadas en parejas antes y después de la zona con campo magnético, para determinar la trayectoria de las partículas cargadas y, a partir de la curvatura producida por el campo magnético, su momento. Cada plano está dividido en seis módulos independientes, uno por sector, siguiendo la geometría hexagonal del espectrómetro. Cada módulo está compuesto por seis planos de hilos sensores (a tierra) y de campo (a alto voltage negativo), intercalados entre siete planos con hilos (cátodos), también a alto voltage negativo, que configuran celdas independientes de deriva. Los electrones generados por la ionización del gas que llena las cámaras (una combinación de Helio e Isobutano elegida por su baja longitud de interacción) derivan hacia el hilo sensor. Para cada plano de hilos sensores, se mide el tiempo que tarda en llegar al hilo la nube de electrones a través del retraso de la señal que induce en el hilo con respecto a una señal común, generada por el detector de inicio de la interacción. La estimación de la trayectoria de la partícula se obtiene a partir de las posiciones en los distintos planos de hilos sensores de cada cámara, los cuales están dispuestos según diferentes direcciones (configuración de mariposa) para eliminar la posibilidad de una identificación errónea y mejorar la resolución.

- **Pre-Shower o detector de cascadas**, basado en la comparación de la carga producida por las partículas que se generan mediante cascadas hadrónicas o electromagnéticas antes y después de convertidores de plomo. Tres detectores gaseosos con lectura en pads y trabajando en modo SQS (Self Quenching Streamer o modo de avalancha autoextinguida), intercalados entre los convertidores de plomo, miden la carga depositada por las partículas y determinan el tipo de avalancha y el tipo de partícula que la origina. El detector cubre la zona de bajo ángulo polar, donde los electrones tienen mayor energía y probabilidad de generar una cascada electromagnética.
- **TOF (Time Of Flight o detector de tiempo de vuelo)**, consistente en un conjunto de barras de plástico de centelleo, con fotomultiplicadores en ambos extremos de la barra para la detección de la luz generada. Usando la referencia temporal dada por el detector de inicio (diamante) se calcula, a partir de las señales en los fotomultiplicadores, el tiempo de vuelo de las partículas cargadas que atraviesan los plásticos. A bajos ángulos polares, un conjunto de plásticos centelleadores con lectura en un sólo extremo, denominado TOFino, ayudan a determinar la multiplicidad, así como a la reconstrucción en el detector Pre-Shower.
- **Detector de diamante**, que proporciona las señales de inicio de la reacción utilizadas por los detectores para el cálculo del tiempo de vuelo y en su proceso de adquisición. El detector esta hecho a partir del crecimiento de un fino substrato de carbón policristalino, por deposición química, al que se le añaden electrodos de lectura metálicos. Los pares hueco-electrón generados por los iones son directamente amplificados por una electrónica de bajo ruido. La resolución es del orden de los 30 ps y es capaz de detectar mas de 10^8 iones pesados por segundo. Se incluye también un detector de “veto” que inhibe la señal de comienzo cuando el ion que la origina no colisiona con los iones del blanco.

Además de este conjunto de detectores, una parte fundamental del diseño del espectrómetro es el imán superconductor toroidal, que genera un campo magnético inhomogéneo y localizado entre los dos grupos de cámaras de deriva, y que proporciona un cambio en la dirección polar de las partículas cargadas que lo atraviesan.

Para poder obtener una muestra estadísticamente significativa en un periodo de tiempo razonable es necesario imponer unos niveles de selección (o de trigger, usando el vocablo inglés), para aceptar aquellas reacciones

que contengan pares de leptones candidatos a provenir de una desintegración de mesones vectoriales. La mayoría de la electrónica de adquisición está altamente paralelizada para soportar una lectura rápida de los miles de canales electrónicos; las señales digitalizadas se guardan en distintos niveles de memorias mientras se esperan otros resultados. Los detectores de start y veto producen pulsos lógicos que serán utilizados para crear una señal de disparo o start; los detectores TOF y TOFino son capaces de determinar en un breve intervalo el número de partículas cargadas que participan en la reacción. La multiplicidad de partículas cargadas está relacionada con la centralidad de la colisión y por tanto con las propiedades del medio denso y caliente. Un primer nivel de trigger o selección requiere que la multiplicidad supere un umbral, determinado por los sistemas en colisión. Aproximadamente un 10% de las colisiones pasan esta primera selección.

Una serie de procesadores verifican, para aquellas reacciones aceptadas, la existencia de anillos en el RICH y de cascadas electromagnéticas en el detector Pre-Shower, y la coincidencia y el ajuste del conjunto de candidatos a leptones dentro de unos límites de momento y ángulo de apertura del par. Este segundo nivel de selección reduce la muestra en un factor 100 adicional, antes de la reconstrucción completa de los datos de los distintos detectores para su escritura en cinta. Un nivel adicional de selección, aun no implementado, incluiría la búsqueda del par candidato en las cámaras de deriva, en las zonas de interés señaladas por el RICH y el Pre-Shower, con el fin de eliminar aquellos candidatos mal identificados (normalmente aquellos en los que uno de los componentes del par es en si mismo un par de conversión, no separado, o del que se ha perdido una de las partículas en su paso por el campo magnético).

El software del experimento está escrito en el lenguaje de programación C++, siguiendo los paradigmas de la programación orientada a objetos, siendo pionera su utilización en un experimento de Física de Partículas. Esta aproximación ayuda a afrontar los problemas en códigos complejos de gran tamaño, permitiendo su gestión y mantenimiento y garantizando la modularidad, reutilización, documentación y legibilidad. El software básico, denominado HYDRA (HADES System for Data Reduction and Analysis o sistema de reducción de datos y análisis de HADES) contiene las estructuras básicas que definen los datos y los algoritmos que los transforman. HYDRA está escrito sobre ROOT, una plataforma de análisis de datos orientada a objetos, que facilita la gestión (I/O) de datos y la creación de histogramas.

Los métodos de alineamiento de las MDCs

La principal función de las cámaras de deriva es la medida de la trayectoria de las partículas cargadas, antes y después de su interacción con el campo magnético. La aproximación utilizada consiste en suponer que el campo magnético está confinado entre los dos grupos de cámaras de deriva, de forma que las trayectorias antes y después de la zona del imán se puedan describir como rectas. De cada una de las cámaras de deriva se obtiene la posición por la que pasa la partícula, además de su dirección. Para ello se utiliza el software de *tracking*, que ajusta las posiciones estimadas del paso de las partículas por las celdas de la cámara de deriva a un modelo determinado. A partir de esta estimación, independientemente para cada grupo de cámaras y suponiendo propagación rectilínea, se construyen los tramos rectos de las trayectorias de la partícula antes y después del paso por el campo magnético creado por el imán superconductor. Mediante la comparación directa del cambio de ángulo de las dos rectas, extrapoladas a un plano intermedio (método del kickplane) o mediante la comparación con una librería de trazas de referencia generadas a partir de una simulación, se calcula el momento de las partículas cargadas.

El impacto sobre la determinación del momento producido por el error en la determinación de la posición de las cámaras puede ser evaluado mediante simulación. Los resultados obtenidos en la simulación llevada a cabo en este trabajo muestran una desviación sistemática en el momento de las partículas con los desplazamientos a lo largo de la dirección en la que el campo magnético las deflecta. La desviación sistemática por unidad de desviación de la posición, toma un valor de $0.2 - 0.4\%/100 \mu m$ para un intervalo de momentos entre 400 y 600 MeV/c , siendo ligeramente superior para momentos mayores. Esta desviación es explicable mediante simples razones geométricas basadas en el cambio de las trayectorias rectilíneas antes y después del imán, y resulta de signo opuesto para las partículas cargadas positiva o negativamente. También resulta de signo opuesto para los desplazamientos de la primera o segunda cámara de cada par, puesto que el mismo desplazamiento modifica en sentidos contrarios la estimación de la trayectoria rectilínea. La estimación del efecto en la determinación de la masa invariante comprende la estimación del error en la determinación del momento en diferentes sectores del espectrómetro, con diferentes desplazamientos relativos. Limitando las desviaciones relativas, a lo largo de la dirección en la que se modifica la trayectoria por el campo magnético, a $30 \mu m$ entre cámaras vecinas y a $50 \mu m$ entre cámaras antes y después del imán, se reduce la desviación en la masa invariante por debajo del 1%. Los desplazamientos de similar magnitud en otras direcciones no influyen

en la determinación del momento y, por consiguiente, de la masa invariante del par de dileptones.

La posición relativa de las cámaras se puede determinar a partir de varios métodos. Un método comúnmente utilizado consiste en la medida mediante teodolitos de ciertos puntos fiduciales visibles en los marcos de las cámaras, con lo que se puede determinar la posición de estos puntos con respecto a un vértice de la zona experimental, con una precisión del orden de $100 \mu m$. Por otra parte, las posiciones relativas de las cámaras de deriva se pueden obtener del estudio de las trazas rectas que cruzan el espectrómetro cuando el imán está apagado. Finalmente, se puede monitorizar la posición o el desplazamiento de los detectores mediante sistemas ópticos o electrónicos.

Todos los detectores están montados sobre raíles en dos grandes estructuras. Se espera encontrar un fuerte desplazamiento relativo entre las cámaras internas y las cámaras externas debido a los cambios de temperatura y, más importante si cabe, a los desplazamientos que produce el campo magnético sobre las estructuras de soporte de los detectores.

La solución elegida por la colaboración para el alineamiento de las cámaras de deriva del espectrómetro consiste en la determinación de la posición de las cámaras mediante el estudio de las trazas rectas que atraviesan el detector, cuando el imán está apagado. Esta solución requiere la monitorización de los desplazamientos relativos entre las cámaras internas y las externas debidos al campo magnético, tarea para la que hemos propuesto, diseñado e instalado un dispositivo basado en el sistema óptico RASNIK.

Alineamiento mediante RASNIK

El sistema RASNIK (Red Alignment System of NIKHEF o sistema rojo de alineamiento de NIKHEF, Amsterdam, Holanda) es un dispositivo óptico de alineamiento de tres elementos. Está constituido por una **cámara de vídeo** que recoge la imagen de una **máscara iluminada por LEDs** infrarrojos, proyectada por una **lente** simple. La máscara contiene un patrón de píxeles blancos y negros sobre el que se colocan líneas con información numérica codificada. El desplazamiento relativo de cualquiera de los tres elementos provoca un cambio de la posición de la imagen de la máscara, que puede ser analizado mediante un software específico. El sistema RASNIK ha ido evolucionando tras su utilización por diversas colaboraciones en Física de Partículas y en los futuros experimentos del LHC en el CERN está prevista su masiva utilización.

El dispositivo experimental completo consta de:

- **La máscara y la matriz de LEDs**; la máscara tiene unos 4 cm^2 y está hecha de cromo sobre cristal. Tiene un diseño ajedrezado de cuadros opacos y transparentes, de $170\ \mu\text{m}$ de lado, con información codificada en cada novena línea del patrón, que informa acerca de la parte de la máscara que está contenida en la imagen. Los LEDs infrarrojos se sitúan detrás de la máscara, que presenta en su parte posterior un difusor para que la iluminación de la matriz de LEDs resulte homogénea. La luz infrarroja, junto con un filtro infrarrojo en la cámara de vídeo, independiza el sistema de las condiciones de luz ambientales.
- **La lente** proyecta el patrón de la máscara sobre la cámara de vídeo. Se usa una simple lente plano-convexa de BK7 de 200 mm de distancia focal y 25 mm de diámetro. Junto con la lente, un filtro infrarrojo impide que llegue otra información a la cámara diferente de la imagen de la máscara.
- **La videocámara**, del tipo CMOS, graba la imagen de la máscara con alta resolución y la envía siguiendo el estándar RS170 al framegrabber.
- **El framegrabber** o tarjeta digitalizadora de vídeo, instalada en un slot PCI de un PC. Recoge la señal de la videocámara y la digitaliza, para su análisis posterior.
- **El sistema electrónico de multiplexado**, diseñado para alimentar alternativamente los distintos LEDs (hasta doce canales) y alimentar, leer y transmitir la señal de las cámaras (hasta seis canales).
- **El software de análisis de las imágenes, ICARAS** (Integrated Control and Analysis for RASNIK, ó control y análisis integrados para RASNIK), programa que controla la adquisición de las imágenes y realiza el análisis que devuelve los desplazamientos de la máscara.

Las distancias entre elementos vienen determinadas por la distancia focal de la lente y por la distancia entre la máscara y la cámara, siguiendo las ecuaciones de la óptica paraxial. Los desplazamientos de la máscara según las direcciones perpendiculares al eje óptico del sistema se obtienen a partir del análisis del desplazamiento de la imagen, mientras en la dirección paralela al eje óptico se utiliza el cambio de magnificación de la imagen.

Para cada sector se monitoriza la posición de dos puntos de las cámaras de deriva exteriores con respecto a las interiores. Para ello, una videocámara

y dos lentes se mantienen sujetas a los soportes de las cámaras de deriva internas, mientras las dos máscaras correspondientes se fijan al marco de la cámara externa inmediata, denominada MDC III. En esta configuración se obtiene una información más precisa cuanto más alejados estén los puntos a monitorizar en los marcos de la MDC III. La instalación del sistema de alineamiento en el espectrómetro implica el estudio minucioso de varios parámetros que afectan a su funcionamiento y resolución. En particular, se han realizado en este trabajo estudios detallados sobre el efecto de la apertura de la lente y el ángulo máximo de inclinación entre el eje óptico del sistema y la superficie de la cámara. A menor apertura, se incrementa la profundidad de campo, pero, por otro lado, para mayores aperturas aumenta el poder de separación y la relación señal/ruído, habiéndose llegado a un compromiso óptimo, dentro del margen estrecho de los requerimientos del sistema.

Se ha comprobado experimentalmente la relación entre la apertura del diafragma limitador de la lente, y la resolución del sistema, así como el ángulo máximo para el que trabaja de forma fiable. Para ello, se ha estimado la resolución mediante el ajuste polinómico (de orden dos) de una serie temporal de medidas. La resolución se asigna a la anchura (σ) del ajuste gaussiano de los residuos del ajuste polinómico. Como resultado se ha encontrado un funcionamiento correcto del sistema hasta ángulos de 25° , encontrándose problemas de estabilidad en el módulo de análisis para ángulos mayores. La resolución se ha incrementado para las aperturas más pequeñas probadas, de 15 mm de diámetro, siendo prácticamente independiente del ángulo de inclinación. El trabajo realizado ha permitido la caracterización del sistema, obteniendo valores en la resolución del orden de $15\ \mu\text{m}$ a lo largo de la dirección del eje óptico, y de $0.2\ \mu\text{m}$ en las direcciones normales, valores compatibles con los obtenidos previamente en la bibliografía.

La integración de los sistemas RASNIK en el espectrómetro requiere el diseño de nuevas piezas de soporte que cumplan exigentes requisitos. El denominado "binocular", la pieza soporte de la cámara de vídeo y de las lentes, ha sido diseñada en fibra de carbono y aluminio, para conseguir una estructura que mantenga la posición relativa lentes-cámara, independientemente de los cambios de temperatura. Se incluye un mecanismo que permite el enfoque y un pequeño desplazamiento del eje óptico, lo que ayuda a centrar la máscara, aún en el caso de que se encuentre desplazada de la posición nominal. La pieza soporte de la máscara está diseñada para situar los ejes principales de la máscara (transiciones opaco-transparente) perpendiculares al eje óptico y paralelos al pixelado de la videocámara.

Los planos técnicos de los componentes expresamente diseñados en este trabajo se incluyen en un apéndice.

Previamente a la instalación en el espectrómetro de los sistemas de alineamiento, se ha procedido a la comprobación y calibración de un canal sobre un banco óptico, situando la máscara sobre un sistema de tres ejes motorizados. Se pretende comprobar la respuesta del sistema de alineamiento a desplazamientos controlados de la máscara. Se estudia la linealidad de la respuesta a los desplazamientos y los coeficientes de calibración en cada una de las direcciones, teniendo en cuenta los diversos factores experimentales (rotaciones relativas de los sistemas de ejes, errores sistemáticos en los dispositivos de posicionamiento) que afectan al resultado. El estudio se realiza en varias zonas de la máscara, y para varias máscaras, con lo que se caracteriza un valor medio y una varianza en cada parámetro de calibración.

El sistema de "Slow Control" de HADES (que monitoriza y controla los valores de los parámetros operativos de dispositivos experimentales) está basado en EPICS, nombre con el que se conoce a un conjunto de aplicaciones cliente-servidor para establecer bases de datos en tiempo real que sirvan información a puestos de monitorización bajo eficientes protocolos de comunicaciones. Para el control y la monitorización de los canales instalados en el espectrómetro, así como para la comunicación de los resultados a las aplicaciones clientes de EPICS, se ha realizado un programa denominado RAHAD (Rasnik Analysys for HADes, o análisis de RASNIK para HADES), que permite simular una base de datos en tiempo real para la transferencia de información de la base de datos ante las peticiones de los operadores. RAHAD monitoriza los cambios en los desplazamientos analizados por los canales RASNIK y calibra cada uno de ellos. Transforma el vector de desplazamientos de acuerdo con la geometría de los módulos y actualiza los valores de su base de datos para que las peticiones de información de los operadores reciban los valores actualizados de la posición de las cámaras de deriva. RAHAD contiene un sistema de monitorización gráfica (basado en ROOT) que permite verificar inmediatamente el comportamiento de cada uno de los canales de alineamiento.

La monitorización de la posición de dos puntos en el marco de las cámaras MDC III con respecto a las cámaras internas permite la estimación del vector de translación relativo y de rotaciones alrededor de los ejes principales (salvo respecto al eje definido por la línea que une los centros de las máscaras). Los movimientos relativos que hay que medir son lo suficientemente lentos como para poder realizar varias medidas antes de que cambie significativamente la posición de las cámaras. Es posible, por

tanto, reducir el error en la estimación de la media del desplazamiento promediando las medidas en un corto intervalo de tiempo. A partir de esta reducción estadística se puede determinar la resolución del sistema experimental, obteniéndose valores de $9.5 \mu m$ en la dirección del eje óptico y de $0.27 \mu m$ y $0.40 \mu m$ en las direcciones normales. Al transformar a un sistema de coordenadas común, se puede estimar que el error estándar cometido en las direcciones principales de la cámara es menor de $7.5 \mu m$, pudiendo reducirse mediante el cálculo de la media de medidas consecutivas, según la raíz cuadrada del número de medidas. Estos valores se han comprobado mediante el ajuste a un polinomio (de tercer grado) de una zona de la serie temporal de desplazamientos en la que no se producen saltos o cambios abruptos. Del ajuste gaussiano de los residuos del ajuste polinomial se obtiene una estimación del error cometido en la determinación de la posición. Para esta serie temporal los resultados confirman una resolución mejor que $7 \mu m$ en la determinación de los desplazamientos según cualquier dirección del sistema de coordenadas común (el de la MDC III); la resolución es mejor que $2.5 \mu m$ si repetimos el proceso para las medias realizadas sobre 16 medidas consecutivas de la posición.

Los desplazamientos medidos en la zona experimental se correlacionan perfectamente con los cambios de temperatura debidos a la disipación de calor de los componentes electrónicos y a la variación día/noche. Asimismo, el encendido del campo magnético provoca un desplazamiento relativo muy grande de las cámaras, que puede ser superior a las $500 \mu m$ para una corriente en el imán del 72.15% de la total.

Alineamiento por medio del estudio de trazas

Una forma precisa de realizar el alineamiento relativo de los módulos atravesados por las partículas cargadas es mediante el estudio de trazas rectilíneas generadas por las colisiones en ausencia de campo magnético. En este trabajo se han diseñado algoritmos para el cálculo de los parámetros que definen las posiciones relativas tanto en aquellos sectores completos, como en los que, de forma temporal, sólo tienen dos o tres módulos de deriva.

El algoritmo para alinear tres módulos minimiza el seno del ángulo formado por los dos vectores que se pueden componer con la información de posición del módulo central y los dos laterales. En este caso, la minimización se ha realizado fijando uno de los doce parámetros que definen las posiciones relativas de los tres módulos, para evitar el colapso del sistema sobre un único plano, que es una solución trivial, pero evidentemente no

válida, que minimiza el funcional. El parámetro así fijado debe encontrarse haciendo un barrido sobre sus posibles valores y obteniendo, de una serie de histogramas de control, el valor que mejor ajusta las pendientes de las trazas en cada módulo o las pendientes de las trazas en un módulo y el vector construido a partir de los módulos contiguos.

Para el caso de alinear dos módulos, se requiere la utilización de una muestra grande de trazas reconstruidas por uno de ellos para, a partir de su análisis, encontrar la posición del blanco. El algoritmo de búsqueda del blanco minimiza la distancia de un punto del espacio a las trazas provenientes de un módulo, o de un conjunto de módulos. Para evitar la desviación producida por trazas provenientes de colisiones fuera del blanco o de secundarios, se utiliza iterativamente un sistema de corte por pesos de Tukey, que combinado con una corrección por la forma de la cámara, lleva a una determinación del punto de interacción del haz con el blanco.

Una vez obtenida la posición del blanco, se utiliza para construir recetas junto con la información obtenida por la misma cámara utilizada para encontrar las coordenadas del blanco. El alineamiento de otros módulos se realiza proyectando las trazas sobre su plano, y comparando con la estimación local de las componentes de la traza. Una minimización analítica encuentra los elementos del vector de translación, mientras que un sistema geométrico de corrección en las rotaciones mejora, de forma iterativa, la aproximación a los parámetros de alineamiento verdaderos.

En el análisis de datos de colisiones de carbono contra un blanco de carbono, tomados sin campo magnético, se ha comenzado por aquellos sectores que tenían tres módulos, utilizando el método más preciso y que devuelve una estimación más completa de su error. Un cuidadoso estudio permite encontrar las desviaciones relativas de las direcciones de las trazas entre módulos. Se han estimado los valores de los parámetros para una minimización que fija el ángulo en el valor medio de los resultados de distintos criterios, tomando la desviación como medida del error cometido en el parámetro que se fija.

En los sectores en los que sólo hay dos módulos, se han encontrado los parámetros de alineamiento buscando inicialmente la posición estimada del target, para luego proyectar las trayectorias del módulo de referencia sobre el módulo a alinear. La desviación de las proyecciones y las estimaciones locales de las trayectorias permite definir el error cometido por la minimización analítica, mientras que el estudio de las diferencias separando por zonas del módulo, permite estimar el error cometido por la corrección geométrica de las rotaciones, y también incrementar la información sobre las particularidades de cada módulo. Los errores sistemáticos debi-

dos al error en el posicionamiento del target dominan frente a los errores estadísticos, que resultan ser de mucha menor envergadura.

Una vez alineados los módulos del espectrómetro, las trazas rectilíneas pueden usarse para reconstruir el camino del haz de iones que colisiona, no sólo con el target principal, sino también con otros materiales a lo largo de su camino. En particular, se ha demostrado con facilidad la separación que puede hacer el espectrómetro entre trazas que provienen de distintos puntos de interacción a lo largo del haz.

Part I

**INTRODUCTION TO THE
HADES EXPERIMENT**

Chapter 1

The HADES experiment

HADES (High Acceptance Di-Electron Spectrometer) [1–3] is the acronym describing a large collaboration where more than 150 scientists from 9 countries in Europe work together. Our main aim is the study of dileptons production as a direct probe of the hot and dense phase of the nuclear matter obtained in the relativistic collisions of heavy nuclei at the energy range of $1 - 2 \text{ AGeV}$, as well as of the in-medium properties of hadrons produced in such collisions. The physical motivation of these investigations is driven by the need for a better understanding of QCD in the non-perturbative regime and by the expectation of a possible signal for chiral symmetry restoration. The spectrometer used for these studies is installed at the GSI experimental area (cave H), where the ions coming from the SIS stage and the pion beam from a production line, can be focused on the target.

In the following sections, the theoretical concepts and the previous results which motivate the HADES developments will be reviewed. Next, the HADES spectrometer will be described.

1.1 Introduction to the HADES Physics

The GSI (Gesellschaft für Schwerionenforschung) is a center for heavy ion research located in Darmstadt, Germany. It is classified as an European Large Facility, being the participation of European teams partly supported by the European Commission. The present accelerator complex (see figure 1.1), consisting of the Universal Linear Accelerator (UNILAC), the 60 meter diameter Synchrotron for Heavy Ions (SIS), a Fragment Separator (FRS) and the Experimental Storage Ring (ESR), permits to accelerate ions of all elements up to a maximum energy of 1 to 2 GeV per atomic mass unit.

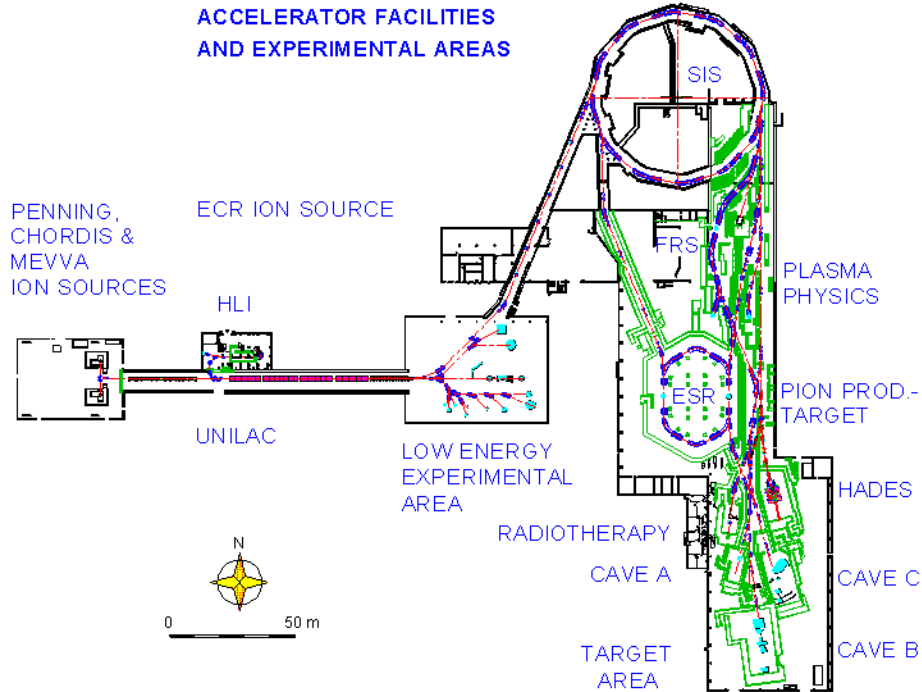


Figure 1.1: GSI accelerator scheme. From the left to the right: the ion sources, the UNILAC, the SIS and the experimental areas.

The UNILAC was upgraded as a high current injector for the SIS in 1999. Being constructed in the seventies as a Wideröe-Alvarez linear ion accelerator for low energies, was continuously improved to add the ability to inject heavy ions on the SIS. A new High Current Injector (HSI) provides an increase of the beam intensities filling the synchrotron up to its space charge limit for all ions [4]. Two ion sources feed the HSI. After stripping and charge state separation, the beam from the HSI is matched to the Alvarez accelerator, which accelerates the highly space charge dominated ion beams without any significant particle loss, up to a few $A MeV$.

The SIS was designed as a high intensity machine with a large magnet aperture. Composed of 24 dipoles working with a bending power of $18 Tm$, 12 triplets and 12 sextuplets, it accelerates the ions while cycling its $216 m$ circumference in 2 resonance cavities at $16 kV$. The SIS main features include the ability to accelerate ions up to Neon between $50 - 2000 A MeV$ and between $50 - 1000 A MeV$ for heavier elements up to the Uranium, with an energy resolution of 10^{-3} . The cycle length is selectable between

1 to 10 seconds, with around 10^{10} ions per cycle. The beam emittance is between $3 - 30 \pi \text{ mm mrad}$ depending on ring filling and extraction time.

1.1.1 Heavy ion collisions at GSI

During a heavy-ion reaction at about 2 AGeV , nucleon densities up to three times the normal nuclear density can be reached. The relative velocity between the colliding nuclei reaches a value around 90% of the light velocity. Many nucleon-nucleon collisions are energetic enough to excite intrinsic degrees of freedom of the nucleons. In this way, new baryon broad resonances can be obtained, and their decays lead to meson emission (π, η, \dots), which interacts with their surroundings. As an example, pions are mainly produced in the decay of $\Delta(1232)$ resonances, the lowest non-strange excited state of the nucleon.

According to various theoretical descriptions (see [5] and references herein), when the nuclei collide, the nuclear matter is compressed in a sequence of nucleon-nucleon collisions; the pressure built up in the reaction zone is released by an expansion of the collision system. During this expansion, meson scattering, absorption and re-emission equilibrate the various hadron species. The abundance and the energies of these mesons are of importance, but cannot be directly observed due to their secondary interactions. After a short time, of the order of a few tens of fm/c ($\sim 3 \times 10^{-23} \text{ s}$), the expansion makes impossible the inelastic reactions between constituents. The hadrochemical composition of the system is then frozen. This point is called *freeze-out* and can be characterized by the products detected: an analysis of the hadronic spectrum, using a thermal model, informs us about the global properties of the nuclear medium such as *freeze-out* temperatures and densities, provided a chemical equilibrium was previously attained in the system. From the number of pions per participant nucleon, the η meson production relative to the pion and the production rates of π, Δ, p, d, \dots the chemical potential and the temperature can be inferred for the different collision systems. These parameter values determined at *freeze-out* are lower limits for the temperatures and densities reached in the high density phase of the reaction.

The problems arise when one wants to obtain accurate information about the previous phases, in particular the high density phase. During a short time (around $10 \text{ fm}/c$) the density reaches values up to three times the normal nuclear density of 0.17 fm^{-3} . It is a perfect room to test the theoretical predictions regarding the change in mass and width of hadrons with increasing density and temperature, associated with a partial restoration of the chiral symmetry, an essential non-perturbative phenomenon as-

	$M(MeV)$	$\Lambda(MeV)$	$\tau(s)$	$c\tau(fm)$
ρ^0	769.3 ± 0.8	150.2 ± 0.8	4.3×10^{-24}	1.3
ω	782.57 ± 0.12	8.44 ± 0.09	7.8×10^{-23}	23.4
ϕ	1019.417 ± 0.014	4.458 ± 0.032	1.48×10^{-22}	44.4

Table 1.1: Basic properties of the vector mesons. Properties are the mass (M), the total width (Λ), the lifetime (τ) and the propagation distance ($c\tau$). Data from [7].

sociated to the particular structure of quantum chromodynamics [6]. One of the most sensitive probes to the effects of the partial restoration of chiral symmetry are the lightest vector mesons ρ , ω and ϕ (see table 1.1). The vector mesons are hadrons of spin 1, which are either isoscalar (isospin 0) or isovector (isospin 1) states. They are composed of a quark and an antiquark. The neutral component of the ρ triplet and the ω meson carry the same quantum numbers as the photon field, which allows the materialization of a virtual time-like photon in an electron pair in their decay. The ϕ meson has the particularity of being made of strange quarks; it has the same type of decays than the ω meson, except that the hadronic decays involve dominantly kaons. The vector mesons are not pure flavor-SU(3) states: there exists a mixing between ω and ϕ due to the different mass of the quarks, and also an electromagnetic mixing between ω and ρ which explains the ω decay into two pions.

A short extension about the vector mesons and their coupling is included in the appendix A. A brief discussion about chiral symmetry and the relation with the meson masses is also included. The appendix B contains a short review of previous dilepton results, which have partially motivated our research.

1.2 The HADES spectrometer

HADES works like a large microscope analyzing the effects on the dense matter obtained in a high energy nuclear collision. The “light” seen by this microscope is made of electron-positron pairs; they are not affected by the strong interaction and therefore transport all the original information about the properties of the particles they are produced from. The dielectrons coming from the vector mesons are emitted in a high-multiplicity hadronic environment and also compete with leptons originated from different sources, like Dalitz decays, bremsstrahlung and external photon

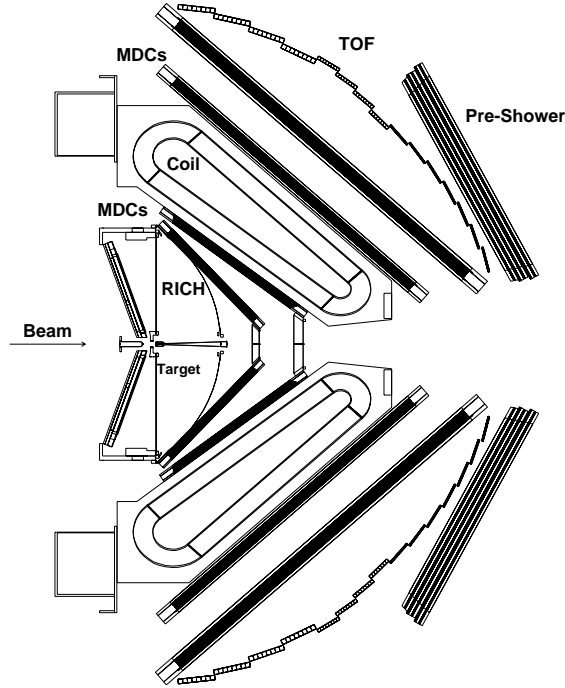


Figure 1.2: Cut of the HADES spectrometer. From the target, the collision products in the spectrometer acceptance crosses through the RICH, the inner drift modules (MDCs), the magnetic field volume, a second set of drift modules, and the TOF or TOFino and Pre-Shower detectors.

conversion. The result is a signal mixed in an enhanced combinatorial background, more complex for the heavier ion collisions.

HADES should investigate the heaviest collision systems in the SIS energy range. Then, several properties are demanded in their design:

- **Large dilepton acceptance**, ($\epsilon_{pair} \approx 40\%$) which results an essential point due to the tiny dilepton branching ratio, in the order of 10^{-5} (see table A.1 in appendix A).
- **Capability to deal with high count rates** to accumulate enough significant events in a finite time, allowing the operation at large beam intensities, up to 10^8 per second. This corresponds to 10^6 minimum bias interactions and 10^5 central collisions per second for a 1% interaction length target. Using these numbers, a pair coming from a ρ decay can be detected approximately every 10 seconds, for

Au+Au collisions at 1 $AGeV$.

- **Capability to support the large particle multiplicity**, produced by the central collision of the heaviest collision systems at large SIS energies. Up to 150 charged hadrons and 25 photons can accompany the lepton pairs within the spectrometer acceptance.
- **A selective trigger scheme**, able to accept only those events with lepton pairs, mainly those of high mass. Pairs coming from pion Dalitz decay or conversion should be recognized and removed from the sample in an early stage.
- **Rejection of hadronic and electromagnetic background**, which could obscure the dilepton signal.
- **Flat acceptance in mass and in transverse momentum.**
- **Improved mass resolution** with respect to the previous experiments. The individual identification of the vector mesons requires a mass resolution of the order of the ω width ($\Delta M/M = 1\%$ (σ) at approximately $780MeV$).
- **Low mass materials** are chosen in all detectors and support structures to minimize the multiple scattering. The target construction and detector materials are optimized to limit the total radiation length to $X/X_0 \approx 10^{-2}$.
- Finally, **a complete event characterization**, including charged particle multiplicity and momentum distributions.

The experimental setup (see figures 1.2 and 1.3) is made of six identical sectors covering a polar angle between 18 and 85 degrees and practically full azimuthal range, only limited by the magnet coils cases and the detector frames. The spectrometer is composed of the following detectors:

- A Ring Imaging CHerenkov (RICH) threshold detector. The RICH identifies the leptons, being practically insensible to hadrons, even to the faster pions (up to 3 GeV pions).
- Two sets of two Multiwire Drift Chambers (MDCs) track the charged particle paths and determine their momenta using a given magnetic field map. The complete particle identification is possible when the particle track is projected onto the other detectors.

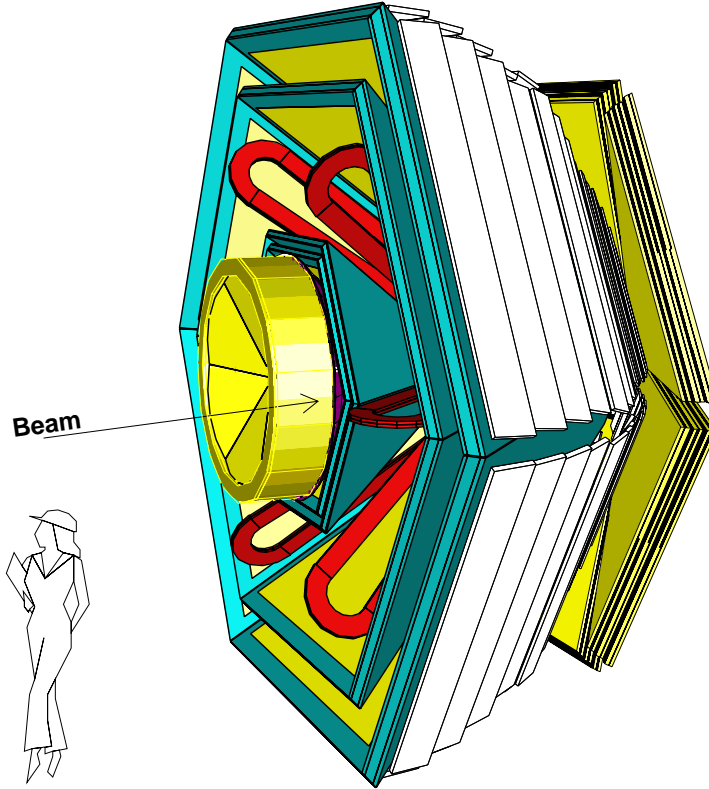


Figure 1.3: A 3D view of the HADES detector, where the hexagonal symmetry of the spectrometer results apparent.

- A superconductor magnet divided in six symmetrical coils, shaping a toroidal magnetic field in a limited space between the two sets of MDCs. The momentum kick is lower or in the order of $100 \text{ MeV}/c$, a compromise value to improve the momentum resolution while the low momenta particles still remain in the detector acceptance. For the same reason, the momentum kick is larger for the smallest track polar angles, which correspond to larger particle momentum due to the Lorentz boost. The magnetic field reaches a maximum value of around 3 T close to the coil case, but produces a maximum magnetic field of 0.7 T in the acceptance region (approx. along 0.5 m path).
- A Time-of-Flight (TOF) plastic scintillator wall, covering the region of large polar angle. It is composed of thin plastic strips, to minimize the double-impact probability. The fast photo-multipliers are

mounted on both extremes of the plastic strips. A set of four plastic scintillators (TOFino) covers the region of small polar angles in each sector, giving a basic information for low multiplicity collisions. The TOF detector is able to discriminate pions and protons from electrons up to $0.5 \text{ GeV}/c$ and $2 \text{ GeV}/c$, respectively.

- Designed explicitly for the lower polar angles, where time-of-flight measurements are less effective in the lepton identification, the Pre-Shower detector closes the spectrometer. The Pre-Shower consists of three gaseous multiwire detectors with two lead converters between the detectors. The charge deposited in the gaseous detectors before and after the converters is compared, to identify and separate those particles able to develop an electromagnetic or hadronic shower.
- A set of fast diamond detectors is used as start and veto detectors.

Given this experimental setup, the sequence of the acquisition can be characterized by the following steps:

1. The particles originated at the interaction target cross the detectors, producing electronic signals in part of the several thousands of the spectrometer channels. As the physical processes which lead to the detection work at diverse velocities for the different detectors, the electronic readout and concentrators should use buffers for the storage of the event information. There, data await for the decision of a preceding trigger level or any other complementary information, before further processing. The readout is a data driven system, where the operation is started by the central trigger unit.
2. A first-level trigger, based on the Start and TOF information, selects central events via the multiplicity information. Events passing a cut in the charged particle multiplicity in the TOF detector acceptance are considered in the next steps, while those with less charged particles are removed. The decision should be taken in a few tens of ns and the trigger signals are used to gate the start signals. This will reduce the events rate by a factor 10. A positive first-level trigger initiates the readout of all detectors at a rate of up to 10^5 Hz . The DAQ first-level pipe of the readout system is filled with data sampled on each valid first-level trigger, and remain stored there until a decision of the second-level trigger is available.
3. A second-level trigger selects events with dilepton pair candidates within a given invariant mass range, using the information coming

from the RICH, Pre-Shower and TOF detectors. Accepted events should present electron signatures in the detectors: ring candidates in the RICH and the corresponding electromagnetic cascade in the Pre-Shower detector or the correct time-of-flight in the TOF. Furthermore, the candidates are correlated taking into account the magnetic field; they are required to have a minimum opening angle and a minimum momentum, to create a candidate with sufficiently high invariant mass. The second-level trigger reduces the event rate by a factor of about 100 with a latency time of about $150 \mu s$. A positive second-level trigger will result in the event data passing from the first-level DAQ pipe to the second-level pipe. A negative decision initiates the removal of the event from the first-level pipe without storing it.

4. A third-level trigger, not yet implemented, would perform a consistency check of the potential electron candidates determined in the second-level trigger, evaluating the hit pattern of wires from the MDC modules. Regions of interest, defined by the extrapolation of the electron candidates path from the RICH, Pre-Shower and TOF detectors onto the MDC modules, are observed and those tracks compatible with the lepton candidates are searched for, in a minimum number of planes. The third-level trigger would gain a reduction factor of 10 working within $10 ms$.
5. Data from the second-level DAQ pipe are matched together to construct a complete event in the event builder, and then stored in tapes for a subsequent off-line analysis.

Using all the trigger levels it is possible to reduce the number of events stored for later analysis by a factor 10^4 . The spectrometer is designed to cope around 10^6 primary interactions per second (intensities of 10^8 primary ions on a 1% reaction rate target). Combining both numbers, around 100 events containing a lepton pair in the most interesting mass range will be moved to the tape for further analysis every second.

1.2.1 The diamond detectors

Two identical diamond detectors of octagonal shape provide the "start" and the "veto" detectors for the spectrometer.

The diamond detectors [8] are polycrystalline carbon substrate synthesized using a Chemical Vapor Deposition (CVD) technique, which allows the diamond to grow in an environment under control. Due to a band gap

of 5.5 eV, no pn-junction is needed. After metallization of the electrodes, the detectors are ready to work. The detector signals are amplified with low noise, broad-band amplifiers. This detector-electronics combination presents an intrinsic time resolution of up to 29 ps and a count rate capability of more than 10^8 particles per second for a single detector channel. The detectors are radiation resistant and can be constructed in very thin layers.

For the HADES spectrometer, two CVD-diamond detectors of $25 \times 15 \text{ mm}^2$ are installed 75 cm upstream and downstream the target position. The first one is to provide the “start” signal, whilst the downstream detector shall veto all particles that have not collided with the target nuclei. The strip widths are optimized such that a coincidence of one start detector strip with three veto detector strips is sufficient for a veto efficiency of 96.5%. The detectors are very thin (100 μm) to keep multiple scattering and secondary reactions very low, within their bulk.

1.2.2 RICH detector

The RICH (Ring Imaging CHerenkov) [9] detector identifies unambiguously leptons in the large hadronic background, made of pions and protons. The identification principle is the Cherenkov light production, emitted whenever charged particles pass through matter with a velocity v exceeding the velocity of light in the medium

$$v > v_t = \frac{c}{n} \quad \text{or} \quad \beta n > 1 \quad (1.1)$$

where n is the refractive index of the medium and v_t the threshold velocity. Cherenkov light is emitted under a constant angle α with respect to the particle trajectory, given by

$$\cos \alpha = \frac{v_t}{v} = \frac{1}{\beta n} \quad (1.2)$$

The threshold velocity for particles is determined by the radiator refraction index, and quoted by the Cherenkov threshold

$$\gamma_t = n/\sqrt{(n^2 - 1)} \quad (1.3)$$

The detector consists of a gaseous C_4F_{10} radiator placed around the interaction point, closed in the back part by a VUV spherical mirror, divided in 18 sections. The refraction index of the radiator gas takes the value $n = 1.00151$, giving $\gamma_t = 18.2$; leptons with momenta between 100 and 1500 MeV/c will produce Cherenkov radiation, while hadrons in the

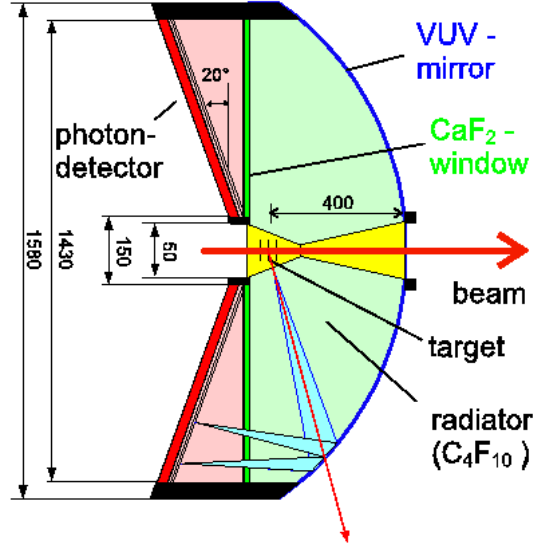


Figure 1.4: The RICH detector.

same momentum region have velocities far below the threshold. The radiator gas was chosen due to the transparency to the ultraviolet light (down to wavelengths of 145 nm , this requirement eliminates high molecular weight gases) and the absence of significant scintillation from charged particles (this condition practically eliminates CF_4), being the number of generated photons in the short path sufficient for the detection.

The light reflected in the mirror crosses a 5 mm thick CaF_2 window used to separate the radiator gas from a gaseous photon detector operated in pure CH_4 . The window is made of 64 single crystals of hexagonal shape. The material, CaF_2 was chosen due to the high transmission in the VUV wavelength region (around 70% at 140 nm). The photon detector consists of six multiwire proportional chambers with three wire layers and cathode pad readout. The size of the 28272 pads varies from 7×6.6 to $4 \times 6.6\text{ mm}^2$ to compensate for the mirror spherical aberration. The Cherenkov photons enter in the gaseous detector through the window and are converted to photo electrons in a solid CsI photo-cathode evaporated onto the pads. The chamber is photo sensitive only in the VUV wavelength region (approximately between 145 and 210 nm), where the CH_4 has a good transmission. The readout system consists of a front end part for analog signal processing and a digital part for readout control and data transport. It is highly modularizable and presents a multi-level pipe-line

architecture, interfaced to standard VME bus connections. The final detection efficiency for single photo electrons is larger than 95%.

The spherical VUV-mirror has a diameter of 145 cm and a curvature radius $R = 870$ mm. It is segmented into six sectors, with three trapezoidal mirror panels per sector. To minimize multiple scattering and photon conversion, the panels are made of pure Carbon, machined to a thickness of 2 mm. Then, they are polished and coated with a thin Al and MgF₂ layer. The average reflectivity is around 80%. Due to the large acceptance of the mirror and the location of the target ($0.46 R$, closer to the mirror than the curvature center), the azimuthal and polar focal surfaces have non-negligible curvature, which leads to the formation of ellipses instead of rings for large polar angles. The pad size and shape corrects to first order the eccentricity of the ring images and leads to rings of almost constant diameter of about nine pads (~ 5.5 cm) for all track angles.

The effect of the quantum efficiency of the photocathode, the mirror reflectivity and the transmission of the radiator, detector gas and CaF₂ window has been measured, resulting in a figure of merit $N_0 \cong 109$. This corresponds to 12-21 detected photons per ring, which should allow a lepton trigger efficiency above 90% at a reduction of 1% for first-level trigger signals.

The readout of the RICH [10] has to be designed to handle trigger rates of up to 10^5 events per second. To achieve the desired speed and performance a large part of the signal processing and buffering is done at the detector. Signals from 16 pads are handled by an analog signal processing chip, which sequentially passes the pulses to an 8 bit ADC. The pulse heights are compared to a threshold, adjusted independently for each channel, and then written to a FIFO memory. Also the hit pattern is accumulated in a shift register and stored in a separate FIFO. The pattern information, of a fixed length, is first readout and passed to the trigger processor searching for rings. The pulse-height, of variable and larger size, is stored later in an intermediate buffer until a trigger decision is available.

The analysis of the detector output comprises a “cleaning-out” to remove noise or isolated hits, and a “labeling”, where the image is decomposed in parts containing groups of hit pads, to perform the ring recognition on them. Two independent algorithms are used for the ring recognition: the *Pattern matrix*, where the algorithm is based on fitting a pattern image of a ring to the pad plane, and the *Hough transformation*, where the ring centers are found in the local maxima of a two dimensional histogram filled with centers of the circumferences obtained from all possible sets of three hit pads. The first algorithm is fast but its accuracy can decrease for

deformed rings, corresponding to large polar angles, and also for double crossing rings, while the second algorithm does not depend on the radius of the ring and is able to identify a ring even in case of shape distortions, losing less efficiency with noisy samples.

For the second-level trigger ring recognition, a fast pattern matrix algorithm is implemented, where weights are replaced by booleans (ring and veto regions). Moving the pattern matrix over the pad surface, in a highly parallelized process for velocity reasons, rings are searched for based on a criterion in the minimum number of pads in the ring region, while keeping the number of pads in the veto region below a threshold. Efficiencies of around 93% are achievable at mis-identification rates of 0.26 fake rings/event [11].

1.2.3 Multiwire Drift Chambers (MDCs)

The HADES tracking system consists of four drift chambers (divided in 6 modules, one per sector), two before and two behind the field area of the superconducting magnet. The module sizes range from $88\text{ cm} \times 80\text{ cm}$ for the inner one to $280\text{ cm} \times 230\text{ cm}$ for the outer. Each module is composed out of six drift cell layers, defined between cathode wire planes. The layers are oriented in five different stereo angles, shaping a butterfly pattern, to enhance the precision along the coordinate of the momentum kick and reduce ghost reconstruction. The MDCs are operated using an Helium-Isobutane mixture, the Helium being selected to minimize the multiple scattering.

The next chapter will deal with the HADES MDCs in detail, including a description of the track reconstruction software.

1.2.4 Pre-Shower detectors

The Pre-Shower detectors [2,3] are located in the external part of the spectrometer. Their main task is the measurement of electromagnetic showers produced in lead material, for lepton/hadron discrimination at forward (low polar) angles.

The HADES Pre-Shower detectors consist of 2 lead converters ($X/X_0 = 2.5$ each one) interleaved between three wire chambers with pad read-out. The three chambers have the same basic construction and differ only slightly in dimensions, adjusted to cover the same solid angle with respect to the target. The detector has the shape of a trapezium, covering low polar angles (between 18° and 45°) and full azimuthal angle in each sector. This corresponds to the zone where particles with larger energy crosses

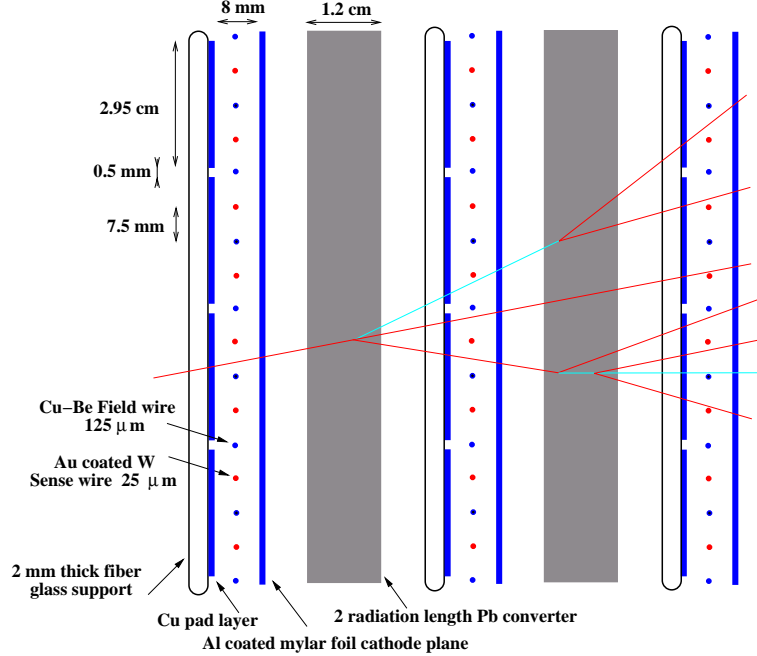


Figure 1.5: *The Pre-Shower detector.*

the spectrometer; they have a larger probability to create an electromagnetic shower and their identification is more difficult using time-of-flight methods alone. Shower recognition is performed by comparing the number of particles measured before and after the lead converters. Particle hits are identified via the charge produced in ionization processes in the wire chambers working in self quenching streamer mode (SQS). The main advantage of the SQS mode is that the induced charge is nearly independent of the particle specific energy loss and, therefore, low energy protons do not produce larger signals in the post converter chambers.

The Pre-Shower detector chambers consist of a cathode pad plate, a plane of sense and field wires and a second cathode plane, symmetrically disposed to the cathode pad plane to configure the drift cells. The cathode pad plate is made of 8 fiber glass plates covered with thin copper layer, 1.5 mm thick, where pads are organized in rows and columns aligned with respect to the target. In this way, particles coming from the target cross a set of fixed pads in the three modules. Pads are manufactured using an etching technique, and have been optimized to minimize the double hit probability, maintaining a reasonable area for shower integration. There are 32 pad rows and between 32 (in the top part) and 20 (in the bottom

part) columns, with heights between 4.5 and 3 *cm*, for a total number of 942 pads. Two rigid frames made out of Stesalit epoxy resin support the wire plane, made of 25 μm golden tungsten sense wires and 125 μm copper-beryllium field wires. The 89 sense wires are maintained at around +3400 *V* whereas the field wires are grounded. Large tensions are applied to guarantee a small gravitational wire sagitta and to minimize the distortion due to the high electric field. The chamber cells defined by the wires and the cathode pads are aligned, to cover an integer number of cells per pad. Sense and field wires are separated by 7.5 *mm* and both are 8 *mm* away from the cathode planes. A polished stainless steel cathode plane (0.5 *mm* thick) closes the symmetrical drift cells. This choice simplifies the detector construction when compared to a multiwire plane, having very good gas aging properties and uniform field configuration at the cathode surface. The lead converters are sandwiched between two stainless-steel plates, being fixed to the aluminum frames of the gas chambers.

The pads for each row in the cathode pad plane are connected via twisted pairs to 32 channels Front-End ASIC boards. 32 ASICs are needed for the readout of a module and a total of 576 for all the sectors, for a maximum number of 18432 channels. The data from the Front-End boards are transmitted to a control board to be digitized and transferred within 10 μs (first-level trigger decision time) to the shower processor, where an image processing unit (IPU) determines the position of the possible shower events. The results are transmitted to the Matching Unit where the information will be used in the second-level trigger.

The identification analysis is based on the detector response to the lepton electromagnetic shower. First, the charge measured on the Pre-Shower detector is compared to a predefined threshold value and local maxima are searched in order to assign the central pad to a shower candidate. Then, the sum of the induced charge in the pad where the maxima was found and the eight closest pads is performed. The same sum is calculated for the corresponding nine pads in the second and third chambers. The electromagnetic showers are shorter than the hadronic showers, and the ratio between the charges in the second and third chambers with respect to the first chamber informs about the shower type. An electromagnetic shower is detected when the total charge in the second or in the third chamber is larger than a function of the charge in the first one, determined by simulation, to increase the lepton detection efficiency while minimizing the number of fake lepton candidates.

1.2.5 TOF (Time-Of-Flight) detectors

TOF and TOFino detectors [12] cover the complete spectrometer acceptance, measuring the time-of-flight of the charged particles (relative to a given start detector time). The TOF main tasks are:

- Measure the charged particle multiplicity, in order to trigger on the centrality of the collision (first-level trigger).
- Perform electron/hadron identification and participate in the second-level trigger.
- Characterize the full event in the analysis phase, identifying all charged particles using the time-of-flight information.

The TOF detector is made of scintillating plastic bars (BC408), read out at both ends by EMI 9133B photo-multipliers. This double-reading allows the reconstruction with a good accuracy of the time-of-flight from the target ($\sigma = 100 - 150$ ps) and the hit position along the bar itself ($\sigma = 1.5 - 2.3$ cm). Eight bars are included in each carbon case, and eight carbon cases are assembled in each sector, covering the polar angles between 85° and 45° . The pads profile is a 2.0×2.0 cm² rectangle for the inner four carbon cases and 3.0×3.0 cm² for those at larger polar angle.

The TOFino detector is made of four scintillating planes covering the low polar angles, up to an angle close to 45° . Only one photo-multiplier is used in the case of the TOFino. The substitution of the TOFino detector by an RPC (Resistive Plate Chamber) wall is foreseen in the next future, in order to improve dramatically the granularity, to deal with heavy ion reactions.

From the photomultipliers signal not only a time is obtained, but also an amplitude. TDC and ADC are integrated on the same VME motherboard that hosts 32 channels and implements zero suppression and a fast VME block transfer. For the second trigger unit, two ADC and two TDC values per scintillator strip and event must be first calibrated; then position and time-of-flight information must be calculated and corrected. This task is performed in an array of six digital signal processors (SHARC) containing 32 floating point computing units.

1.2.6 The trigger scheme

The selection of dilepton events from central collisions is designed to work using a three levels trigger system [11, 13, 14]. The large amount of raw

data (evaluated in up to 9 Gb/s) is reduced, enhancing those events with potential dilepton candidates in an online analysis.

The first-level trigger (LVL1) selects the 10% most central heavy ion collisions via the multiplicity of charged particles which is measured in the TOF scintillator array. A positive first-level trigger initiates the readout of all detectors at a rate of up to 10^5 Hz. The fast logic pulses from the TOF constant fraction discriminators are received by a Multiplicity Trigger Unit (MTU), which performs an analog sum of these signals as a first step in determining the multiplicity. The multiplicity information generated by the unit is used to gate the (externally provided) start signal with a variable time window.

The second-level trigger (LVL2) consists of two stages. In a first step a search for electron signatures is performed by looking for ring images from Cherenkov light on the RICH pad plane. Moreover, clusters with the signature of an electromagnetic shower on the three planes of the shower detector as well as particles with appropriate time-of-flight in the scintillator detector are selected.

The resulting position information from this first stage is correlated (between the inner RICH and the outer Pre-Shower and TOF detectors) taking into account the bending in the magnet field between the two detectors and thereby applying a selection on the particle momenta. This task is performed in the Matching Unit, which receives the information from the IPUs (Image Processing Units) and transforms it to a common coordinate space using a memory look-up. First, the hit patterns for each lepton candidate must be within a small azimuthal and a larger polar window (momentum dependent). In a second step, all combinations of lepton candidates with opposite polarity with a minimum opening angle are selected. Their invariant mass is calculated and pairs within a predefined mass window are selected. The Matching Unit must provide a second-level trigger decision in less than 10 μ s, on average. A second-level trigger signal is generated by the Matching Unit. The second-level trigger reduces the event rate by about a factor of 100 with a latency time of about 15 events (150 μ s). The maximum latency allowed corresponds to the second-level trigger pipe depth, around 200 μ s.

The third-level trigger (LVL3) would perform a consistency check of the potential electron candidates determined in the second-level trigger, evaluating the hit pattern of wires in the MDC modules. The electron hit positions determined in the second level trigger both for the RICH and the Pre-Shower and TOF detectors define regions of interest in the MDC modules. The regions of interest must be determined from a simple

approach which assumes a single kick plane in the magnet and basic logical correlations must be evaluated for the corresponding wire pattern. The third-level trigger gains a reduction factor of 10. After the three trigger levels, and following the designed discriminations and rates in each level, approximately 100 events per second will be finally written to the tape, reducing the minimum bias event rate by a factor of 10000.

The communication between the detectors is realized via a dedicated trigger bus between a central unit (CTU) for each trigger level and several detector trigger units (DTU). The bus distributes the two levels trigger decisions, Event-IDs, trigger codes and detector busy and error conditions. The CTU generates and distributes the trigger decisions, generates unique event IDs and handles event types as well as busy and error conditions. It also controls the VME access to all functions for slow control and debugging purposes. This information is distributed over the trigger bus to several DTU modules, which convert the incoming information into detector specific signals and data formats. The DTUs are responsible for the handling of the incoming HADES trigger bus signals and control the various readout components via local readout system trigger buses. They monitor the readout systems and generate their busy and error conditions, forwarding the status information to the CTU.

1.2.7 The data acquisition (DAQ)

The data acquisition system [12] is based on a dedicated ATM data network from the various detector subsystems, transferring asynchronously the subevents from the VME CPUs to the common event builder which assembles the full events. A data tapping speed of up to 5 MB/s could be achieved, corresponding to up to 2000 events/s for a C+C collision.

The DAQ system uses a two pipe architecture. The first pipe of the readout system is filled with data sampled on each valid first-level trigger. In the first-level pipe a trigger tag is distributed for each subevent. Trigger tags are used to simplify identification of faulty modules with errors in the data transmission. The data remains stored until a decision of the second-level trigger is available. After a positive decision, the event data are written to the second-level pipe. A negative decision initiates the removal of the event from the first-level pipe without storing it. The second-level pipe is implemented in the RAM memory of the VME bus system, being directly mapped in their address space for direct access by a fast data transport interface to the event builder. The CPU controllers for the different detector subsystems are accessible via Ethernet for configuration, diagnostic and error handling purposes.

1.2.8 Software overview

In the previous description of the spectrometer has been stated the complexity, the diversity and the big amount of data produced. Therefore, a comparably large and complex software code must be used for the organization, reconstruction and analysis of these data. The simulation of the different possible scenarios and the continuous test and comparison with the real results is a crucial point, during all the development of the experiment, from the initial design up to the experimental comparison with available physical codes.

The HADES software package for the data simulation, reconstruction and analysis is called HYDRA (HADES System for Data Reduction and Analysis) [15]. HYDRA is written in C++, an object oriented programming language. Object oriented represents a new paradigm for software modeling, including the design, evaluation and implementation and enforces the code modularity, reusability and readability. These features allow the management and maintenance of large and complex programs, made by distant collaborators. The use of the object oriented paradigm represents an innovative advance with respect to previous FORTRAN-based analysis codes, commonly used in previous experiments.

The concept of the object, a significative representation of a real or abstract entity, which is the element of a class composed of a set of related entities, is a semantic approximation, closer to our minds organization. The main tools to manage the complexity given by the object oriented approximation are the encapsulation, the inheritance and the polymorphism. The *encapsulation* is related with the concept of object, represented as a set of data of members (its state or basic features) and a set of functions or methods (its behavior or reaction). Hiding or encapsulating the implementation of these elements, being private (not accessible to non-class methods), allows the modification of the internal code and the correction of errors without any impact in another parts of the code, even those parts using the modified features. The *inheritance* is used to specialize and generalize concepts, reducing dramatically the code volume and systematizing the data organization within the code. The *polymorphism* allows the use of identical semantics applied to the functions of different classes which inherits from a common parent. The parent can define virtually the behavior, if there is no knowledge at this point of their details. The correct interpretation of the behavior (the election of the right code for each case) is performed automatically by the language based on the object type. From the programmer's point of view, the polymorphism allows an easy code expansion and simplification and force the use of inheritance to structure

the code.

HYDRA is an application based in ROOT [16], an Object Oriented Data Analysis Framework. ROOT is designed for its use in High Energy Physics experiments, providing an user interface, data organization and streaming, histogramming, automatic documentation and many other interesting features. For simulation, a HADES Simulation package called HGeant has been developed, based on Geant 3.21 [17].

The HYDRA classes can be categorized in a few groups. There is a fundamental class called HADES which encapsulates the whole reconstruction program, providing methods to control the different tasks which can be realized. The HADES class contains: the data source where the events data are read from, the tasks set (see below), the information about the spectrometer structure, the output files, the output tree and the parameters database. There are classes for the storage of the data in different levels of refinement (see section D.1) as well as classes to manage the input/output of the data. An important group of classes contains and manages the parameters, including a version management for parameters which can be modified. Finally, there are classes to perform tasks; the tasks are the representation of algorithms or groups of algorithms.

The basic unity in the data processing is the event, either real or simulated. A physical event comes from an interaction between a beam particle and the target. One event is reconstructed in steps, so each step in the reconstruction process produces one level of reconstructed data. The data inside an event are contained in “categories”, classes specialized in the efficient storage of the information and its iterative retrieving. A category is essentially a container of objects within an event, with the extra characteristic that every object in a category belongs to the same class. The simulated events generated by HGeant can be used as input for the reconstruction program, instead of real ones, in order to test the software. Therefore the simulated events must conform to the same structure as the real ones, so the software can seamlessly process both real and simulated events. This is automatically granted by inheriting the simulated event class from the generic event class.

Two additional tools are also used regarding the parameters and geometrical data storage and the software development. The huge set of parameters needed for the calibration and control of the reconstruction tasks are stored in an ORACLE database [18]. From the database the parameters can be automatically used in the HYDRA routines via a built-in interface. The code is being continuously updated and improved, using a control version system (CVS) [19], a tool for the development of software

between different working groups (sometimes really far away one from the others). It is organized in independent modules, grouped in libraries which can be dynamically linked in run time, freeing machine resources.

1.3 Commissioning and planned studies

The installation of the HADES spectrometer began in April 1998, with the installation of the superconducting magnet. The mainframe and detectors were installed in successive commissioning processes. All 6 sectors of the Pre-Shower detector, the outer TOF wall and the forward TOFino and the RICH detector are now installed. The complete two inner planes of the MDCs (12 modules) and 6 outer modules (four modules MDC III and two modules MDC IV) are also complete.

The following collision systems were used up to now in the spectrometer commissioning:

- November 2000: C+C collisions at $E = 1.5 \text{ AGeV}$, recording several millions of events and 1.5×10^6 events with magnetic field on. The analysis performed has demonstrated the ability of the reconstruction software to find the different event vertices along the beam line (as will be shown later in this work). Using the information of several subdetectors, a successful identification of particles was performed for the first time, allowing the lepton identification in the large hadronic background and measuring the particles momenta.
- April 2001: C+C collisions at $E = 1.5 \text{ AGeV}$, extending the setup and testing improved electronics.
- May 2001: A Chromium beam on Aluminum target served to test for the first time larger charged particle multiplicities on the detectors.
- November 2001: 1.9×10^8 C+C collisions at $E = 2 \text{ AGeV}$, mainly used to commission the second-level trigger mechanism and to improve the data acquisition system.

The preliminary studies performed by the spectrometer show their capability to perform the high resolution invariant mass spectra in the heaviest collision systems. Proton beams can be used to determine the η Dalitz decay in elementary pp reactions and to determine quantitatively the HADES acceptance for e^+e^- pairs. After compiling a larger statistical in C+C systems and testing the DLS results, it is planned to study the heaviest collision systems, searching for the clearest hints of the in-medium effects.

Before, it is also planned to study $\pi^\pm p$ reactions, using the pion beam facility. In these interactions the meson production can be more easily linked to the parent baryonic resonance. The pion beam can inject pions to study the production of ω and ϕ vector mesons at normal matter density, in reactions $\pi^- p \rightarrow n\omega$ and $\pi^+ p \rightarrow \rho\Delta^{++}$. The precise measurement of the dilepton production from the channels opened in these reactions has to be used later in π^- Pb collisions, which can probe ω meson properties inside ground state nuclear matter. The interpretation of such data requires detailed knowledge of the dielectron yield from competing processes. In a heavy ion collision, the production of dileptons by different sources (even the vector mesons) happens during the different stages of compression and expansion, involving high as well as low baryon densities. Then, the dilepton invariant mass spectrum from such a collision contains contributions from decays at different densities, being not specific of the high density phase. The pion beam can inject pions to study the production of ω and ϕ vector mesons at normal matter density. If the vector mesons are produced recoilless by choosing specific kinematical conditions, a large fraction of the vector mesons will decay into lepton pairs within the nuclear medium.

Bibliography

- [1] H. Neumann *et al.*; Acta P. P. **B44** (1994) 195.
- [2] P. Salabura *et al.*; Nucl. Phys. **B44** (1995) 701.
- [3] P. Salabura; Acta P. P. **B27** (1996) 421.
- [4] W. Barth *et al.*; *Beam Measurements at the GSI High Current Injector*, in PAC 2001, Proceedings of the 2001 Particle Accelerator Conference, Chicago, Illinois, 2001.
- [5] V. Metag; *Heavy-ion Reactions at the GSI Darmstadt*, GSI-Preprint 98-67, 1998.
- [6] M. Soyeur; *Vector Mesons in the Nuclear Medium*, in International School of Heavy ion Reactions, 3rd Course, Erice, Italy, October 1993. World Scientific, Singapore, 1994.
- [7] Groom *et al.*; Particle Data Group. *Review of Particle Physics*, Eur. Phys. J. **C15** 1-878 (2000).
- [8] E. Berdermann *et al.*; Nucl. Phys. (Proc. Suppl.) **B78** (1999) 533-539.

-
- [9] K. Zeitelhack *et al.*; Nucl. Instr. and Meth. **A433** (1999) 201.
- [10] A. Kastenmüller *et al.*; *A Prototype Readout for the HADES RICH Detector*, Internal HADES report, 1999.
- [11] J. Lehnert *et al.*; Nucl. Instr. and Meth. **A433** (1999) 268.
- [12] HADES Technical Proposal, GSI Darmstadt, 1994.
- [13] J. Lehnert, W. Kühn, E. Lins, M. Petri; *The Trigger System for the HADES Detector*, Internal HADES report, 1997.
- [14] M. Traxler *et al.*; *The second Level Trigger System of the HADES Detector*, Internal HADES report, 1999.
- [15] M. Sanchez; *Diseño y programación orientados a objetos de la reconstrucción de sucesos en el experimento HADES de colisiones nucleonucleo*, Tesina, Univ. Santiago de Compostela, 1999.
- [16] R. Brun, F. Rademakers; *ROOT - An Object Oriented Data Analysis Framework*, Proceedings AIHENP'96 Workshop, Lausanne, Sep. 1996. Nucl. Inst. and Meth. **A389** (1997) 81-86.
See also <http://root.cern.ch/>
- [17] *GEANT, Detector Description and Simulation Tool*, <http://wwwinfo.cern.ch/asd/geant/index.html>
- [18] *ORACLE Database*, <http://www.oracle.com>
- [19] *Concurrent Versions System*, <http://www.cvshome.org>
See also <http://www.gnu.org/directory/cvs.html>

Chapter 2

The HADES multiwire drift chambers

The measurement of the particles momentum requires the precise determination of their trajectories, deflected by a well known magnetic field. A set of four drift chamber planes, two before and two behind the magnetic field volume, is used as tracking system in the HADES spectrometer. In the next sections, a complete description of these detectors follows.

2.1 Introduction to the drift chambers

A drift chamber is an apparatus for measuring the space coordinates of the trajectory of a charged particle. This is achieved by detecting the ionization electrons produced by the charged particles in the gas of the chamber and by measuring their drift times and arrival positions on sensitive electrodes [1].

The charged particles crossing the gas of the drift chamber randomly ionize the gas atoms. Each collision with a gas molecule can produce atomic excitations and a primary ionization where one or more electrons are ejected. Most of the charge along the track comes from secondary ionization, where the primary fast electrons interact with other molecules not affected by the original charged particle. The primary electrons, emitted basically perpendicular to the incident track, lose their kinetic energy in collisions with the gas molecules, scattering almost randomly and producing secondary electrons, until they have lost their kinetic energy.

The frequency distribution of the (k) encounters along a length L follows a Poisson distribution with mean L/λ , where λ represents the mean

free path between ionizing encounters

$$P(L/\lambda, k) = \frac{(L/\lambda)^k}{k!} e^{-L/\lambda} \quad (2.1)$$

The mean free path is inversely proportional to the electron density and the ionization cross section per electron. It depends also on the particle velocity, due to the minimum in the primary ionization cross section of the gases for an approximate value of $\gamma = 4$. Approximate values for the inverse mean free path in gases at normal density run from the minimum values 3.5 /cm in Helium to several tens of ionizing collisions per cm in the heavier gases. The probability distribution of the distance l between encounters results in an exponential distribution

$$f(l)dl = P(l/\lambda)P(dl/\lambda, 1) = \frac{(l/\lambda)^0}{0!} e^{-l/\lambda} \frac{(dl/\lambda)^1}{1!} e^{-dl/\lambda} = \frac{1}{\lambda} e^{-l/\lambda} dl \quad (2.2)$$

The ionization does not account for the complete fast particle energy loss but, for the detection of the particles, one has to know first the amount of ionization along the track and the associated fluctuation phenomena. On average, the creation of a free electron takes an energy W , which can be obtained from the average number of ionization electrons $E(N_i)$ created along a trajectory of length L

$$W = L \frac{E(dE/dx)}{E(N_i)} \quad (2.3)$$

where $E(dE/dx)$ is the average total energy loss per unit path length of the fast particle. The energy W depends on the gas composition and density, and on the charge of the incident particle, being practically independent of the initial particle energy (above a few *KeV* for electrons and a few *MeV* for alphas). For pure noble gases, W varies between 46 *eV* for He and around 25 *eV*, typical value for organic vapors. These numbers are larger, in a factor between 1.5 and 3, than the corresponding minimum ionization potential for each gas. The total ionization in a noble gas can be increased by adding a small concentration of molecules with low ionization potential. In this case, the mechanism corresponds to the de-excitation of excited (metastable) states of the noble gas via collisions with the larger molecules. Then, the ionization production delay can be as large as several microseconds.

The average energy loss between a traveling particle and a single atom was calculated by Bethe in 1930 using a quantum mechanics approach. The

energy lost per unit path length (not only by ionization) can be obtained adding the energy lost by all the atoms in the vicinity of the fast particle

$$\begin{aligned} \frac{dE}{dx} &\cong \frac{4\pi N e^4 z^2}{m c^2 \beta^2} \left(\ln \frac{2m c^2 \beta^2 \gamma^2}{I} - \beta^2 \right) \\ &\cong 0.3071 \left(\frac{MeV}{g/cm^2} \right) \rho z^2 \frac{Z}{A} \frac{1}{\beta^2} \left(\ln \frac{2m c^2 \beta^2 \gamma^2}{I} - \beta^2 \right) \end{aligned} \quad (2.4)$$

where $m c^2$ is the electron rest energy, N the density of the electrons in the matter, I the mean excitation energy of the atom and z and β the charge and velocity of the transverse particle ($\gamma^2 = \frac{1}{1-\beta^2}$). In the second expression Z/A is the atomic number to atomic weight ratio, ρ the gas density and it was used $N = N_A \rho Z/A$, with N_A the Avogadro's number. Then, Bloch calculated values of I using the Thomas-Fermi theory of the atom. Equation 2.4 is known as Bethe-Bloch formula¹. The mean excitation energy is often considered a parameter to be fitted from the measurements of the ionization energy loss near the minimum.

The ionization energy loss is, to a good approximation, proportional to the electron density in the medium (given by the term $N_A \rho Z/A$) and to the square of the projectile charge, and otherwise depends mainly on the projectile velocity. The energy loss rate is displayed in figure 2.1 as a function of the particle momentum, for different materials. It decreases with $1/\beta^2$ for increasing velocity until reaching a minimum around $\beta\gamma = 3$ to 4 (minimum ionization), then starts to rise logarithmically leveling off finally at a constant value (the Fermi plateau). The numerical value of the minimum energy loss is $dE/\rho dx \sim 2 \text{ MeV cm}^2/g$. After the minimum is reached, the logarithm term describes the so-called relativistic rise. The relativistic rise does not continue to indefinitely large values of γ , as obtained from the Bethe-Block equation. Fermi introduced in 1939 the density effect, the coherent effect of the surrounding polarizable atoms, which shields the

¹Previous equation is sometimes called the energy loss "low energy" approximation. A more general expression would be

$$\frac{dE}{dx} = 0.3071 \left(\frac{MeV}{g/cm^2} \right) \rho z^2 \frac{Z}{A} \frac{1}{\beta^2} \left(\frac{1}{2} \ln \frac{2m c^2 \beta^2 \gamma^2 T_{max}}{I^2} - \beta^2 \right) \quad (2.5)$$

where

$$T_{max} = \frac{2m c^2 \beta^2 \gamma^2}{1 + 2\gamma m/M + (m/M)^2} \quad (2.6)$$

is the maximum kinetic energy which can be given to a free electron in a single collision with a particle with mass M . For $2\gamma m/M \ll 1$, the maximum kinetic energy transferred takes the approximate form $T_{max} = 2m c^2 \beta^2 \gamma^2$. The approximation is obviously not valid for electrons.

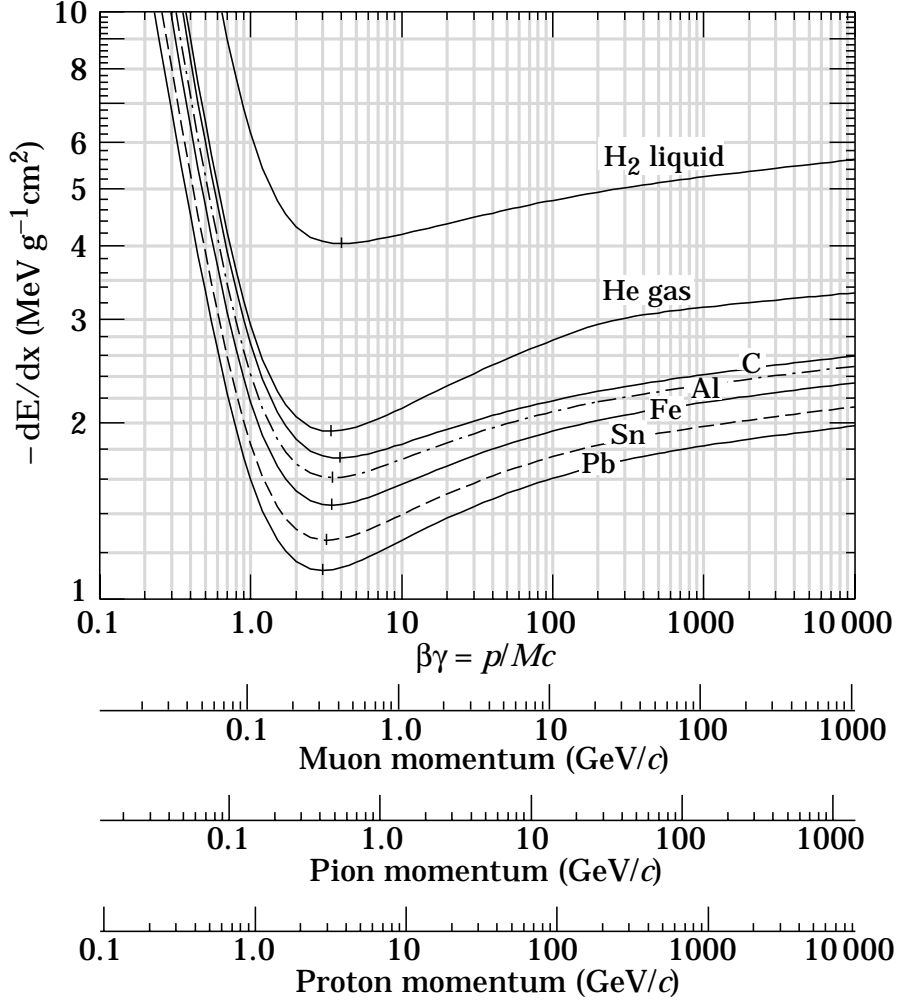


Figure 2.1: Energy loss rate in liquid hydrogen, gaseous helium, carbon, aluminum, iron, tin and lead. The energy loss in this figure is measured in mass per unit area MeVcm^2/g , avoiding the use of a fixed medium density in the Bethe-Bloch equation. Taken from [2].

field of the traveling particle. A correction term $(-\delta(\beta)/2)$ should be introduced in the Bethe-Block formula to account for this effect. The medium where the high energy particle travels become polarized, limiting the field extension of distant collisions. At very high energies this truncation term takes the form

$$\frac{\delta(\beta)}{2} = \ln(\hbar\omega_p/I) + \ln \beta\gamma - \frac{1}{2} \quad (2.7)$$

with $\hbar\omega_p$ the plasma energy. This effect depends on the medium density, being more important in solids and liquids than in gases, since the plasma frequency scales as the square root of the electron density.

Equation 2.4 cannot be used for electrons (projectile), due to the approximation in the maximum kinetic energy transferred to the atomic electrons. In this case one should use directly

$$\begin{aligned} \frac{dE}{dx} &= \frac{4\pi N e^4 z^2}{m c^2 \beta^2} \left(\frac{1}{2} \ln \frac{2 m c^2 \beta^2 \gamma^2 T_{max}}{I^2} - \beta^2 - \frac{\delta(\beta)}{2} \right) \\ &= 0.3071 \left(\frac{MeV}{g/cm^2} \right) \rho z^2 \frac{Z}{A} \frac{1}{\beta^2} \left(\frac{1}{2} \ln \frac{2 m c^2 \beta^2 \gamma^2 T_{max}}{I^2} - \beta^2 - \frac{\delta(\beta)}{2} \right) \end{aligned} \quad (2.8)$$

Once it is known the average energy required to produce one ion pair, one should determine the energy spectrum of the primary electrons to know the amount of ionization along the track. The energy spectrum $F(E)$ can be obtained from $d\sigma/dE$, the differential cross section per electron to produce a primary electron with an energy between E and $E + dE$

$$F(E) = \frac{N(d\sigma/dE)}{1/\lambda} \quad (2.9)$$

where N is the electron density in the gas. From the differential cross section one can obtain also the mean free path as

$$1/\lambda = \int N \frac{d\sigma}{dE} dE \quad (2.10)$$

In order to calculate $d\sigma/dE$, one should study the energy loss of a moving charged particle in a polarizable medium of complex dispersive dielectric constant, given by its atomic structure. Different approximations have been used to describe the dielectric constant from photo-absorption cross section measurements [3, 4], with similar results; they describe basically the energy transfer from the contributions of the atomic shells as well as an extremely long tail in the $F(E)$ spectrum.

Also the cluster size distribution can describe effectively the ionization left by the particle along its trajectory. The probability distribution of the number of electrons liberated directly by the fast particle (primary) or indirectly (secondary) in each primary encounter is called cluster size distribution. The secondary electrons are normally created in the vicinity of the primary encounters, leading to clusters which drift together toward the anode wire. From the cluster size distribution, the ionization distribution in the track length can be calculated by summing the cluster size for all primary encounters in the track length. The calculus of the cluster

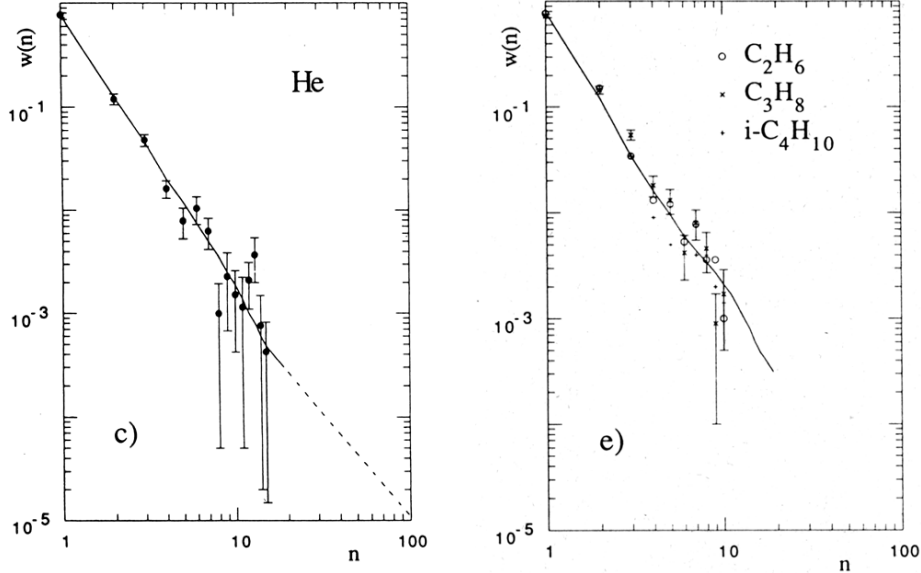


Figure 2.2: Experimental cluster size distribution $w(n)$ for Helium and organic vapors (including Isobutane). The continuous lines are eye-fits through the data points, while the dashed lines are extrapolations corresponding to the $1/n^2$ law expected for large n . Taken from [5].

size distribution $w(n)$ comprises the knowledge of the primary electron energy spectrum $F(E)$, as well as the probability of producing n ionization electrons per primary electron, $p(E, n)$

$$w(n) = \int F(E)p(E, n)dE \quad (2.11)$$

Experimentally such quantities can be determined. Figure 2.2 shows the results reported by Fischle *et al* [5], where an individual count of the cluster electrons is performed, after their separation by diffusion in a drift path.

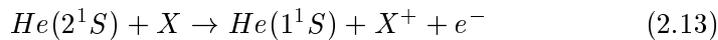
The extrapolation from the data to larger values of n is obtained assuming a binomial probability distribution with probability $p = I_0/W_0$, the ionization potential of the molecule over the average energy required to produce an electron-ion pair. The fraction of events with energy transfer large enough to ionize n electrons is proportional to the Rutherford cross section multiplied by the effective number of electrons per molecule given the $1/n^2$ behavior at large n .

The cluster size distribution ($w_{12}(n)$) of a mixture of gases 1 and 2 can be estimated from the individual distributions $w_1(n)$ and $w_2(n)$ using the

relation

$$w_{12}(n) = \frac{\pi_1}{\pi_1 + \pi_2} w_1(n) + \frac{\pi_2}{\pi_1 + \pi_2} w_2(n) \quad (2.12)$$

where π_1 and π_2 are the partial pressures of the components 1 and 2, multiplied by the specific primary ionization cross sections. For Helium, nevertheless, this expression should be corrected by the Jesse effect: the secondary ionization involves physical processes which are absent in the corresponding pure gases, for example



which reduces the average energy required to produce an ion pair and increases the cluster size [5].

2.2 The HADES drift chambers

The HADES tracking system has been designed for the precise determination of pairs of track points before and behind the space where the magnetic field bends the track trajectories. From this information, the particle momentum can be determined and the invariant mass for lepton pairs obtained. The detectors have the same six-sector symmetry of the spectrometer, being each sector completely identical to the others. There are four modules per sector, two before the magnetic field zone and two behind. They are notated in this text with the Latin numbers I, II, III and IV, being the lower the closer to the interaction point.

The tracking system was built according to the following requested features:

- **High position resolution:** the position estimate obtained from the drift modules should be sufficient for an accurate determination of the particle momentum. This represents a resolution below $100 \mu m$ (σ) in the relevant direction, the one which results modified by the trajectory kick in the magnetic field.
- **Low mass:** the materials used in the entry layer and wires and the gases used in the modules volume are selected to maximize the radiation length and to minimize the electrons multiple scattering, allowing measurements with sufficient momentum resolution. Also the reduction of the materials of end-plates, frames and other mechanical supports contributes to the minimization of interactions.

- **Two track detection ability:** the offline rejection of leptons from pair conversion out of the interaction point, and from π^0 decay, requires the separation of the close pairs, in particular in the inner modules. These close pairs represent the largest fraction of the combinatorial background.
- **Geometrical constrains:** the shape of the modules is fixed by the high acceptance and the symmetry of the spectrometer. To increase the active volume and reduce the multiple scattering, the frames have to be reduced to the minimum and the electronics mounted in this reduced area. In the adopted solution, the thin frames occupy just the area before and behind the magnetic coil cases.
- **Ability to cope with high multiplicities:** up to 200 charged particles can cross simultaneously the spectrometer in central $Au + Au$ collisions at SIS energies. The high multiplicity leads also to a large granularity to separate individually the tracks and supplementary electronics for dealing simultaneously with the signals. The maximum mean cell occupancy is around 30% for those zones with higher multiplicity.

The trajectory of the tracks is approximated, before and after the magnetic field zone, using straight lines. The straight lines are obtained from the two estimates in the drift modules. This approximation results in several interesting benefits:

- The determination of the deflection angle in the magnetic field zone is not affected by the angular straggling in the space between the target and the drift modules.
- The scheme improves the close pairs separation, mainly coming from conversion of photons in leptonic pairs.
- Each straight piece can be independently extrapolated to other detectors devoted to the particle recognition, as the inner RICH or outer TOF or Pre-Shower.

Each module consists of six independent sense and field wire planes surrounded by seven cathode planes which determine the drift cells. The sense wires are grounded, while the cathode and field wires have a negative voltage. The approximate cell configuration is shown in figure C.1 (see appendix C); in the normal direction to the MDC plane, the cell is limited by the cathode wires. The second dimension of the cell plane is normal

Plane	sense wires (#)	cell size ($x \times z$) mm^2	active area m^2	inner size $cm \times cm$
MDC I	1006	5×5	0.35	$76(12) \times 79$
MDC II	1104	6×5	0.53	$86(20) \times 100$
MDC III	1098	12×8	2.21	$185(30) \times 206$
MDC IV	1159	14×10	3.21	$220(32) \times 255$
Totals	4367		6.3	
Grand total	26202		37.8	

Table 2.1: Basic properties of the HADES MDCs. The inner size column quotes the active-area larger side (shorter side in brackets) times the active-area height.

to the previous one and to the sense wires (corresponds to that between the parallel frames of the module for the inner sense wires) and the cells are separated by the field wires. The cell sizes are shown in table 2.1; the dimensions grow up from the inner to the outer modules to maintain constant the granularity per solid angle and, therefore, the mean occupation. In all cases the cell dimensions are extremely small, being the maximum drift length of about 17 mm in the largest cells.

The sense wires of the different wire planes follow different directions, the so-called butterfly geometry [6]. The two inner sense wires are parallel to the parallel frames of the module, while the outers are tilted 20° and 40° degrees respectively, as shown in figure 2.3. This disposition improves the drift chamber resolution in the direction where the magnetic field deflects the particles and eliminates more efficiently identification errors. For a hit wire one can assign the ionization at any of both sides of the wires. The identification errors come from the assignment of wrong sides in the impinged wires when the *Hits* are constructed (see the *Hit* definition in appendix D). The cathode wires are disposed perpendicular to the top and bottom frames.

The field and cathode wires are made of bare aluminum, with diameters of $100\ \mu m$ and $80\ \mu m$ respectively. The material and their reduced diameter are chosen for the common goal, i.e., to reduce the multiple scattering along the spectrometer. The sense wires are made of gold and tungsten with a diameter of $20\ \mu m$. The wire planes are glued to Stesalit frames, where they are soldered to the electrical connections. The Stesalit frames are glued together and bolted to external aluminum frames in order to fix the Stesalit frames and to reduce their stress due to the wire tension. The external aluminum frames are quite thin, only 30 mm for the inner plane

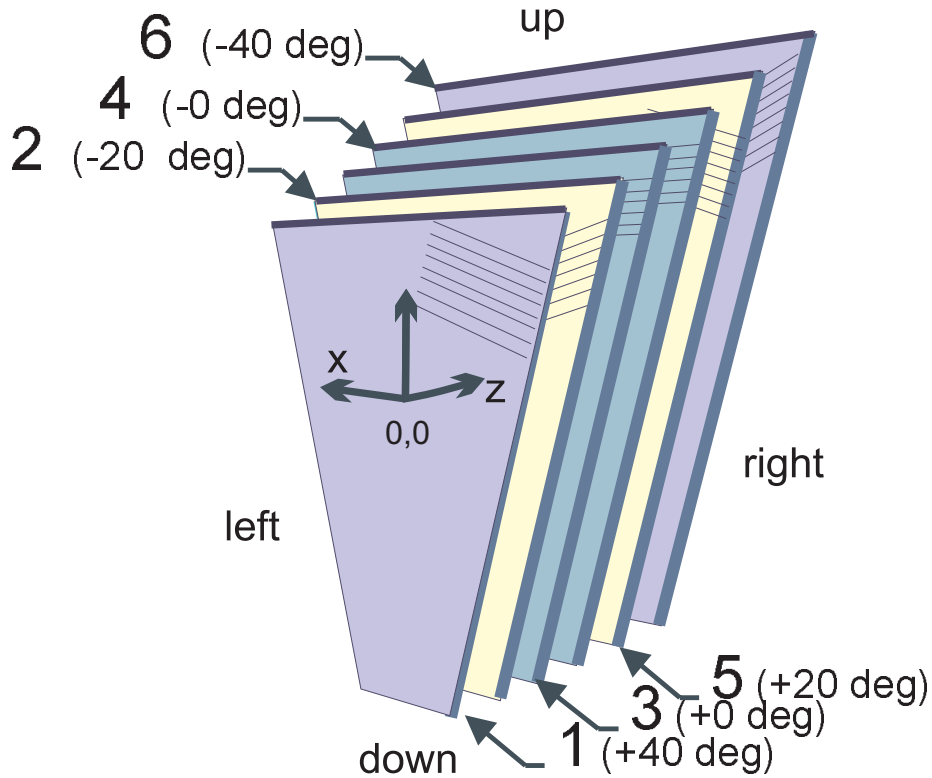


Figure 2.3: Configuration of the six sense wire layers in a HADES multiwire drift chamber. The two central layers have parallel sense wires, but staggered by half a pitch.

and 70 mm for the outer. In some cases (plane I) thin pre-stressed steel plates were placed between layers of Stesalit to make the chamber stronger. The pre-stressing of the stainless steel frames is done in such a way that it compensates the force caused by the tension of the wires [7]. The wire tension, 40 g for sense wires and 120 g for field and cathode wires in the plane II modules, has been optimized for minimum sag due to gravitational and electrostatic forces, taking into account a 10%-15% tension loss of the aluminium wires after the first few weeks [8]. The measured precision of the sense wire pitch is below 20 μm , being the accumulated deviation in the wire position along the complete chamber below 60 μm [7]. This last number was measured for an individual wire layer and is basically originated by a bending of the frame, which can be partially reduced when mounting all six layers together.

The gas volume is limited in each module by aluminized Mylar layers with a thickness of $12\ \mu\text{m}$. The diffusion of the Helium gas through such a thin layer was previously studied [9], to ensure the correct chamber tightness.

Part of the electronics, including the amplifiers and TDCs, are mounted on the module frames. In this way, the electronics can be placed really close to the MDCs without overrun the experimental active area and minimizing the cable length. The amplification of the signal is performed in an eight channels amplifier (ASD-8 chip) which also shapes the signal and discriminate short pulses using a configurable threshold value. The differential signal delivered by the chip represents the time of the amplified analog pulse above the threshold. This logical signal is moved to a fast eight channels TDC (Gleichmann GmbH) where two different times are digitized. Up to now, the TDC was used to store the two times when one signal crosses the threshold voltage, that is, once in the leading edge and once in the trailing edge. It can alternatively work triggering the counter on the leading edges of two pulses, for those cases when two tracks cross the same cell, giving two consecutive pulses. The number of TDC channels corresponding to a well defined time (the TDC gain) changes with temperature (approximately $-6.3\ \text{channels}/K$) and also changes more subtly with threshold. The gains of all the TDCs are monitored using an internal calibration mode, which serves six channel contents for six fixed times. The TDC gain is obtained, individually for each one of the eight TDC lines in each chip, fitting to a straight line the channel-time pairs. The obtained values are close to $0.5\ \text{ns}/\text{channel}$.

Two amplifier-shaper-discriminators are mounted in a small PCB board called daughter-board, which contains sixteen channels. A set of four or six daughter-boards can be plugged in a motherboard, which contains the TDCs and drivers to transmit the signals.

The high voltage is provided independently to each cathode layer² and to the field wires in each module, for a total of 288 high voltage channels. Two HV mainframes (CAEN SY527 Model-Universal Multichannel Power Supply) with programmable power boards (CAEN A934AN Programmable Fast Trip Power Supply Board) are used to supply the power. Each high voltage channel can be controlled individually allowing the configuration of different settings in the modules, or inside each module, including voltages ramp and down, maximum intensities and trip times when overcurrent.

The requested features for the drift modules include the use of low mass

²The most external cathode layers use the same high voltage channel, being the expected current for these planes just half the current in the other layers.

gases which present a large radiation length, to keep the multiple scattering along the spectrometer low. The contribution of the multiple scattering to the momentum resolution results crucial, being of the same order as the intrinsic resolution of the drift modules for electrons in all the studied momentum range. Multiple scattering dominates at low ($< 0.4 \text{ GeV}/c^2$) dilepton invariant mass [8]. The most interesting mixture is that made of Helium and Isobutane. The Helium's radiation length is almost 50 times longer than that of Argon, the most used noble gas in drift modules (see table 2.2). The Helium presents the problem of a small primary ionization, which can be compensated partially using the Isobutane as a quencher.

The gas proportions of the tested mixture ranged from 50% – 50% to 80% – 20%, where the first proportion corresponds to the Helium [8]. A low concentration of the quencher does not allow to extend the efficiency plateau, presumably due to the large amount of UV photons produced in the avalanche at high gains. For the mixture with maximum quencher content tested, 50% – 50%, the voltage needed to obtain enough amplification becomes too high and the plateau gets shortened again. The mixture containing a 60% Helium and 40% Isobutane was selected as optimal choice, providing enough primary ionization under stable operation at moderate gains. The total gain is approximately 10^5 and the drift velocity is $4 \text{ cm}/\mu\text{s}$ in most of the drift path³. The working plateau extends for around 300 V. With this mixture and the contribution of the low mass materials in wires and entrance windows the radiation length per module is about $X/X_0 = 5 \times 10^{-4}$. The degradation in the overall momentum resolution due to increased multiple scattering when the percentage of Isobutane is increased, around a 4%, is clearly compensated by their improvement due to the increased position resolution, approximately 20%.

For a mixture 60% Helium and 40% Isobutane, there are about 35 clusters/cm path length. The ionization electrons drift toward the wire, reaching this point at different times, as shown in figures C.1 and C.2 (see appendix C). The drift in the cells follows the paths given by the electrostatic configuration. The number of clusters per path length is large enough to work with the hypothesis that there are ionization electrons in a narrow interval around the closer point of the trajectory to the wire. Then, the signal gives us a measurement of the distance from the wire to the point of the trajectory which passes closer to the wire.

To obtain the drift distance, the time of an external reference, the

³For a MDC II with a mixture 60% Helium and 40% Isobutane at a voltage of -2 kV in cathode and field wires, it was determined a mean drift velocity $v_d = 0.042 \text{ mm/ns}$, constant in around 80% of the cell [10, 11]

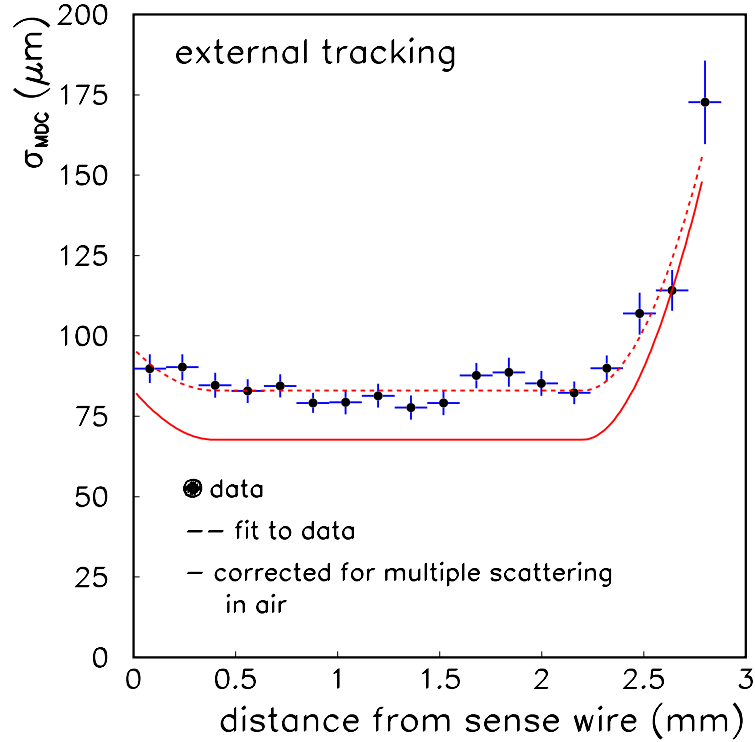


Figure 2.4: Resolution in the determination of the track distance to the wire, as a function of the distance from the sense wire. The lower line indicates the intrinsic resolution after correcting for multiple scattering of protons in air. An external Silicon tracker ($50 \mu\text{m}$ readout pitch) was used to measure the track position. Taken from [10].

Start detector, is used. The leading and trailing edges of the pulse over the threshold define the start time for two different channels in the TDC, counting up to the arriving of a stop signal. The drift time is given by the difference between the first (leading edge) signal and the stop signal in the TDC, which is a delayed line from the Start detector. But this time contains also an offset and should be calibrated from TDC channels to time. Once one knows the time, the distance can be obtained. The details about this calibration procedure as well as a short introduction to the drift modules reconstruction software are included in the appendix D.

The position resolution of the modules was measured in several tests and by different methods [10, 11]. For plane II, the position resolution is below $75 \mu\text{m}$ (sigma) over most of the cell volume, well below the design value. The position resolution depends on the distance from the sense

Gas	Radiation length		density (g/l)	Total primary ionization (1/cm)
	(g/cm ²)	(m)		
Helium	94.32	5300	0.178	8
Argon	19.55	109.8	1.396	27
Isobutane	45.2	169.3	2.67	200

Table 2.2: Basic properties of the gases used in the MDCs. Argon is included for comparison (note the short radiation length compared with Helium). Properties are quoted at N.T.P. Data from [1].

wire. Figure 2.4 shows the position resolution as a function of the distance from the sense wire during a test performed with 2.1 GeV protons. The measured spatial resolution has not been corrected for electronic noise contribution. The figure shows a planar resolution in approximately 70-80% of the cell; close to the wire it is visible the expected resolution decrease due to the Poisson statistics, while for larger distances the inhomogeneities of the voltage configuration close to the field wires and the larger diffusion reduces strongly the resolution (see appendix C).

2.2.1 Coordinate systems

The coordinate systems used for the description of the MDCs and other detectors are introduced, previously to a longer discussion in section 4.5, being especially important in the next sections.

The *Laboratory Reference System*, notated (X, Y, Z) , is defined unequivocally as that centered in the target, having the Z axis pointing in the beam direction and sense, the Y axis pointing in the direction of the gravity but contrary sense, and the X axis settling down a right-handed system [12].

The *Module Reference System* is notated as $(X_{MDC}, Y_{MDC}, Z_{MDC})$ and is module dependent. Its origin is attached to the physical center point⁴ of the drift chamber module [13]. The axes X_{MDC} and Y_{MDC} lie inside the fourth cathode plane, while Z_{MDC} is normal to this plane pointing in the opposite sense to the target. The axis X_{MDC} follows the direction of the wires in the central layers of the module and its sense coincides with the sense of X in the laboratory system for sector 1 (see figure 2.3, where the axis X_{MDC} and Z_{MDC} are simple denoted x and z).

⁴The physical center point is precisely defined in each module as the cross point of the fourth cathode plane in the module and a straight line normal to the plane and crossing the target.

Bibliography

- [1] W. Blum, L. Rolandi; *Particle Detection with Drift Chambers*, Springer Verlag, Berlin, 1994.
- [2] D.E. Groom et al.; *The European Physical Journal* **C15** (2000) 1.
- [3] W.W.M. Allison, J. H. Cobb; *Ann. Rev. Nucl. Sci.* **30** (1980) 253.
- [4] Chechin *et al*; *Nucl. Instr. and Meth.* **98** (1972) 577.
- [5] H. Fischle, J. Heintze, B. Schmit; *Nucl. Instrum. Methods* **A301** (1991) 202.
- [6] F. Bruyant, J.M. Lesceux and R.J. Plano; *Nucl. Instr. and Meth.* **176** (1980) 409-413.
- [7] H.W. Daues, J. Hehner and H. Stelzer; *GSI Scientific Report* 1997, 185.
- [8] C. Garabatos *et al*; *Nucl. Instr. and Meth.* **A412** (1998) 38-46.
- [9] C. Garabatos; *Measurement of water and Helium diffusion through thin windows*, MDC Note 12/95.
- [10] C. Müntz; *Nucl. Phys.* **B78** (1999) 139-144.
- [11] C. Müntz; *Results from MDC Prototype-1 Analysis - Test Beam April'97*, MDC Internal report, October 1997.
- [12] M. Dahlinger; *HADES Geometry and Database* (<http://depc14.gsi.de/hades/Geometry.htm>).
- [13] J. Stroth; *MDC reference systems*, MDC Note 03/98.

Part II

**HARDWARE
ALIGNMENT**

Chapter 3

Introduction to the alignment methods

This chapter introduces and motivates the next part of this work, devoted to the MDC modules alignment. Alignment refers, in a wide sense, to the methods and tools used to determine and correct the proper positioning of the spectrometer detectors. This thesis work deals only with the MDCs positioning diagnostic.

First, the physical effects of a MDC misalignment are studied in a detailed simulation. From the results, it is possible to infer more properly the requested features for the systems performing the alignment. The possible alignment devices and methods are schematically shown, being more deeply described in the next chapters.

3.1 Simulation of misalignment effects

The purpose of the simulation is to test the effects of the MDC misalignment, the main tracking detectors, in the momentum resolution and the dilepton invariant mass. The basic requirements of the systems, devices or methods for the alignment of the spectrometer elements can be extracted from the simulation conclusions. The analysis is performed using a set of 14000 dileptons in the geometrical acceptance, coming from an originally flat mass distribution. The simulation takes into account secondary particles production, energy loss (bremsstrahlung) and multiple scattering.

HGeant is used to propagate the tracks through the spectrometer, reporting the crossing coordinates for each detector, as well as the lepton properties. The detection procedure is simulated by a digitization routine, where a gaussian dispersion is introduced according to the estimated

detector resolution. In the case of the MDCs, the detection is simulated individually in each cell, assuming an individual gaussian error per plane in the track coordinates estimate. To introduce the misalignment, the detection coordinates are modified before any track reconstruction. The complete track reconstruction from the modules information and the track momentum calculation has been performed using the original simulation made during the experiment design and proposal. The results of this simulation are a valuable approximation to determine the necessities of the spectrometer regarding the alignment systems. Additional results about the decrease of efficiency are not discussed due to the strong dependency on the momentum reconstruction model.

The effects on the momentum resolution have been measured by comparing the original momenta (p_i) of the generated leptons with the value after the track reconstruction (p_f). In particular, the distribution of the difference in momenta (original minus reconstructed momenta), divided by the original momenta, represents a percentile measurement of the momentum resolution. The mean value of the distribution should center on zero for a correct momentum reconstruction. Any deviation from this zero value shows a systematic error in the momentum reconstruction. The standard error of the distribution represents an estimate of the reconstruction resolution. A gaussian distribution fits quite correctly the peak of the histograms; the mean value and the sigma of the fit will represent the bias and the resolution in the momentum reconstruction.

Let us begin the description of the possible displacement from the design position and their effects. Obviously, the effect of the displacement is not uniform, but depends strongly on the MDC plane suffering the misalignment and on the direction of the movement. The first and most important displacement is that in the direction of the momentum kick by the magnetic field, corresponding basically to a change in the track polar angle. Analysing locally the track incidence on the module coordinate system, the relevant displacement corresponds to that along the Y_{MDC} coordinate (see the definition in section 2.2.1, and figure 2.3). Figure 3.1 shows the distribution of the differences between original and reconstructed momentum, divided by the original momentum, for electrons and positrons with momenta between 600 and 800 MeV/c . In the top pads, there is no misalignment in the modules. In the bottom pads a misalignment of 200 μm is introduced in MDC I along the positive sense of the Y_{MDC} direction. For electrons, the main effect is a displacement of the mean value toward negative values, reflecting a larger reconstructed momentum than the original value. There is an easy explanation based on the geometry

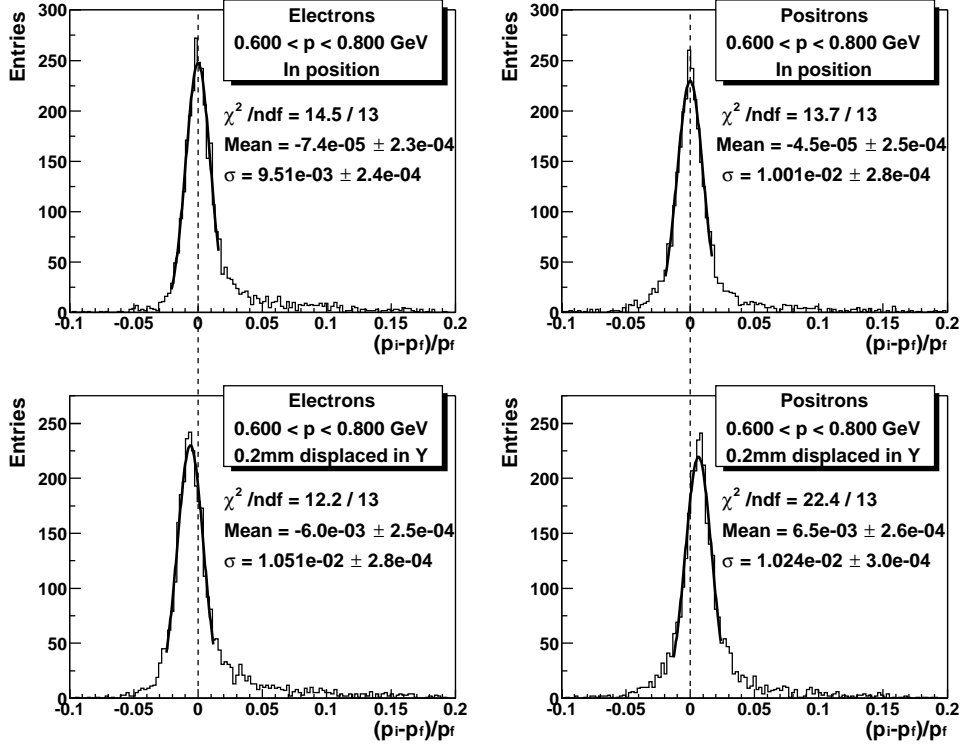


Figure 3.1: Electron (left) and positron (right) $\frac{p_i - p_f}{p_i}$ distributions. The top pads represent the distributions when the modules are in their design position, while the bottom pads represent the result after a misalignment in MDC I of $200 \mu m$, along the Y_{MDC} direction. In both cases the leptons momentum was selected to be between $600 \text{ MeV}/c$ and $800 \text{ MeV}/c$. The distributions are fitted to a gaussian around the maximum region; the fit parameters are shown.

of the spectrometer: the momentum is obtained from the angle between the two straight lines representing the track before and after the magnetic field: the kick angle. A larger kick angle represents a larger charged particle momentum. Due to the polarity of the field, electrons are deflected in such a way that the straight part of their trajectories after the magnet has a larger polar angles, while positrons feel the opposite effect, being deflected toward smaller polar angles. When module I is displaced $200 \mu m$ in the positive sense of Y_{MDC} direction, the ionization is produced in a lower (more negative in the Y_{MDC} direction) part of the module, and therefore the estimate of the track cross point in module I is displaced $200 \mu m$ in the negative sense of Y_{MDC} direction, because the reconstruction software

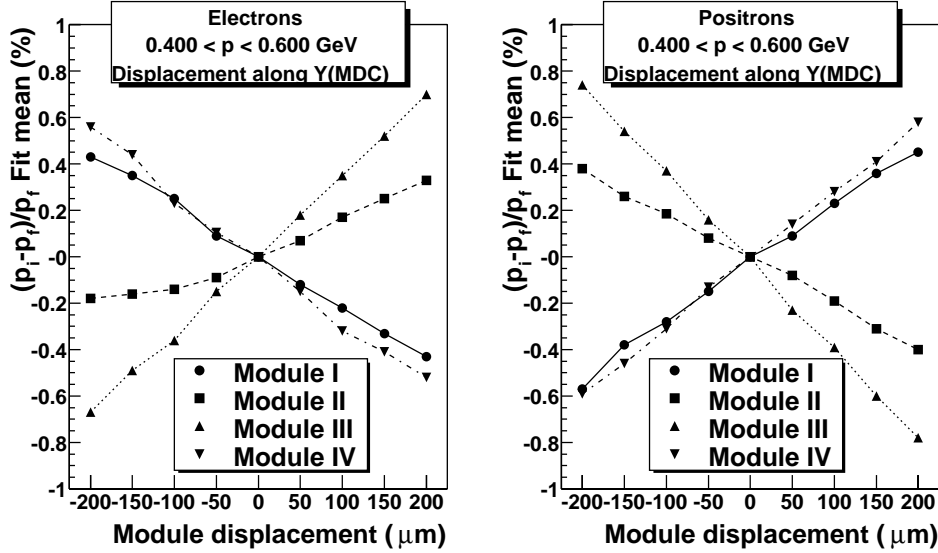


Figure 3.3: Displacement of the mean value of the fit of the $\frac{p_i - p_f}{p_i}$ distribution, for electrons (left) and positrons (right), as a function of the misalignment introduced in each module in Y_{MDC} direction. In both cases the tracks momentum has been selected to be between 400 MeV/c and 600 MeV/c. The lines between the points are plotted to guide the eye.

MDC II the less one. The difference is given by the geometrical aspects of the track estimate modification and the proximity to the magnetic field region. The obtained values are quoted in table 3.1. The approximate momentum shift is also calculated (in MeV/c) for an electron (or positron) with a momentum in the center of the interval.

The displacement along the local Y_{MDC} module coordinate produces also other visible effects. The width of the distribution increases as the modules move away from the design position, and the sigma increment is below 0.1%/100 μm . It was also observed a drop in the efficiency for larger deviations, but both factors are strongly dependent on the tracker software and their effects on the analysis are less important than the shift in the mean, for the same module displacement.

Up to this point, displacements of one module have been studied. The simultaneous displacement of the two modules before or after the magnetic field area is also of interest, because the support structures do not fix the external modules to the inner ones, as will be explained in next section. Table 3.2 contains the measured values for the displacement of the exter-

e^- Module	$400 < p (e^-) < 600 \text{ MeV}/c$		$600 < p (e^-) < 800 \text{ MeV}/c$	
	$\Delta p/p$ (%/100 μm)	Δp ($\frac{\text{MeV}}{c}/100 \mu\text{m}$)	$\Delta p/p$ (%/100 μm)	Δp ($\frac{\text{MeV}}{c}/100 \mu\text{m}$)
I	-0.21	-1.1	-0.32	-2.2
II	0.13	0.7	0.19	1.3
III	0.34	1.7	0.47	3.3
IV	-0.27	-1.4	-0.37	-2.6

e^+ Module	$400 < p (e^+) < 600 \text{ MeV}/c$		$600 < p (e^+) < 800 \text{ MeV}/c$	
	$\Delta p/p$ (%/100 μm)	Δp ($\frac{\text{MeV}}{c}/100 \mu\text{m}$)	$\Delta p/p$ (%/100 μm)	Δp ($\frac{\text{MeV}}{c}/100 \mu\text{m}$)
I	0.26	1.3	0.35	2.5
II	-0.21	-1.1	-0.24	-1.7
III	-0.39	-2.0	-0.49	-3.5
IV	0.29	1.4	0.41	2.9

Table 3.1: Shift in the peak mean of the momentum gaussian fit for electrons and positrons. The shift is quoted for the movement of an individual module in Y_{MDC} direction, and represents the momentum fit mean displacement per 100 μm of positive misalignment. $\Delta p/p$ is obtained directly from the fit, while the Δp is the estimate for a momentum in the center of the interval range.

Module	$400 < p (e) < 600 \text{ MeV}/c$		$600 < p (e) < 800 \text{ MeV}/c$	
	$\Delta p/p$ (%/100 μm)	Δp ($\frac{\text{MeV}}{c}/100 \mu\text{m}$)	$\Delta p/p$ (%/100 μm)	Δp ($\frac{\text{MeV}}{c}/100 \mu\text{m}$)
e^-	0.1	0.5	0.12	0.6
e^+	-0.07	-0.6	-0.12	-0.6

Table 3.2: Shift in the peak mean of the momentum gaussian fit for electrons and positrons. The shift is quoted for the movement of the external pair of modules (MDC III and MDC IV) in Y_{MDC} direction, and represents the momentum fit mean displacement per 100 μm of positive misalignment. $\Delta p/p$ is obtained directly from the fit, while the Δp is the estimate for a momentum in the center of the interval range.

nal modules with respect to the inner ones. The momentum shift is less marked; the straight lines obtained from the MDC data before and after the magnet are just displaced relatively, but the angle constructed from the straight lines do not change¹.

The dilepton invariant mass can be calculated from the angle α between the electron and the positron and their momenta

$$M = 2 \sin \frac{\alpha}{2} \sqrt{p(e^-) p(e^+)} \quad (3.1)$$

The shift observed in the mean values of the momentum distributions with the misalignment has been obtained introducing the same misalignment for all modules in a plane, irrespective of the sector. Now, to determine the invariant mass, one has to consider the electron and the positron crossing different sectors. The invariant mass formula depends on the angle between the reconstructed positron and electron, and this can slightly vary if different misalignment in different sectors are introduced. Moreover, the shifts in the momentum of the positron and the electron could compensate or, in the worst case, both contribute to shift the invariant mass in the same direction. Then, for an estimation of the mass shift after a misalignment, an expression can be derived directly from the observed momentum shifts. From the invariant mass formula, a roughly estimate of the mass change, introducing the deviations in the momentum of positron $\Delta p(e^+)$ and electron $\Delta p(e^-)$, is

$$\Delta M = 2 \sin \frac{\alpha}{2} \left(\sqrt{p(e^+)} \frac{\Delta p(e^-)}{2\sqrt{p(e^-)}} + \sqrt{p(e^-)} \frac{\Delta p(e^+)}{2\sqrt{p(e^+)}} \right) \quad (3.2)$$

for a fixed α angle. From the tables, let us just take as example a typical value of $\Delta p \sim 2.5 \text{ MeV}/c$ for low energy electrons and a value in the modules deviation of around $100 \mu m$. Then the invariant mass variation calculated from equation 3.2 is $\Delta M \sim 3 \text{ MeV}/c^2$. Therefore, the relative misalignment along the direction Y_{MDC} between neighbor modules should be maintained below $30 \mu m$, to fulfill the criteria on the invariant mass resolution below 1% at the ρ - ω masses. With respect to the relative misalignment between the inner and the outer modules, the deviations in the momentum of the leptons are a factor 2 lower, and therefore the relative misalignment should be maintained below $50 \mu m$.

¹Note again that this effect is very dependent on the method used for the momentum determination. For methods based on a kickplane determination, the relative displacement of the two straight lines contributing to the track can lead to mis-identification or inefficiency.

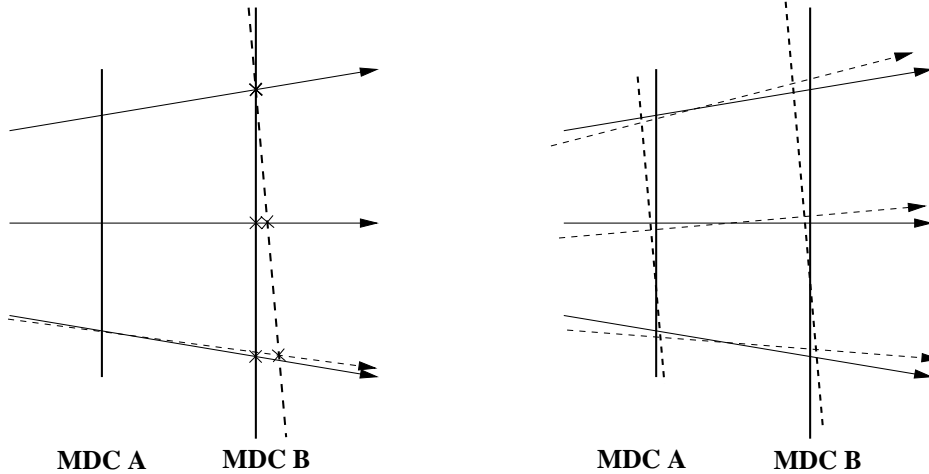


Figure 3.4: Scheme showing the change in the charged particles track estimate (arrows) after a rotation in a drift module (lines) around the X_{MDC} (or Y_{MDC}) direction. The left scheme shows the rotation of a module, while the right scheme shows the simultaneous rotation of both modules. The dashed lines represent the position of the rotated modules, while the dashed arrows represent the track estimates from the rotated modules.

The displacement of the individual modules, or set of modules, in other directions (local module X_{MDC} and Z_{MDC} directions) has also been analysed. The effects on the reconstructed momentum shift are below a factor ten smaller than equivalent displacements in local Y_{MDC} direction. In particular, a displacement along the Z_{MDC} direction would lead to large momentum shifts only for those particles crossing the detectors at large incidence angles.

The rotation of individual modules around their main axis has been also checked. A rotation around the direction Z_{MDC} , normal to the wire planes, (“in plane” rotation, in the notation of chapter 5, see also figure 5.14) produces a change in the position of the cross point of the particle, more important as one moves away from the rotation axis. A rotation around X_{MDC} or Y_{MDC} (“out of plane” rotation), produces a slight change in the direction of the track estimate, larger as the track crosses the module at a larger distance of the rotation axis. In particular, a rotation around X_{MDC} produces a change in the polar angle of the estimate, relevant for the momentum determination. The left part of figure 3.4 shows an example of the effects of such a rotation on the straight line constructed from two modules. Even more important is the simultaneous rotation of both

modules, before or after the magnetic field area. In this case the complete set of track estimates obtained from the pair of modules is rotated the same amount. The right part of figure 3.4 shows the change in the track estimate after the simultaneous rotation of the modules. A rotation around X_{MDC} is again more important, modifying the polar angle of the track estimate. The effects of a change in the polar angle due to this rotation can be compared to those given by a displacement of a module along the Y_{MDC} direction. For instance, for the outer modules, separated by a distance of about 300 mm, a displacement of 50 μm along Y_{MDC} , produces similar effects than a rotation around X_{MDC} of 0.0002 rad. From our knowledge about the effects in the momentum of this translation in a module, it can be determined a limit of 0.0002 rad for the maximum error in this rotation angle (or maximum value of the difference between the true angle and that used in the reconstruction of the tracks).

3.2 Hardware and software solutions

The simulation has shown the importance of the positioning of the detectors to achieve the restraining spectrometer goal in resolution.

The main and first mandatory action concerns to the monitoring of the position of the detectors. Monitoring means to measure the positions of the relevant sense elements in the spectrometer during their active periods, with a sufficient accuracy to fulfill the detection goals. The monitoring can be performed using software or hardware methods, or a combination of both. A software method is able to determine relative geometrical parameters of the sense elements based on the study of a large number of tracks. Hardware methods include information obtained from external sensors which can determine the detector position.

After the monitoring of the detectors position, two alternative actions can be settled: to introduce actuators for an active correction of the detector positions or just determine the parameters for a subsequent correction in the analysis of the output data. This election conditions the monitoring system, in the sense that an active system allows the use of threshold or limit sensors triggering actuators, while the passive election forces the use of methods able to determine complete position information.

From its original design, the HADES spectrometer was built to be installed as close to the design position as a careful installation permits, and to correct the position deviation by the modification of the geometrical parameters during the track reconstruction. The accuracy of the methods used to obtain the geometrical parameters should be sufficient to guarantee

the physical requirements, taken different values for different detectors.

Regarding the software methods, the relative positioning of tracking elements with high accuracy requires the detection of tracks following straight paths and crossing neighbor modules (for examples in the literature, see [1–4]). The best approximation to the straight lines are the tracks of energetic particles without magnetic field in the spectrometer. Obviously, this setup cannot be reproduced during the normal operation of the spectrometer, where the magnetic field should work at full intensity to allow the required dilepton mass resolution. Then, the alignment software methods require specific data taking periods, with the magnet switch off.

The hardware methods comprise electronic, optical and opto-electronic methods for determining the relative position or distance between sensitive elements or between a sensitive element and a reference point (for examples in the literature, see [5, 6]). The sensors are sensitive to the position or distance changes through the modification of a measurable property. For instance, potentiometric sensors change their output voltage when a movable bar is displaced over a length, modifying the internal electric resistance. Measuring this output voltage, and calibrating the results with known displacements, the potentiometric sensor renders accurate measurements of one-dimensional displacements.

Included also in the category of hardware methods for alignment, the so-called “survey” is based in the use of external optic or opto-electronic devices for the accurate positioning of marks in the visible frames of the detectors. The three-dimensional position measurements are normally referred to a common measurement vertex. Survey methods can achieve resolutions in the order of $100 \mu m$. The spectrometer survey is rarely performed due to its high cost. Normally, it is only made after large setup modifications or new installations.

3.2.1 Scheme of the HADES alignment

The study of the hardware alignment systems which can be installed in the HADES spectrometer is largely determined by its geometrical configuration and architectural design. The inner drift modules (plane MDC I and plane MDC II) are mounted plane by plane in a common hexagonal support. The six modules in a plane are rigidly screwed on the same hexagonal support along the larger side of their trapezoidal shape (see figure 4.23, the hexagonal support structure of MDC II). The hexagonal support is designed to lie on rails on the support structure (the so-called yellow table) and to allow a delicate modification of the three-dimensional

configuration of the frustum. The shorter sides are screwed on a common inner ring, which is not supported by any structure, just stabilizing the frustum. Then, both frustum structures are attached together by large screws. Under this configuration, the relative positions of the inner modules can be maintained within strict limits, provided a tight temperature control is maintained.

We should be confident that the mechanical supports are able to guarantee that the relative position between points in different inner modules should not vary more than approximately $50 \mu m$ in any direction, within the time between consecutive data taking for the software re-alignment. Effects of the magnetic field on this relative positioning has not been measured and are quite difficult to estimate. The previous estimation of the change in the relative position of the inner modules should not be mistaken with the accuracy of the module position with respect to the design parameters. During the installation, the modules are located as close as possible to the design parameters (sometimes the precision of this operation only can ensure a positioning within a few mm). Once installed, and after a reasonable time to release any material stress, the structure is supposed to be stable enough to ensure the commented relative stability.

The relative positioning between the inner modules is altered due to temperature changes, as the materials of the support structures, mainly aluminum and steel, suffer large deformations under temperature changes. The linear thermal expansion coefficient of aluminum and steel are, respectively, about $\alpha = 23.1 \times 10^{-6} K^{-1}$ and $\alpha = 11 \times 10^{-6} K^{-1}$ at $300 K$. Then, for a one meter long structure made of aluminum, the change in the length is about $115 \mu m$ if the temperature changes 5 degrees. The complex geometrical disposition of the modules on their support structures does not allow the extrapolation of these expansions to calculate real misalignment without a detailed simulation. The drift chamber electronics are installed directly on or close to the support structures. The normal behavior of the electronics leads to temperatures above $40^\circ C$ in the surroundings, which, for these inner modules, are closed volumes with poor heat transfer with the cave atmosphere². A continuous working state leads to a stable position, but the interruption of the (low voltage) power on part or all the drift chambers electronic produces significative temperature changes.

For the set behind the magnet, the modules are mounted independently in each sector. For each sector, the modules are attached by a complicate

²Additional cooling systems have been installed to control the maximum temperature around the inner modules, an subsequently to reduce the damage risk on electronics and drift modules.

mechanism of screws and spring-bolts to a common structure (see again figure 4.23). Due to the complexity of the mechanism, it is not easy to estimate the accuracy in the relative position of points in modules of the same sector.

The knowledge of the relative position of the inner and outer modules determines the resolution in the momentum estimate of the track crossing the spectrometer. To determine the track momentum it is necessary to measure the bending angle from both trajectory estimates, before and behind the magnet. But the supporting structures of the inner and the outer modules are completely unrelated. The relative position of points in the sense area of an inner and an outer module are, then, only determined on a millimeter base after the commissioning. This inaccuracy leads to inefficiency and large reconstructed momentum shifts, as pointed in the previous section, independently of the momentum reconstruction method employed. The effect of temperature changes displaces the external modules more largely than the internal ones, leading to a relative displacement between inner and outers and between different sectors of the outer planes. Even more important, the effect of the magnetic field modifies the relative position of inner versus outer modules in the same sector. An important part of the structure sustaining the large rails, where the external modules stand on, are made of steel, which is very sensitive to the magnetic field effects (even the residual fields far away from the maximum field zone). The deformation of this support is the largest contribution to the global displacement of the external structure, as we will see in section 4.8.

For maintenance purposes, the support pieces of both the inner or the outer modules can be displaced from the original position, following rails parallel to the beam direction. The inner modules displace on their common hexagonal frustum support, plane by plane, or both planes together if their link is not removed. After a displacement, the original position cannot be perfectly recover, but it is estimated a reproducibility of the original position along the rails within $150 \mu m$, using reference pins. Then, after a displacement of a module or set of modules it is mandatory to obtain a new study of their position. The relative positioning between inner modules in the same frustum should not suffer large modifications, but the relative positioning between modules in different frustum could be modified, since the link between both frustum supports is sometimes removed previously to the displacement. For the external modules, each sector is displaced along the rails independently. The movement of the heavy structures in a sector can even modify the relative position of the other sectors with respect to the inner modules, or between themselves.

There are several additional facts which should be considered with respect to the drift chambers and the spectrometer geometry. The surfaces of the MDC planes in front of the magnet are neither parallel between them, nor parallel to the set of planes behind the magnet. The space between the inner modules is tiny and cannot be accessed once the detectors are in measurement position, and any massive device installed for the alignment of the detection elements should not cross the active area of the spectrometer, to avoid multiple scattering. Moreover, most of the frame surfaces are occupied by the module electronics. The available room for the alignment sensors is severely limited to lie in the frames of the detectors. Another relevant requisite is the independence between the detectors which can be accessed for maintenance independently. The set of commonly supported modules (each plane frustum for the inner modules or each sector for the outer) must allow an independent displacement, avoiding the use of devices or mechanism fixing or linking their frames. All this facts have limited the election of sensors for determining the relative displacement of the modules.

Given this design features, we have proposed, installed and studied in the spectrometer the following solutions:

- Software algorithms, based on the analysis and minimization of residuals, employed for the accurate determination of the relative position parameters, using large amounts of data taken without magnetic field. The software algorithms should return the relative position of the tracking modules before short data taking periods or after any setup modification which can alter the positions.
- A custom-made installation of an opto-electronic standard solution, the so-called RASNIK (*Red Alignment System of NIKHEF*). The system monitors continuously the relative displacements of the outer modules structure with respect to the inner modules structure, independently for each sector. Its information is used to correct the initial detector positions during the data taking.

The chosen software approximation allows the determination of the relative positions of the coordinate systems, for modules in the same sector, by studying the *Hits* (as defined in appendix D) obtained using the tracking reconstruction. The *Hit* data level, filled by the tracking software with the best track approximation from each track module, contains an estimate of the cross point and the direction of the original track. Under the assumption that the tracks are straight lines in the magnetic field free setup, the extrapolation of the track estimate in a module can be used to find the track

estimate in other modules. The transformation to other coordinate system depends on the relative position of the modules. By requesting an unbiased distribution of the differences between the local track estimate and the extrapolation from other module track estimate, the relative transformation can be obtained. The extrapolation of the track estimate to other detectors with lower position resolution (TOF, Pre-Shower and RICH) allows the determination of the relative transformation to this detectors. The resolution of the parameters obtained during this research depends on several elements: the individual detector resolution limits fundamentally the resolution, but also the track sample size, the multiple scattering, the relative geometry and sizes of the detectors, and the detection internals can reduce the accuracy or bias the determination, in extreme cases. Also the target position can be estimated by extrapolating the track estimate, given by one or more modules. The same scheme can be used to obtain the relative positions of modules in different sectors provided the tracks cross simultaneously the modules in both sectors. Chapter 5 will deal with the technical aspects of the proposed solution.

The hardware monitoring system is based on the analysis of the displacements of an image projection on a video camera. This basic idea is refined by several technical improvements to increase the sensor resolution up to the micrometer level. After the analysis of the image, it is possible to obtain two transverse coordinates, the image magnification (which can be used to obtain the longitudinal coordinate), the magnitude of the image rotation around their longitudinal axis and a (less precise) estimation of the rotations around the other transverse axes. The normal operation of these sensors did not correspond to the conditions imposed by the HADES setup, regarding the geometry of the optical elements and the mounting elements. Then, a complete bench test was performed to ensure the correct behavior and accuracy of the proposed solution. Chapter 4 will deal with the technical aspects of the proposed solution.

As was explained before, the outer modules of the same sector could need additional monitorization, if their relative position changes more markedly than expected. The module geometry (the modules are parallel and the frames are quite close) favors the installation of additional hardware systems between these modules, including inexpensive potentiometer solutions. Other possible relative displacements affecting the momentum or mass resolution of the spectrometer, including any deviation from the supports stability estimation, should be latterly recognized and corrected for.

Bibliography

- [1] A. Cervera-Villanueva; Nucl. Instr. and Meth. **A447** (2000) 100-109.
- [2] F. Linde, M. Woudstra; *Geometry Reconstruction using Muon Tracks in DATCHA CERN*, ATL-MUON-98-250, CERN, Geneva, 1998.
- [3] ATLAS Technical Proposal, CERN/LHCC/94-43, CERN, Geneva, 1994.
- [4] M. Dima; Analytical and Numerical Flash-Algorithms for Track Fits, hep-ex/0002021.
- [5] J. A. Paradiso; Nucl. Instr. and Meth. **A386** (1997) 409-420.
- [6] F. Klumb, M.J. Price, P. Grussenmeyer; Nucl. Instr. and Meth. **A437**, (1999) 12-22.

Chapter 4

The MDC RASNIK System

This chapter contains the description of the RASNIK relative alignment system as well as the results of their implementation in the HADES spectrometer.

First, the RASNIK systems are introduced and their components individually described. Next, the custom-designed support pieces are explained, including those details concerning the thermal behavior of the materials. The complete set of technical drawings are included separately in the appendix I.

The implementation of the RASNIK elements in the spectrometer requires the calculation of their precise positions and the design of specific support pieces. The calculations, basically a set of coordinate transformations, are required firstly for the accurate location of the system elements on the support structures of the drift modules, and secondly, are required to obtain the real displacements of the drift modules after a measurement of a given RASNIK channel. The next section in this chapter encompasses the complete transformations between coordinate systems.

Before the installation in the spectrometer, the final setup, including optics, electronics and support structures, was tested and calibrated to ensure a reliable transformation from the measured mask displacements into real module transformations. The new software implemented to control, check and monitor the alignment systems is next described. This software has been integrated in the common “slow control” tools of the HADES experiment.

Finally, the results obtained during a data taking period in November 2001 are reported. The measured relative displacement of the modules has been used to correct the position parameters of the drift modules.

4.1 RASNIK: a relative alignment device

RASNIK [1] is the acronym of *Red Alignment System of NIKHEF*. It is a three elements alignment system developed at NIKHEF (National Institute for Nuclear Physics and High-Energy Physics, Amsterdam, Holland), originally for the L3 collaboration at CERN. After this pioneering application, it was continuously and extensively improved, and now it is being used in several HEP experiments. The version we have used is based on that done by NIKHEF for ATLAS (see a description in references [1, 2]).

The basic idea behind the system is very simple. An image is projected onto a sensor, using a projecting lens. The analysis of the displacement of the image can inform us about the relative positioning of the three elements (image-lens-sensor) that compose the system. Selecting adequately the component characteristics, several accurate systems can be built with an ample range of light path lengths, from several millimeters to several meters between the emitter and the sensor.

From this base, the physical components and the ancillary software were evolving dramatically. At the beginning, the image was made using a simple squared or circular aperture homogeneously illuminated, and the light detector was a four-quadrant diode, where the ratio of the amount of light measured in each quadrant defines the misalignment. This setup was used successfully in the L3 collaboration [3, 4], where the information was used to correct the alignment of the inner layers composing the large Muon Chambers. This primitive RASNIK devices presented a short range, limited mainly by the size of the quadrant diodes. The light aperture quality and uniformity was a relevant parameter concerning the position resolution. Both limitations were clearly the elements to be improved. On the other hand, the rise of new technologies made possible the determination of distances also in the longitudinal direction, by studying the image magnification.

The image sensing world changed abruptly with the arrival of the CCD (Charge-Coupled Devices), invented by Boyle and Smith in 1970 (for a complete revision see [5]). The ulterior development of these techniques and their wide use, reduced strongly their price and made possible their common use in all kind of applications, while the number of pixels and the signal to noise ratio increase.

Regarding the image to be projected onto the sensor, the techniques of metal on glass grabbing using photo-plotters, employed in Optics and Electronics for the integrated circuit production, were used for the construction of large surface masks. In this way, the use of a coded image allows the recognition of the mask position, being the range no longer lim-

ited by the sensor size but rather by the size of the image of the coded mask onto the CCD sensor. Different designs (from Fresnel-like plates to the current chessboard-like mask) were tested in NIKHEF; these experiments lead to the idea of a code describing the rough position inserted in a field of black-white transitions. The black-white transitions provide the better and sharper position definition of the emitter.

The resolution obtained with a RASNIK system depends strongly on their relative distances and other features of the components. Examples of reported values, characterized by the focal length f of their lens are shown in [6]. For $f = 1355 \text{ mm}$, an accuracy of $2 \mu\text{m}$ in the transverse direction and below $70 \mu\text{m}$ for the longitudinal direction is reported. For $f = 60 \text{ mm}$, an accuracy up to $0.3 \mu\text{m}$ in the transverse direction and around $1 \mu\text{m}$ for the longitudinal direction was measured. The same report states that the biggest constraint to the accuracy is the thermal fluctuation in the air. The influence of the quality of the available masks and the framegrabber synchronization errors are found to be negligible.

Regarding the linearity, reference [7] reports measurements both in translation and rotation with an rms of $0.1 \mu\text{m}$ in the X_R and Y_R coordinates (both perpendicular to the light path) and a relative random error in the magnification of 3×10^{-5} , for a $f = 63.5 \text{ mm}$ system. The determination of the mask-camera relative rotation is much less accurate, given only a rough indication of the present rotation values. Also it is presented in the report a study of the illumination effects on the resolution: the minimum required LED current for illuminating the mask was indicated by a failure of the ICARAS system rather than a rise of the random error.

RASNIK in HEP

RASNIK was originally designed as a straightness monitor for the support bridges of the high resolution muon detectors in the L3 experiment [4]. The L3 muon spectrometer was designed to measure the momentum of the high energy muons from the LEP e^+e^- collisions, with a dimuon invariant mass resolution of 1.5% at the vector boson Z resonance. The requested resolution implies an alignment precision of about $30 \mu\text{m}$ in the large muon chambers. The frames supporting the sensing wires were instrumented with the primitive version of the RASNIK monitor, composed of a LED, a simple lens and a four quadrant photodiode. Any deviation of the symmetrical light response on the quadrant diodes signals a displacement, which is corrected by mechanical actuators. Also another RASNIK monitor was used to check displacements between the three chamber layers in each octant. The lens supports and the quadrant diode were directly

related to wires using an electric pin connection. This original application proved to successfully correct the misalignment within the requested $30\ \mu\text{m}$.

The CHORUS experiment [8] was one of the first employing a set of channels of a RASNIK modern version. The RASNIK systems were mounted on the honeycomb tracker, with a total length of $610\ \text{mm}$ and between support elements with a length of $4000\ \text{mm}$ between the light source and the camera. They reported a repeatability from one measurement to the next better than $2\ \mu\text{m}$, which may well be due to the limited rigidity of the detector and not to an instability of the RASNIK response.

The massive use of RASNIK channels is the base of the projective alignment system of the ATLAS Muon Spectrometer [2]. A pure three elements alignment is performed between the distant muon chambers, disposed as projective towers. The correction of the muon track sagitta is performed off-line from the optical measurement. It is planned to control the positioning accuracy of the optical sensors by using straight muon tracks. Also it is foreseen the use of proximity sensors, short focal length RASNIK channels, for determining accurately displacements of adjacent volumes. The muon detection system of the CMS spectrometer [9] also contains a complete net of RASNIK channels, composing a geodesic network with other optical sensors.

All RASNIK components (LEDs, CCDs, CMOS) have been irradiated by neutrons for testing the radiation hardness. These tests were performed taken into account their use in the ATLAS collaboration, where the radiation levels are much higher than in the HADES environment. The conclusion from these studies was that the recommended setup, which is explained in the following sections, is sufficiently radiation resistant [10].

4.2 RASNIK description

This section is dedicated to the description of the RASNIK setup, as it is being used in the HADES spectrometer. The basic elements of every RASNIK channel, that are described in detail in the next subsections, are shown in figure 4.1:

- The light emitter (RasLed), divided in two pieces: one containing a matrix of infrared LEDs (Light Emitting Diode) and the other with the diffuser and the mask.
- The projecting lens.
- The video camera using CMOS technology.

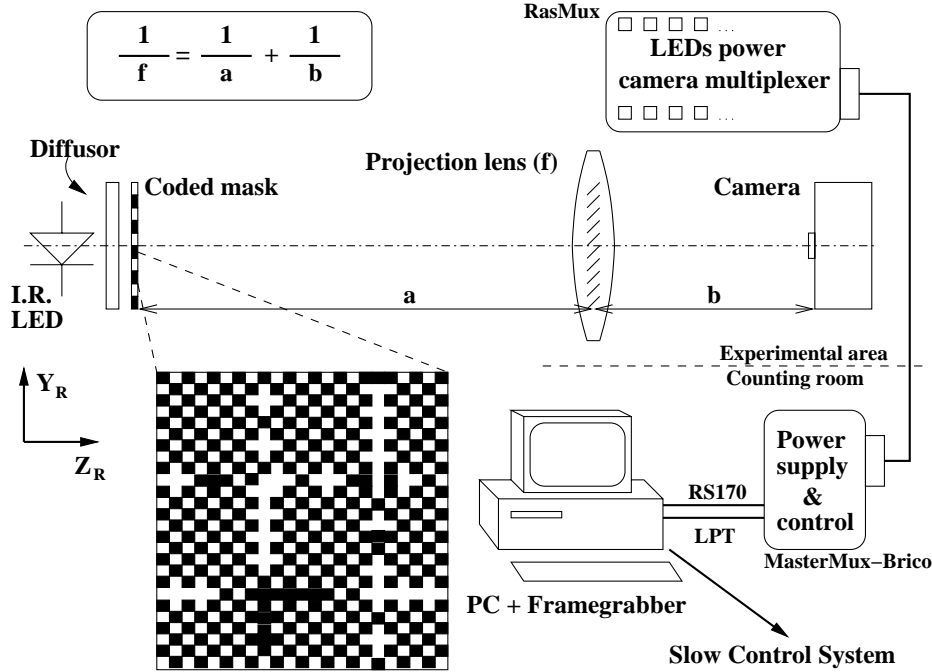


Figure 4.1: A working RASNIK channel. The multiplexer, the power box and the framegrabber in the PC are included. See the components description in the text.

- The electronic system for the multiplexing of the video camera signals (RasMux) and the power supply for the camera and LEDs (MasterBrico) [11].
- The video framegrabber installed in a PCI slot in a Personal Computer. The framegrabber digitalizes the signals according to the RS170 (EIA170) standard.
- The image is analysed by ICARAS, a NIKHEF program which receives the signal digitized by the framegrabber. The output is an estimation of the relative position of the elements.

In advance to the complete description in section 4.5, the RASNIK coordinate system (X_R, Y_R, Z_R) is defined as that with the Z_R axis following the optical axis (straight line joining the lens and camera centers) while the X_R and Y_R axis follow the main camera pixel directions, defining a right handed system.



Figure 4.2: *A mask image recorded by the camera.*

4.2.1 The Mask and LEDs board

The image emitting system is composed of two elements: the electronic board where the LEDs are inserted (the so-called RasLeD [11]) and the mask, glued to an aluminum machined piece. Both pieces are fasten together using three brass press-fit Snap-Top Standoffs, electrically isolated from the circuit. Their complete volume is around $50 \times 42 \times 25 \text{ mm}^3$.

The RasLeD system has nine high efficiency IR emitters arranged in a two dimension square matrix on a circuit board. The IR emitters are 875 nm LEDs of two different types, for different RasLeD versions: HSDL-4420 #011 from HP and SFH421 from Siemens. The LEDs from HP are tested to be radiation hard, while the others are less resistant by a factor 10 or more. The LEDs square size is approx. $1.3 \times 1.3 \text{ mm}^2$ and the viewing angle is 24° . The RasLeD circuit places the nine IR emitters in series with a 165Ω current limiting resistor, being feed by a nominal input of 24 V at 65 mA . The input connector is a standard unshielded RJ11 type. The circuit is reverse voltage protected with a parallel diode. The connection scheme as well as further features are reported in reference [11].

A diffuser (Opaline glass, 3 mm) placed between the mask and the LEDs board and glued to the mask support is used to reduce the imperfections in the light definition, producing an improved homogeneity in the illumination source.

The image projected onto the camera should contain multiple black-white transitions to improve statistically the position resolution. The projected black-white transitions cover several pixels, making possible a fine interpolation of the transition, that is an order of magnitude more accurate than the pixel size [10]. Also it should contain a code able to allow the identification of the part of the mask seen by the camera. Remember that the mask determines the range of the off-axis displacements, that can be larger than the light sensor surface, depending on the optical arrangement. The mask is made of chromium on glass, grabbed with high accuracy (below 0.5 μm) following the techniques of metal on glass grabbing using photo-plotters. The printed pattern represents a set of alternate black and white squares, forming a chessboard of a given length, which should be optimized for the relative distances between the elements and the image size in the sensor. The chessboards are separated by rows and columns of squares with unique coded information. The code can be extracted using a logical operation (OR) on the mask with a normal chessboard pattern. A more detailed description of the process is included in reference [12]. A mask image recorded by the video camera is shown in figure 4.2.

The mask size depends on the application. We use a $20 \times 20 \text{ mm}^2$ mask; the length of each black square (mask pixel) side is 170 μm .

4.2.2 The Camera and the image recording system

The image projected by the lens is recorded by a monochrome camera. Two different models were used in our setup, belonging to two different technologies. At the beginning of this work, a standard CCD camera (Chiper CPT-8933) was used for the aperture and angle studies as well as for the first tests. Finally, as the low cost of the improved CMOS based cameras moved the preference of RASNIK users toward these models, we also adopted CMOS cameras, even showing lower performance than the more expensive CCDs.

Both CMOS and CCD imagers have similar sensitivity over visible and IR light, being both made of silicon and performing the same photo-conversion process. In the CMOS sensors, the charge packets are not transferred like in CCDs, but detected by charge sensitive amplifiers, made of CMOS transistors. It is normally a major problem to match the multiple different amplifiers within each sensor, but once done it reduces the resid-

ual level of fixed-pattern noise to a minimum [13]. Also CMOS cameras normally have a better integration and lower power consumption.

The adopted model is a Vision VV5430 integrated composite video sensor [14]. It is a monochrome dual standard EIA/CCIR device, providing a complete video camera on a single chip. It is made of a 384×287 pixel array and includes automatic exposure and gain control as well as timing signals for external ADCs, a feature we are not using due to our limited framegrabber performance. It allows the selection between linear or gamma correction video signal on the video output levels. The pixel size is $12 \times 12 \mu m^2$ and the array size is $4.66 \times 3.54 mm^2$; the power consumption is below $300 mW$. The minimum useful sensor illumination for the analysis algorithm is about $0.5 lux$.

The so-called gamma correction is a modification of the electric camera output, introduced originally to eliminate the imperfections and non-linearities of television tubes and cameras. In these devices, the intensity is not a linear function of the input signal. The electric camera signal is then reduced accordingly with the formula

$$\text{output} = (\text{linear output})^\beta \quad (4.1)$$

where β is a number between 0.45 and 0.7. In the official CCIR standard $\beta = 0.5$. For the RASNIK mask pictures, the gamma correction enlarges the white areas, leading to larger errors in the determination of the position, mainly in the Z_R direction, where the black-white transition detection is essential. The problem is apparent mainly when mask edges and code lines appear and disappear in different images (after a displacement). Therefore, the Z_R coordinate can change when scanning over X_R and Y_R . The gamma correction should be disabled if the camera offers this option, as it is in our selected model. Also auto-gain and auto exposure options are switched on.

The camera chip is mounted on a board called RasCaM [15]. The board contains the light sensor and a complete I²C bi-directional bus to control or monitor various camera settings. I²C is an acronym for Inter-IC bus, from Phillips Semiconductors, and is a bus to provide a communication link between Integrated Circuits. The camera control is transparent to the user, being implemented in the ICARAS software. The board size is around $42 \times 50 mm^2$ and the card draws approx. $80 mA$ at $12 V$. It is connected to the multiplexer via a FTP cable with four twisted pairs transmitting power, semi-differential video, pixel clock and I²C signals. As stated before, the gamma correction pin is set to high (no gamma correction). Several control lines are also available in the board as solder terminals.

The signals from the different cameras are multiplexed in order to use a unique framegrabber for the complete system. The same board powers up the LEDs board in a definite order. In reference [16], a preliminary version of the multiplexer (RasMuX) corresponding with our setup is presented. A maximum of twelve RasLeDs boards and eight RasCaMs can be connected to the multiplexer, which can be located in the cave, close to the detectors. The multiplexer also translates the JTAG instructions from the PC to I²C commands, which are sent to the camera. The module requires three voltages, which are supplied by the so-called MasterBrico board. This board is located close to the PC and is connected to the framegrabber for sending the video signal and to the PC parallel port for transporting the control signals. These signals are converted in the MasterBrico from single ended printer port signals to differential signals, and vice versa. Also the differential video signals are converted to single ended signals as needed by the framegrabber.

In our setup we use a DT3155 PCI framegrabber from Data Translation [17]. The model is a PCIbus-based high accuracy framegrabber. It can acquire monochrome video images and transfer the image to memory or display in real time, digitizing and synchronizing 8 bit (monochrome) video from 50 or 60 *Hz* video inputs. The board supports monochrome RS-170, NTSC, CCIR and PAL video formats.

The number of available black-white transitions along the X_R direction is approximately 1.5 times bigger than in Y_R . But, when measuring a fixed system, the stability of the results is better in Y_R due to the CCIR definition. The lines in the video signal are well defined, while the pixels on the line are not; the number of pixels available for the image reconstruction mainly depends on the framegrabber clock rate. The quality of the framegrabber clock determines the fit quality and stability, and limits the system resolution.

4.2.3 RASNIK software

ICARAS (Integrated Control and Analysis for RASNIK, v.4.3.3.7) is the software that integrates the control of the RASNIK hardware and the analysis of the images. The program was made at NIKHEF using Visual C++ and runs under several Windows operative systems, in particular Windows NT (see a description in reference [1]).

To find the position of the image captured by the camera, four steps are performed sequentially. First, the data is filtered to remove harmful effects as smudges or inhomogeneous mask illumination. Standard computer algorithms like differential filters are used for this. Typically an individual

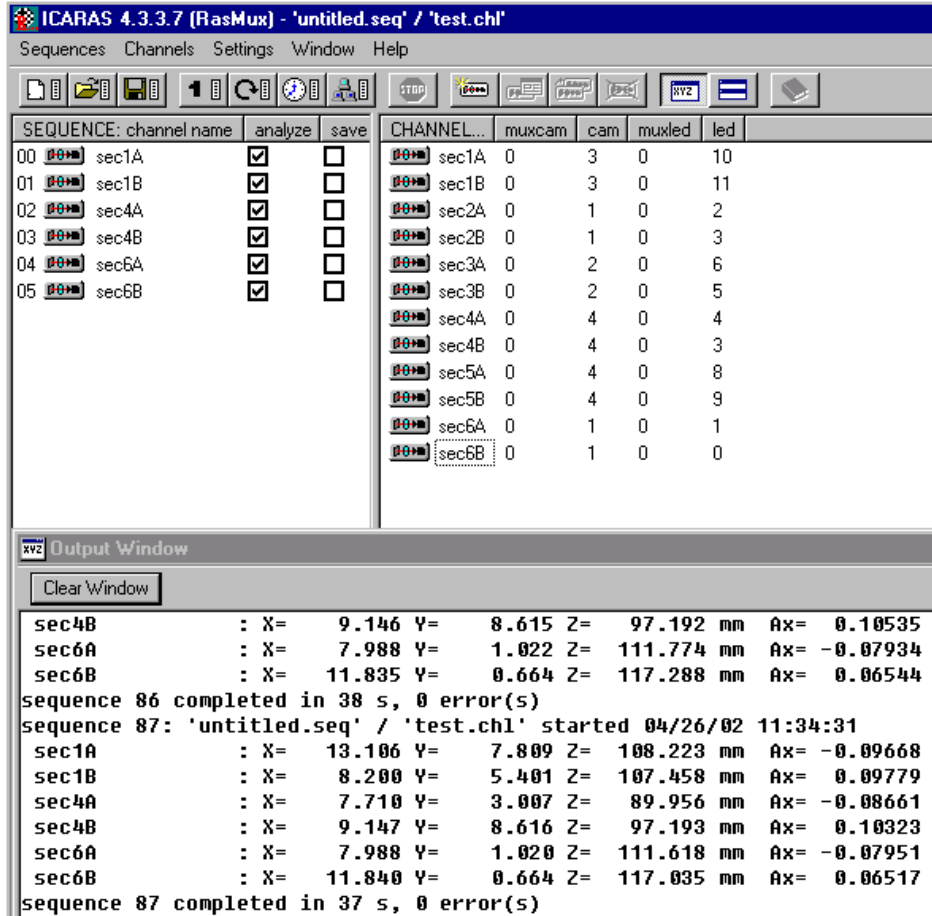


Figure 4.3: Snapshot of the ICARAS main window. The right pad shows the channel properties, independently configured. A set of channels configures a images sequence in the left pad, which can be acquired and analyzed just one time or continuously (round arrow icon). The lower pad displays the analysis results.

transition is reconstructed within a $5 - 10 \mu m$ precision [6]. The quality of the picture is analyzed, to define gradients and black-white differences. Secondly, an accurate fit is used to find the global position, that is, the main directions, orientation and the magnification. The number of points (total pixel number) considered in the analysis is reduced more than an order of magnitude by locating the black-white transitions. These transitions are optimized by interpolation and used from now on in consecutive fits. Then, the location of the code line is found with respect to the sensor center. The

black-white transitions previously determined are fitted independently in X and Y, due to the difference in the definition of columns and rows in the CCIR 170 video standard (the number of lines are well defined, but the number of pixels in the line not; depends on the framegrabber behavior). Finally, the code in the row and column is recognized and the position of the image determined. The conversion to user coordinates is performed, taken into account the sensor and mask geometry, the lens specification and the relative position of all the elements, following the paraxial optics approximation.

To perform the analysis, the code requires the input of a large set of parameters: distances, lens features, mask and camera pixel dimensions and relative orientation of the axis ..., each one defined individually for each channel. The software allows the control of camera and framegrabber via configuration parameters. After an image analysis, the output of the program contains a set of channel identification, time and sequence information and flags determining the status; the displacement, the magnification, a low resolution identification of the relative rotations and the errors given by the analysis program to each parameter complete the output file. An array of channels configure a sequence. The program allows the monitoring of the channels in a sequence and the continuous repetition of the sequence, or just a snapshot of the present situation running the analysis for the channels in the sequence once. Also triggered analysis can be performed, on external events or on a determined system time. An ICARAS main window snapshot is displayed in figure 4.3.

4.2.4 Image projection

The lens should project a sharp mask image on the camera sensor plane. The image production can be studied using the paraxial optics approximation. Any displacement of the mask along the normal direction to the optical axis is observed directly as a displacement of the sensor image, corrected by a geometrical factor. The displacement in the longitudinal direction, corresponding to the optical axis, is obtained from the study of the image size. When a sharp image is obtained on the camera, the relationship between the elements distances is given by:

$$\frac{1}{f} = \frac{1}{a_0} + \frac{1}{b} \quad (4.2)$$

where f is the lens focal length, a_0 is the mask-to-lens distance for perfect focusing and b is the camera-to-lens distance. The image magnification M , defined as the ratio between the image size and the object size, depends on

the relative distances as $M_0 = b/a_0$ for one image perfectly focused. The subindex in M_0 stands for the magnification of the perfectly focused image. If the camera-to-lens distance is fixed, one can determine the mask-to-lens distance from the magnification measured by analysing the image on the camera. The use of the relation $a = b/M$ requires a precise determination of the distance b (camera-to-lens), which normally cannot be performed. Instead of this, one can depart from equation 4.2 for the perfectly focused image to determine b , and then obtain the new relation

$$a = f(M_0 + 1) \frac{1}{M} \quad (4.3)$$

for any image.

The lenses are made of BK7, a commonly used cheap lens material which offers sufficient quality. The BK7 presents a flat transmission coefficient above 350 *nm* and up to 2000 *nm*. An infrared filter (Edmund Scientific Optcast IR filter) is mounted on the camera cover (test setups) or coaxial to the lens (final setup) to avoid the entrance of environmental light on the camera which can degrade the signal to noise ratio.

There are two important parameters that define the relation between the lens diameter and the focal length: the image sharpness and the signal to noise ratio of the video image. The last ratio depends on the camera features, but for a given model is mainly a function of the illumination. A value of the lens diameter over focal length of about 0.03 is recommended for large systems with condenser (field lens or Fresnel lens). For shorter distances, a higher number is easily reached, even without condenser (only with an opaque diffuser) [1].

When using a LED source, which produces almost monochromatic light, there is no chromatic aberration and a single lens is adequate. A simple plane-convex lens was chosen due to the low system apertures and their low cost. The spherical aberration and the cushion deformation was not observed for such a system.

4.3 Mechanical construction

Based on the results of the laboratory tests of the RASNIK performance and the studies of the spectrometer geometry, it has been proposed the use of two RASNIK channels per spectrometer sector, by attaching a camera onto the inner set of MDCs and two light sources onto the frame of the MDC III, in such a way that the light from both sources impinges upon the same camera. The camera and the two lenses are mounted on the

same piece, the so-called *binocular* (see figure 4.4), ensuring a fixed relative position. The objective of such a setup is the determination of the relative position of two points of the MDC III frame with respect to the inner modules. The knowledge of the position of two points in the MDC III frame determines completely the relative position of the chamber, with the exception of a rotation around the line joining both points.

The *binocular* was designed according to the following principles:

- Fix the camera strongly to the MDCs support, while shaping the two optical axis (camera and lens centers line) to the chosen angles.
- Minimize the change in camera-to-lens distance due to the material thermal expansion or to any other mechanical deformation.
- Should allow the lens displacement along the optical axis for further image focusing possibilities.
- Should have a mechanism for the fine positioning of the lens for easy image finding and centering. This allows a simple fixation of the mask support in the MDC III frame, without complex positioning mechanisms.
- The infrared filter is placed contiguously to each lens, to simplify the mounting of the camera. Therefore, the piece should be opaque.

In the following paragraph, the numbers in parentheses refer to the pieces in the figure 4.4. All the detailed technical drawings are shown in the appendix I. The lateral pieces (3,4) and the upper piece (6), which support the structure, are made in epoxy carbon fiber (Stesapreg EP 121 c15/53, Stesalit AG, CH-4234 Zullwil, Switzerland), due to its rigidity, low weight, stress resistance and the low thermal coefficient expansion (below $10^{-6} K^{-1}$ longitudinally). The segmented side covers (25) are made of EPC205 (Durostone, Röchling Haren KG, D-4472 Haren, Germany), painted with conductive graphite, while the camera base (2), wedge (1) and the *binocular* chamfers (5) are machined on aluminum alloy. The lens (200 mm focal length) and the infrared filter (Edmund Scientific Optcast IR filter) are mounted in an optical barrel (T-Mount, 25 mm thick lens mount plus extension tube, Edmund Scientific Company Inc., 08007-1380 New Jersey, USA) which can be displaced along the optical axis, and finally fixed with screws once the image is correctly focused.

The main purpose of the *binocular* piece is to maintain the relative position of the lenses with respect to the camera sensor. The thermal

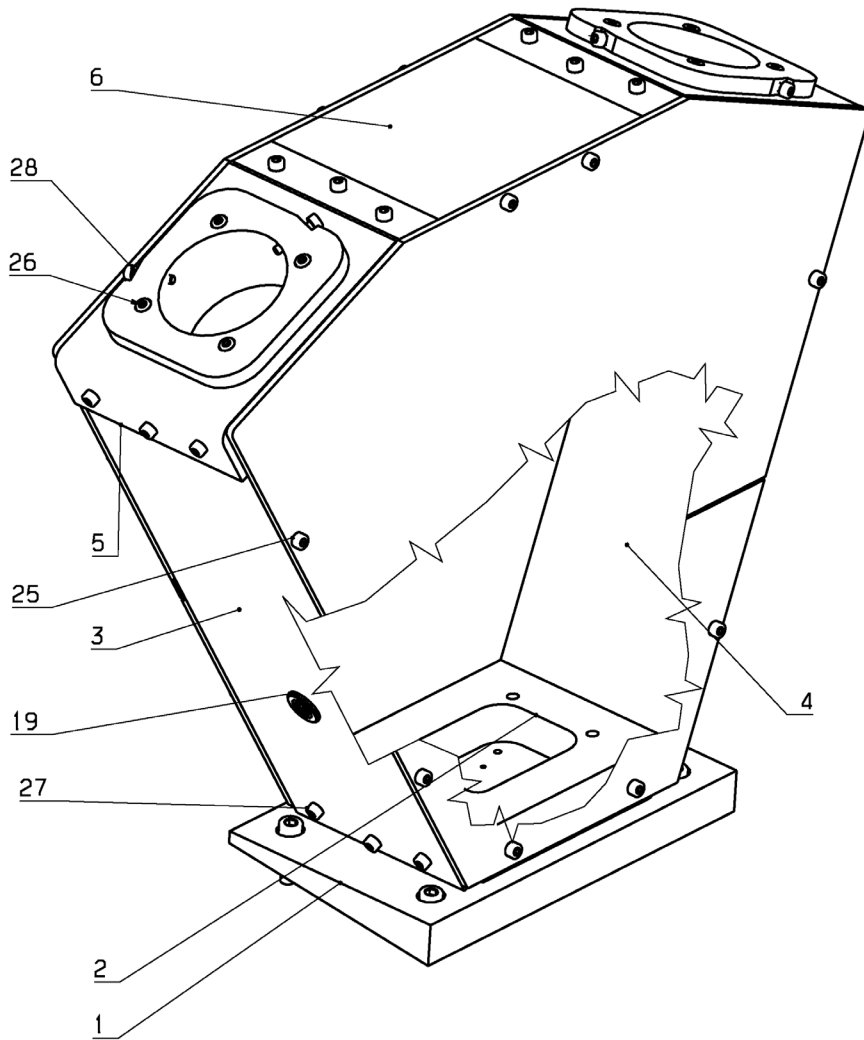


Figure 4.4: Scheme of the RASNIK binocular. The cut allows the observation of the inner camera support piece. The pieces are identified along the text by the number in this figure.

expansion due to the change in the material temperature, is the main effect which modifies the camera-to-lens distance. The thermal expansion of the aluminum is around $23.1 \times 10^{-6} K^{-1}$ [18]. If aluminum were used in the construction of the *binocular* body, the lens-to-camera distance could vary up to $70 \mu m$ when the temperature changes ten degrees. The piece

is located close to the MDC electronics, and their large power consumption leads to large changes in the temperature. Then, it is mandatory the use of a material with very low thermal expansion coefficient. Otherwise, most of the plastic materials *flow* or present deformation when suffer stress, so that one should avoid the use of plastics on the supporting structures. Therefore, for the critical support structures, epoxy carbon fiber has been used. The mechanical properties of this material are well suited for this application; but, nevertheless, the thermal behavior is the critical point. Longitudinally, the thermal expansion coefficient is very small and negative, around $-0.5 \times 10^{-6} K^{-1}$, but the value depends strongly on the fabrication and curing methods. Anyway, the expected change in the lens-to-camera distance due to a temperature change of ten degrees is well below $10 \mu m$. The use of this material has been restricted to the minimum needed for the supporting structures due to its huge price (both in raw material and part machining).

The aluminum chamfers (5) are also structural pieces that shape the top corners of the *binocular*. The complexity of these parts forbids the use of the epoxy carbon fiber. But their size has been reduced (below $100 mm$ of effective length) and are symmetrically disposed around the lenses to avoid any thermal displacement¹. The lateral covers are made of a strong plastic material (EPC205), much cheaper than the epoxy carbon fiber; they have no structural function, and simply cover the sides of the opaque box. The thermal expansion coefficient of EPC205 is $10 \times 10^{-6} K^{-1}$, but the covers are screwed to the carbon fiber pieces in such a way that there is no deformation on the shape due to thermal expansion. For the same reason, each cover is divided in two overlapping parts.

The aluminum chamfer (5) where the optical barrel is fixed on, is actually made of three aluminum elements allowing a slight displacement (around one *cm* in any direction of the chamfer plane) on the plane normal to the optical axis. The scheme of the mounting is shown in figure 4.5. An annular piece (blue in the figure) fits perfectly to the outer side of a cylindrical mount (in red). Both elements are screwed together (26), and press the chamfer (green) which is sandwiched between both. The optical barrel containing the lens fits in the cylindrical mount and is fixed at the focus point by two screws (28). The range for the lens barrel positioning along the optical axis is of a few *cm*. The design allows the image search and optimal focusing and centering after a modification of the light source position during the initial installation or when the MDCs are removed for

¹Actually the positive thermal expansion due to this pieces can approximately compensate the negative value of the larger structural epoxy carbon fiber pieces.

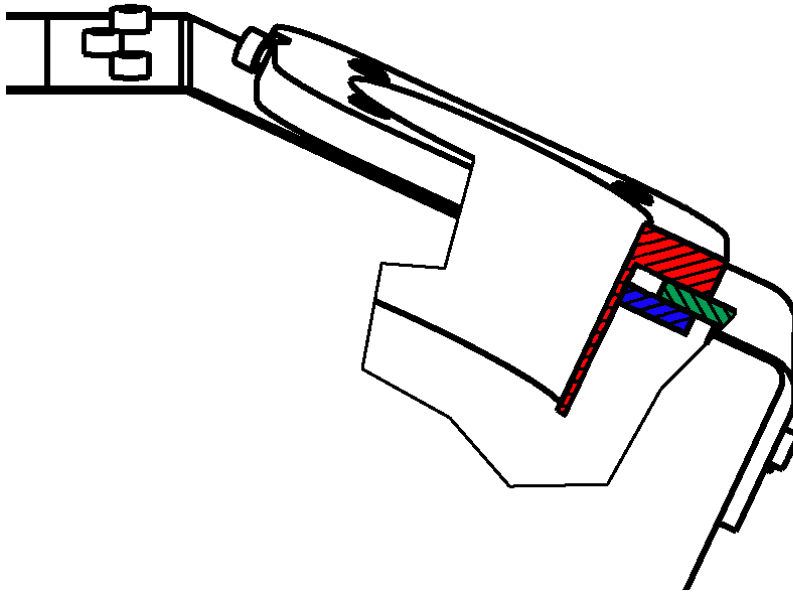


Figure 4.5: Detail of the lens barrel support pieces. The optical barrel is inserted into the cylindrical support (in red), which is screwed to a ring (in blue). The mounting allows the displacement in the lens plane of about 1 cm in any direction, on the plane normal to the optical axis.

maintenance and the original position is not perfectly recovered.

All the pieces have been designed using CATIA [19]. CATIA is a commercial CAD/CAM/CAE tool for digital design processes, encompassing the initial conceptual modeling, the 3D detailed mechanical implementation and the 2D drafting and annotation for the final production. The integration of the alignment pieces in the spectrometer has been accomplished inside the complete virtual spectrometer model. Some of the figures (for instance, figures 4.6, 4.12 and 4.23) and all the technical drawings of the pieces shown in the appendix I, has been made using CATIA. From the mechanical point of view, the complete system has been designed under the standard ISO 2768-1 m, providing a reasonable machining accuracy at a medium price. All screws are M3 of different lengths, using M5 for the camera base and wedge. Threads have been drilled directly on the aluminum, while the epoxy carbon fiber pieces contain inserts (Kern-Kobus Model 302025). An 8 pins LEMO 1B (308CLL) connector (19) has been

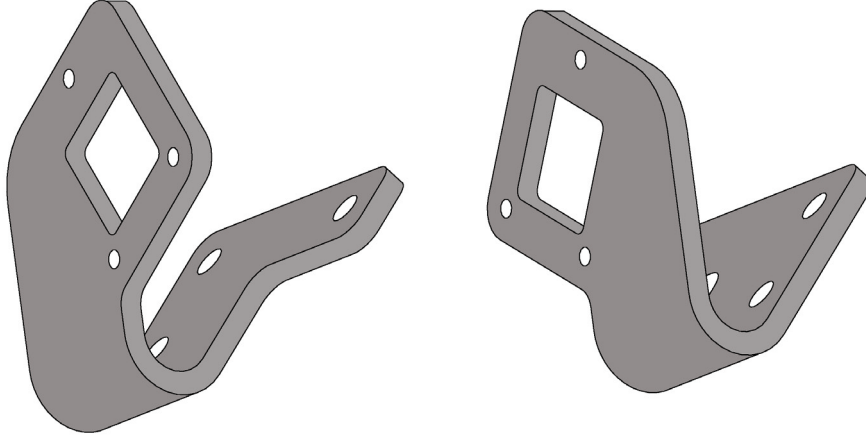


Figure 4.6: *The mask and LEDs support pieces.*

inserted in the lateral piece to control, read-out and power the camera. The complete *binocular* piece became electrically conductive, by painting the plastic covers with graphite.

The light sources are fixed to the MDC III frames using aluminum support pieces, shown in figure 4.6. The fixing points on the MDC frame and the support shape were chosen to fit the light beam in the lens-camera axis. The appendix G includes a complete explanation of their geometry.

4.4 Bench test of angle and aperture dependence

The setup explained in the previous section requires the use of RASNIK under non previously tested working conditions. Due to the geometrical location of the drift chambers, there are three parameters in the design of the RASNIK solution which determine the attainable resolution. These parameters are: the lens-to-camera and lens-to-mask distances (b and a respectively in figures 4.1 and 4.11), the angle α between the two optical axis defined by the *binocular* (see figure 4.11) and the effective diameter of the lens or lens aperture. The values of these parameters have been fixed after a set of tests in an optical bench.

Camera-to-lens distance

The distance b between the camera and the lenses must be short enough to fit in the available room, between the hexagonal support where it lies on and the refrigeration ring of the magnet. The available room limits the size of the piece containing the camera-lens system to one third of the camera-to-mask distance. Moreover, it would be difficult to build a support that guaranties that the relative position of lenses and camera is kept under a certain accuracy for a larger camera-to-lens distance.

As a consequence, the linear magnification ($M = \frac{b}{a}$) is reduced to a value close to or lower than 0.5. A further reduction of the camera-to-lens distance implies a smaller magnification of the image in the camera pixel pattern, and a reduction of precision. Moreover, apart from this reduction of precision, there is another effect on the measurement of displacements along Z_R . As it was explained in section 4.2.4, the measurement of a ΔZ_R is based on the relation 4.3, and for the same displacement, the change in the magnification is reduced. For example, a displacement $\Delta Z_R = 0.1 \text{ mm}$ represents a change of 0.25×10^{-3} in magnification for a system where $a = 300$ and $b = 600 \text{ mm}$; but for a system with $a = 200$ and $b = 700 \text{ mm}$, the change of the magnification is only 0.184×10^{-3} .

The angle α

As we are using only one camera receiving light from two distinct sources through two different lenses, the light impinges upon the camera forming an angle α with the sensor normal direction. The ideal image plane is perpendicular to the optical axis and, then, in our case the image on the camera plane is not well focused. The analysis of the image allows the study of these tilted images and is able to find out the value of the angle, up to a limit. Unfortunately, the resolution gets worse when the angle α increases, due to the focus defect. It is mandatory to determine the maximum allowed angle between the optical axis and the sensitive surface of the detector and evaluate the resolution losses per channel and direction.

The lens aperture

Given a focal length, the lens aperture (or effective diameter) is a relevant parameter. Larger apertures increase the luminosity but reduce the image depth of field. The depth of field, the capability of an optical system to display sharp images or resolve details for objects out of the focus distance, is of great importance in our case. As the determination of the image magnification out of the perfect focus position leads to the identification

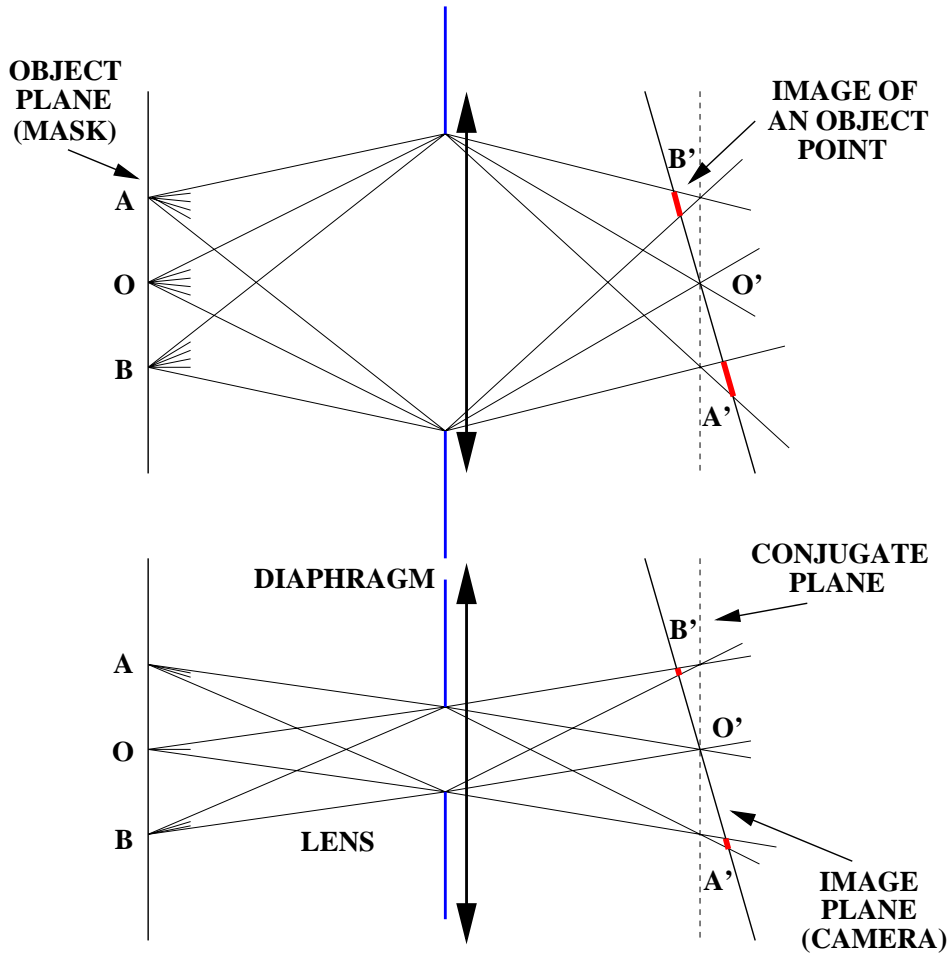


Figure 4.7: Simple scheme showing the effect of the clear aperture on the image depth of field. In the upper picture the complete lens aperture is used; the image of the object plane points is represented by a thick red line. In the lower picture the diaphragm reduces the lens clear aperture, and the size of the image points decrease.

of displacements along the optical axis direction, a large depth of field increases the useful range without faults in the analysis module. But, even more important, a large depth of field is mandatory because the image plane does not coincide with the sensor plane, being tilted as commented out in the previous point. Only a part of the image (actually only a line perpendicular to the picture plane passing through point O in figure 4.7) is perfectly focused, while the rest of the image is gradually blurred from this line. Figure 4.7 displays the effect of a diaphragm: reducing the

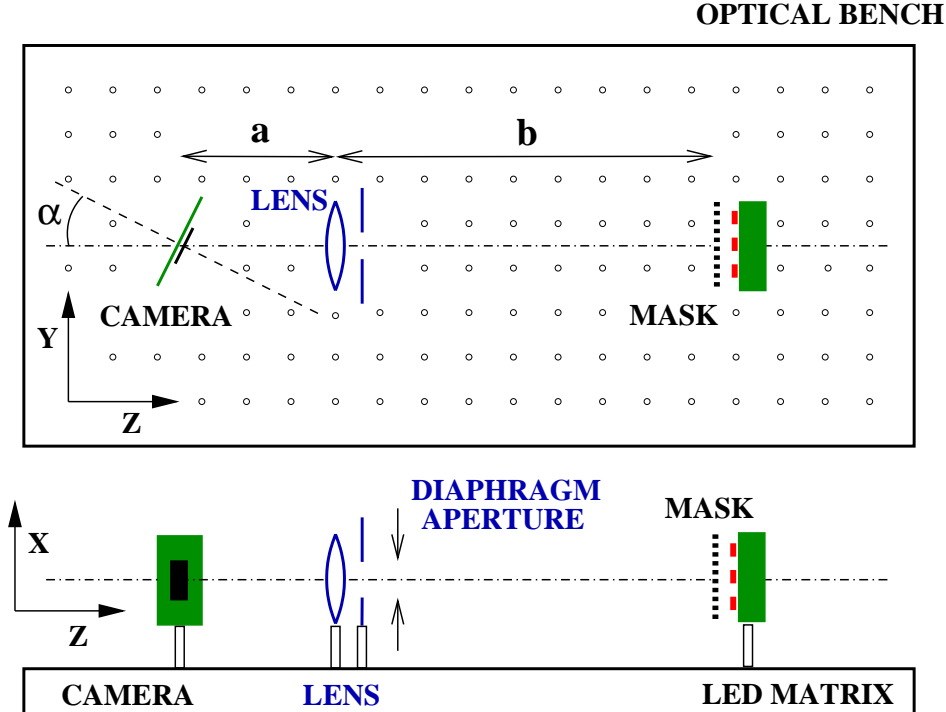


Figure 4.8: *Experimental setup for testing the effects of the aperture and incidence angle (α) of the light on the camera sensor.*

lens effective aperture, the complete image results sharper on the screen. But, on the opposite direction, due to the Fraunhofer diffraction, a small aperture decreases the image resolution, which can be represented by the diameter of the focused spot produced from plane wave illumination

$$d = 2.44 \cdot \lambda \cdot f/\# = 2.44 \cdot \lambda \frac{\text{focal length}}{\text{aperture}} \quad (4.4)$$

where λ is the wavelength of the light being focused and $f/\#$ (or f-number) is defined as the focal length over the lens clear aperture. However, the real resolution is obtained from the statistical study of multiple black-white transitions, each one presenting the sharpness given by the previous equation, so that the improvement of the resolution by increasing the aperture is irrelevant with regard to their harmful effect of the reduced depth of field. A compromise solution has been investigated between enough light-gathering and depth of field.

Lens focal length	254 mm
Lens diameter	50 mm
focal number ($f/\#$) (for an aperture of 15 mm)	5.08 (16.9)
Mask pitch	170 μm
Mask size	$15.4 \times 15.4 \text{ mm}^2$
Camera sensor size	$4.64 \times 3.68 \text{ mm}^2$
Camera pixel size	6.4 μm
Mask-lens distance	1000 mm
Mask-camera distance	340 mm
Total length	1340 mm
Perfect focusing magnification	0.34

Table 4.1: Main features of the channels used in the optical bench test. The focal number is calculated for an aperture of 50 mm, and for an aperture of 15 mm (result between brackets).

4.4.1 Bench test

A RASNIK system has been tested with its parameters tuned to the HADES requirements. The distances camera-lens-mask are chosen to be near to those in the HADES available place, using a 254 mm focal length lens and a mask of $170 \times 170 \mu\text{m}^2$ (pixel area). Also a mask with $85 \times 85 \mu\text{m}^2$ pixel was tested, but the analysis module found continuous errors using this setup. The RASNIK elements were mounted on an optical bench² (TMC Large Optical Top), fixing the lens and the camera to the bench in such a way that the image of the mask centers on the camera sensitive area, as shown in figure 4.8. No special steps have been taken to ensure the relative parallelism of the mask, lens and camera surfaces, or to align their main directions. This apparent lack of care in the installation is made on purpose, in resemblance with the final experimental use. The position in the spectrometer will not permit the access for fine tuning of the components relative parallelism. The camera was tilted to test the effects in resolution of the non-perpendicular light incidence up to an angle of 30° . Several diaphragm apertures were tested from 15 mm to 50 mm.

Data were taken during several hours for each parameters set, reporting several hundred points. The analysis procedure was the following (see figure 4.9): the taken data are plotted versus time to recognize systematic features, like day-night movements. The data show a continuous but sinuous line, sometimes broken by an occasional abrupt jump of several

²The used optical bench was installed in an inner, ground floor room of the Optics Holography laboratory in the Optics Department of the University of Santiago.

tens or hundreds of microns, clearly identified as real displacements of the floor or the optical table. The continuous flow of the data shows clearly the modification of the temperature in the room when additional computers were switched on. In the absence of any disturbing effect, the heat produced by the sunshine on the room walls, in the middle day hours, is visible (the test was performed during a sunny summer).

Selected data are fitted to a second order polynomial which shows the general trend of the data during that time. The residuals of this fit shapes quite well to a gaussian, showing that the deviation from the general trend comes mainly from statistic source and the second order polynomial is enough to follow the data trend. Anyway, in most of the cases the data follows a curve more sinuous than the simple second order polynomial, as can be seen in the left-bottom pad of figure 4.9. This sinuosity enlarges the width of the gaussian-like distribution, which is actually composed of several gaussian curves with close means. So, the final resolution measured using this method is an upper limit of the real resolution of the system, and will correspond to the real resolution only if the data display an exact second order polynomial behavior.

This method is used for several data cuts, reporting several values of the resolution. Figure 4.10 shows the mean value of the considered cuts, together with the respective square root of the mean variance.

From the results plotted in figure 4.10, the following conclusions are extracted:

- The resolution seen in the directions perpendicular to the optical axis (X_R and Y_R in figure 4.10) is two orders of magnitude smaller than the resolution in the light axis direction.
- The resolution improves for apertures of 15 *mm*, the smaller value tested. The resolution improvement with decreasing aperture looks a general trend in the tested range. This aperture value should not be reduced further due to the possible lack of illumination seen by the camera. A fault in the analysis module due to this effect was never seen in our test, but the recommended value [1] for the ratio diameter/focal length is about 0.03 if a condenser lens is used, and up to 0.3 for simpler systems without condenser lens. A 15 *mm* aperture on a 254 *mm* focal length lens corresponds to a ratio 0.06, already low for a simple system without condenser.
- For apertures of 15 *mm* the resolution is almost independent of the light incidence angle. Visually, the image is clearly sharper for the smaller apertures. Also the range, defined by a fault in the analysis

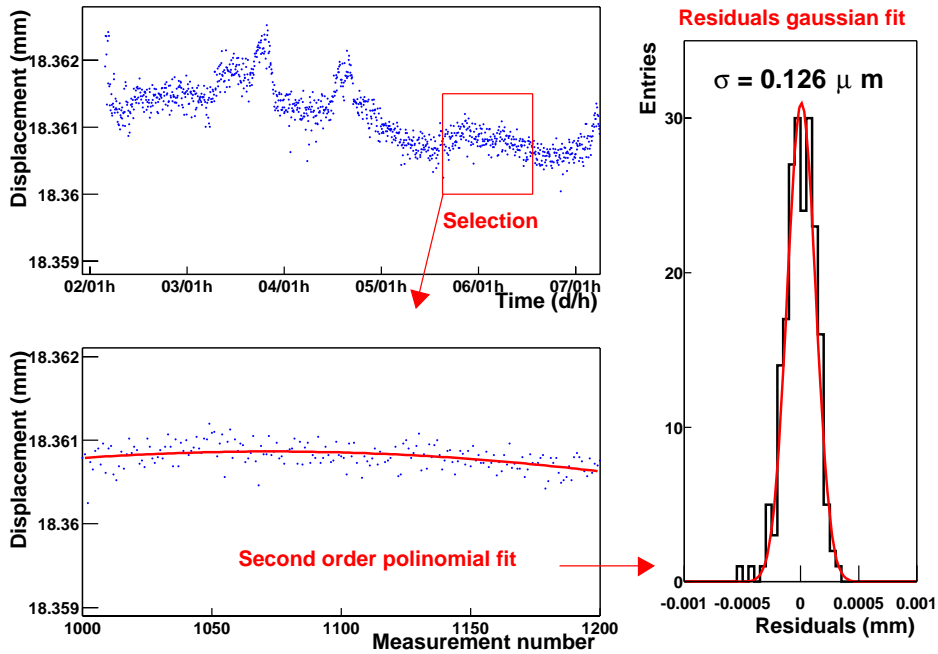


Figure 4.9: A graphical explanation of how the resolution estimation is obtained. In the top-left pad, the data obtained during several days are displayed on a time series (the day/hour is represented in the abscissa), and the squared zone is selected for further analysis. In the bottom-left pad, the selected data are fitted to a second order polynomial. The residuals of the fit shapes a gaussian-like histogram whose width determines the system resolution, as is shown in the right pad.

module when the image is too much blurred to determine the black-white transitions precisely, is larger.

- For the maximum tested angle, 30° , the image analysis fails frequently, mainly for large apertures. The occurrence of this fail limits the angle where the system runs in a reliable way.

The test has shown a robust behavior of the analysis module of the ICARAS program. The analysis reports reliable and accurate results even for blurred images and along all the coded masks surface.

The maximum angle where stable and reliable operation is warranted, without visible resolution losses, is 25° . This value has been taken, together with an aperture close to 15 mm for the alignment setup.

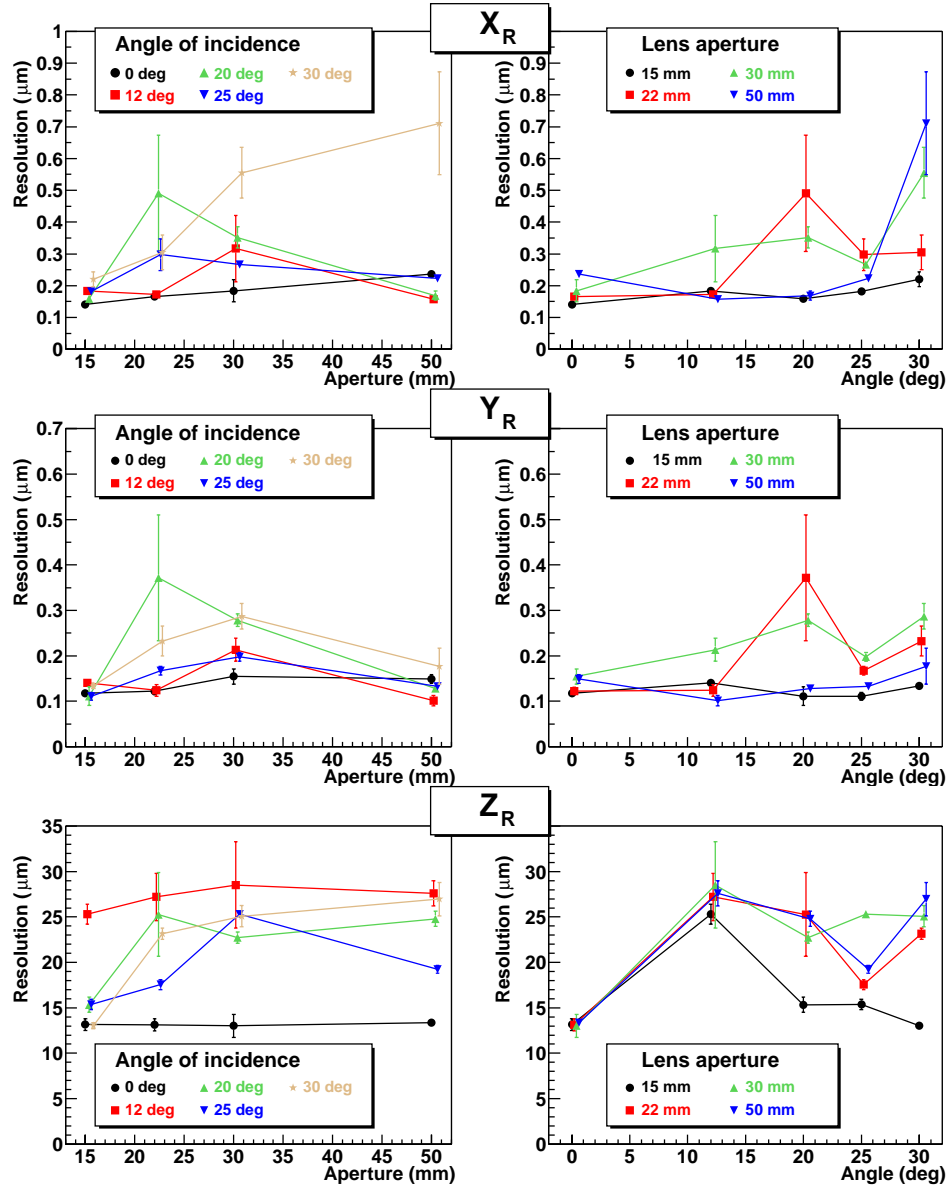


Figure 4.10: Resolution dependence on angle and aperture. X_R and Y_R are the directions perpendicular to the light axis, while Z_R is the optical axis. The left plots show the dependence on the aperture for different incidence angles α , while the plots in the right column display the dependence on the angle α for different apertures.

4.5 Integration in the spectrometer

Several coordinate systems that have been used are explained in detail below:

- **Laboratory coordinate system.** Following the HADES standard, it is used the notation (X, Y, Z) or $(X_{lab}, Y_{lab}, Z_{lab})$ to describe a point in this system. It is described [20] unequivocally as that having Z axis pointing in the beam direction and sense, Y axis pointing in the direction of the gravity but contrary sense, and X axis settling down a right-handed system.
- **MDC coordinate system.** The notation $(X_{MDC}, Y_{MDC}, Z_{MDC})$ is used, adding the MDC order number, if necessary. It is described [20, 21] individually for each MDC, centered in the point where a straight line coming from the center of the laboratory coordinate system crosses normally the fourth cathode plane of the MDC (the module symmetry plane). The Z_{MDC} axis follows the direction and sense of such a straight line, being the X_{MDC} parallel to the sense wires of the central anode planes (the sense is chosen in such a way that transforming to the sector 1 via a simple azimuthal rotation, coincides with the laboratory coordinates system X axis) and Y_{MDC} axis settling down a right-handed system.
- **RASNIK coordinate system.** It is used the notation (X_R, Y_R, Z_R) to describe a point in that system. It is described individually for each RASNIK channel as that having Z_R along the optical axis, that is, the direction and sense of the vector between the center of the sensitive camera area and the lens center. The directions X_R and Y_R follow the horizontal and vertical light-dark transition lines of the RASNIK image; which transitions are vertical and which horizontal are determined by their image on the camera chip [22]. If the image rotation around the Z_R axis, the optical axis, exceeds a certain value, the analysis routine may generate an error³. The coordinate system is centered in the lens optical axis; the mask displacements are reflected directly in the measured coordinates. For simplicity, let us consider the initial mask position as the center of the RASNIK coordinate system and to calculate any displacement from the origin.

³Actually, the X and Y directions resulting from the analysis of an image depends on the relative position of the mask and the camera. The calculations in this chapter are performed for an arbitrary election of the axis name and increase sense. The output from the real situation is formatted according to the election herein.

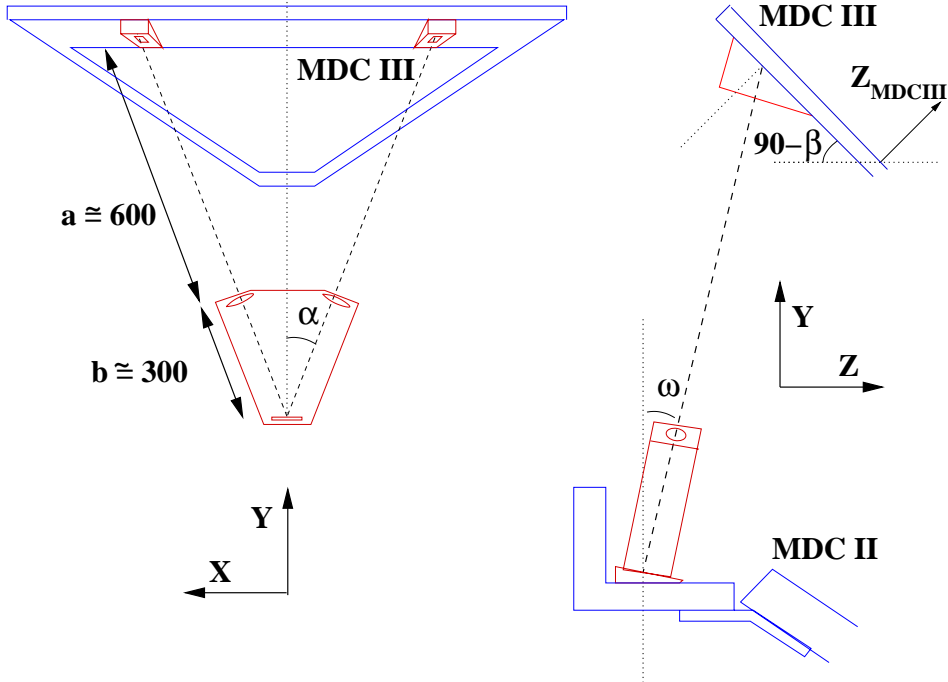


Figure 4.11: Angles between the RASNIK elements. Both drawings show the scheme of the (top sector) binocular piece and the LED's and mask support on the MDC III frame. In the left pad, the observer is located in the entrance of the beam line in the cave and is looking toward the positive Z direction. The schemes are not to scale.

The relation between the three coordinate systems depends on their relative orientation. The situation of the RASNIK channels on the spectrometer is fixed by several constrains, mostly related with the available space between the MDC modules and the modules frames. Figure 4.11 shows the three relative angles (α , β and ω) which are relevant in the transformation between the RASNIK channel coordinate systems and the laboratory or module coordinate system. The angle α was already dealt with in the previous section; corresponds to the angle between the RASNIK optical axis and the normal to the sensitive surface of the camera detector. A value $\alpha = 25^\circ$ ($\alpha = -25^\circ$ for the symmetric channel) was found to be a suitable compromise. The angle $\omega = 7^\circ$ is fixed by the mounting of the mask and LEDs support on the module frame. The third angle used in the transformation, $\beta = 49.10^\circ$, is given by the disposition of the MDC III on the spectrometer. Figure 4.12 displays an artistic view of the RASNIK elements on the spectrometer.

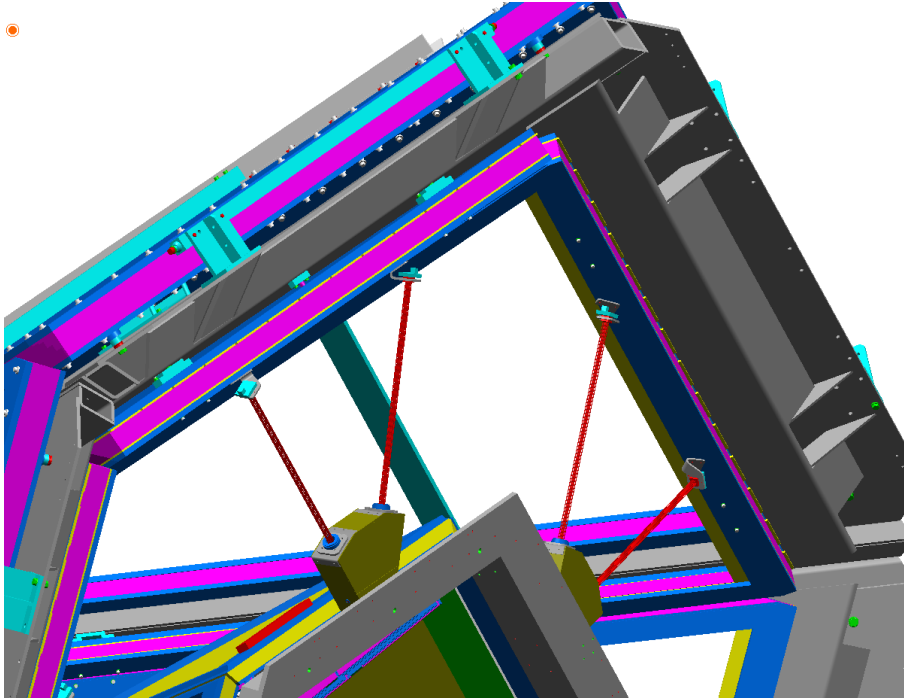


Figure 4.12: *Implementation of the RASNIK alignment system. The binocular piece, supporting the camera in its base and two lenses on the top corners, is installed on the hexagonal support of the MDC II modules. A pair of IR LED's and masks are mounted on the MDC III frames, geometrically oriented to emit the light following the optical camera-lens axis. The IR light path is artistically seen as a red line.*

The transformations between the RASNIK channels and MDC coordinate systems can be obtained for any sector, being exactly the same for the others. Transformations to the laboratory system depend on the sector; in the following, calculations containing such a transformation are performed for the top sector (sector 1).

Let us follow the usual angular sign convention where anti-clockwise rotations are taken as positive and clockwise rotations are negative, when the rotation axis points in the sense of the observer. For a right-handed coordinate system (X, Y, Z) , the rotation is positive if we rotate around X , and the Y axis initially moves toward the original Z axis. It is also positive if we rotate around Y , and the Z axis moves toward X axis. Finally, it results positive if we rotate around Z and the X axis moves toward Y axis.

The rotation between RASNIK and laboratory coordinate systems implies two elemental rotations. First, one can define an auxiliary system

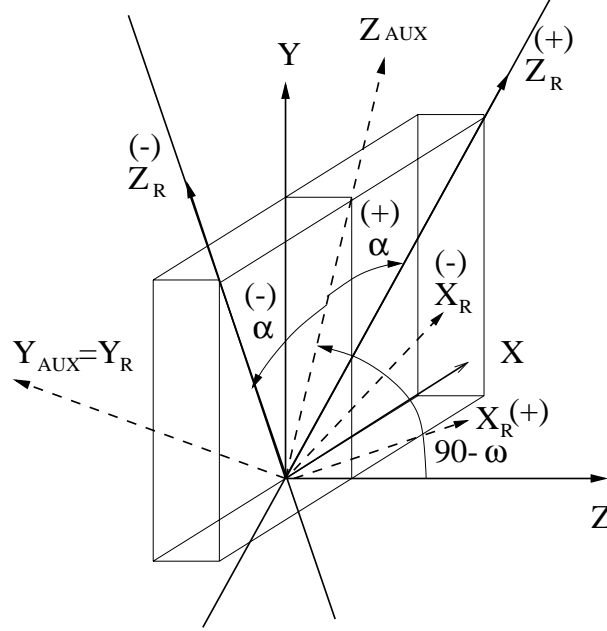


Figure 4.13: Laboratory, RASNIK and auxiliary coordinate systems and the angles between them. The (+) sign shows the axis for a positive rotation ($\alpha > 0$) and vice versa.

$(X_{AUX}, Y_{AUX}, Z_{AUX})$, obtained from the laboratory coordinate system by a rotation around X following an angle $-(\frac{\pi}{2} - \omega) = (\omega - \frac{\pi}{2})$. The Y_{AUX} axis of the obtained auxiliary system should coincide with the Y_R axis of the RASNIK system, as observed in figure 4.13. The transformation is

$$\begin{aligned} \begin{pmatrix} X_{AUX} \\ Y_{AUX} \\ Z_{AUX} \end{pmatrix} &= \begin{pmatrix} 1 & 0 & 0 \\ 0 & \cos(\omega - \frac{\pi}{2}) & \sin(\omega - \frac{\pi}{2}) \\ 0 & -\sin(\omega - \frac{\pi}{2}) & \cos(\omega - \frac{\pi}{2}) \end{pmatrix} \begin{pmatrix} X \\ Y \\ Z \end{pmatrix} \\ &= \begin{pmatrix} 1 & 0 & 0 \\ 0 & \sin \omega & -\cos \omega \\ 0 & \cos \omega & \sin \omega \end{pmatrix} \begin{pmatrix} X \\ Y \\ Z \end{pmatrix} \end{aligned}$$

Second, rotating the auxiliary system an angle α around the direction $Y_{AUX} = Y_R$ will render the orientation of the RASNIK coordinate system. Following our convention, the sign of angle α is positive in the right part of figure 4.13 ($X > 0$ hemisphere) and negative in the left part ($X < 0$ hemisphere), but both transformations are described by the same matrix

$$\begin{pmatrix} X_R \\ Y_R \\ Z_R \end{pmatrix} = \begin{pmatrix} \cos \alpha & 0 & -\sin \alpha \\ 0 & 1 & 0 \\ \sin \alpha & 0 & \cos \alpha \end{pmatrix} \begin{pmatrix} 1 & 0 & 0 \\ 0 & \sin \omega & -\cos \omega \\ 0 & \cos \omega & \sin \omega \end{pmatrix} \begin{pmatrix} X \\ Y \\ Z \end{pmatrix}$$

Then, it is immediate the relation between the RASNIK and laboratory coordinate systems

$$\begin{pmatrix} X_R \\ Y_R \\ Z_R \end{pmatrix} = \begin{pmatrix} \cos \alpha & -\sin \alpha \cos \omega & -\sin \alpha \sin \omega \\ 0 & \sin \omega & -\cos \omega \\ \sin \alpha & \cos \alpha \cos \omega & \cos \alpha \sin \omega \end{pmatrix} \begin{pmatrix} X \\ Y \\ Z \end{pmatrix} \quad (4.6)$$

Using the transpose matrix, the laboratory coordinates of any point can be derived from the point expressed in the RASNIK coordinate system.

$$\begin{pmatrix} X \\ Y \\ Z \end{pmatrix} = \begin{pmatrix} \cos \alpha & 0 & \sin \alpha \\ -\cos \omega \sin \alpha & \sin \omega & \cos \omega \cos \alpha \\ -\sin \omega \sin \alpha & -\cos \omega & \sin \omega \cos \alpha \end{pmatrix} \begin{pmatrix} X_R \\ Y_R \\ Z_R \end{pmatrix} \quad (4.7)$$

The simplest transformation between the laboratory coordinate system and the MDC coordinate system is obtained from a rotation of angle β , around $X = X_{MDC}$ (note that the calculations are valid for the top sector, for simplicity). The matrix rotation results

$$\begin{pmatrix} X \\ Y \\ Z \end{pmatrix} = \begin{pmatrix} 1 & 0 & 0 \\ 0 & \cos \beta & \sin \beta \\ 0 & -\sin \beta & \cos \beta \end{pmatrix} \begin{pmatrix} X_{MDC} \\ Y_{MDC} \\ Z_{MDC} \end{pmatrix} \quad (4.8)$$

Using the transpose matrix, the MDC coordinates of any point can be derived from its coordinates in the laboratory system.

$$\begin{pmatrix} X_{MDC} \\ Y_{MDC} \\ Z_{MDC} \end{pmatrix} = \begin{pmatrix} 1 & 0 & 0 \\ 0 & \cos \beta & -\sin \beta \\ 0 & \sin \beta & \cos \beta \end{pmatrix} \begin{pmatrix} X \\ Y \\ Z \end{pmatrix} \quad (4.9)$$

From the previous matrices, the relative rotation between the RASNIK and MDC coordinate systems can be obtained

$$\begin{pmatrix} X_R \\ Y_R \\ Z_R \end{pmatrix} = \begin{pmatrix} \cos \alpha & \sin \alpha (\sin \omega \sin \beta - \cos \omega \cos \beta) & -\sin \alpha (\cos \omega \sin \beta + \sin \omega \cos \beta) \\ 0 & \sin \omega \cos \beta + \cos \omega \sin \beta & \sin \omega \sin \beta - \cos \omega \cos \beta \\ \sin \alpha & \cos \alpha (\cos \omega \cos \beta - \sin \omega \sin \beta) & \cos \alpha (\cos \omega \sin \beta + \sin \omega \cos \beta) \end{pmatrix} \begin{pmatrix} X_{MDC} \\ Y_{MDC} \\ Z_{MDC} \end{pmatrix}$$

and simplifying

$$\begin{pmatrix} X_R \\ Y_R \\ Z_R \end{pmatrix} = \begin{pmatrix} \cos \alpha & -\sin \alpha \cos(\omega + \beta) & -\sin \alpha \sin(\omega + \beta) \\ 0 & \sin(\omega + \beta) & -\cos(\omega + \beta) \\ \sin \alpha & \cos \alpha \cos(\omega + \beta) & \cos \alpha \sin(\omega + \beta) \end{pmatrix} \begin{pmatrix} X_{MDC} \\ Y_{MDC} \\ Z_{MDC} \end{pmatrix} \quad (4.11)$$

This transformation is going to be used later to determine the displacement of the drift modules for a given RASNIK result.

4.6 On-bench calibration

Previous to the installation in the spectrometer, the individual channels have been calibrated. The aim of the calibration is to determine the relationship between the mask real displacements and the results obtained from the analysis of the images. The experimental setup is shown in figure 4.14; all elements in the setup correspond to their final version, selected for the installation in the spectrometer, to obtain the closest characterization to the installed elements. The main RASNIK channel features are included in table 4.2. It consists of a *binocular*, containing the camera and the lenses, fixed on an optical bench. The mask is installed on a three-dimensional motion controller system (Newport model 850 Series) with three independent motorized axes and rotary encoders for the displacement reading. The linear actuators engines are calibrated in the factory to render a repeatability better than $1 \mu m$, with a resolution in the encoder pulse of $0.1 \mu m$. The backlash is below $6 \mu m$, while the accuracy is below 0.2% of the travel, and is an accumulative quantity. Most of the systematic deviation from the linearity is given by the mounting system (ball bearing), which present some systematic irregularities along their path. The setup allows the independent displacement on each axis. The distances between the elements resembles the design values of the final installation. The mask is mounted in the linear actuator mount, trying to match the main axis of the alignment system (X_R, Y_R, Z_R) with the mount axis, labeled (x, y, z) .

First, the linearity and homogeneity of the results are tested as a func-

Lens focal length	200 mm
Lens diameter	25 mm
focal number (f/#) (fixed aperture of 15 mm)	13.3
Aperture	15 mm
Mask pitch	170 μm
Mask size	20 \times 20 mm
Camera sensor size	384 \times 287 pixels
Camera pixel size	12 \times 12 μm^2
LED type	HP HSDL-4420 #011
Mask-lens length	\sim 547 mm
Lens-camera length	\sim 315 mm
Total length	\sim 862 mm
Perfect focusing magnification	\sim 0.576

Table 4.2: Main features of the calibrated and finally installed RASNIK channels.

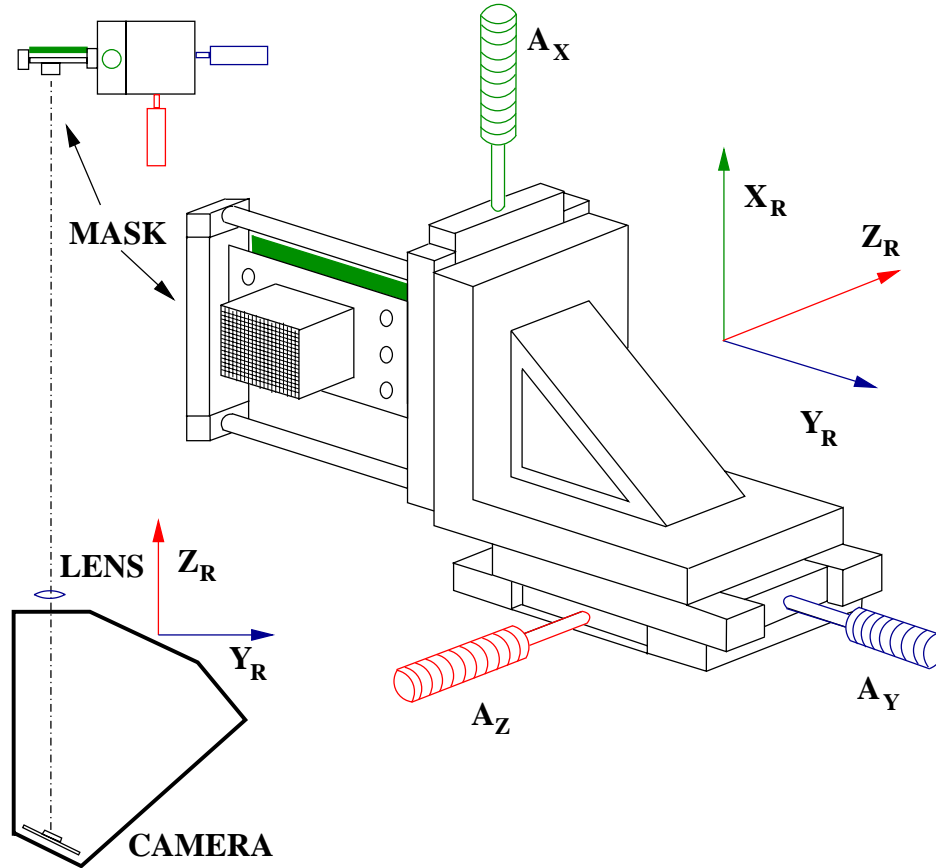


Figure 4.14: Experimental setup for the calibration of MDC displacements. The left figure shows the channel elements on the optical bench. The right figure recreates the mask attached to the three dimensional linear actuators mounting.

tion of the mask position and focusing. Two of the dimensions are fixed and the third axis is scanned along the range of the RASNIK channel (the range of the motion controller system is larger than the range of the alignment channel). For a set of n measurements of the motorized axis along its range, a set of n positions $P_{axis}(n)$ is obtained, where the subindex *axis* stands for x , y or z . The analysis of the images reports a set of coordinates $(R_{X_R}(n), R_{Y_R}(n), R_{Z_R}(n))$ for each value $P_{axis}(n)$. The data are fitted according to a linear relation. For a displacement of the linear

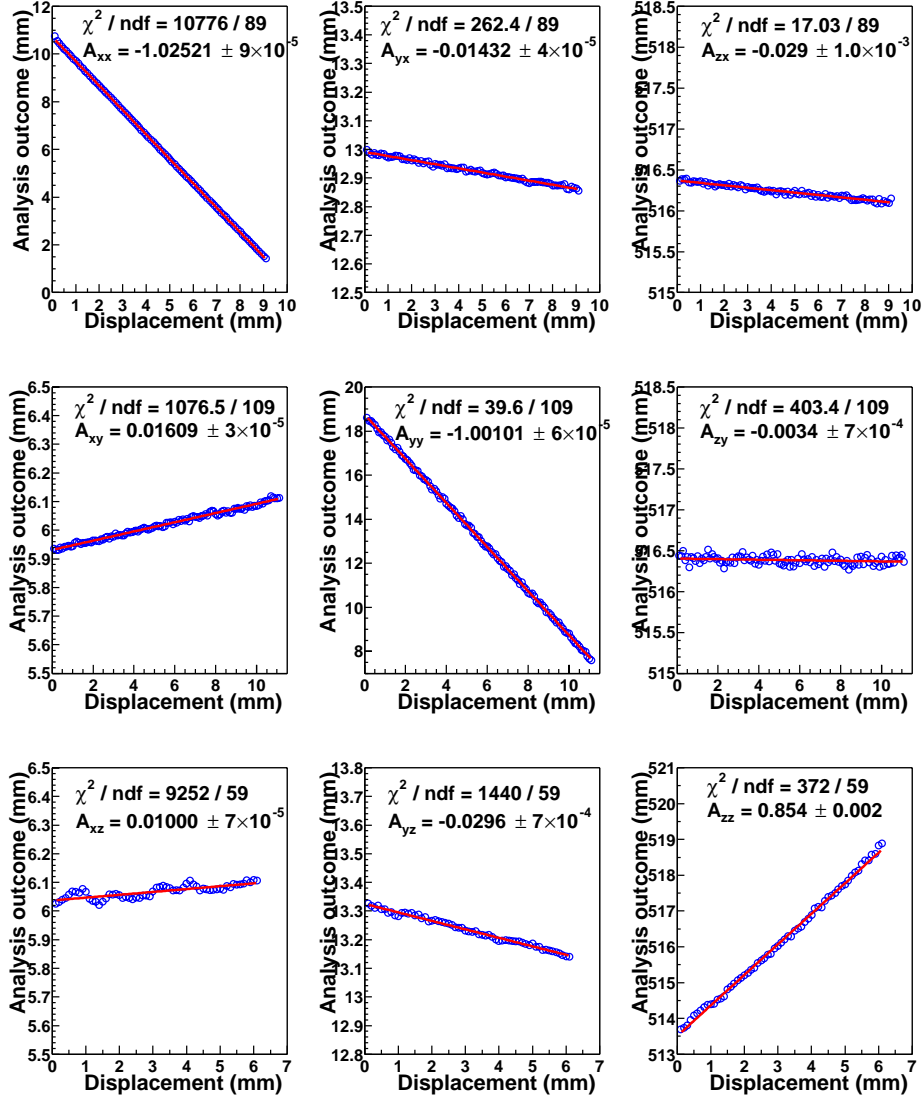


Figure 4.15: Image analysis results plotted vs. the scanned coordinate. The three top pads show the results in X_R , Y_R and Z_R when the linear actuator scans the x direction. The second and third rows correspond to the scan in y and z directions. Each scan has been made locating the other axis in the middle part of the mask range. The χ^2 over the degrees of freedom and the calibration matrix terms are displayed for each pad.

actuator along the x direction, the relations are

$$\begin{aligned}
 R_{X_R}(n) &= A_{xx}P_x(n) + B_{xx} \\
 R_{Y_R}(n) &= A_{yx}P_x(n) + B_{yx} \\
 R_{Z_R}(n) &= A_{zx}P_x(n) + B_{zx}
 \end{aligned} \tag{4.12}$$

The coefficient A_{xx} represents the displacement obtained along X_R from the image analysis when the actuator A_x moves the mask one unit of length and is expected to be close to the unity. The cross coefficients A_{yx} and A_{zx} represent the change in the position measured by the analysis of the images in the Y_R and Z_R directions respectively, when the linear actuator moves along the x direction. These coefficients are different from zero, reflecting basically the fact that the (x, y, z) frame of the linear actuator does not match perfectly with the RASNIK frame. Other systematic errors in the determination of a coordinate could also be contained inside the cross coefficients. The coefficients B_{xx} , B_{yx} and B_{zx} are merely offsets in each measurement. The same type of coefficients can be defined for the linear actuator displacement along y and z .

Neglecting the offsets, it is possible to write the calibration coefficient matrix A_{ij} , defined by

$$\begin{pmatrix} R_{X_R}(n) \\ R_{Y_R}(n) \\ R_{Z_R}(n) \end{pmatrix} = \begin{pmatrix} A_{xx} & A_{xy} & A_{xz} \\ A_{yx} & A_{yy} & A_{yz} \\ A_{zx} & A_{zy} & A_{zz} \end{pmatrix} \begin{pmatrix} P_x(n) \\ P_y(n) \\ P_z(n) \end{pmatrix} + (\text{offsets}) \quad (4.13)$$

To determine these matrix coefficients, each axis was scanned, keeping fixed the two others in the middle point of their range. Figure 4.15 shows the results of the linear fit, where the errors in both coordinates have been taken into account. The figure presents the nine matrix elements of equation 4.13 (note that the ordering does not coincide, rows and columns are interchanged). The errors assigned to the image analysis in the preliminary analysis (see results in section 4.4.1) and according to a conservative criteria, are below 0.001 mm in X_R and Y_R and 0.020 mm in Z_R , while the error in the linear actuator displacement has been taken to be 0.002 mm . The χ^2 fit and the linear fit parameter is plotted for each fit. The large value of the χ^2 for some pads indicates a large error underestimation or a systematic trend along the linear actuator displacement, and should not be assigned to a lack of linearity of the response, given the perfect visual fit along the complete axis scan. The linear fit residuals are shown in figure 4.16, including the residuals root mean square; the residuals represent the difference between the data and the straight line obtained from the linear fit. Each pad corresponds to the data in the same pad in figure 4.15. Those pads with large χ^2 present a residuals distribution which is not randomly distributed, but shows a definite trend. Then, the error of the measurement of each individual device has been correctly settled, and there is a systematic deviation of the linearity. After the explanation of the matrix terms, the source of the systematic error is discussed.

The diagonal terms A_{xx} , A_{yy} , A_{zz} of the calibration coefficients matrix contain the basic information, reflecting the outcome of the alignment system to an unitary mask displacement. Their negative values (in two cases) indicate that the axis of the alignment channel and the corresponding axis of the linear actuator points in opposite senses. The term A_{zz} differs clearly from the unity. This fact does not come from a large relative angle between the linear actuator and the alignment system axes, but it is simply a feature of the analysis software due to the inclination angle of the light on the camera sensor⁴.

The non-diagonal terms are all below $30 \mu m$ per mm of displacement of the linear actuator. In all cases, the relation between the displacement of the mask obtained by the analysis of the image in any direction and the displacement of the linear actuator is well approximated by a linear function. In the case of the non-diagonal terms, where the mask image analysis corresponds to a different direction than the linear actuator displacement, a linear dependence is expected simply from the geometry of the setup: the cross terms correspond to the projection of the linear actuator scanned axis on the other RASNIK axis. The axes system of the linear actuator was not tested to be perfectly orthogonal. It is possible to estimate the error introduced in the diagonal terms due to the relative rotation between the linear actuator and the alignment device axes. The largest angle between the axes is approximately given by $\arctan(\sqrt{0.030^2 + 0.014^2}) = 0.033 \text{ rad}$. Therefore, the calibration matrix diagonal term results about $\cos 0.033 = 0.9995$ times smaller than should be for a perfect axes matching. In all cases, the systematic error in the determination of the RASNIK response to an unitary mask displacement, due to the relative axis rotation, is below than $1 \mu m$ per mm .

Let us now discuss about the source of systematic deviation from the linearity. From the observation of the residuals one can distinguish between those coming from the analysis of the X_R and Y_R directions (the six pads in the left and medium columns of 4.16) and those from the analysis of the Z_R direction. In the first case the result is a continuous line following a path, while the last one corresponds to a cloud of points distributed quite randomly (maybe with the exception of the last pad where a systematic displacement is blurred by the random data distribution). The residuals reflect the impressive resolution of the system along the X_R and Y_R directions, enough to seemingly observe the systematic deviation from the

⁴The calibration terms are strongly dependent of the analysis software parameters and the total channel distance. A reasonable set of parameters are fixed along the calibration and final installation, for simplicity.

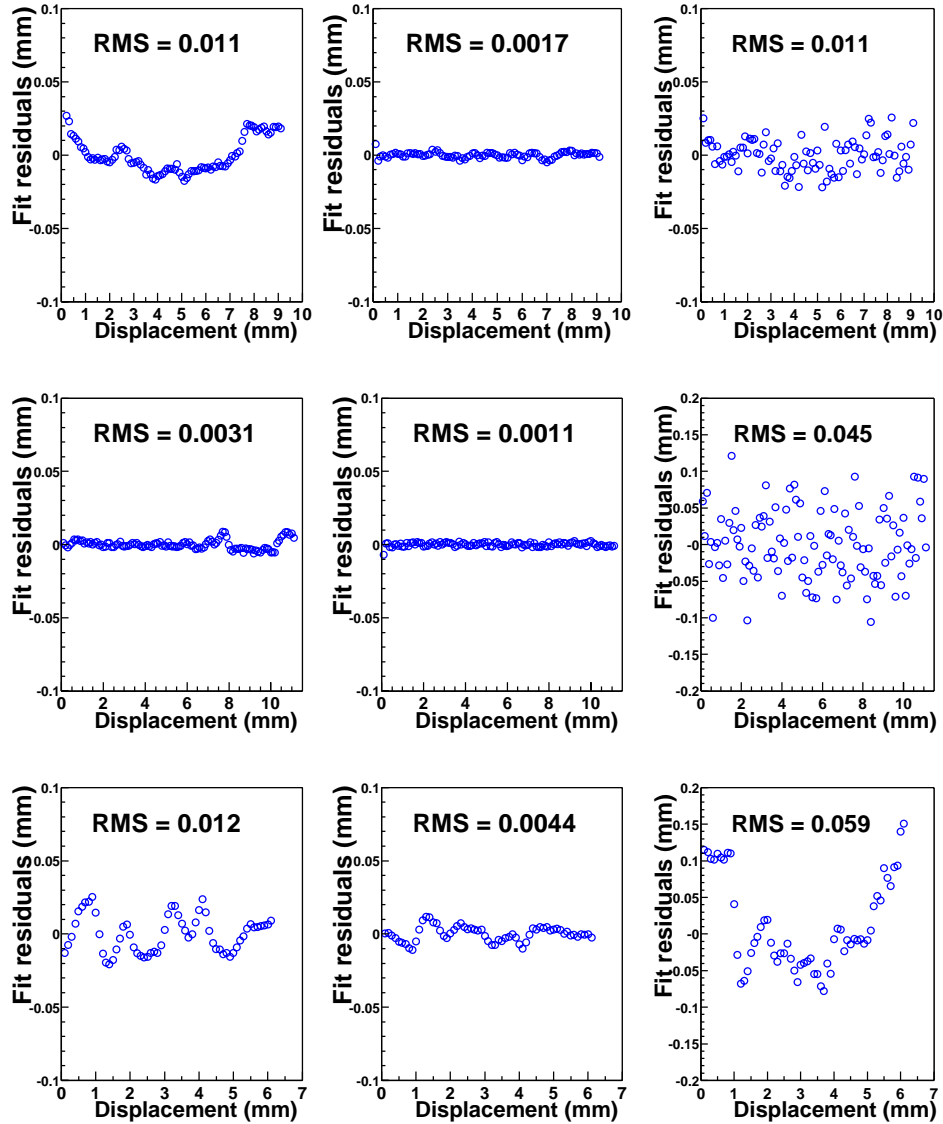


Figure 4.16: Residuals corresponding to the linear fits in figure 4.15. The residuals RMS are displayed in each pad.

linearity of a component in the linear actuator (the ball bearing system). The much poorer resolution along the Z_R axis does obscure the systematic on the linear actuator, and the random errors in the magnification analysis dominate.

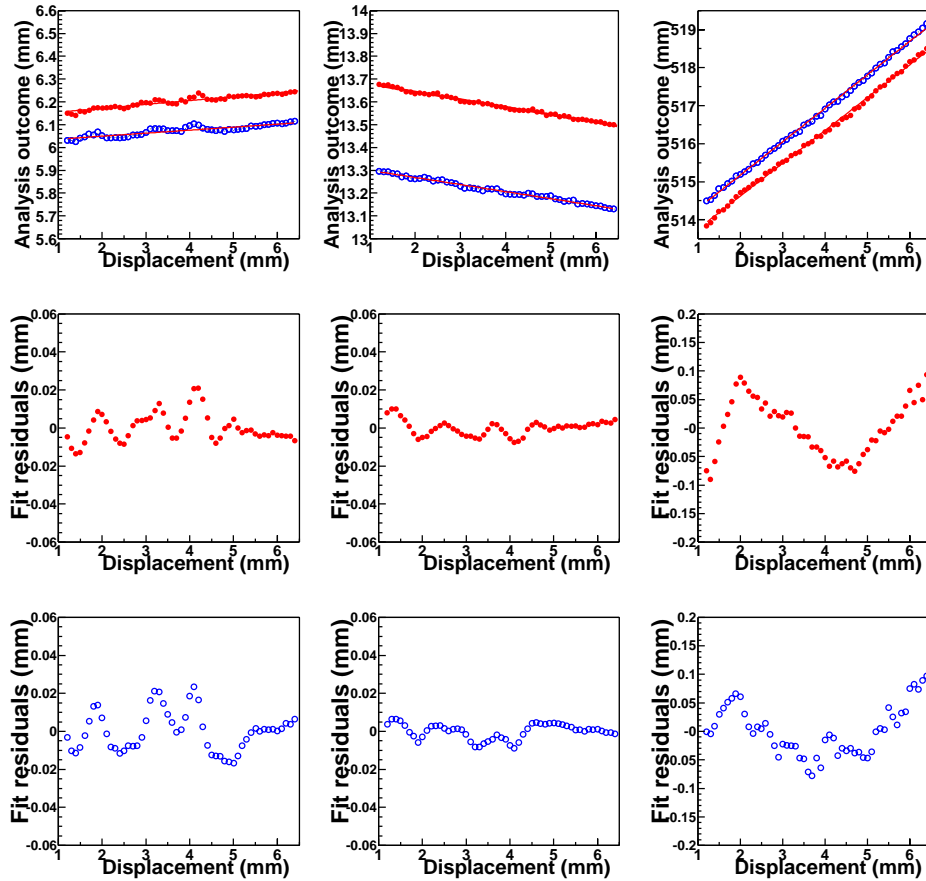


Figure 4.17: Linear fit residuals for a scan along the z linear actuator axis. The top pads represent two different fits (X_R , Y_R and Z_R measurement vs. displacement, respectively) in two close zones of the mask. Below, the linear fit residuals on X_R , Y_R and Z_R coordinates, respectively, are represented (color and icon matches in residuals and data points). The residuals on the three bottom pads also correspond to those in the bottom pads of figure 4.16, but performing the fit on a shorter range.

To prove these statements about the systematic error source, the mask position has been slightly displaced in a new set of measurements. Figure 4.17 shows the results of this test. The three top pads show the image analysis results along X_R , Y_R and Z_R when the scan is performed along z . The blue open circles represent the same data already plotted in the bottom three pads of figure 4.15, while the red filled circles correspond to a

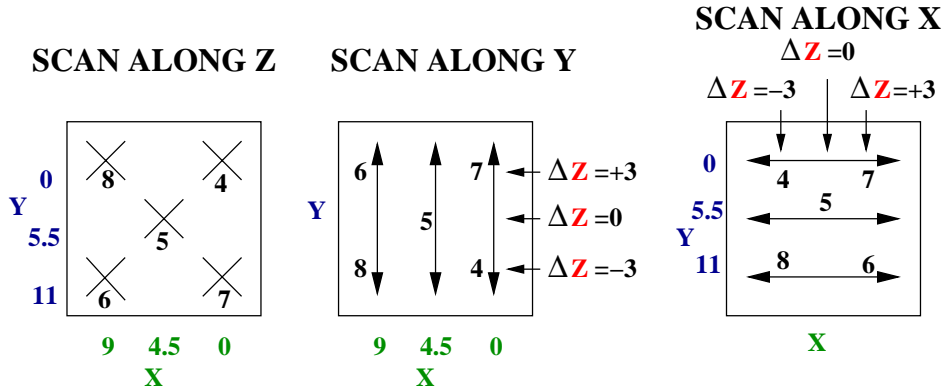


Figure 4.18: Graphical guide to localize the position of each scan in the mask. The squares represent the mask surface. The numbers on the mask represent the scan number, as displayed in figure 4.19. Left: scanning along the z linear actuator direction. The five fixed (x, y) points in the mask are numbered from 5 to 8, for the coordinates shown in the sides. Center: scanning along the y linear actuator direction. The arrows indicate the direction along the linear actuator scans the mask. The five fixed (x, z) points in the mask are numbered from 5 to 8, for the coordinates shown in the sides. Right: scanning along the x linear actuator direction. The arrows indicate the direction along the linear actuator scans the mask. The five fixed (y, z) points in the mask are numbered from 5 to 8, for the coordinates shown in the sides.

slightly displaced mask position. Below each pad, the residuals are plotted as a function of the linear actuator displacement, for both data samples. The main features of the systematic deviation from the linearity repeat at a fixed linear actuator reading, irrespectively of the alignment system outcome. Then, the source of the deviation is a component of the linear actuator, in particular the ball bearing system of the mounting.

To test the homogeneity along the mask area of the alignment system, the matrix coefficients in equation 4.13 has been calculated scanning in several different positions along the three axes. Figure 4.18 summarizes the procedure: first, a complete range scan in the z direction is performed in 5 points of the mask. The chosen points correspond to the center, already seen, and the four corners, close to the mask edges. The number displayed on the mask in figure 4.18 has been assigned to each data sample according to their position on the mask, and serve as reference to recognize the sample in figure 4.19. Then, the y linear actuator coordinate has been scanned for five different combinations of the position along x and the position along z (normal to the mask). Finally, the x axis has been scanned

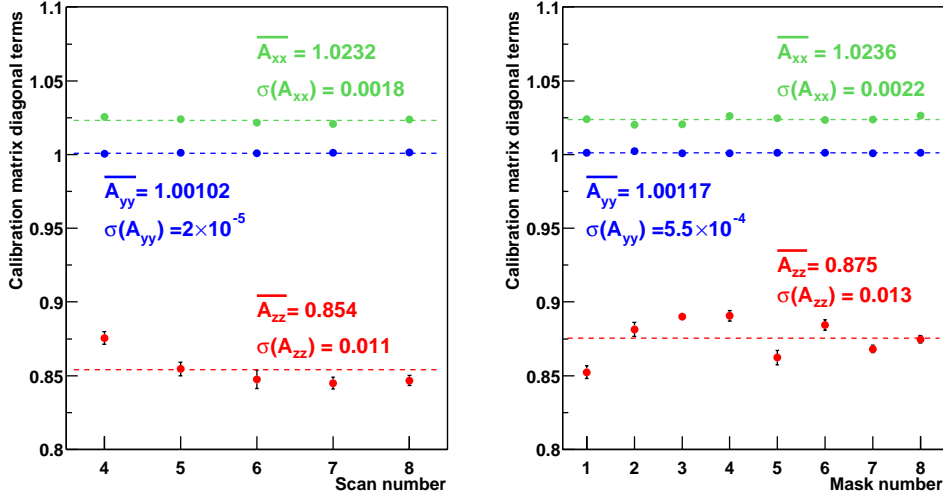


Figure 4.19: The diagonal terms A_{xx} (green), A_{yy} (blue), A_{zz} (red) of the calibration coefficients matrix. Note that the sign has been changed for A_{xx} and A_{yy} . The left pad displays the terms for different zones of the mask ($\neq 1$). The scan number corresponds to those of figure 4.18. The right pad displays the values for different masks. The arithmetic mean value and the standard deviation from the mean is shown for each diagonal term.

for five different combinations of the position along y and along z . The selected points in the coordinate z , normal to the mask, are $z = 0$ where the mask is better focused, and the extremes of the useful range $z = -3$ and $z = +3$, where the image is quite defocused.

For each position the three dimensional outcome from the image analysis are fitted to a straight line and the calibration coefficient matrix is constructed. The left pad of figure 4.19 shows the results for the calibration matrix diagonal terms. The differences in the calibration matrix diagonal terms found in different points of the mask are small enough to use an unique calibration parameter all along the mask. The larger deviation occurs for the calibration term when the mask displaces along z . The differences are slightly larger than the errors in each term from the linear fits, both scanning along x and y . But along the z direction again the differences are much larger. Actually, this can be partially explained due to the special image analysis performed to obtain the position along this axis. The magnification of the image is obtained after a detailed calculation of

the black-white mask transitions. But a small part of the mask image was missing (black) when studying mask edges, resulting in less black-white transitions to analyze. Also along the mask edges, the imperfections in the mask cut, some glue rests, and the metal border reflected by the IR light can mislead the image analysis. The cross terms (not shown in the figures) have also been checked, resulting very stable for all mask positions, as expected from their geometrical origin. The calibration matrix is

$$A_{ij} = \begin{pmatrix} -1.023 \pm 0.002 & 0.0157 \pm 0.0009 & 0.012 \pm 0.001 \\ -0.0144 \pm 0.0002 & -1.00102 \pm 0.00002 & -0.0298 \pm 0.0005 \\ -0.022 \pm 0.007 & -0.013 \pm 0.007 & 0.854 \pm 0.011 \end{pmatrix} \quad (4.14)$$

The conclusion is that the matrix terms are constant within the resolution of the individual directions, and the calibration can be performed using a common set of numbers for all the mask surface.

Finally, eight masks were individually scanned, to determine the differences between the analysis of their images. The calibration matrix diagonal terms obtained from the fits of the analysis outcome vs. the linear actuator displacement are shown in the right pad of figure 4.19; the arithmetic mean value and the standard deviation from the mean are also included. Again, the differences between the masks are small enough to use an unique set of calibration parameters.

Let us summarize: the geometrical disposition of the relative axis introduces a systematic error, estimated to be below $1 \mu m$ per mm in each axis. The influence of the systematic error associated to the ball bearing system is difficult to estimate, but must be very small on the diagonal terms, which are obtained from a fit on a large range. The random error due to the motorized axes and the rotary encoder was previously considered to be below $2 \mu m$. Introducing the variation in the calibration terms with the mask position or focus and with the mask-LEDs board model, using the standard deviation from the mean, then

$$\begin{aligned} A_{xx} &= 1.023 \pm 0.004 \pm 0.001 \\ A_{yy} &= 1.001 \pm 0.002 \pm 0.001 \\ A_{zz} &= 0.875 \pm 0.017 \pm 0.001 \end{aligned} \quad (4.15)$$

where the random errors are first stated and, then, the systematic errors.

The individual measurements along the X_R , Y_R and Z_R directions for all measurement channels should be corrected by the previous factors, to determine the mask displacements.

4.7 On-line monitoring: RAHAD and EPICS

The alignment system reports a large amount of data, which should be adequately displayed, calibrated and stored. ICARAS, the RASNIK analysis software developed by NIKHEF [1], is able to obtain the position from a mask image in less than six seconds, running in a PIII450MHz standard PC (Windows NT 4.0 OS). Up to now three sectors have been furnished with the alignment system, giving a total of six RASNIK channels, which can be analyzed in approximately 33 seconds. For the complete setup (12 channels) it is expected a complete position analysis approximately every minute. The amount of data is not really large (six floats, the channel identifier and the date is stored per channels and measurement for a total of about 2 Mb per day).

The alignment data belong to a set of parameters which are essential for the final goal of the experiment but are not included in the data acquisition chain. This set also contains voltages, VME and detector status, offsets, temperatures... for lots of devices under the generic name of “slow control” parameters. Such a large number of parameters should be monitored during the acquisition and stored for data or device calibration. Some parameters like (high) voltages and thresholds must be remotely controlled. We would like to have alarms when the values of the parameters are not consistent with the expectations and security or shutdown procedures when a dangerous operation or device fault is present. For all these tasks, HADES has adopted EPICS.

EPICS [23] consists of a set of software components and tools with which developers can create a control and monitoring system. It uses a tool-based approach, that means the use of software tools that are designed with carefully chosen boundaries between layers and modules, and using good protocols allowing independent development. EPICS makes use of standards like C programming, TCP/IP communication protocol, the VME/VXI bus/crate system, and some field-bus protocols [24].

The basic organization of the EPICS control system software can be divided into three parts:

- First, the IOC (Input/Output Controller) memory resident database, supporting a large and extendible set of record types (Analog Input, Analog Output,...). Each record type has a fixed set of fields, with a field name and a field value or values, which can be common to several types or type specific. The first field of every database record holds the record name, which must be unique across all IOCs that are attached to the same TCP/IP subnet. The database runs nor-

mally on the processor of a VME/VXI based chassis, running a real time operative system and containing various I/O modules and VME modules that provide access to other I/O buses (such as GPIB).

- Second, the client-side tool set, which consists of client applications for graphical interface, alarm management and archiver tool. These software tools run on PC or workstations running UNIX-LINUX flavors or Windows operative systems, which are called Operator Interface (OPI), in the EPICS slang. Most of the tools are real time software, used to monitor and control IOCs.
- Third, a local area network (LAN) allows the IOCs and OPIs to communicate. EPICS provides a software component, the Channel Access, which provides network transparent communications between a Channel Access client and an arbitrary number of Channel Access servers in a distributed way. An arbitrary number of IOCs and OPIs can be supported, as long as the network is not saturated.

Channels Access is a client/server application: normally the client runs on a workstation (the OPIs), and the server on the processor of a VME system (an IOC). The server is loaded onto the IOC when the database is initialized. The client is created when any client-side program calls any of the requests from the Channel Access Client Library (which consists of a number of simplified function calls that a client application can use to establish connections or channels to process variables and then read from or write to them). The client's requests are sent to the server, which merely calls the database routines to perform all read, write or monitor actions. The approach is not congruent with the appropriate design and use of client/server software, in which the client side should hold most of the burden for storing and converting data, leaving the server to perform more crucial tasks. But also, and more important, it is necessary to interface the large number of client tools written specifically for EPICS with non-EPICS applications that are not tied to the EPICS database and its IO routines. For all these reasons a new server-level application interface, called the Channel Access Portable Server software [25], has been developed. Instead of being tied to the I/O routines of the EPICS database, the new server can be tied to non-EPICS I/O routines, thus allowing any EPICS client applications to interface with those applications. The Portable Server consists of a C++ library with a simple class interface, which hides most of the complexity beneath the interface using the object-oriented approach.

The analysis of the RASNIK images is performed by the specific analysis program (ICARAS), following a set of parameters (geometry, mask

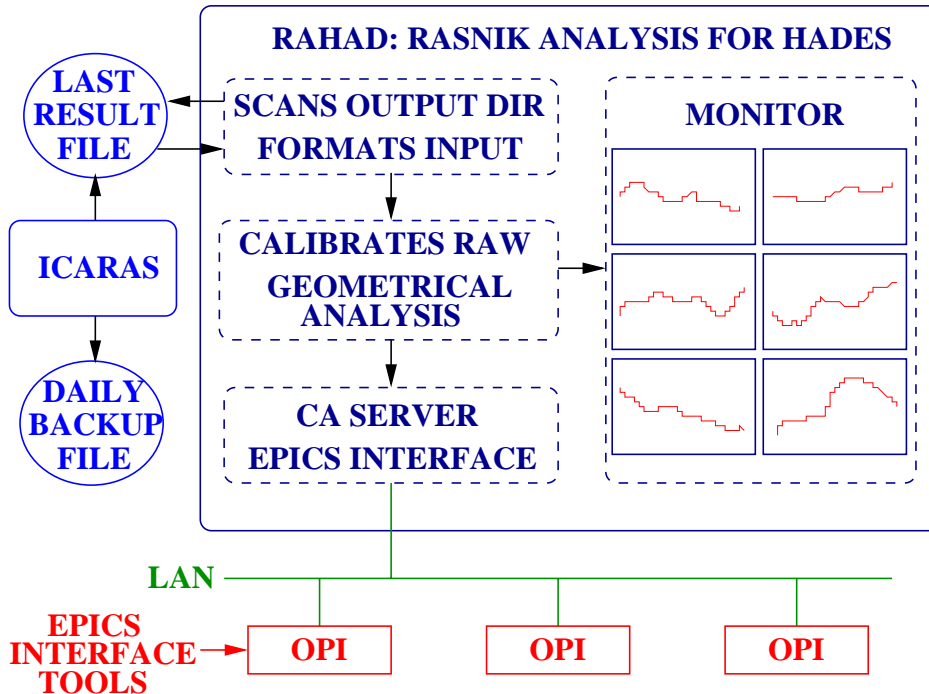


Figure 4.20: Scheme of the RAHAD analysis module. The graphical display uses the output facilities of the ROOT libraries. The integrated Channel Access Portable Server (CAS) allows the communication with the EPICS client tools.

and camera features...). Between this raw outcome and the final module displacements, a set of calibration, statistical analysis and geometrical transformations are needed. For this purpose, a C++ program called RAHAD (Rasnik Analysis for HADes) has been developed.

RAHAD has the following main purposes:

- Monitors the ICARAS output directory taking the latest result file as soon as it is produced.
- Calibrates the raw channel data.
- Transforms the data according to the geometry of the sector and expresses the displacements in the MDC III coordinate system.
- Provides a graphical interface for the immediate monitoring of the last analysis output.

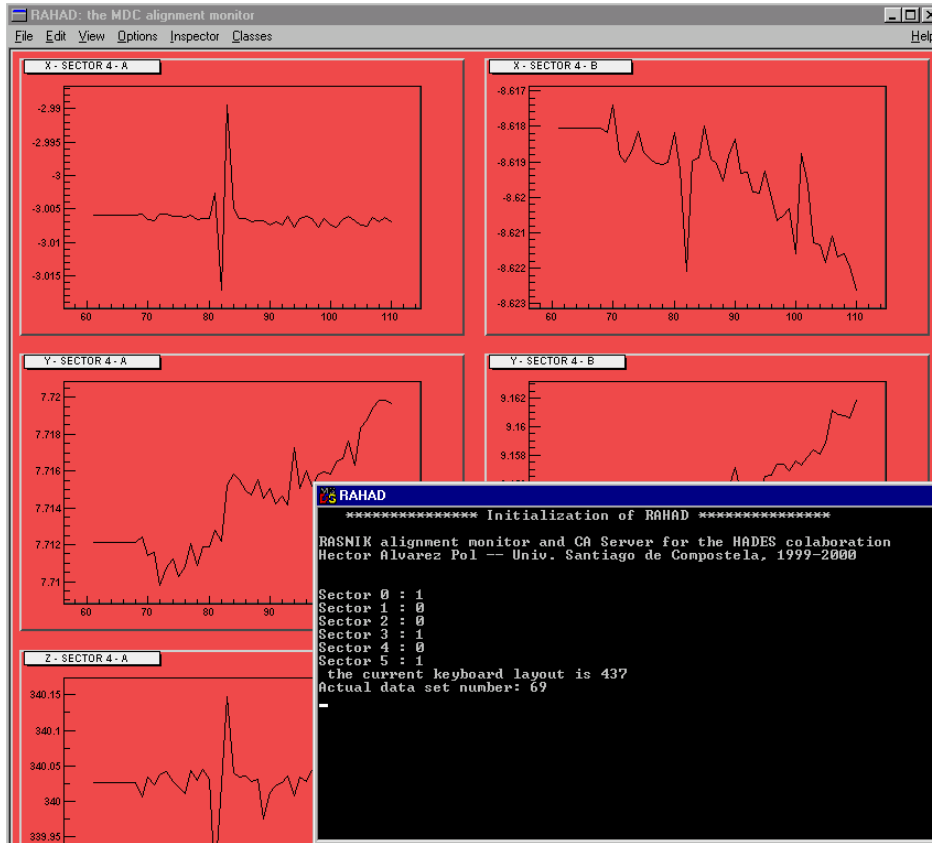


Figure 4.21: A screen of RAHAD: the HADES analysis and interface with the slow control.

- Interfaces with the EPICS scheme, by integrating a Channel Access Portable Server.

RAHAD scans the output directory of the ICARAS software looking for the latest analysis outcome (see scheme in figure 4.20). After the analysis of an image two files are produced, one short file with only the last outcome and a daily file which is permanently stored on the hard disk for security. The short file is read by RAHAD. The first scanned data is taken as a reference value. The difference between the immediate measurement and the reference value determines the displacement of the monitored points in the spectrometer. Each displacement from the reference value is calibrated taken into account the result of section 4.6.

RAHAD deals with data transformation from RASNIK to MDC own axes. The results of section 4.5 are implemented to obtain the displace-

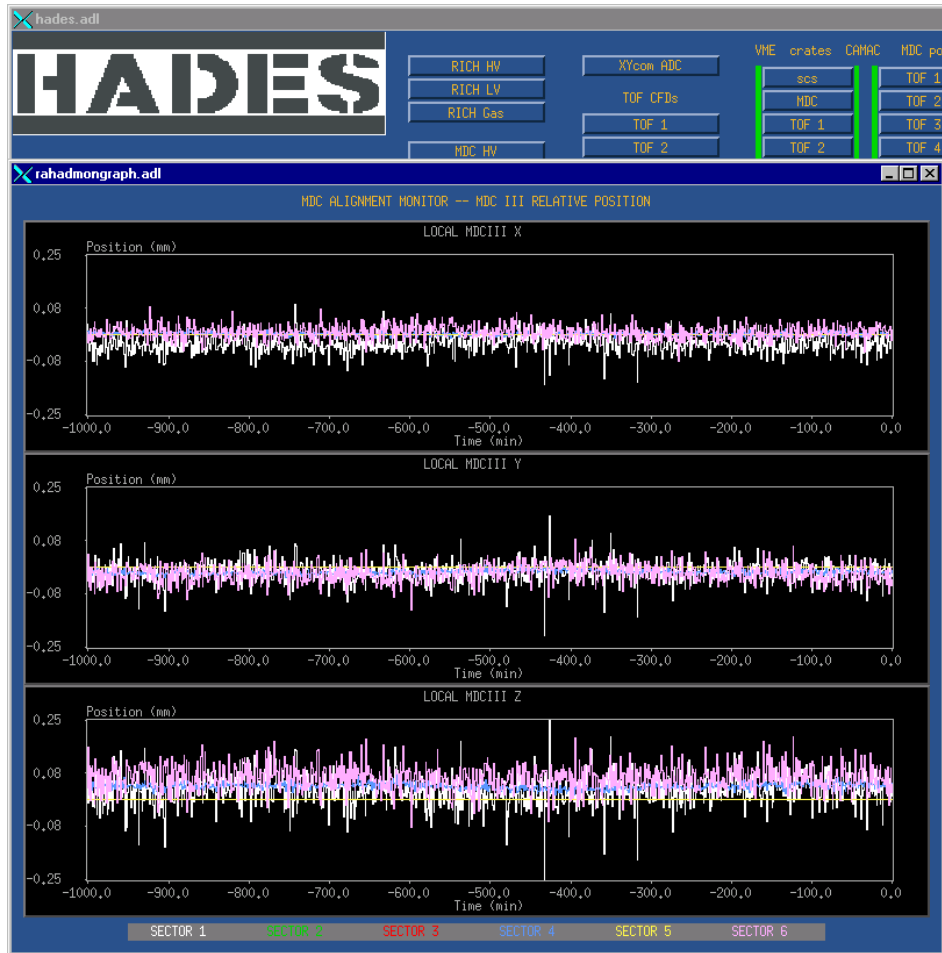


Figure 4.22: EPICS graphical display for the alignment monitoring.

ments of each point in the MDC III coordinate system. From the two points it is possible to obtain information about the displacement of the MDC. This detailed transformations are the topic of the next section, where the analysis of the data is shown.

RAHAD contains a graphical data displayer, shown in figure 4.21. To integrate easily a 2D histogram facility and other standard tools, it links with the ROOT (the Object Oriented Data Analysis Framework) libraries, accessing to the complete I/O possibilities of ROOT. Figure 4.21 displays the RAHAD monitoring window. The monitor plays an essential role in the data debugging and the checking of the system behavior. RAHAD is also an EPICS Channel Access Server, using the Channel Access Portable

Server software. Then, we have got a distributed system where operators can monitor the alignment results, integrated with other slow control tasks. Figure 4.22 shows a set of screens of the HADES monitor and control graphic interface. The outcome of the alignment analysis for the three installed sectors is integrated in the complete HADES control and monitoring system. A button in the main screen introduces a submenu from where several time data series can be displayed.

The EPICS software components are designed to be event driven to the maximum extent possible. Rather than having to poll for changes in the Channel Access Servers, the clients can request that it be notified when a change occurs, leading to efficient use of the resources and quick response time. Inside the Channel Access Server the programmer can specify the update time of the data or force an update for each new value. The updated values are stored in a unique Archiver, an EPICS application which stores a restricted set of important database records. It is foreseen the implementation of an interface between the Archiver data and the general ORACLE database, to introduce or correct relevant parameters in the data analysis.

4.8 In situ experimental results

The present section shows the results obtained after the installation of a set of alignment devices in several spectrometer sectors. The first sector was installed in November 2000. Up to now (autumn 2002), three sectors have been completed, namely sector 1, sector 4, and sector 6. The installation of the other sectors will be performed as soon as the corresponding MDC III are installed. Figure 4.23 shows a 3D view of the *binocular* pieces on the support structure of the inner modules and the mask and LEDs support pieces on the frame of MDC III. The IR light paths are artistically depicted as a red line. Sector number 1 corresponds to the upper sector, being the other sectors ordered clockwise. In the picture, the external MDCs in sector 2 have been removed.

In the installed sectors, there are two points whose position is continuously monitored in the frame⁵ of the MDC III. Let us call the two points *A* and *B* and the corresponding RASNIK channels also *A* and *B*, in a sector independent way (see the right part of the figure 4.24): an observer situated upstream (that is, looking to the spectrometer from the entry point of the beam in the HADES cave) would see point *A* to the left of point *B*

⁵Actually, the monitored points are those in the surfaces of the masks, and not in the MDC III frame. The mask-LEDs supports are rigidly attached to the frame.

in sector 1 and the opposite in sector 4. The notation for the other sectors is obtained from the first, by a rotation of an integer multiple of 60° . The RASNIK channel A corresponds to a positive α angle, while for channel B , α is negative, according to the notation of section 4.5. In previous sections and in the following, most of the figures are made for sector 1, but can be directly applicable to the other sectors by rotating the picture.

The outcome of a channel image analysis is a set of numbers, representing the position of the mask code image on the camera sensor. This set of numbers represents a real mask displacement only after the comparison with a previous image of the mask position and after the right calibration (as shown in section 4.6). Performing these steps for all channels, the result is a displacement vector from an initial position for each channel, expressed in its own coordinate system. For the sake of notation, we are going to call $(\Delta X_R^A, \Delta Y_R^A, \Delta Z_R^A)$ to the displacement from an initial given analysis values of RASNIK channel A of the sector, in the coordinate system defined by the main channel axis⁶ (X_R, Y_R, Z_R) .

Figure 4.24 schematizes the mask, lens and camera positions and the coordinate systems for two channels in the same sector. The figure is quite simple; it does not take into account the tilt introduced by the *binocular* wedge (the angle denoted as ω , in section 4.5), but several effects can be explained using this simple scheme. A displacement ΔY of the MDC III frame in the laboratory Y direction, moves points A and B into A' and B' . The resultant mask image analysis experiments an increment in the Z_R direction (the optical axis direction) in both channels. In the normal direction X_R , the images report displacements in opposite directions. The channel A , in the left side of the figure, is displaced toward the negative values of X_R , meanwhile for the channel B the result is an increase of the coordinate X_R .

The previous effect is clearly seen in the data analysed on the installed sectors. Figure 4.25 shows the results obtained during three days of monitoring in December 2001, for sector 1. The black points (the top curves in both pads) represent the outcome for channel A , while the red points the outcome for channel B . In both cases the channels have been properly calibrated, but still are represented in their own channel coordinate system. The data curves have been vertically displaced from the zero to allow a better comparison. The large changes in the X_R analysis outcome points in opposite sense in each channel, while the displacement along Z_R

⁶The directions X_R and Y_R have been interchanged along the data analysis inside the code RAHAD, with respect to the notation in sections 4.4 and 4.6 (and also with respect to the usual RASNIK convention) for the sake of simplicity in the geometrical transformations between RASNIK and MDC coordinates.

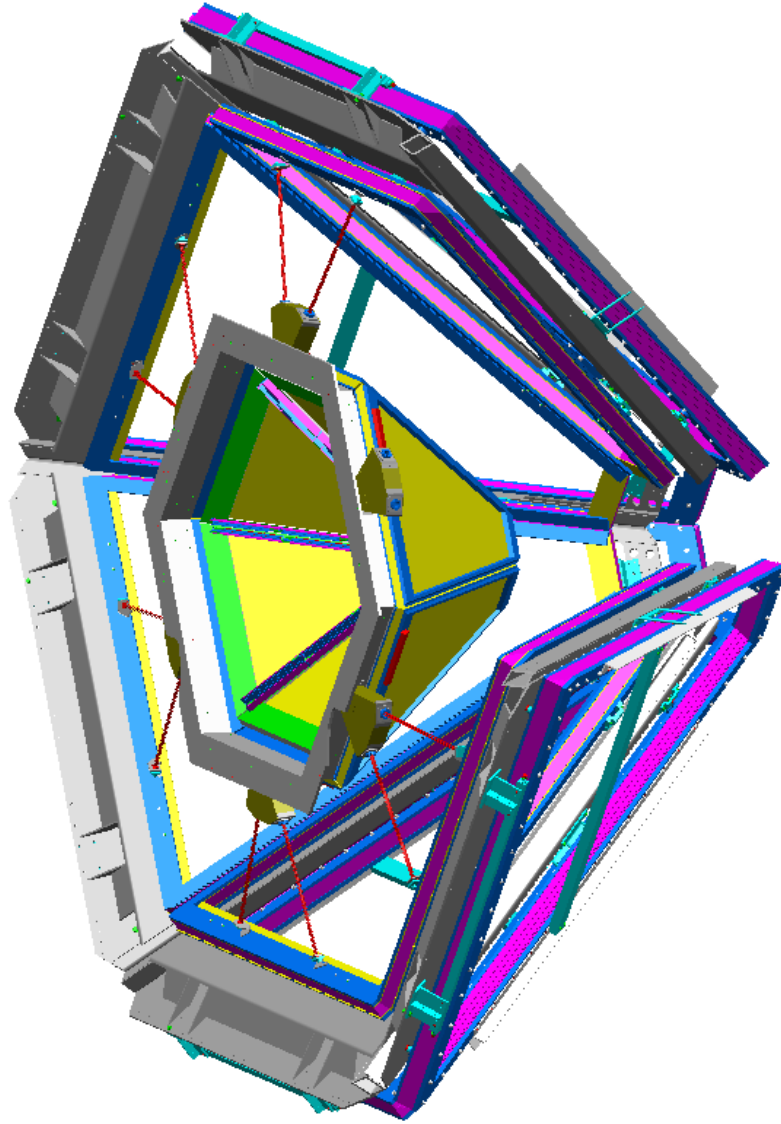


Figure 4.23: 3D view of the complete installation of the alignment system. The red lines between the LEDs and mask support in the MDC III frames and the lenses on the binocular piece are artistic approaches to the IR light path. The external MDC modules in sector 2 have been removed for a better observation of the inner modules.

is very similar. Then, the results along X_R do not correspond to any real displacement of the MDC III frame on the X direction, but they are a consequence of the large displacement along Y . The plot also shows smaller

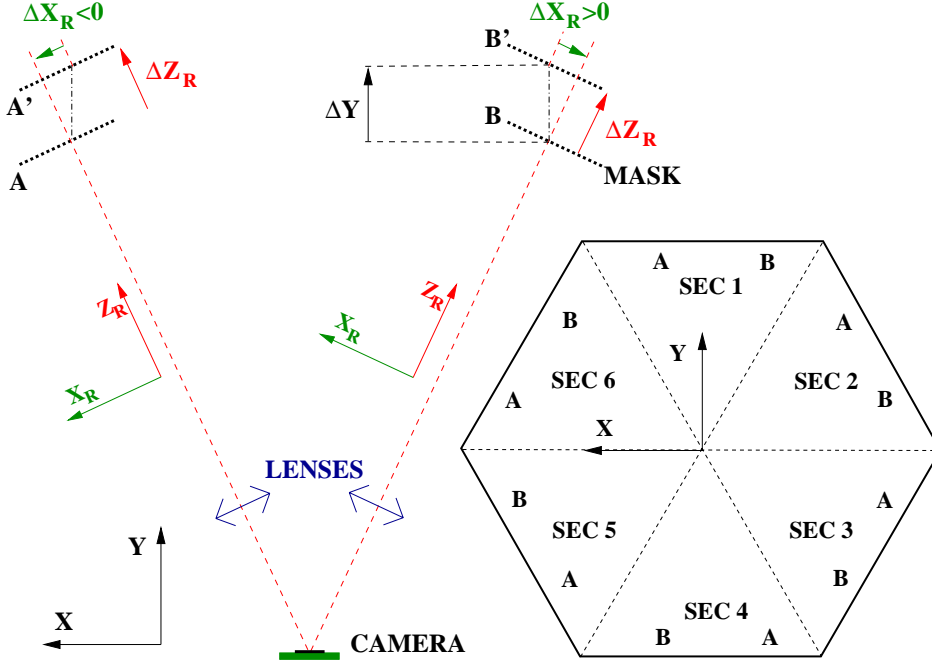


Figure 4.24: *Right: simplified scheme of the notation. The mask-lens-camera relative position of the monitored points A and B are sector independent (invariant under a $n \times 60^\circ$ rotation). Left: simplified scheme of the camera-lens mask disposition for both channels in a sector. After a displacement ΔY , both masks change their position. Note the opposite sign of ΔX_R .*

features, for instance those signaled by arrows, that correspond to real displacements of the MDC III frame with respect to the inner modules in the X direction. In this case, both channels show the same behavior.

From the transformations found in section 4.5, it is possible to obtain the displacement vectors of the two points in the same coordinate system, the MDC III coordinate system (equation 4.11, which is sector dependent) or the laboratory coordinate system (equation 4.6). Both transformations mix (linearly) the coordinate systems where the displacements of points A and B are expressed. For instance, the transformation of the displacement for the point A, $(\Delta X_R^A, \Delta Y_R^A, \Delta Z_R^A)$, into the MDC III coordinate system is

$$\begin{pmatrix} \Delta X_{MDC}^A \\ \Delta Y_{MDC}^A \\ \Delta Z_{MDC}^A \end{pmatrix} = \begin{pmatrix} 0.90631 & 0 & 0.42262 \\ -0.23571 & 0.83001 & 0.50549 \\ -0.35078 & -0.55774 & 0.75225 \end{pmatrix} \begin{pmatrix} \Delta X_R^A \\ \Delta Y_R^A \\ \Delta Z_R^A \end{pmatrix} \quad (4.16)$$

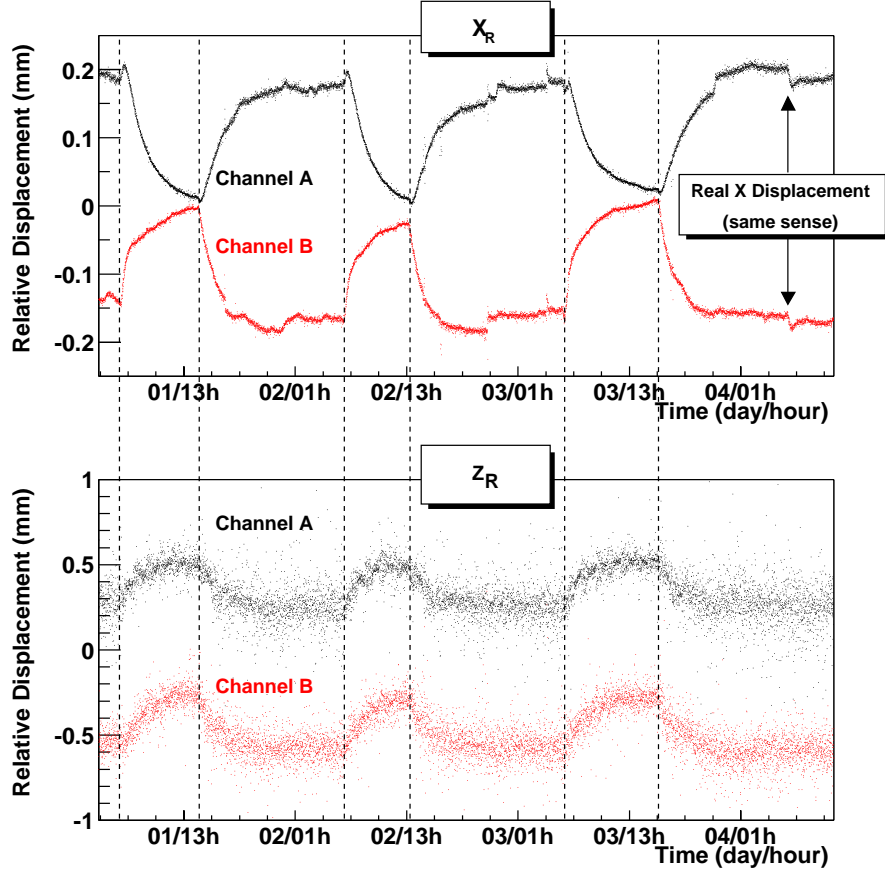


Figure 4.25: Displacements obtained in sector 1 along three days of December 2001. The top pad shows the results for channel A (black) and B (red) along X_R . The bottom pad shows the displacement along Z_R obtained from the image magnification. In both cases the curves have been vertically displaced to allow the comparison.

For the point B , the angle α results negative in equation 4.11 and therefore the transformation is

$$\begin{pmatrix} \Delta X_{MDC}^B \\ \Delta Y_{MDC}^B \\ \Delta Z_{MDC}^B \end{pmatrix} = \begin{pmatrix} 0.90631 & 0 & -0.42262 \\ 0.23571 & 0.83001 & 0.50549 \\ 0.35078 & -0.55774 & 0.75225 \end{pmatrix} \begin{pmatrix} \Delta X_R^B \\ \Delta Y_R^B \\ \Delta Z_R^B \end{pmatrix} \quad (4.17)$$

Both transformations are sector independent.

Once it is known the relative displacement of two points in the frame of the MDC III with respect to the inner support frame, and both displacement vectors are expressed in the same coordinate system, meaningful

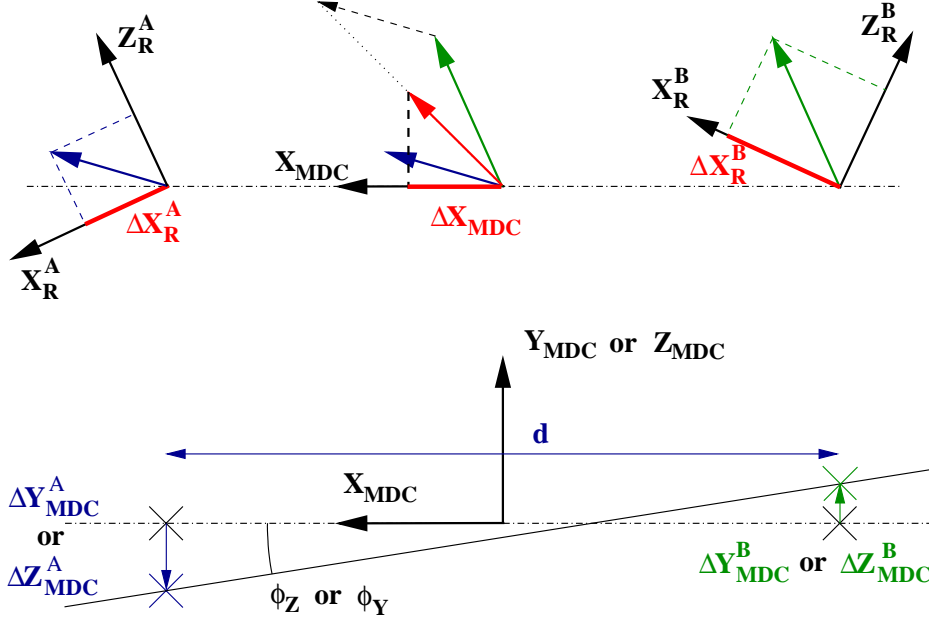


Figure 4.26: The MDC III displacement is obtained for a point in between points A and B; in the drawing, the graphical construction of their projection on X_{MDC} is shown. The displacement vectors (blue and green arrows) are transformed to the common coordinate system and averaged. In the lower scheme the angles ϕ_Z (when the axis is Y_{MDC} and the displacements ΔY_{MDC}^A and ΔY_{MDC}^B) and ϕ_Y (when the axis is Z_{MDC} and the displacements ΔZ_{MDC}^A and ΔZ_{MDC}^B) are constructed from the differences in the displacements.

quantities describing the relative movement of the planes can be written. First, it is possible to define a relative displacement vector, denoted $(\Delta X_{MDC}, \Delta Y_{MDC}, \Delta Z_{MDC})$, of the MDC III frame with respect to the inner modules

$$\begin{aligned}\Delta X_{MDC} &= \frac{\Delta X_{MDC}^A + \Delta X_{MDC}^B}{2} \\ \Delta Y_{MDC} &= \frac{\Delta Y_{MDC}^A + \Delta Y_{MDC}^B}{2} \\ \Delta Z_{MDC} &= \frac{\Delta Z_{MDC}^A + \Delta Z_{MDC}^B}{2}\end{aligned}\quad (4.18)$$

The MDC III relative displacement vector is simply the arithmetic mean value of the displacements vectors measured for both points A and B, as it is shown in the upper scheme of figure 4.26. Second, and considering

the distance between the two points fixed ($d \simeq 700mm$), two angles can be defined, describing rotations around the MDC axis. In particular, the angles

$$\begin{aligned}\phi_Z &= \arctan \frac{\Delta Y_{MDC}^A - \Delta Y_{MDC}^B}{d} \\ \phi_Y &= \arctan \frac{\Delta Z_{MDC}^A - \Delta Z_{MDC}^B}{d}\end{aligned}\quad (4.19)$$

represent the angles rotated around the Z_{MDC} and Y_{MDC} axes, respectively. The lower scheme of figure 4.26 displays the angles ϕ_Z and ϕ_Y for an opposite displacement of points A and B in the directions Y_{MDC} or Z_{MDC} . There is still a third possible angle which cannot be measured. It corresponds to the rotation around the symmetry line between the points A and B , which corresponds to the X_{MDC} direction. This rotation cannot be recognized by any change in the alignment devices measurement. The MDC displacement vector, defined in equation 4.18, describes the displacement with respect to the initial position of a point in the middle of the symmetry line between A and B . The vector can only be applied directly on the coordinates origin (or in other point of the MDC) if the module does not suffer any rotation.

An example of the results of the transformations from the channel outcome in their own coordinate system up to the final displacement vector for a module are shown in figure 4.27, for a data sample taken in January 2002. The three first pads in the left column display the results from the channels A (black) and B (red) in sector 1, in their own coordinate systems. All pads represent the data without any modification of the offset (vertical displacement). The initial value (the zero of the relative displacement) corresponds to a previous date and is not represented. The transformation to a common coordinate system, following equations 4.16 and 4.17, combines linearly the three independent coordinates. The three pads in the second column display the channel outcome in the common coordinate system of the module. The large value of the displacement along the Z_R direction dominates ΔY_{MDC} , for both channels, in spite of the moderate geometrical contribution of such a displacement (the matrix element is 0.50549). The difference in the resolution along the channel axis is smeared after the transformation to a common system due to the variance transformation, as it is shown below. The three first pads in the last column show the components of the MDC III displacement vector, calculated using equation 4.18 from both channels data in the common coordinate system of the module. The two bottom pads display the angles ϕ_Z and ϕ_Y defined by equation 4.19.

Most of the physical effects (temperature changes, material stress, gravity) produce continuous but slow module displacements. The fast image acquisition and analysis allow the use of statistical calculations to improve our position estimation. For a set of N different image analysis along the same direction, the average is given by the arithmetic mean value of the observations

$$\bar{x} = \frac{1}{N} \sum_{i=1}^N x_i \quad (4.20)$$

with an error (supposing independent variables)

$$\sigma(\bar{x}) = \sqrt{V(\bar{x})} = \frac{\sigma(x)}{\sqrt{N}} \quad (4.21)$$

The standard error in the determination of the mean decreases with the square root of the number of measurements. The actual setup allows the acquisition of approximately two images per minute and channel, and therefore, sixteen images in less than nine minutes can be analyzed. If the displacement of the modules presents a slow time variation, the population mean of the displacements distribution does not change during the acquisition of the sixteen independent measurements.

The previous statement shows a method to evaluate the resolution along the main channel directions, X_R , Y_R and Z_R . For each group of sixteen measurements the arithmetic mean and the variance are defined as

$$\begin{aligned} E(\Delta X_R) &= \frac{1}{16} \sum_{i=1}^{16} \Delta X_R \\ V(\Delta X_R) &= \frac{1}{16} \sum_{i=1}^{16} (\Delta X_R - E(\Delta X_R))^2 \end{aligned} \quad (4.22)$$

with equivalent equations for the displacements along Y_R and Z_R . The results of this analysis are displayed in figure 4.28. The complete sample is divided in groups containing sixteen analysis results, and for each group the mean and the variance is obtained. The three lower pads in the left column present the time series of the complete sample and the means of the groups, in the three channel directions. To observe the differences, the means have been shifted $5 \mu m$ for the data set along X_R and Y_R and $50 \mu m$ along Z_R with respect to the complete sample. The main trend or time variation of the complete data sample is perfectly reproduced by the means, while the variation around the mean, seen as the time series thickness, is reduced. The effect is more evident along the Z_R direction, where the

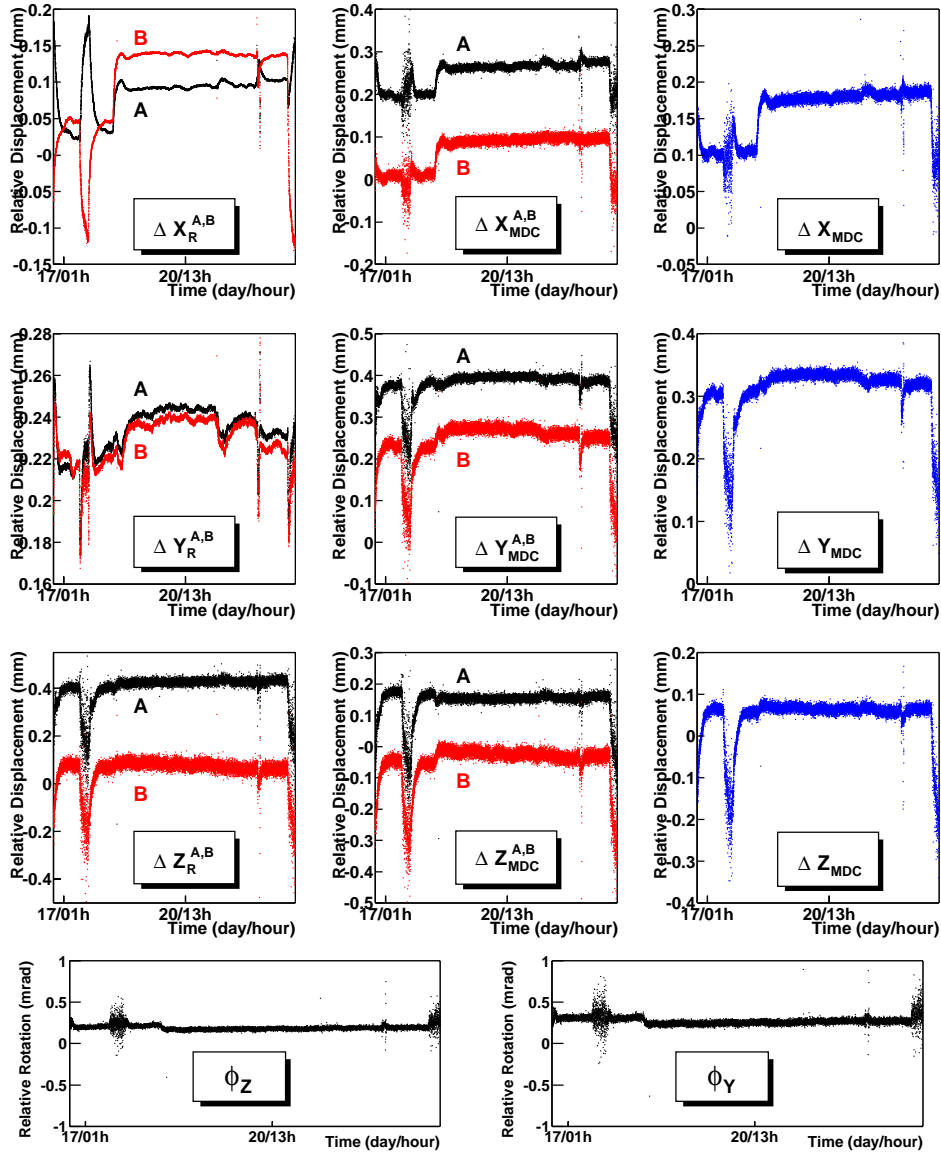


Figure 4.27: Results of a data taking period expressed in different coordinate systems. The first three pads in the left column display the channel outcome in their own coordinate system while in the second column a common coordinate system is used. The last column and the bottom two pads represent averaged values of the channels. See the text for further explanation about the represented variables.

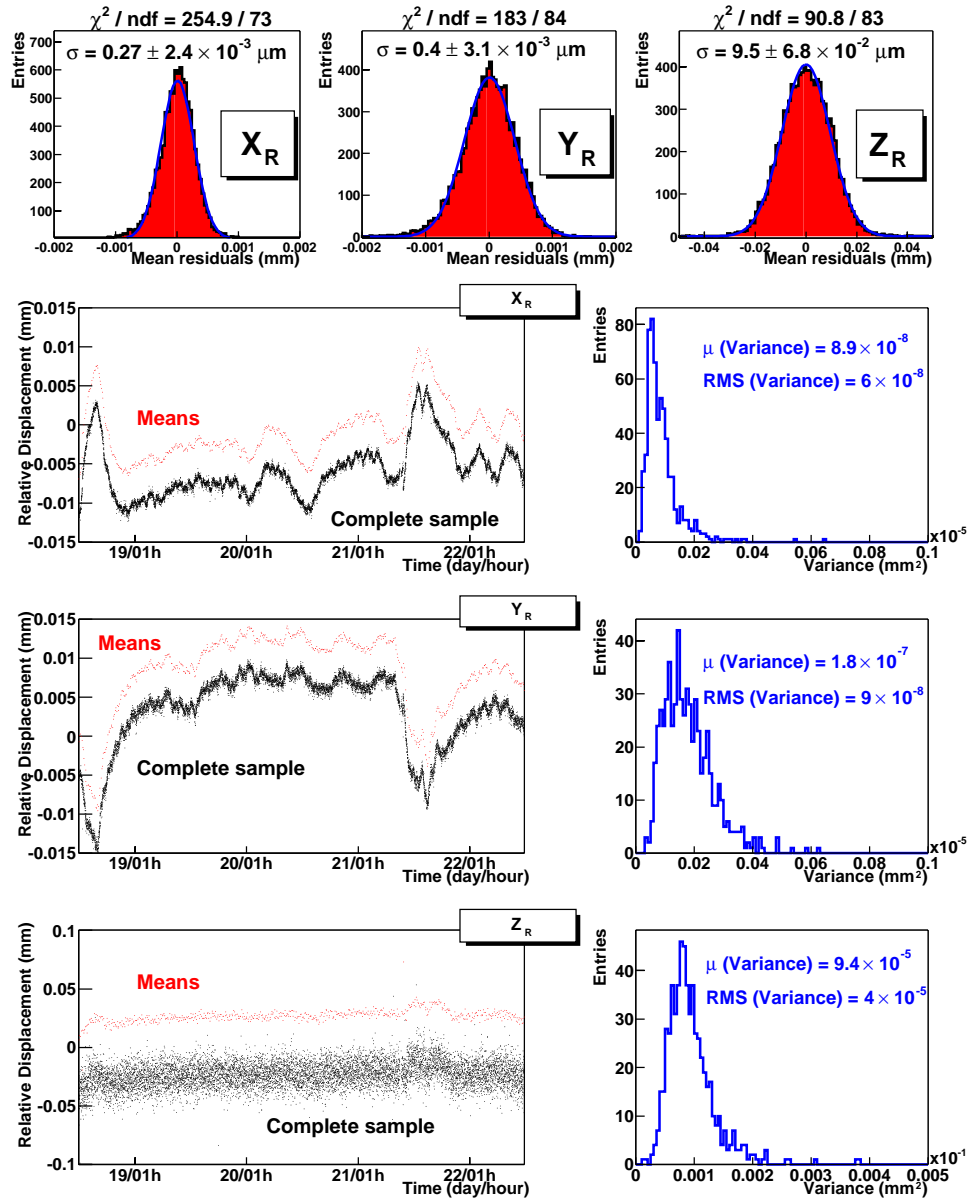


Figure 4.28: The three top pads represent the accumulated residuals distribution around the group means. Below, the left column displays the time series of the three studied samples compared with the group means, displaced 5 μm (50 μm along Z_R) to permit a clear observation. The right pads show the variance distributions.

complete sample shows a larger spread around the mean, smearing the small displacement details. The three lower pads in the right column shows the distribution of the variances for all groups. The distribution shows a gaussian-like shape⁷ with a significant deviation toward large values. The deviations are explained easily: the population mean all along the group measurement time has been approximated by the mean of the sixteen image analysis; but there are displacements faster than the time required for the analysis of the sixteen images, and the population mean is not constant in the time period. Then, the variance from the mean of the data group increases, reflecting a real mask displacement. Taking the square root of the variance mean along each direction, the standard error in the measurements is

$$\sigma(X_R) = 0.30 \mu m, \quad \sigma(Y_R) = 0.42 \mu m, \quad \sigma(Z_R) = 9.7 \mu m \quad (4.23)$$

Let us suppose that the real relative displacement of the module takes the value x and our alignment system returns a value x' . The resolution function $r(x, x')$ is the probability density of the outcome x' for a real displacement x . Then, if the true density of x is $f(x)$, the measured probability density [26] will be

$$g(x) = \int r(x, x')f(x)dx \quad (4.24)$$

In the case of $f(x) = \delta(x_0)$, the output is just the resolution function. The resolution function can be sometimes approximated by a gaussian function

$$r(x, x') = \frac{1}{\sqrt{2\pi}\sigma} \exp \frac{(x' - x)^2}{2\sigma^2} \quad (4.25)$$

where σ is the (numerical) experimental resolution. If the mean value of a set of sixteen measurements is considered a good approximation to the instant population mean (being in any case the best estimator), then the distribution of the residuals ($\Delta X_R - \mathbb{E}(\Delta X_R)$) approximates the resolution function along the direction X_R . Histogramming the residuals, that is, the differences between the mean of each set of sixteen measurements and each one of the measurements for all the groups, the distributions shown in the top three pads of figure 4.28 are obtained. The gaussian approximation agrees perfectly with the residuals distribution along Z_R , but for the other directions X_R and Y_R , the fit χ^2 is quite poor. Again, the fast displacements are apparent, and the assumption that the population mean does

⁷The variances would have a $\chi^2(N = 16)$ distribution, if the sixteen independent measurements were normally ($N(0, 1)$) distributed.

not change is not exact; the population mean changes also in the case of Z_R , but below the experimental resolution, explaining the better agreement of the data along Z_R . Fitting the distributions to a gaussian and ascribing the numerical resolution to the σ of the fit,

$$\sigma(X_R) = 0.27 \mu m, \quad \sigma(Y_R) = 0.40 \mu m, \quad \sigma(Z_R) = 9.5 \mu m \quad (4.26)$$

The results are coincident with the estimate of the standard error from the variance distribution. The larger values obtained in the variance distribution correspond to the influence in the histogram mean of the larger variances of those groups with a large real displacement.

The expected numerical resolution of the vector describing the displacements in the MDC coordinates is simply a combination of the previous numerical resolutions. In particular, from the linear combination 4.16,

$$\begin{aligned} V(\Delta X_{MDC}) &= 0.8214 V(\Delta X_R) + 0.1786 V(\Delta Z_R) \\ V(\Delta Y_{MDC}) &= 0.0556 V(\Delta X_R) + 0.6889 V(\Delta Y_R) + 0.2555 V(\Delta Z_R) \\ V(\Delta Z_{MDC}) &= 0.1230 V(\Delta X_R) + 0.3111 V(\Delta Y_R) + 0.5659 V(\Delta Z_R) \end{aligned} \quad (4.27)$$

Taken the mean of the variances distribution for each direction shown in figure 4.28, the square root of the variances⁸ along the common MDC III coordinate system are

$$\sigma(X_{MDC}) = 4.1 \mu m, \quad \sigma(Y_{MDC}) = 4.9 \mu m, \quad \sigma(Z_{MDC}) = 7.3 \mu m \quad (4.29)$$

The means over sixteen measurements are going to be used to determine the relative displacements. Applying equation 4.21, the standard error in the mean displacement determination decreases a factor 4 when the means of sixteen independent analysis are used to determine the mean, provided the population mean does not change.

Finally, it is possible to make a simple test of the previous resolution estimation. Selecting a time interval where the relative displacements vary slowly, the complete time series can be approximated by a low order polynomial. The difference between the polynomial and the time series

⁸The present result is valid for each channel and also for the mean value of both channels defined by equation 4.18. Note that the correlation between the channels is close to one and, therefore, the variance for the mean value is

$$V(\Delta X_{MDC}) = \frac{\sigma^2(\Delta X_{MDC}^{AorB})}{2} + \frac{2}{4}\sigma^2(\Delta X_{MDC}^{AorB}) = \sigma^2(\Delta X_{MDC}^{AorB})$$

provided $\sigma(\Delta X_{MDC}^A) = \sigma(\Delta X_{MDC}^B)$

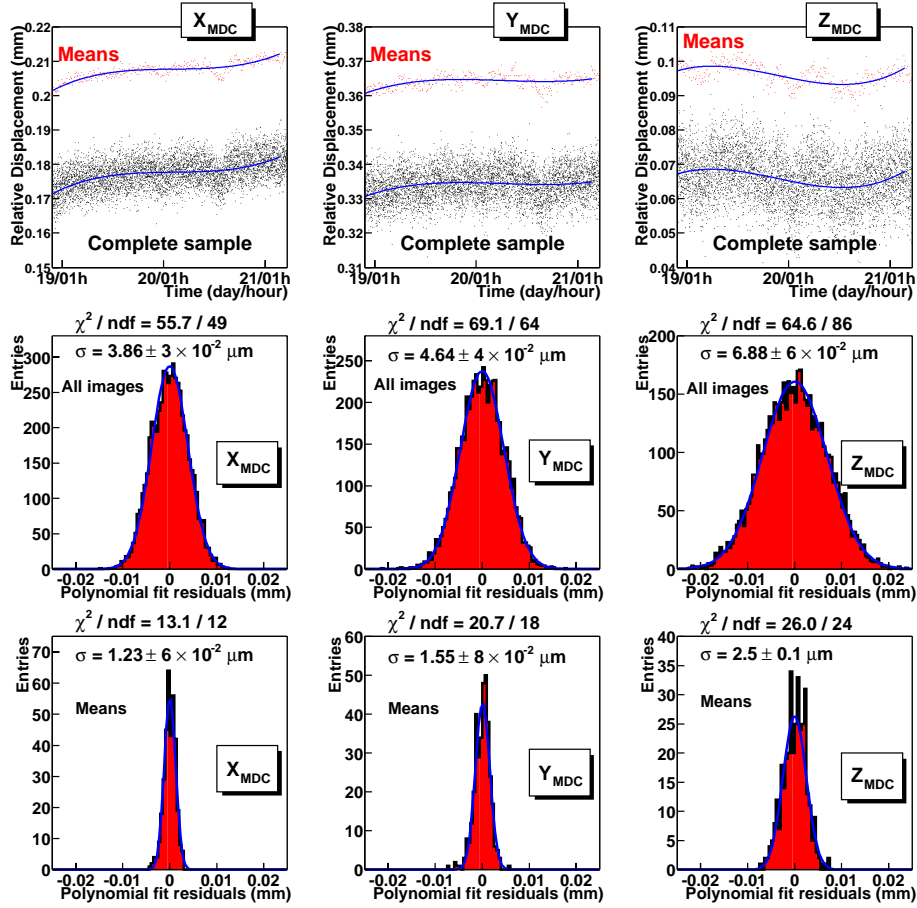


Figure 4.29: Polynomial fit and residuals for a slowly-varying short data sample in January 2002. The three top pads show the complete sample and the means of the grouped sample, displaced $30 \mu\text{m}$. The residuals distribution for the complete sample (second row) and the grouped sample (third row) are fitted to a gaussian; the fit χ^2 and σ are shown in each pad.

are called the polynomial fit residuals. The polynomial fit residuals are distributed according to the resolution distribution, provided the polynomial approximation accounts for the real displacement. Or, using the language of equation 4.24, the polynomial represents $f(x, t)$, the true time-dependent density. Figure 4.29 shows the displacement during two complete days (January 2002); the means are fitted to an order three polynomial, which approximates the basic daily features. Nevertheless, the polynomial fit does not account for the complete fine structure of the dis-

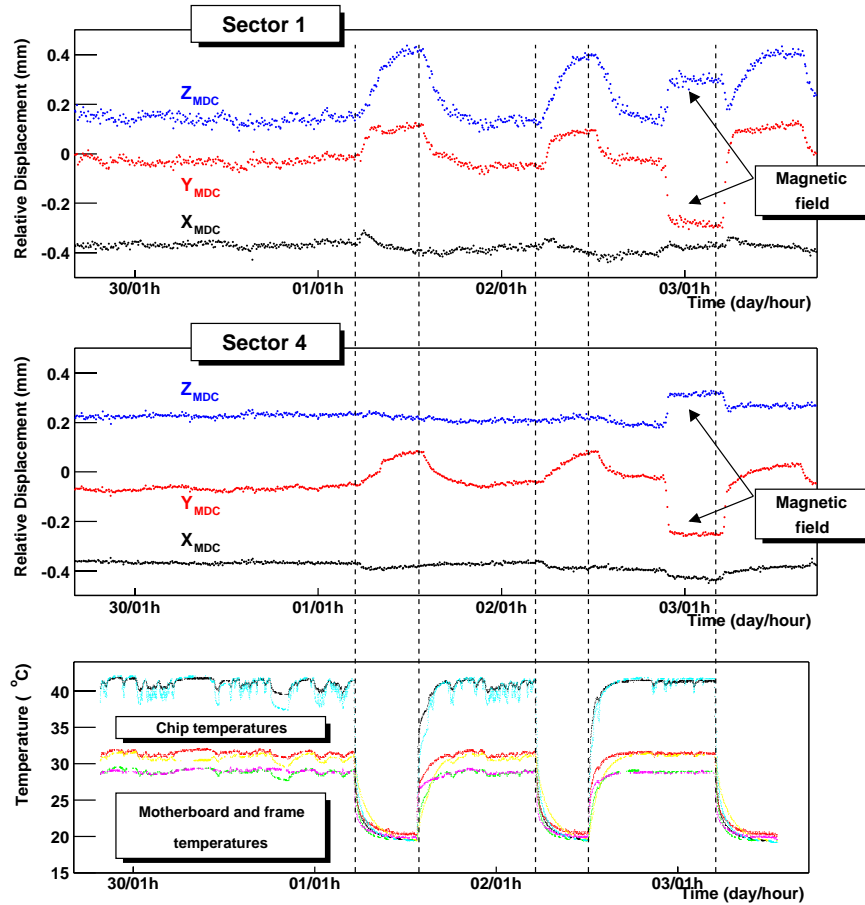


Figure 4.30: Temperature dependence of the observed MDC III displacement in sectors 1 and 4 (top and middle pads). The temperature (bottom pad) drops abruptly due to the shutdown of the electronics power supply after the data taking period (the magnetic field was firstly used during the night of December, the second). The observed series correspond to November/December 2001.

placements. The complete sample and the means are relatively displaced to observe both series, and the order three polynomial is plotted against both. The polynomial fit residuals in each direction are shown in the lower pads, for the complete sample and for the means of the sixteen elements groups. The sigma of the gaussian fit for the complete sample (see the values in the middle row of histograms in the figure 4.29) are compatible with those found previously (equation 4.29). For the means time series, the gaussian fit sigmas are approximately a factor 3 smaller (see the val-

ues in the lower row of histograms in the figure 4.29). A factor 4 would be expected from the theory, but the fine structure of the displacements affects more strongly the means series than the complete sample, where are comparable to the experimental resolution.

After the installation in the cave, the alignment system was running continuously to determine the main relative movements of the MDC modules and their dependence on different environmental properties. The data taking periods were studied with the maximum interest to determine the corrections in the MDC III position with respect to the inner modules. The main disturbing effect is the temperature change, which leads to deformations of the module frames and, more important, the support pieces and the pillars. During the data acquisition period, the strong magnetic field is the main source of displacements.

The dependence of the relative displacements with the temperature is displayed for sector 1 and 4 in figure 4.30. The temperature is measured in different points: several probes⁹ are directly attached to the electronic components to check the temperature during the working period. Other probes are attached to the motherboards and the aluminum frames. The temperature in the vicinity of the electronic components is quite high, close to $50^{\circ}C$, while the complete volume between the MDCs and around the electronics heats up to ten or fifteen degrees above the room temperature. While the electronics is switched on, the temperature changes slightly, depending on the work load. But the sudden shutdown of the electronics power reduces dramatically the temperature, leading to large displacements in the module position. The upper pads in figure 4.30 represents the displacements in sectors 1 and 4. In the bottom pad the temperatures of several probes are displayed in the same time scale (November/December 2001). After the data taking period, the electronic power supply was switched off three consecutive days. Immediately the temperature decreases and the relative position of MDC III changes. The large displacement in Z_{MDC} in the sector 1 (top spectrometer sector) is not observed in the lower sector (sector 4); the support structures are not symmetrical in different sectors, mainly in the opposite top and bottom sectors where the pillars length and ground (base support) proximity makes a difference. Along Y_{MDC} , the displacements are quite similar in different sectors. Large temperature changes are not expected (and therefore is not usually required to correct for) during the data taking periods, where the electronics should run continuously.

An opposite situation appears in the case of the magnetic field. The

⁹The temperature monitoring system was designed by Antonio Cardesín, and is described in his Ph.D. work, to be presented in the University of Santiago de Compostela.

software methods employed for the relative MDC alignment uses the study of straight tracks crossing the spectrometer, and therefore a data taking period with the magnet switched off is required. The geometrical parameters we obtained correspond to the situation without magnetic field. When the magnetic field is back, the modules are displaced. The main aim of the alignment system is to determine (and correct for, in the analysis parameters) the relative MDC III displacements with respect to the inner modules due to the magnetic field effects. The dependence of the relative displacements with the magnetic field is displayed for both sector 1 and 4 in figure 4.31. The relative displacement occurs immediately after the change in the magnet current, which ramps up to the maximum current in a period of about one hour. When the working magnetic field is reached, the large change in the position stops and a new position plateau is found. If the zone previous to the magnetic field increase is flat, the new plateau results flat, while those changes in position due to a temperature gradient still continues after the step. The displacements can be larger than 0.5 mm , along the Y_{MDC} direction, sufficient to produce an important systematic error on the momentum reconstruction.

The analysis software requires, as an input, the position of the drift chambers. The alignment software methods finds the relative position of the modules by analysing the data obtained without magnetic field. The original position obtained by the software algorithms should be modified when the magnetic field is present. The correction requires the determination of the baseline or plateau before and after the large displacement caused by the magnetic field. As shown in figures 4.31 and 4.32, the position plateaus are clearly defined as the mean of the measurements in the assigned interval. The parameters corresponding to the outer modules are corrected in each direction according to the differences between the plateau mean values¹⁰. The data files acquired during the time interval of a well defined plateau are ascribed to the same corrected parameter file.

To estimate the error on the correction performed by the hardware alignment system from an initial unbiased software determination, one should take into account both the resolution and the errors in the calibration coefficients to determine the alignment system experimental error. Once a plateau is defined, the actual error committed when the plateau mean value is assigned to the analysis parameters is a composition of the alignment system experimental error and the plateau variance from the mean in the interval. The alignment system experimental error can be

¹⁰The angular value of the rotations ϕ_Z and ϕ_Y is constant (variation below $0.5 \times 10^{-2} \text{ mrad}$) during the complete November/December beam time.

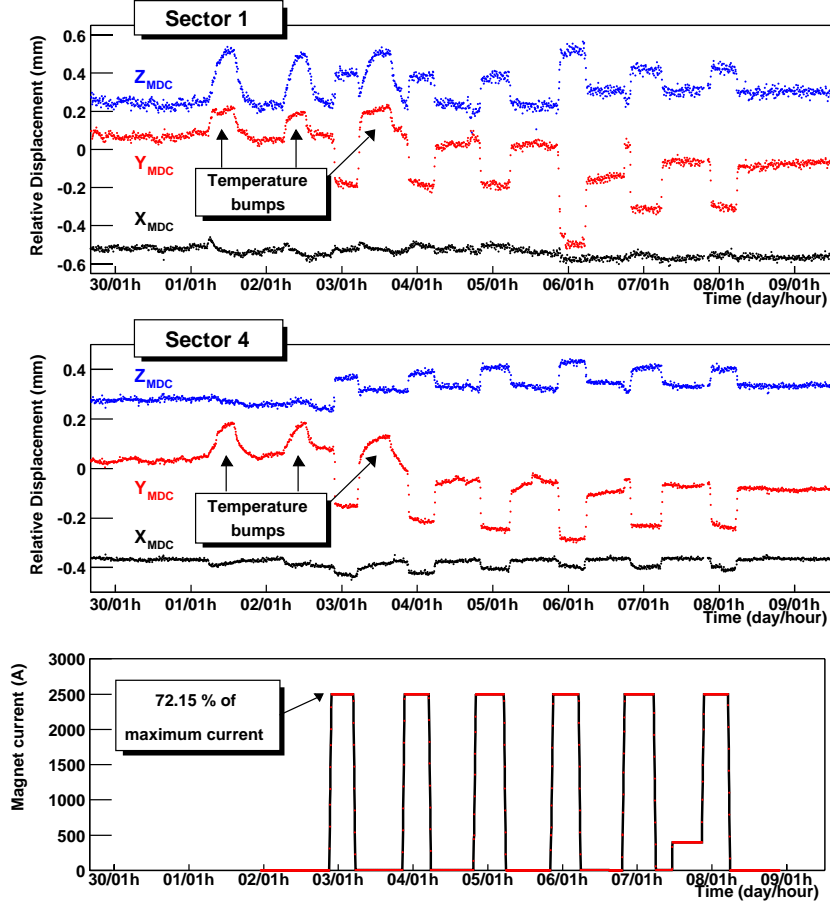


Figure 4.31: Magnetic field strength dependence of the observed MDC III displacement in sectors 1 and 4. The temperature bumps correspond to those signaled in figure 4.30. The observed series correspond to November/December 2001.

estimated from equations 4.15, 4.16 and 4.29 for the channels axes

$$\begin{aligned}
 \sigma(\Delta X_R) &= 0.002 * \Delta X_R \pm 0.27 \mu m \\
 \sigma(\Delta Y_R) &= 0.004 * \Delta Y_R \pm 0.40 \mu m \\
 \sigma(\Delta Z_R) &= 0.017 * \Delta Z_R \pm 9.5 \mu m
 \end{aligned}
 \tag{4.30}$$

where the first term is the calibration error estimate¹¹ and the second one is the error given by the alignment system experimental resolution.

¹¹Remember the change of notation already commented. The directions X_R and Y_R are in this section interchanged, with respect to the notation in sections 4.4 and 4.6 for

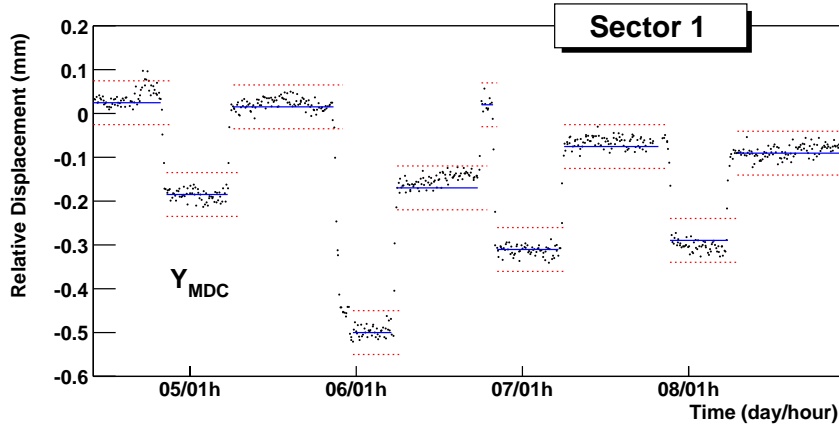


Figure 4.32: Example of the relative displacement analysis. The plateaus of mean values (here calculated for the first ten entries) are plotted as blue lines, while upper and lower variation limits are plotted at $50 \mu m$ as dashed red lines.

An additional contribution, corresponding to the systematic error in the calibration should be taken into account; it was estimated to be below a micron per mm of displacement (see equation 4.15 and the subsequent explanation). The error in the calibration diagonal terms introduces an error in the final displacement measurement which depends on the size of the displacement. Comparing the experimental resolution and the error in the calibration diagonal terms, the first is more important for most of the displacements; the error estimation was quite conservative during the calibration. The error in the final correction is calculated applying the transformation 4.16 to those values obtained from equation 4.30.

A new scheme has to be used to automatize the position correction as soon as the connection between the slow control parameters and the analysis is available. Figure 4.32 shows the proposed scheme, which is actually close to the procedure which it is now used for the displacement analysis and parameters correction: a short set of data, of the order of ten measurements, is used to obtain a mean value of the position along each direction. Two limits, upper and lower are defined at a fixed distance from the mean value. In the figure, a distance value of $50 \mu m$ is chosen. If the measured position along the coordinate exceeds the limits, a new position is found. The new position can be initially obtained from a short number

the sake of simplicity in the geometrical transformations between RASNIK and MDC coordinates.

of data points, but discarding those after the fast displacement which can lead to a biased mean value.

Bibliography

- [1] *RASNIK Web Pages at NIKHEF*,
(http://www.nikhef.nl/pub/departments/et/ccd_rasnik).
- [2] ATLAS Technical Proposal, CERN/LHCC/94-43, CERN, Geneva, 1994.
- [3] P. Duinker *et al*; Nucl. Instr. and Meth. **A273** (1988) 814-819.
- [4] B. Adeva *et al*; Nucl. Instr. and Meth. **A323** (1992) 109-124.
- [5] G. C. Holst; *CCD Arrayys, Cameras and Displays*. Spie Optical Engineering Press, Washintong, USA (1985).
- [6] A. van der Horst; *Measurements on RASNIK*, 1995, NIKHEF.
- [7] G. Dicker; *Linearity, Resolution and Systematic Errors*, May 1997, NIKHEF.
- [8] J. Dupraz, D. Saltzberg, G. Van Beek; Nucl. Instr. and Meth. **A388** (1997) 173.
- [9] CMS MUON Technical Design Report, CERN/LHCC 97-32, CMS TDR 3, CERN, Geneva, 1997.
- [10] H. van der Graaf, H. L. Groenstege, F. Linde, P. A. M. Rewiersma; *RasNiK, an Alignment System for the ATLAS MDT Barrel Muon Chambers. Thecnical System Description*, ET38110, April 2000, NIKHEF.
- [11] H. L. Groenstege, P. A. M. Rewiersma; *RasLeD. The lightsource for the RasNik alignment system*, ETR 99-04, September 1999, NIKHEF, Depart. of Electronic Thechnology.
- [12] H. L. Groenstege; *The coding of the mask for CCD-Rasnik*, ETR 94-10, NIKHEF, Depart. of Electronic Thechnology.
- [13] P. B. Denyer; *CMOS vs CCD*, Vision whitepapers, 1999, Vision.
(<http://www.vvl.co.uk/whycmos/whitepaper.htm>).

-
- [14] *VV 5430 Monolithic Sensor. Multi Standard Monochrome CMOS Image Sensors*, 1998, Vision. (<http://www.vvl.co.uk/>).
- [15] H. L. Groenstege, P. A. M. Rewiersma; *RasCaM. The sensor for the RasNik alignment system*, ETR 99-03, September 1999, NIKHEF, Depart. of Electronic Thechnology.
- [16] H. L. Groenstege, P. A. M. Rewiersma; *RasMuX. The multiplexer for the RasNik alignment system*, ETR 99-05, September 1999, NIKHEF, Depart. of Electronic Thechnology.
- [17] *MACH Series DT 3155 User Manual*, Data Translation Inc., 1995, Marlboro. (<http://www.datatranslation.com>).
- [18] Y.S. Touloukian, R.K. Kirby, R.E. Taylor and P.D. Desai; *Thermal Expansion. Metallic Elements and Alloys*, IFI/Plenum, New York, 1972.
- [19] CATIA-CADAM Solutions Version 4, Dassault Systemes. <http://www.catia.com>
- [20] M. Dahlinger; *HADES Geometry and Database* (<http://depc14.gsi.de/hades/Geometry.htm>).
- [21] J. Stroth; *MDC reference systems*, MDC Note 03/98.
- [22] H. van der Graaf; The RASNIK-ICARAS coordinate system, internal discussion paper. Private communication.
- [23] EPICS home page, <http://www.aps.anl.gov/epics>.
L. R. Dalesio, M. R. Kraimer, A. J. Kozubal; *EPICS architecture*, <http://www.aps.anl.gov/epics/docs/general.php>
- [24] M. Knott *et al*; EPICS: A Control System Software Co-Development Success Story, 1997.
- [25] P. Stanley; *Channel Access Portable Server Tutorial and Reference* <http://mesa53.lanl.gov/lansce8/Epics/ca/ca.html>
- [26] W.T. Eadie *et al*; *Statistical Methods in Experimental Physics*, North-Holland Publishing Company, Amsterdam, 1971.

Part III

SOFTWARE ALIGNMENT

Chapter 5

Relative Alignment Methods

5.1 Introduction

The Multiwire Drift Chambers (MDCs) have to measure the space coordinates of the charged particle trajectories. The momentum of the charged particles is calculated from the bending of their path in the magnetic field. The trajectories are divided in two “lever-arms”, one upstream and the other downstream the bending gap. The straight part of each lever-arm is defined by the information from two drift chamber modules. The combination of the resolution of the measurements done by the drift chambers and the knowledge about their spatial relative positions determine the quality of the estimate. Actually, only if the relative position between the modules is known, the module position resolution plays a role in the estimate accuracy. In other words, the resolution of the track estimate cannot be better than the alignment accuracy of the modules contributing to the estimate.

When the magnet is off, the charged particles follow approximately a straight path through the spectrometer. Once a track trajectory can be estimated by any means, it is possible to extrapolate the position of the track and, in particular, to calculate the cross point between the track trajectory and a plane (for example, other module). The true relative position of a module (with respect to the device used to estimate the track trajectory) is that which minimizes the statistical mean value of the differences between the track extrapolations and the information about these tracks given by the module (the so-called position residuals). Charged particle trajectories differ from the straight line because of many small-angle deviations. This multiple scattering produces the so-called angular straggling. The effects of the angular straggling are isotropic; there is not a privileged spatial direction and then it does not affect to the mean value of the residuals

distribution. Due to geometrical factors, the angular straggling introduces an additional spread of the residuals distributions which is not gaussian, even for gaussian errors in the coordinates and slopes of the track estimate given by the modules.

Let us begin by establishing the geometrical transformation between the coordinate systems. The definition of the laboratory and module coordinate systems has been already seen in section 4.5. For every detector, there is a unique transformation which renders the laboratory coordinates of a point expressed in its inner reference system

$$\vec{X} = R_A \vec{X}_A + \vec{T}_A \quad (5.1)$$

$$\vec{X} = R_B \vec{X}_B + \vec{T}_B \quad (5.2)$$

where \vec{X} represents the point expressed in the laboratory coordinate system, R and \vec{T} are, respectively, the rotation matrix and the translation vector between the coordinate system origins, and \vec{X}_A and \vec{X}_B are the coordinates of a point given in the coordinate system of module A and B .

It is immediate to get the point \vec{X}_A expressed in the coordinate systems of the module B

$$\vec{X}_B = M \vec{X}_A + \vec{V} \quad (5.3)$$

where

$$\begin{aligned} M &= (R_B)^{-1} R_A \\ \vec{V} &= (R_B)^{-1} (\vec{T}_A - \vec{T}_B) \end{aligned} \quad (5.4)$$

The notation $(R_B)^{-1}$ is used to signify the inverse matrix of R_B , equivalent to the transposed one in the case of a rotation matrix. The left part of figure 5.1 shows the translation vectors and the relation between the coordinate systems in different modules.

Any rotation matrix can be expressed as a function of the Euler angles (as it is shown in appendix E). For the particular case in equation 5.3, the rotation matrix M takes the form

$$\begin{pmatrix} \cos \phi \cos \theta \cos \psi - \sin \phi \sin \psi & -\cos \phi \cos \theta \sin \psi - \sin \phi \cos \psi & \cos \phi \sin \theta \\ \sin \phi \cos \theta \cos \psi + \cos \phi \sin \psi & -\sin \phi \cos \theta \sin \psi + \cos \phi \cos \psi & \sin \phi \sin \theta \\ -\sin \theta \cos \psi & \sin \theta \sin \psi & \cos \theta \end{pmatrix}$$

when the angles (ϕ, θ, ψ) are those shown in the three right pads of figure 5.1. When the modules are in the design position, and for modules of the same sector, the first rotation around Z_B equals $\zeta = Y_B$ and $\eta = -X_B$, being the angle $\phi = \pi/2$ (the notation of the intermediate axis corresponds

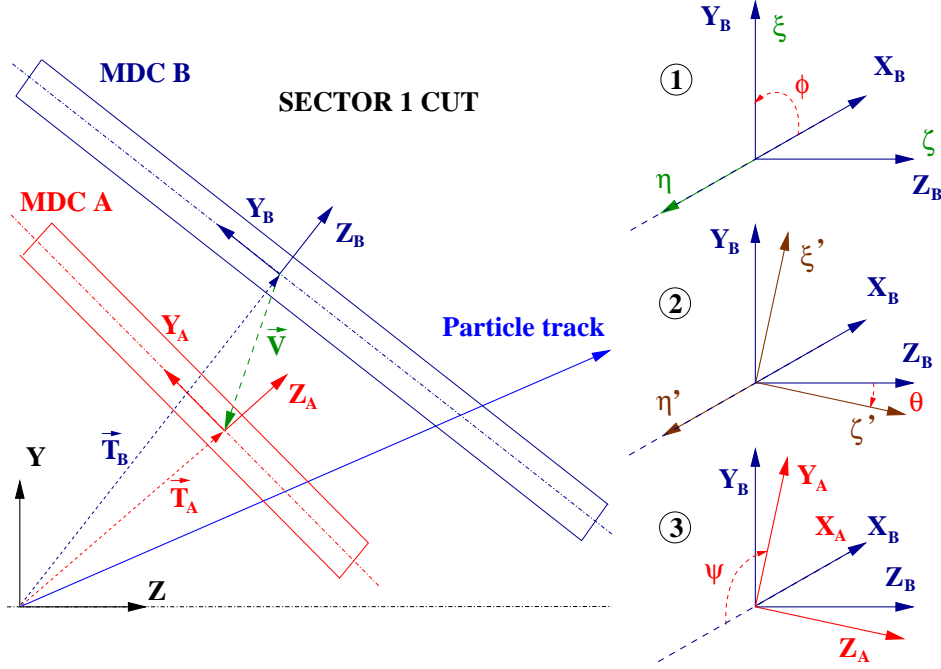


Figure 5.1: Left: laboratory and module coordinate systems. The vectors \vec{T}_A , and \vec{T}_B represent the translation vector of the modules coordinates origin, while \vec{V} is the translation vector of the module A origin seen by module B. Right: the Euler angles of the rotation matrix in the transformation 5.3; the names of angles and auxiliary axis and the ordering follow the notation given in appendix E.

to that given in the appendix E). The second rotation depends on the modules; it is the real tilt angle between the surfaces of the planes. The third rotation returns the axis X_A to point in the same direction than X_B , and therefore $\psi = -\pi/2$. In a general case both ϕ , ψ and θ can take other values, usually not far from the design ones.

In the next sections two methods for the relative alignment of, respectively, two and three modules are introduced. The need of an algorithm for the alignment of two modules was motivated by the provisional setup in the spectrometer, containing several sectors where only two modules are available. The entry point to the algorithms are the *Hits* (as defined in appendix D), containing the parameters of the straight line which better approximates the charged particle path when is crossing the module. A *Hit* contains the position of the estimated cross point of the track with the plane $Z_{MDC} = 0$ of the module coordinate system. For the sake of

notation, in the following we are going to call x and y to these coordinates, adding the pertinent subindex or superindex to identify the module origin. The estimate of the track inclination with respect to the $Z_{MDC} = 0$ plane is also stored, in the form of the unit vector along the direction of the track. Its components along the axis X_{MDC} and Y_{MDC} are taken, notated as $xDir$ and $yDir$.

The algorithm designed to align three modules minimizes the sinus of the angle between the track estimates obtained from pairs of modules. This is equivalent to require that the coordinates of the *Hits* in the three modules are closest to a straight line, for all the selected tracks.

To align two modules, the algorithm minimizes the differences between the projection of the track estimate in a module and the local estimate of the same track in the second module. The angular information about the charged particle track contained in a *Hit* could be used to match the *Hits* in other modules originated from the same track and determine the residuals, but this angular information lacks of precision, due to the small thickness of the drift modules. There is an alternative procedure to avoid the direct use of the *Hit* slopes in the residuals calculation: first, a set of *Hits* from a module, or set of modules of the same plane, can be used to estimate the position of the target with respect to the modules. Then, the straight lines representing the particle paths can be constructed using two points: the cross point in the module plane (x, y) , obtained from every *Hit*, and the target position estimate that was found from the whole set of *Hits*. Selecting *Hits* in the central part of the modules, the tracks coming from the target impinge upon the modules perpendicular and possible problems associated with the error in the module thickness or calibration of tracks with large incidence angle are diminished. This chapter contains the description of both approximations, but only the method which uses the target estimate is evaluated, to compare it with the real data analysis in the next chapter.

5.2 The Target Finder algorithm

This section describes the procedure used in this work to estimate the target center position from a single MDC module, or from a set of modules of the same plane but different sectors. Basically, the method uses straight lines, constructed from the track estimates in the modules, to define a common origin, the point that minimizes the sum of its distance to these straight lines. The method is first presented in a general way, and then the particularities of each case are discussed.

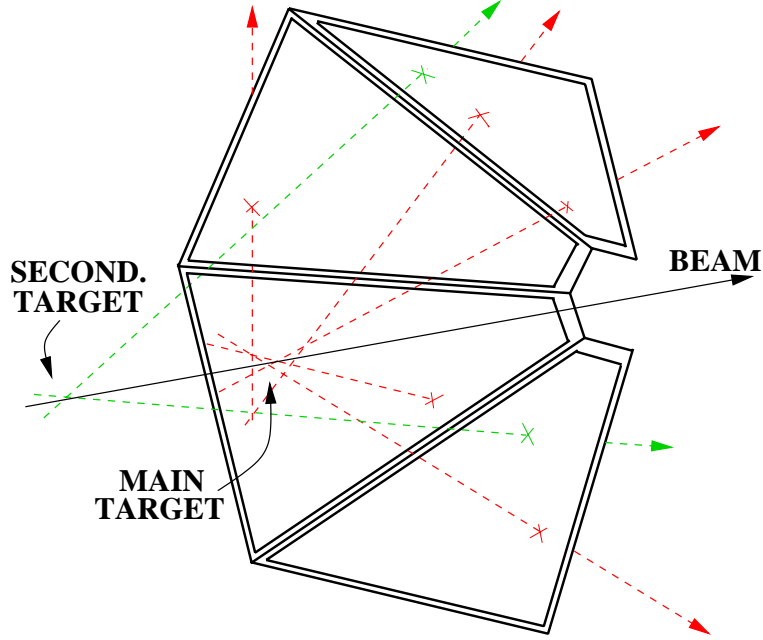


Figure 5.2: Target reconstruction from the Hits in different modules. The straight lines calculated from the module track estimates come from the interaction points along the beam.

For each given *Hit* in the module A , a straight line is given by the point $\vec{r}_{MDC} = (x_A, y_A, 0)$ and the vector

$$\vec{\alpha}_{MDC} = \left(xDir_A, yDir_A, \sqrt{1 - (xDir_A^2 + yDir_A^2)} \right) \quad (5.5)$$

This straight line is our estimate of the real particle trajectory. If we use several modules of the same plane but different sectors to estimate the target center, then the straight lines should be expressed in a common coordinate system (the laboratory coordinate system)

$$\vec{r} = R_A \vec{r}_{MDC} + \vec{T}_A \quad (5.6)$$

$$\vec{\alpha} = R_A \vec{\alpha}_{MDC} \quad (5.7)$$

The target center estimate $(v(x), v(y), v(z))$ is obtained by minimizing its distance to the straight lines¹. The equation of the squared distance be-

¹The described minimization procedure is coded in the vertex finder algorithm (HGeomVertexFit) inside the HYDRA package, written by Manuel Sánchez.

tween the straight line passing through the point \vec{r} with normalized direction vector $\vec{\alpha}$, and the target estimate is

$$\begin{aligned} d^2 = & [(v(x) - r(x))\alpha(y) - (v(y) - r(y))\alpha(x)]^2 \\ & + [(v(y) - r(y))\alpha(z) - (v(z) - r(z))\alpha(y)]^2 \\ & + [(v(z) - r(z))\alpha(x) - (v(x) - r(x))\alpha(z)]^2 \end{aligned} \quad (5.8)$$

Let us consider a set of track estimates, each one contributing to the target estimate with a weight w . Our best estimation of the vertex point is given by the minimization of the merit function

$$Q^2 = \sum_i w_i d_i^2(v(x), v(y), v(z)) \quad (5.9)$$

where i runs over all the available *Hits*. From 5.9, three independent equations are obtained

$$\begin{aligned} \frac{\partial Q^2}{\partial v(x)} = & 2 \sum_i w_i \alpha_i(y) [(v(x) - r_i(x))\alpha_i(y) - (v(y) - r_i(y))\alpha_i(x)] \\ & - 2w_i \alpha_i(z) [(v(z) - r_i(z))\alpha_i(x) - (v(x) - r_i(x))\alpha_i(z)] = 0 \\ \frac{\partial Q^2}{\partial v(y)} = & -2 \sum_i w_i \alpha_i(x) [(v(x) - r_i(x))\alpha_i(y) - (v(y) - r_i(y))\alpha_i(x)] \\ & + 2w_i \alpha_i(z) [(v(y) - r_i(y))\alpha_i(z) - (v(z) - r_i(z))\alpha_i(y)] = 0 \\ \frac{\partial Q^2}{\partial v(z)} = & -2 \sum_i w_i \alpha_i(y) [(v(y) - r_i(y))\alpha_i(z) - (v(z) - r_i(z))\alpha_i(y)] \\ & + 2w_i \alpha_i(x) [(v(z) - r_i(z))\alpha_i(x) - (v(x) - r_i(x))\alpha_i(z)] = 0 \end{aligned} \quad (5.10)$$

Writing the previous equation in matrix form, the Cramer methodology gives us the immediate solution. The target center estimate is

$$v(x) = \frac{D_x}{D}; \quad v(y) = \frac{D_y}{D}; \quad v(z) = \frac{D_z}{D} \quad (5.11)$$

where D is the determinant

$$D = \begin{vmatrix} \sum_i w_i [\alpha_i^2(y) + \alpha_i^2(z)] & -\sum_i w_i [\alpha_i(x)\alpha_i(y)] & -\sum_i w_i [\alpha_i(x)\alpha_i(z)] \\ -\sum_i w_i [\alpha_i(x)\alpha_i(y)] & \sum_i w_i [\alpha_i^2(x) + \alpha_i^2(z)] & -\sum_i w_i [\alpha_i(y)\alpha_i(z)] \\ -\sum_i w_i [\alpha_i(x)\alpha_i(z)] & -\sum_i w_i [\alpha_i(y)\alpha_i(z)] & \sum_i w_i [\alpha_i^2(y) + \alpha_i^2(x)] \end{vmatrix}$$

and

$$\begin{aligned}
D_x &= \begin{vmatrix} \sum_i \zeta_i & -\sum_i w_i [\alpha_i(x)\alpha_i(y)] & -\sum_i w_i [\alpha_i(x)\alpha_i(z)] \\ \sum_i \eta_i & \sum_i w_i [\alpha_i^2(x) + \alpha_i^2(z)] & -\sum_i w_i [\alpha_i(y)\alpha_i(z)] \\ \sum_i \kappa_i & -\sum_i w_i [\alpha_i(y)\alpha_i(z)] & \sum_i w_i [\alpha_i^2(y) + \alpha_i^2(x)] \end{vmatrix} \\
D_y &= \begin{vmatrix} \sum_i w_i [\alpha_i^2(y) + \alpha_i^2(z)] & \sum_i \zeta_i & -\sum_i w_i [\alpha_i(x)\alpha_i(z)] \\ -\sum_i w_i [\alpha_i(x)\alpha_i(y)] & \sum_i \eta_i & -\sum_i w_i [\alpha_i(y)\alpha_i(z)] \\ -\sum_i w_i [\alpha_i(x)\alpha_i(z)] & \sum_i \kappa_i & \sum_i w_i [\alpha_i^2(y) + \alpha_i^2(x)] \end{vmatrix} \\
D_z &= \begin{vmatrix} \sum_i w_i [\alpha_i^2(y) + \alpha_i^2(z)] & -\sum_i w_i [\alpha_i(x)\alpha_i(y)] & \sum_i \zeta_i \\ -\sum_i w_i [\alpha_i(x)\alpha_i(y)] & \sum_i w_i [\alpha_i^2(x) + \alpha_i^2(z)] & \sum_i \eta_i \\ -\sum_i w_i [\alpha_i(x)\alpha_i(z)] & -\sum_i w_i [\alpha_i(y)\alpha_i(z)] & \sum_i \kappa_i \end{vmatrix} \quad (5.12)
\end{aligned}$$

where

$$\begin{aligned}
\sum_i \zeta_i &= \sum_i w_i \{r_i(x)[\alpha_i^2(y) + \alpha_i^2(z)] - r_i(y)\alpha_i(x)\alpha_i(y) - r_i(z)\alpha_i(x)\alpha_i(z)\} \\
\sum_i \eta_i &= \sum_i w_i \{r_i(y)[\alpha_i^2(x) + \alpha_i^2(z)] - r_i(x)\alpha_i(x)\alpha_i(y) - r_i(z)\alpha_i(y)\alpha_i(z)\} \\
\sum_i \kappa_i &= \sum_i w_i \{r_i(z)[\alpha_i^2(x) + \alpha_i^2(y)] - r_i(x)\alpha_i(x)\alpha_i(z) - r_i(y)\alpha_i(y)\alpha_i(z)\}
\end{aligned} \quad (5.13)$$

A first target estimation is obtained directly by applying the previous procedure for all the *Hits*, with identical weights.

Let us check the previous algorithm on a simulated set of tracks. The simulation contains the tracks generated by 5×10^4 collisions of a Carbon beam at 2 AGeV against a Carbon target, with approximately 2.3×10^5 charged particles being propagated along the six sectors. The Carbon target is a cylinder of 4 mm radius and 10 mm long. The tracks of the charged particles generated in the collisions are propagated along the spectrometer, with the magnetic field off. The simulation includes both the multiple scattering created by the interposed matter and the secondary particles randomly produced. The position of the tracks when they cross the detectors is used to generate the *Hits*, including a gaussian smearing in their coordinates that simulates the experimental resolution ($\sigma_x = 160 \mu m$, $\sigma_y = 80 \mu m$). The polar angles θ and ϕ of each simulated track, calculated in the module coordinate system, are used to obtain the angular components of the *Hits*. Gaussian errors, close to the experimental ones, are also introduced in the angles ($\sigma_\theta = 1 \text{ deg}$ and $\sigma_\phi = 2 \text{ deg}$), previously to the conversion to components along the directions X_{MDC} and Y_{MDC} of the unit vector in the direction of the track. The estimate of the target position is obtained using all the *Hits* reconstructed in the six-sector modules of the second plane (MDC II).

Under these conditions, the first estimation of the target position shows a large deviation along Z , the direction of the ion beam, of more than 80 mm in the downstream direction. The reason of this deviation is the large number of particles which, instead of from the Carbon target, come from either the beam interaction with matter along the beam line (vacuum windows, beam detectors) or the interaction of the primary particles, mainly emitted at small polar angles, with the beam pipe, the output window of the vacuum pipe or the RICH and inner support structures of the MDCs. The lower pad of figure 5.3 shows a two dimensional (Y-Z) histogram of the emission point for each particle, along the beam line (with an additional cut: the vertex X coordinate is kept below 100 mm). The beam pipe and the inner RICH radiator case tube are clear scatter centers for the primary particles from the target. The target area, around the $(Y, Z) = (0, 0)$ coordinate, is extended in the left square. Most secondaries are emitted inside the target in the $Z > 0$ region, creating an additional asymmetry which is inherent to the target geometry.

The track estimate can be extrapolated up to the beam proximities, but there is no clue about the position of the vertex along the trajectory. A useful approximation is to take the closest point to the beam line (or the Z axis of the laboratory system); but one should keep in mind the difference between this information and the real vertex of the particles. The closest point always exist if the trajectory is not parallel to the Z axis (see the mathematical details in section 6.5). In the top pad of figure 5.3, a histogram of the Z coordinate of the closest-approach point of the trajectory to the Z axis is represented. The large number of secondaries coming from the scatters in the $Z > 0$ region are better seen in the left inserted pad where the histogram is zoomed.

As the *Hits* created by tracks coming from secondary targets contribute to the target estimate equally that those *Hits* created by tracks coming from the main target, the target position estimate is biased by these contributions. A better approximation assigns a weight to each track, which is a function of the distance to the target estimate obtained in a previous step. It is implicit in this iterative approximation, that the number of tracks coming from the main target is large, when compared with the number of tracks coming from other secondary targets. The weight should be a smoothly decreasing function of the distance; a bi-squared Tukey function represents a good candidate. The bi-squared Tukey weights are defined as

$$w_i = \begin{cases} (1 - t_i^2/k_T^2)^2 & \text{if } |t_i| < k_T \\ 0 & \text{if } |t_i| > k_T \end{cases} \quad (5.14)$$

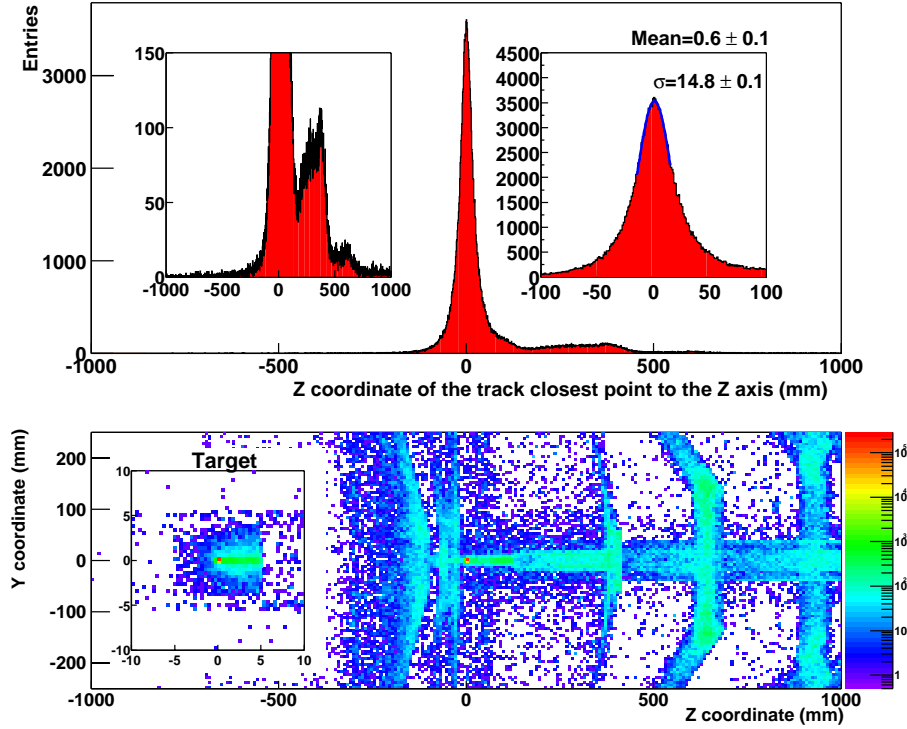


Figure 5.3: The top pad shows the Z coordinate of the track's closest point to the Z axis in a (C+C) simulation. The inserted small pads are two zoomed views, showing the bins with less entries to the left and a peak gaussian fit to the right. The lower pad shows the particle vertex given by the simulation along the beam line, for the first 5000 interactions.

where $t_i = d_i/e$ is the ratio between the target distance d_i and e , the standard error in the distance distribution, which can be estimated from the difference between the reconstructed and the original track angles.

The bi-squared Tukey function is plotted in the top pad of figure 5.4 and in the middle pad of figure 6.1, for two different values of the constant k_T . The function decreases continuously from the unity up to zero. The Tukey constant k_T defines the point where the Tukey function vanishes, and corresponds to k_T times the error estimation, following the function definition 5.14.

Usually, the minimization is performed introducing weights with an optimal Tukey constant, which is strongly dependent on the background source (calling background to the all the contributions which do not belong to the relevant signal). Here, the bi-squared Tukey function is used to get

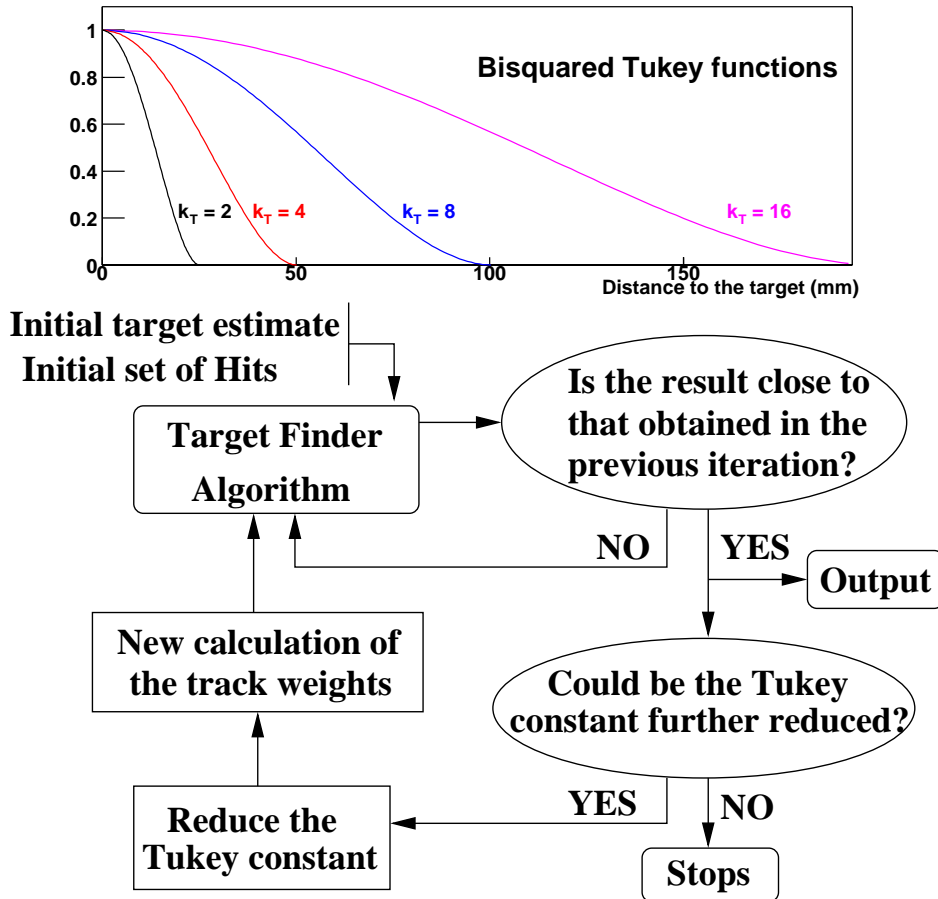


Figure 5.4: Top: Tukey function for $e = 12.6$ and several values of k_T . Bottom: Scheme of the iterative procedure to find the target position estimate.

rid of tracks coming from the secondary targets which can be close to the target. The error in the distance could be also overestimated, leading to larger weights than ideal. Then, the optimal Tukey constant should be tested iteratively for each individual case (see figure 5.4):

- An initial target position estimate is obtained from all the *Hits*.
- From the initial target estimate one can calculate a weight for each track, using the equation 5.14. The Tukey constant should be, in this first step, large enough to contain (most of) the tracks coming from the main target. A significant number of tracks coming from

k_T	Entries	x_t	y_t	z_t
	220830	0.169	-0.108	63.828
10	190088	0.031	-0.008	2.293
8	187284	0.023	-0.004	1.598
6	183782	0.015	0.002	1.066
4	179087	0.011	0.004	0.713
3	175445	0.008	0.004	0.593
2	166818	-0.001	0.001	0.487
1	108206	-0.016	-0.020	0.442
0.5	39076	-0.039	-0.080	0.719

Table 5.1: Results of the Target Finder algorithm for different Tukey weights. The first row includes the result for all Hits (weighting 1).

secondary targets is still present at this stage. A new estimate of the target position is obtained.

- The Tukey constant is reduced and a new target position search is performed. The number of *Hits* accepted in the search is reduced as well as the secondary targets contribution (in a larger ratio than those coming from the main target). For each Tukey constant, a new position estimate is obtained.
- The procedure stops for a small value of the Tukey constant, small enough to get rid of most of the tracks coming from secondary targets. Reducing further the Tukey constant reduces the sample statistics without any improvement in sample quality.
- Within each step, that is, for each Tukey constant, the minimization is first calculated using, as initial value, the outcome of the immediate Tukey constant. To check the independence on the initial value, the minimization is iteratively performed using as initial value the position estimate from the previous step (or the previous Tukey constant in the first iteration), up to a stable solution is found.

The described mechanism could be dramatically biased in some well defined situations, when the number of tracks coming from secondary targets is large enough to get the target estimate far away from the main target position, the minimization could converge around a secondary target. In all cases, the procedure should be performed checking the distance distribution between the tracks and the estimated target for each step.

Let us apply the complete procedure, now including the Tukey weights, to the track estimates in the simulation. The target estimate for the different Tukey constant k_T and the number of entries considered in each minimization are shown in table 5.1. The standard error has been fixed to be 12.6 mm for all tracks, which results from the sigma of the difference between the reconstructed and simulated polar angles multiplied by the distance from the target.

The results have shown a clear approach to the simulated target position as the Tukey constant decrease to the shortest values. The entries considered in the minimization decreases, slowly at the beginning down to a constant k_T of 2 or 3. Up to this point, the secondary targets contribution reduce in a larger ratio than those from the main target; from this point on, we begin to lost tracks contributing to the target, and the signal/background decreases.

The target position estimate along Z is different from zero, even being the target centered at the coordinate $Z = 0$. There are two main reasons: first, there are still tracks contributing to the target position estimate generated outside the target, in the $Z > 0$ region. In particular, there are trajectories obtained from *Hits* in the bottom part of the modules, coming from the beam pipe. These trajectories pass close to the target, and are accepted inside the Tukey cuts, displacing the target position estimate in the forward direction. Second, the production of particles is not completely symmetric inside the target volume, due to the secondary interactions of the collision products.

The first effect can be eliminated by using all *Hits* reconstructed in the modules but those in their lower part, close to the beam line. The left part of figure 5.5 schematizes the situation. Let us suppose a secondary particle generated by the interaction of a primary particle with the beam pipe. The secondary can follow a path with small polar angle with respect to the beam (track 3 in the scheme) and generate a *Hit* in the drift module. Then, the *Hit* is used to obtain a straight line, which contributes to the target position calculation, even for the smaller Tukey constant values (the extrapolation of the straight line enters inside the small sphere around the target, representing the accepted volume). Then, the target position estimate obtained is biased toward positive values of the laboratory Z coordinate. If the secondary track is propagated with a larger polar angle (track 2 in the scheme), the extrapolation of the straight line obtained from the *Hit* does not enter in the target vicinity, and it does not contribute to the target position estimate. It is possible to correct the bias by discarding the *Hits* with local module coordinate Y_{MDC} lower than a

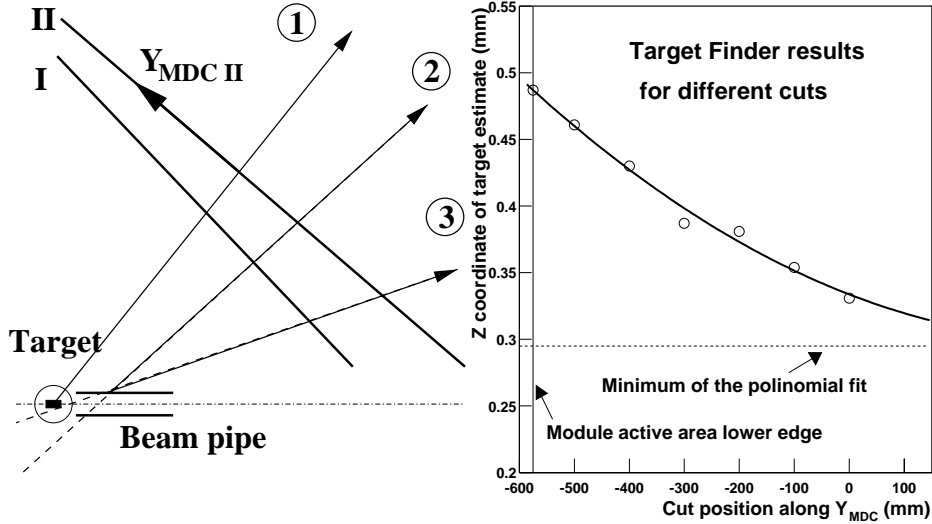


Figure 5.5: The left scheme represents the possible paths of a primary (1) and two secondaries (2,3) generated in the beam pipe. The track estimate obtained from the secondary particle with lower polar angle (3) enters inside the target vicinity and contributes to the target position estimate. The scheme is not to scale. The right pad shows the dependence of the Z coordinate of the target position estimate with a cut parameter; Hits with Y_{MDC} coordinate below the parameter are not accepted. The points are fitted to a second-order polynomial.

given cut parameter. The right part of figure 5.5 shows the Z coordinate of the target position estimate, obtained for different cuts; the first value corresponds to the estimate obtained using all *Hits* (without cut). The Z coordinate of the estimate decreases as the cut parameter increases from the lower edge of the modules active area. The number of *Hits* also reduces fastly preventing a calculation for a larger cut. A second-order polynomial fits nicely the points in the graph; from the minimum of the polynomial, the limit value of the target estimate Z coordinate can be extracted within a good approximation.

The second effect is inherent to the asymmetric particle production in the target, as it is shown in the zoomed view in the bottom pad of figure 5.3. In the simulation, the target geometry is close to that used up to now in the C+C reactions (thick target): a simple cylindrical carbon piece, with the cylinder axis along the beam direction. The particles are generated in collisions all along the target length and the radial extent of the collisions

volume depends on the focusing status of the beam, being limited by the target radius. Longitudinally it is expected a constant number of primary reactions per unit length. Then, they propagate following their momenta, which is strongly peaked in the forward direction by the Lorentz boost, and they interact with the nucleus in the target volume. In the simulation, all the particles from the ion interaction are generated in the center of the target volume. The obtained target position estimate is, therefore, a mean position of the particle production, instead of a measurement of the real target center.

The Target Finder error depends on the error in the track distance to the target, which is obtained by the propagation of the errors in position and slope delivered by the tracking. We can roughly estimate this error by running the code several times for different track samples and check the results dispersion. The original 50000 events have been divided in ten groups, and a target position estimate is found for each one. The average and the square root of the variance of the position average, in each direction are

$$\begin{aligned}
 \bar{x}_t &= -0.002 & \sigma(\bar{x}_t) &= \sqrt{V(\bar{x}_t)} = 0.077 \\
 \bar{y}_t &= 0.003 & \sigma(\bar{y}_t) &= \sqrt{V(\bar{y}_t)} = 0.052 \\
 \bar{z}_t &= 0.487 & \sigma(\bar{z}_t) &= \sqrt{V(\bar{z}_t)} = 0.062
 \end{aligned} \tag{5.15}$$

for the ten groups, with approximately 13000 tracks contributing to each target position determination. It is expected a reduction of the error as number of measurements increases which, in the simplest case, where the variance of the average can be calculated from the groups distribution and their results were independent, would be of a factor $\sqrt{10}$, giving an error below $25 \mu m$ in all directions for the 50000 simulated events.

The *Hits* employed in this method come from all modules of the same plane in different sectors. Therefore, a known relative position is assumed to convert the track estimate from the module coordinate system to the laboratory coordinate system. It must be noted that this is not the case when the method is applied to real data. It is worthy to mention here that the knowledge of the precise laboratory transformation of the modules is not required; what is required is the relative positioning of the modules. The laboratory system is just used to convert all *Hits* to the same coordinate system, but we could obtain the same results just by converting all the *Hits* to the coordinate system of one of the MDCs. Or, said in another way, the method obtains a target position estimation which is relative to the MDCs position.

The Target Finder method can be used on an individual MDC module or in a set of modules in the same plane. In the first case, the target estimate is easily obtained in the module coordinates, where the straight lines defined by the *Hits* are immediately obtained. When using the Target Finder in a single module, the *Hits* passing close to the target come predominantly from a small solid angle centered slightly below the modules coordinate center. Due to this geometry, the target estimate is less accurate in the coordinate normal to the module plane than in the others. The situation is much better when the Target Finder is used on several modules of the same plane. Then, the straight lines contributing to the minimization comes from a large solid angle region, a full azimuthal band.

5.3 Relative alignment for 2 MDCs

In this section, the mathematical formalism of the relative alignment for two MDCs is presented. First, the procedure is briefly shown, to give an overview of the detailed calculations.

Let us suppose a particle track crossing a pair of MDC modules, let us call generically MDC *A* and MDC *B*, with the result of a *Hit* in each module. From the *Hit* information, the track position (x, y) and incidence angles $(xDir, yDir)$ (see section 5.1), it is possible to obtain a track estimate. When the magnetic field is not present, the track model is a straight line. Then, it is easy to extrapolate the track estimate obtained from the *Hit* in MDC *A*, and find its cross point with a plane in the space, in particular with the middle plane of the MDC *B*, where the *Hit* parameters are defined. To obtain such a cross point, we have to assume a relative transformation to express a point in the coordinate systems of both modules, as shows in section 5.1 (equation 5.3). The comparison between the position of the cross point and the *Hit* in the MDC *B* will inform us about the relative transformation between the modules.

There are two possibilities for the construction of the extrapolation. The *Hit* itself contains enough information to create a straight line. We can also use the coordinates on the MDC middle plane (x, y) contained in the *Hit* and the target position obtained by the Target Finder, as it was shown in the previous section. Actually, the estimate using the target is by far much more precise than the estimation from the *Hit* alone, as will be shown. Independently of the method, we proceed as follows:

1. The *Hit* parameters in MDC *A* are transformed to the MDC *B* coordinate system. This transformation depends only on the rotations and translation between the MDCs coordinate system. In case the

4. From the compatible *Hits* it is possible to select those pairs passing quality criteria or restrictions (for instance, select those pairs in a given position in the module).
5. Finally, the selected *Hit* pairs are used for the relative MDCs alignment. Different algorithms minimize the residuals distribution as a function of the relative transformation between the modules.

Next subsections explain in detail the different steps.

5.3.1 Track estimate transformation and extrapolation

Let us use the simple transformation (equations 5.3 and 5.4) seen in the introduction

$$\vec{X}_B = M \vec{X}_A + \vec{V}$$

where

$$\begin{aligned} M &= (R_B)^{-1} R_A \\ \vec{V} &= (R_B)^{-1} (\vec{T}_A - \vec{T}_B) \end{aligned}$$

are the relative rotation and translation. This relative transformation can be expressed in a minimum set of six parameters (six degrees of freedom). We will adopt the usual convention; the six parameters are the three Euler angles which construct the rotation matrix and the three components of the translation vector.

Let us use the following notation: x^A , y^A , $xDir^A$ and $yDir^A$ are the *Hit* parameters in the module A , while x^B , y^B , $xDir^B$ and $yDir^B$ are those in module B , each parameter expressed in their own module coordinate system. We use x_B^A , y_B^A , $xDir_B^A$ and $yDir_B^A$ to notate the *Hit* parameters in MDC A , but given in the MDC B coordinate system. First, the angular projections are changed into slopes ($S(x)$ and $S(y)$) for both *Hits*, which are equivalent variables, simplifying some expressions

$$\begin{aligned} S(x) &= \frac{a}{c} = \frac{xDir}{\sqrt{1 - (xDir^2 + yDir^2)}} \\ S(y) &= \frac{b}{c} = \frac{yDir}{\sqrt{1 - (xDir^2 + yDir^2)}} \end{aligned} \quad (5.17)$$

where $a = xDir$, $b = yDir$ and c are the components along X_{MDC} , Y_{MDC} and Z_{MDC} of the unit vector following the track direction (see figure 5.7). Now, $S(x)$ and $S(y)$ are the track slope projections, that is, $S(x)$ is the increment in x direction per unit z increment and $S(y)$ the increment in y

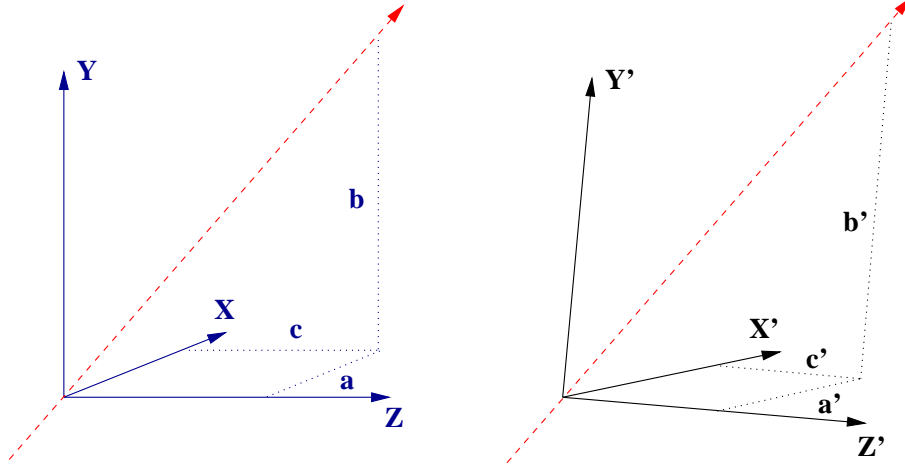


Figure 5.7: Slopes transformation: the same track is represented in two different coordinate systems.

direction per unit z increment. Following the previous notation, $S(x)^A$ is the X projection of the track slope of MDC A *Hit* in their own coordinate system, while $S(x)_B^A$ is the same, but in the MDC B coordinate system. The inverse transformations are

$$xDir = c S(x) = \frac{S(x)}{\sqrt{S(x)^2 + S(y)^2 + 1}} \quad (5.18)$$

$$yDir = c S(y) = \frac{S(y)}{\sqrt{S(x)^2 + S(y)^2 + 1}} \quad (5.19)$$

If the target coordinates $(v^A(x), v^A(y), v^A(z))$ are known in the coordinate system of the MDC A , then the straight line constructed with the MDC A *Hit* coordinates and the target has the slopes

$$S(x)^A = \frac{x^A - v_x^A}{-v_z^A} \quad S(y)^A = \frac{y^A - v_y^A}{-v_z^A} \quad (5.20)$$

To transform the slopes between coordinate systems, it is important to realize that the slope is the ratio of two projections of a unit vector. These unit vector projections, in the new coordinate system, define the new slopes. As it is shown in figure 5.7 we can express

$$S(x)' = \frac{a'}{c'} \quad S(y)' = \frac{b'}{c'} \quad (5.21)$$

being a' and b' the projections in the new system.

Writing the relative rotation matrix as

$$M = \begin{pmatrix} M_{00} & M_{10} & M_{20} \\ M_{01} & M_{11} & M_{21} \\ M_{02} & M_{12} & M_{22} \end{pmatrix}$$

then the transformed slopes are

$$\begin{aligned} S(x)' &= \frac{M_{00} a + M_{10} b + M_{20} c}{M_{02} a + M_{12} b + M_{22} c} = \frac{M_{00} S(x) + M_{10} S(y) + M_{20}}{M_{02} S(x) + M_{12} S(y) + M_{22}} \\ S(y)' &= \frac{M_{01} a + M_{11} b + M_{21} c}{M_{02} a + M_{12} b + M_{22} c} = \frac{M_{01} S(x) + M_{11} S(y) + M_{21}}{M_{02} S(x) + M_{12} S(y) + M_{22}} \end{aligned} \quad (5.22)$$

Therefore, the slopes of the *Hit* reconstructed in MDC A, when they are transformed to the MDC B coordinate system are

$$\begin{aligned} S(x)_B^A &= \frac{M_{00} S(x)^A + M_{10} S(y)^A + M_{20}}{M_{02} S(x)^A + M_{12} S(y)^A + M_{22}} \\ S(y)_B^A &= \frac{M_{01} S(x)^A + M_{11} S(y)^A + M_{21}}{M_{02} S(x)^A + M_{12} S(y)^A + M_{22}} \end{aligned} \quad (5.23)$$

To conclude the first step, the MDC A *Hit* coordinates in the MDC B system are

$$\begin{pmatrix} x_B^A \\ y_B^A \\ z_B^A \end{pmatrix} = \begin{pmatrix} M_{00} & M_{10} & M_{20} \\ M_{01} & M_{11} & M_{21} \\ M_{02} & M_{12} & M_{22} \end{pmatrix} \begin{pmatrix} x^A \\ y^A \\ 0 \end{pmatrix} + \begin{pmatrix} V_0 \\ V_1 \\ V_2 \end{pmatrix} \quad (5.24)$$

where $\vec{V} = (V_0, V_1, V_2)$ is the relative translation vector ($z^A = 0$ because the *Hit* lies in the plane $Z_A = 0$).

The second step comprehends the track extrapolation to the plane $Z_B = 0$ (middle plane of the MDC B). The coordinates of the cross point between the plane and a line passing through (x_B^A, y_B^A, z_B^A) with slope projections $(S(x)_B^A, S(y)_B^A)$, are

$$x_p = x_B^A - S(x)_B^A z_B^A \quad y_p = y_B^A - S(y)_B^A z_B^A \quad (5.25)$$

or, explicitly expressed as a function of the initial MDC A *Hit*,

$$\begin{aligned} x_p &= M_{00} x^A + M_{10} y^A + V_0 \\ &\quad - \frac{M_{00} S(x)^A + M_{10} S(y)^A + M_{20}}{M_{02} S(x)^A + M_{12} S(y)^A + M_{22}} (M_{02} x^A + M_{12} y^A + V_2) \\ y_p &= M_{01} x^A + M_{11} y^A + V_1 \\ &\quad - \frac{M_{01} S(x)^A + M_{11} S(y)^A + M_{21}}{M_{02} S(x)^A + M_{12} S(y)^A + M_{22}} (M_{02} x^A + M_{12} y^A + V_2) \end{aligned} \quad (5.26)$$

Let us now introduce four new variables

$$\begin{aligned}\Delta x &= x^B - x_p & \Delta S(x) &= S(x)^B - S(x)_B^A \\ \Delta y &= y^B - y_p & \Delta S(y) &= S(y)^B - S(y)_B^A\end{aligned}\quad (5.27)$$

describing the differences between the parameters in the MDC *B Hit* and the extrapolation of the *Hit* in MDC *A*. Usually, these variables are called *residuals* in the different *Hit* parameters, and each distribution of these variables for a track selection is called residuals distribution. Δx and Δy are going to be called the position residuals, while $\Delta S(x)$ and $\Delta S(y)$ are angular or slope residuals.

5.3.2 Hit compatibility and sample selection

At the beginning of the section, our working hypothesis was a particle track crossing a pair of MDC modules, with the result of a *Hit* in each one. But, when a set of *Hits* in different modules are reconstructed, the problem is to determine whether a pair of *Hits* corresponds to the same charged particle or not. Those *Hits* which are found to be generated by the same particle are going to be called compatible *Hits*. The study of the *Hit* compatibility will allow us to determine if they belong to the same track and, therefore, can be used in the next alignment steps.

Several approaches can be used to assign *Hit* compatibility. As in the previous section, let us consider a *Hit* in the module *A*, from which a straight line is constructed; the cross point of the extrapolation and the $Z_B = 0$ plane is called (x_p, y_p) (given in the coordinate system of the module *B*). The easiest approach is simply to accept a module *B Hit* if its coordinates are inside a narrow window centered in the point (x_p, y_p) . This is plainly sufficient in case of low multiplicity reactions, where only a track or a pair of tracks crosses each spectrometer sector (for example, Carbon on Carbon). Then, it is enough to impose the condition that one and only one *Hit* is present in a rectangle ($\Delta x < C_x$ and $\Delta y < C_y$, with $2C_x$ and $2C_y$ the rectangle sides) around the position of the extrapolation point (x_p, y_p) , to accept them. This selection loses those *Hit* pairs when two real tracks produce close *Hits* (within $\Delta x < C_x$ and $\Delta y < C_y$) in the module *B*, or when close to a *Hit* produced by a real track in the module *B*, there is an additional *Hit* reconstructed by the tracking software using the impinged wires of the real *Hit* or/and noisy wires. The conservative criterion is to remove from the sample both cases and, therefore, use a sample as clear from ambiguities in the pair identification as possible.

For larger multiplicities and also to perform an additional sample selection, the previous approximation must be improved. A better approach

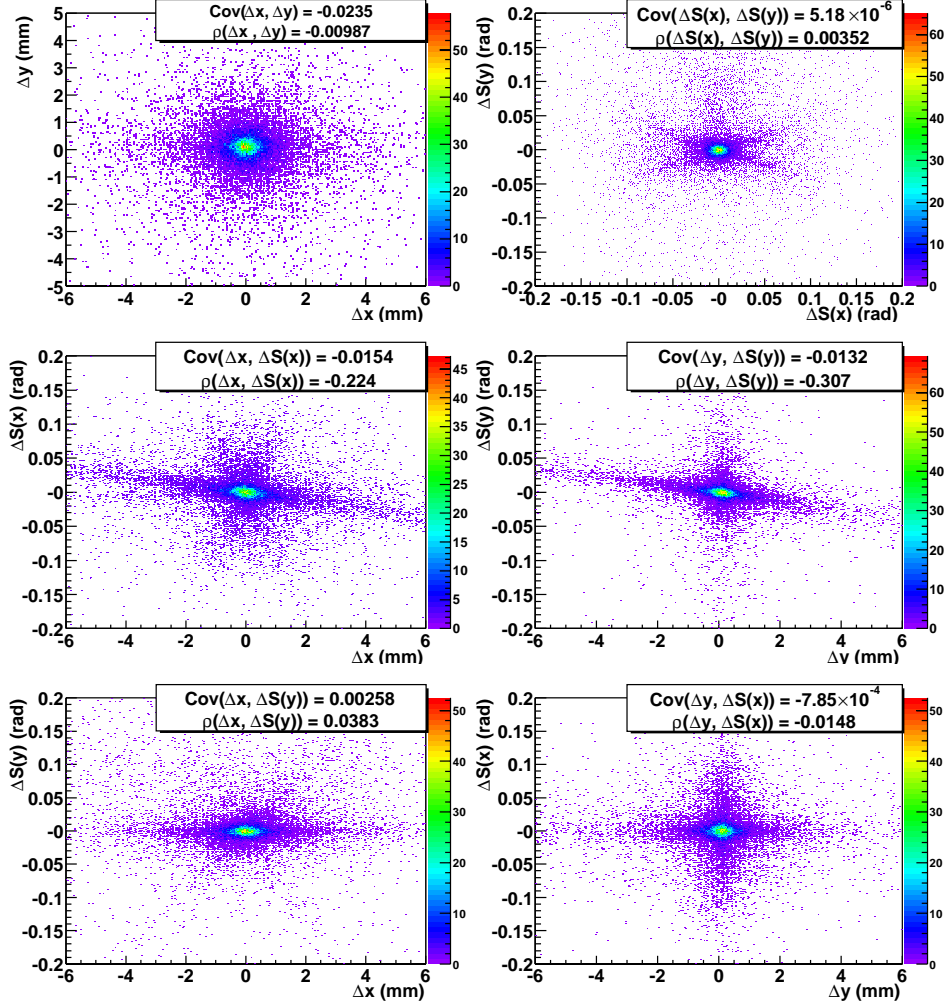


Figure 5.8: Correlation between the residuals after the projection of plane II track estimates in plane I.

would correspond to that used in the tracker software [1], for the matching of *Hits* in different modules. Then, it is possible to approximate the distribution of the four variables in equation 5.27 by a normal 4-dimensional probability distribution [2]. Calling the four-dimensional vector of the four variables $\vec{X} = (\Delta x, \Delta y, \Delta S(x), \Delta S(y))$ with means $\vec{\mu}$ and covariance matrix V , then the probability density function becomes

$$f(\vec{X}) = \frac{1}{(2\pi)^2 \sqrt{|V|}} \exp\left\{-\frac{1}{2}(\vec{X} - \vec{\mu})^T V^{-1} (\vec{X} - \vec{\mu})\right\} \quad (5.28)$$

where the covariance matrix V is

$$\begin{pmatrix} \sigma_{\Delta x}^2 & \rho_{xy}\sigma_{\Delta x}\sigma_{\Delta y} & \rho_{xS_x}\sigma_{\Delta x}\sigma_{\Delta S(x)} & \rho_{xS_y}\sigma_{\Delta x}\sigma_{\Delta S(y)} \\ \rho_{xy}\sigma_{\Delta x}\sigma_{\Delta y} & \sigma_{\Delta y}^2 & \rho_{yS_x}\sigma_{\Delta y}\sigma_{\Delta S(x)} & \rho_{yS_y}\sigma_{\Delta y}\sigma_{\Delta S(y)} \\ \rho_{xS_x}\sigma_{\Delta x}\sigma_{\Delta S(x)} & \rho_{yS_x}\sigma_{\Delta y}\sigma_{\Delta S(x)} & \sigma_{\Delta S(x)}^2 & \rho_{S_xS_y}\sigma_{\Delta S(x)}\sigma_{\Delta S(y)} \\ \rho_{xS_y}\sigma_{\Delta x}\sigma_{\Delta S(y)} & \rho_{yS_y}\sigma_{\Delta y}\sigma_{\Delta S(y)} & \rho_{S_xS_y}\sigma_{\Delta S(x)}\sigma_{\Delta S(y)} & \sigma_{\Delta S(y)}^2 \end{pmatrix}$$

and the correlation coefficient is defined as

$$\rho_{xy} = \frac{\text{cov}(x, y)}{\sigma_x \sigma_y} \quad (5.29)$$

Such an approximation is interesting due to the simple form of the distribution, which allows us to construct geometrical contours of constant probability density. One interesting property is that a set of variables, each of which is a linear function of a set of normal variables, has itself a many-dimensional normal distribution.

To determine the covariance matrix using a simulation, two-dimensional histograms for all reconstructed pairs were filled. The simulated tracks come from 5×10^4 Carbon on Carbon collisions, propagated, through the spectrometer, and reconstructed inside the drift modules using the Santiago tracking (including slope correction, see appendix D). The result depends on the set of modules A and B , used to construct the variables in equation 5.27. In particular, it was used the set of *Hits* in the modules of plane II and the target position (defined by the Target Finder software) to obtain a track estimate (straight line) which can be extrapolated to the other MDCs. The analysis of the extrapolation on the module of plane I shows that only the $\Delta x - \Delta S(x)$ and the $\Delta y - \Delta S(y)$ distributions are correlated, being the other correlations negligible (see figure 5.8). Then, taking into account only the correlations between both pairs of variables, a 4-dimensional probability distribution can be assumed

$$\begin{aligned} P(\Delta x, \Delta y, \Delta S(x), \Delta S(y)) = \\ \frac{1}{(2\pi)^2 \sqrt{|V|}} \exp \left\{ \frac{-1}{2} \left[\frac{1}{1 - \rho_{xS_x}^2} \left(\frac{\Delta x^2}{\sigma_{\Delta x}^2} + \frac{\Delta S(x)^2}{\sigma_{\Delta S(x)}^2} - 2\Delta x \Delta S(x) \frac{\rho_{xS_x}}{\sigma_{\Delta x} \sigma_{\Delta S(x)}} \right) + \right. \right. \\ \left. \left. \frac{1}{1 - \rho_{yS_y}^2} \left(\frac{\Delta y^2}{\sigma_{\Delta y}^2} + \frac{\Delta S(y)^2}{\sigma_{\Delta S(y)}^2} - 2\Delta y \Delta S(y) \frac{\rho_{yS_y}}{\sigma_{\Delta y} \sigma_{\Delta S(y)}} \right) \right] \right\} \end{aligned} \quad (5.30)$$

being ρ_{xS_x} and ρ_{yS_y} the correlation coefficients between $\Delta x - \Delta S(x)$ and $\Delta y - \Delta S(y)$, respectively. From this probability distribution it is possible

to construct equiprobability surfaces (hyperellipsoids)

$$\begin{aligned} & \frac{1}{1 - \rho_{xS_x}^2} \left(\frac{\Delta x^2}{\sigma_{\Delta x}^2} + \frac{\Delta S(x)^2}{\sigma_{\Delta S(x)}^2} - 2\Delta x \Delta S(x) \frac{\rho_{xS_x}^2}{\sigma_{\Delta x} \sigma_{\Delta S(x)}} \right) + \\ & \frac{1}{1 - \rho_{yS_y}^2} \left(\frac{\Delta y^2}{\sigma_{\Delta y}^2} + \frac{\Delta S(y)^2}{\sigma_{\Delta S(y)}^2} - 2\Delta y \Delta S(y) \frac{\rho_{yS_y}^2}{\sigma_{\Delta y} \sigma_{\Delta S(y)}} \right) = \alpha^4 \end{aligned} \quad (5.31)$$

where α is a real number and the exponent refers to the number of dimensions. Here α plays the same role than the standard deviation plays in a one-dimensional normal distribution. Two *Hits* can be considered to belong to the same track segment when the set of values of the variables 5.27, constructed by the *Hits*, fall inside the surface delimited by the contour, for a given α value.

Regarding the pair compatibility, the election of the constant α could be only relevant in those high multiplicity collisions, where the number of particles crossing the module is large enough to reduce significantly the sample if a large α constant is used; remember that a combination is accepted if there is one and only one *Hit* from which the residuals lies inside the equiprobability surface 5.31. In our application, the cut in the equiprobability surface is going to be used not only to check the compatibility between *Hits*, but mainly for the selection of a reduced sample of *Hit* pairs. When the target position is being used to obtain the track estimate, the aim of the procedure is to feed the alignment algorithms with a sample of *Hits* from tracks that are really coming from the target and, therefore, eliminate the large number of *Hit* pairs generated by tracks coming from secondary vertex, which produces extended tails on the residuals distributions.

The meaning of the selection changes if the *Hit* angular information is employed to obtain a track estimate from which one can extrapolate the cross point in the other modules, instead of the target position. Then, the cut in the 4-dimensional probability distribution implies a selection on those *Hits* in the initial module, the one from where the track is estimated, with the best estimate of the angular parameters.

The complex *Hit* selection is performed in individual steps. First, the histograms showing the distributions of the four new variables for all the *Hits* are plotted to observe the distributions shape. Secondly, the histograms are fitted to several functions and the better fit selected. Then, the parameters of the fit are used to construct a 4-dimensional normal probability distribution. Finally, the *Hits* combination is selected if it is contained inside a suitable equiprobability surfaces.

The residuals distributions are shown in figures 5.9 and 5.10 for the extrapolation of the module II track estimate to module III. The golden histograms in 5.9 and 5.10, display all possible combination of a pair of *Hits* (there is a previous simple geometrical cut with a large window). The detailed shape of the histograms depends on several variables, but some general features are common: there is a pronounced peak mainly composed of those *Hit* combinations coming from tracks originated in the target region, and a complex background made of *Hits* from other tracks. The background is already present in the simple simulation shown in the figures, due to the secondary particles generated mainly by the matter in the downstream direction. The study of the real data in the next chapter, shows that the background is larger than in the simulation and present a different structure (for instance, peaks due to strong secondary targets). Then, one should fit the target contribution and the background carefully, to get rid of those background combinations more efficiently.

Figure 5.9 shows the fit of the residuals to several functions which prove to approximate the main features of the residuals distribution, both the peak and the background. The simple gaussian fit is used to obtain initial values for the parameters. The background can be approximated by a polynomial. A second order polynomial has been proven to fit better the background of the real data studied in the next chapter. For simulation, the best results are obtained using a double gaussian, with the thinner one fitting the peak zone and the wider the background, and the Breit-Wigner functions².

When the relative position of the modules is not known a priori, the 4-dimensional equiprobability surface is just a reasonable cut that one can construct, without state anything about the probability of finding a *Hit* inside the surface. Let us suppose a large misalignment between the modules: then, the four distributions centered in their mean values can be skew (do

²The Breit-Wigner or Cauchy distribution is given by

$$P(x) = \frac{1}{2\pi} \frac{\Gamma}{(x - x_0)^2 + (\Gamma/2)^2} \quad (5.32)$$

where Γ is the full width at half maximum and x_0 the position of the distribution maximum, and have no mean and infinite variance if it is not truncated. The total resolution function (see the definition in section 4.8) takes this functional form when the measurement resolution is gaussian, but the variance σ^2 is not the same for all the measurements, distributed accordingly to the expression [2],

$$q(\sigma) = \frac{2}{\sqrt{2\pi} \Gamma \sigma^2} \exp\left(-\frac{1}{2 \Gamma^2 \sigma^2}\right) \quad (5.33)$$

which presents a sharp cut-off for small values of σ and goes to zero as $1/\sigma^2$.

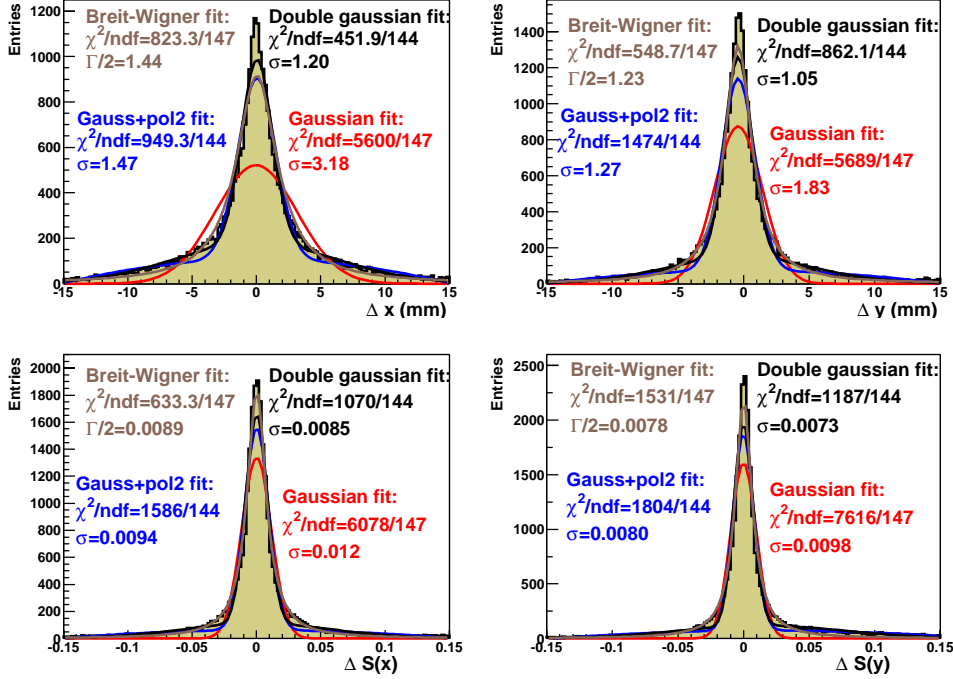


Figure 5.9: Fits to the residuals distribution for 50000 C+C simulated events (pure drift times and tracking using slope correction). The residuals correspond to the extrapolation of module II Hits on module III.

not have to be symmetrical), even if we consider only those *Hits* generated from tracks coming from the target. It is impossible to assign a priori a functional form to the residual distributions without the knowledge of the relative modules position. Figure 5.10 shows the distributions obtained in the same conditions than figure 5.9, but introducing a relative misalignment between the modules (in particular $\Delta V_1 = -2.6$, $\Delta V_2 = -2.194$, $\Delta V_3 = -3.0$ all in *mm* and $\Delta\phi = -0.0132$, $\Delta\theta = 0.0033$ and $\Delta\psi = 0.0052$ measured in *rad*, using the notation of equation 5.3 and followings).

The function which returns the smaller ratio between the χ^2 and the number of degrees of freedom, is used to estimate the peak width. If the Breit-Wigner function is used, the parameter Γ represents the distribution full width at half maximum (FWHM), and it is divided by a factor 2.355 to compare with the gaussian standard deviation σ . The fitting and function selection is made automatically in the alignment code, but it is important to check the residuals distributions and the cuts performed, mainly by two reasons: first, the misalignment can be larger than expected and the

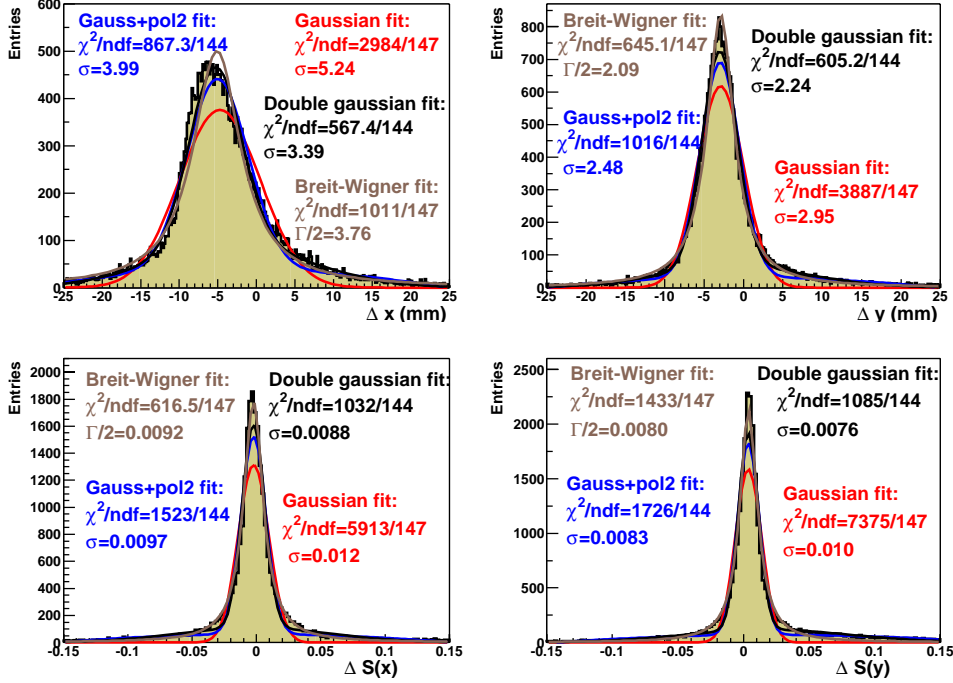


Figure 5.10: Fits to the residuals distribution for 50000 C+C simulated events (pure drift times and tracking using slope correction). The residuals correspond to the extrapolation of module II Hits on module III after a simulated misalignment (see the text).

residuals distributions can be cut by the initial selection window. Secondly, the fit range should be selected after the residuals observation, in order to improve the fit results.

The variances of the gaussian fits to the distribution peaks (or $\Gamma/2.355$ if the Breit-Wigner function is used) have been used to construct the normal 4-dimensional probability distribution. The next point is the construction of suitable equiprobability surfaces and the selection of those combinations inside the surface. The value of the parameter α should be selected to reject the larger amount of tracks that do not come from the target, while accepting those coming from the target region. The efficiency in the rejection depends on the characteristics of the production of secondary particles in the spectrometer matter around the target. The table 5.2 contains the number of accepted *Hit* combinations for several values of the cut parameter α . If the distribution of the residuals would correspond to a normal 4-dimensional distribution, the parameter α would

α	P	II→I	1%	2%	II→III	1%	2%	II→IV	1%	2%
		27795			27459			26286		
5.0	~100	24977	90.0		23611	86.0		23192	88.2	
3.0	~100	20461	73.6		18814	68.5		18751	71.3	
2.0	99.70	14568	52.4	100	13071	47.6	100	12753	48.5	100
1.6	87.60	10750	38.7	73.8	9756	35.5	74.6	9416	35.8	73.8
1.3	41.78	6033	21.7	41.4	5996	21.8	45.9	5785	22.0	45.4
1.0	9.02	1988	7.15	13.6	2682	9.76	20.5	2589	9.85	20.3

Table 5.2: Accepted Hit combinations for different α (cut in the equiprobability surface). The first two columns show the α value and the probability P of the four variables to lie inside the surface. The number of selected Hit combinations is then shown for the projections of the Hits of module II on the other modules. The percentages with respect to the total number of combinations without cuts (1%), and with respect to the cut with probability 99.7% or $\alpha = 2.0$ (2%) are also included.

represent the approximate role of the standard deviation in one dimension. The probability that the four variables corresponding to a set of normal random variables lies inside the ellipsoid characterized by a given value α^n is given by the integral of the probability density function of the χ^2 distribution $f(z; n)$ [3]

$$\int_0^{\alpha^n} f(z; n) dz \quad (5.34)$$

The second column of table 5.2 contains this probability for $n = 4$ and for each α used in the selection. The number of selected Hits for a given α value is also quoted in the table, separately for those combinations obtained by the extrapolation of the Hits of module II to the other modules. A reduction of approximately a 50% in the number of accepted combinations is observed introducing a cut with $\alpha = 2$, which would contain almost all the combinations if the residuals would follow a pure normal 4-dimensional distribution. Taken into account that the normal 4-dimensional distribution is defined using the variances σ^2 from the gaussian part ($\Gamma/2.355$ if the Breit-Wigner function is used) of the fits shown in figure 5.9, (where only the main peak contributes to the gaussian part of the fit), the combinations removed from the sample correspond mainly to the tails in each distribution.

From the observation of table 5.2, it results apparent that the individual residuals distribution are not gaussian; they are thinner, having more combinations close to the mean value than a gaussian distribution (see, for

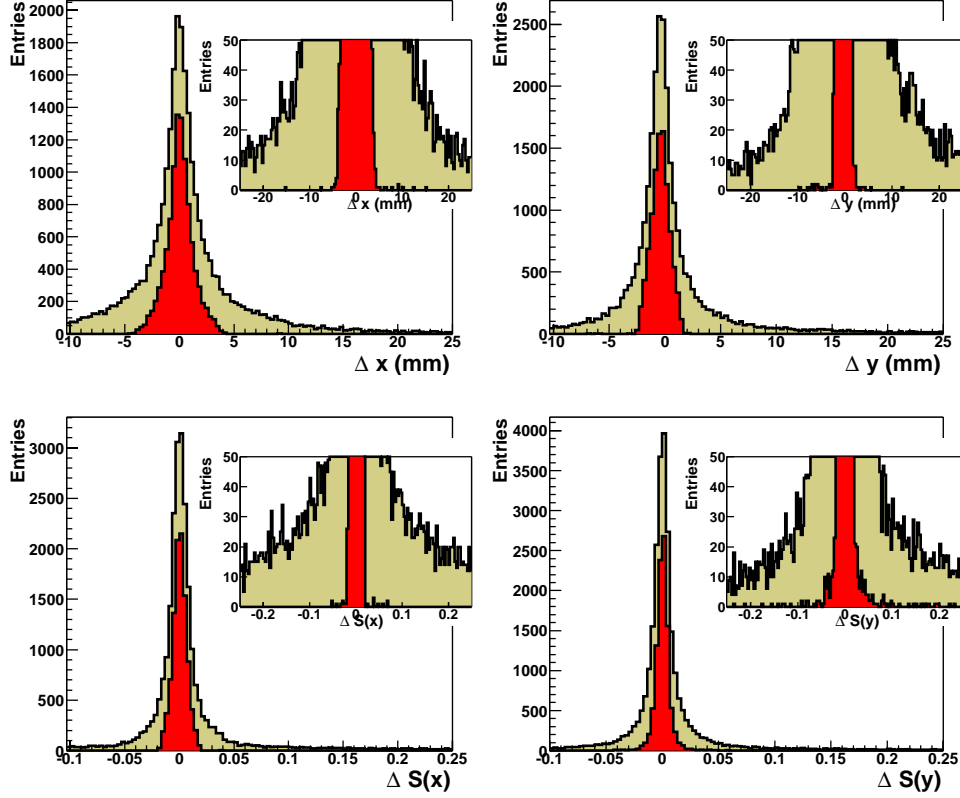


Figure 5.11: Complete (gold) and selected sample (red) residuals distribution for 50000 $C+C$ simulated events (pure drift times and tracking using slope correction). The residuals correspond to the extrapolation of module II Hits on module III, and the selection parameter is $\alpha = 1.64$ (90%).

instance, the peaks in figure 5.9). The residuals 4-dimensional distribution contains also more combinations close to the mean value in the four variables than the normal 4-dimensional distribution. The table 5.2 shows the percentage of accepted *Hit* combinations from both the total number of combinations ($_1\%$) or the number of combinations after a cut ($_2\%$) with $\alpha = 2$ (which should contain a 99.7% of the combinations, in case of a normal 4-dimensional distribution). The percentage of accepted combinations with respect to the $\alpha = 2$ cut ($_2\%$) is larger than the probability of the normal distribution for small α (namely $\alpha = 1$), and vice versa (for instance, $\alpha = 1.6$).

After the selection, both samples of *Hit* pairs are stored for further

elaboration. In the figure 5.11, the complete set of pairs (again inside a previous large window) and the reduced sample using a value $\alpha = 1.64$ is shown, for the C+C simulation already commented in this section.

5.3.3 Minimization procedures

Once a sample of *Hit* pairs generated in the modules has been selected, it can be used to obtain the relative position of the modules. The parameters we are trying to find out are the six numbers which describe the relative position of the MDC coordinate systems. As stated previously, the six parameters correspond to the Euler angles (ϕ, θ, ψ) which determine the Euler rotation matrix and the three components of the translation vector (V_0, V_1, V_2) between the coordinate system centers.

The least squares method is a general procedure for parameter estimation. Consider a set of observations $a_i = a_1, a_2, \dots, a_N$ from a distribution with mean value $E(a_i, \vec{p})$ and covariance matrix C . The vector \vec{p} represents the unknown parameters, while $E(A_i, \vec{p})$ and $C(\vec{p})$ are known functions of \vec{p} . The estimates of the parameters p_k are those values \hat{p}_k which minimize the covariant form

$$Q^2 = \sum_i \sum_j \left\{ [a_i - E(a_i, \vec{p})] (C^{-1})_{ij} [a_j - E(a_j, \vec{p})] \right\} \quad (5.35)$$

The least squares estimator is consistent (the estimate converges toward the true value of the parameter when the number of observations increases) and unbiased (the mean value of the distribution of the parameter estimations coincides with the real parameter value) [2]. The method is often called chi-square method, because the covariant form takes a chi-square distribution $\chi^2(N)$ with N degrees of freedom if the terms X_i in the form

$$Q^2 = \sum_i X_i \quad (5.36)$$

are independent, standard normal variables.

The direct application of the theory to our problem leads to the minimization of the expression

$$\sum_{Tracks} \begin{pmatrix} \Delta x \\ \Delta y \\ \Delta S(x) \\ \Delta S(y) \end{pmatrix} (C)^{-1} \begin{pmatrix} \Delta x \\ \Delta y \\ \Delta S(x) \\ \Delta S(y) \end{pmatrix}$$

for the six alignment parameters, where

$$C = \begin{pmatrix} \sigma_{\Delta x}^2 & \sigma_{\Delta x \Delta y} & \sigma_{\Delta x \Delta S(x)} & \sigma_{\Delta x \Delta S(y)} \\ \sigma_{\Delta y \Delta x} & \sigma_{\Delta y}^2 & \sigma_{\Delta y \Delta S(x)} & \sigma_{\Delta y \Delta S(y)} \\ \sigma_{\Delta S(x) \Delta x} & \sigma_{\Delta S(x) \Delta y} & \sigma_{\Delta S(x)}^2 & \sigma_{\Delta S(x) \Delta S(y)} \\ \sigma_{\Delta S(y) \Delta x} & \sigma_{\Delta S(y) \Delta y} & \sigma_{\Delta S(y) \Delta S(x)} & \sigma_{\Delta S(y)}^2 \end{pmatrix}$$

is the covariance matrix between the four variables.

It is possible to approximate the covariance matrix elements by writing in the diagonal the sigma of the residuals, and in the non-diagonal terms the correlations between the residual distributions obtained from the simulation (according to 5.29). The correlation terms are negligible for all the pairs of variables but $\Delta x - \Delta S(x)$ and $\Delta y - \Delta S(y)$ as stated before in section 5.3.2. The reduced covariance matrix takes the form

$$\begin{pmatrix} \sigma_{\Delta x}^2 & 0 & \rho_{xS(x)} \sigma_{\Delta x} \sigma_{\Delta S(x)} & \rho_{xS(y)} \sigma_{\Delta x} \sigma_{\Delta S(y)} \\ 0 & \sigma_{\Delta y}^2 & 0 & \rho_{yS(y)} \sigma_{\Delta y} \sigma_{\Delta S(y)} \\ \rho_{xS(x)} \sigma_{\Delta x} \sigma_{\Delta S(x)} & 0 & \sigma_{\Delta S(x)}^2 & 0 \\ \rho_{xS(y)} \sigma_{\Delta x} \sigma_{\Delta S(y)} & \rho_{yS(y)} \sigma_{\Delta y} \sigma_{\Delta S(y)} & 0 & \sigma_{\Delta S(y)}^2 \end{pmatrix}$$

Then, the function we have to minimize is

$$Q^2 = \sum_{Tracks} \left\{ \frac{1}{W_x} [\Delta x]^2 + \frac{1}{W_y} [\Delta y]^2 + \frac{1}{W_{S(x)}} [\Delta S(x)]^2 + \frac{1}{W_{S(y)}} [\Delta S(y)]^2 + \frac{2}{W_{xS(x)}} [\Delta x \Delta S(x)] + \frac{2}{W_{yS(y)}} [\Delta y \Delta S(y)] + \frac{2}{W_{xS(y)}} [\Delta x \Delta S(y)] \right\} \quad (5.37)$$

where

$$W = \begin{pmatrix} W_x^{-1} & 0 & W_{xS(x)}^{-1} & W_{xS(y)}^{-1} \\ 0 & W_y^{-1} & 0 & W_{yS(y)}^{-1} \\ W_{xS(x)}^{-1} & 0 & W_{S(x)}^{-1} & 0 \\ W_{xS(y)}^{-1} & W_{yS(y)}^{-1} & 0 & W_{S(y)}^{-1} \end{pmatrix}$$

is the inverse of the reduced covariance matrix. The dependence of the covariant form on the alignment parameters is apparent when the complete expression of the residual variables is shown

$$\Delta x = x^B - x_p = x^B - \left[M_{00} x^A + M_{10} y^A + V_0 - \frac{M_{00} S(x)^A + M_{10} S(y)^A + M_{20}}{M_{02} S(x)^A + M_{12} S(y)^A + M_{22}} (M_{02} x^A + M_{12} y^A + V_2) \right]$$

$$\begin{aligned}
\Delta y = y^B - y_p &= y^B - \left[M_{01} x^A + M_{11} y^A + V_1 \right. \\
&\quad \left. - \frac{M_{01} S(x)^A + M_{11} S(y)^A + M_{21}}{M_{02} S(x)^A + M_{12} S(y)^A + M_{22}} (M_{02} x^A + M_{12} y^A + V_2) \right] \\
\Delta S(x) &= S(x)^B - S(x)_B^A = S(x)^B - \frac{M_{00} S(x)^A + M_{10} S(y)^A + M_{20}}{M_{02} S(x)^A + M_{12} S(y)^A + M_{22}} \\
\Delta S(y) &= S(y)^B - S(y)_B^A = S(y)^B - \frac{M_{01} S(x)^A + M_{11} S(y)^A + M_{21}}{M_{02} S(x)^A + M_{12} S(y)^A + M_{22}}
\end{aligned} \tag{5.39}$$

where M_{ij} are the elements of the Euler matrix (equation 5.4) with angles ϕ , θ and ψ , and V_i are the components of the relative translation vector.

The parameters which minimize the function 5.37 cannot be found analytically. To solve the problem, the function can be introduced in a standard general purpose package for minimization, as it is MINUIT [4]. This package contains several standard approaches to the minimization of multiparametric forms. Unfortunately, the direct introduction of the function 5.37 in MINUIT does not return correct results, as was studied in the simulations. The numerical inaccuracies of the small terms in the fractions have been pointed as the probable cause of the misbehavior.

Therefore, several approximations to the solution of the minimization of the function 5.37 with respect to the relative alignment parameters has been developed.

5.3.4 Realistic approximations to the minimization

The approximation to the actual relative alignment parameters between the MDCs can be performed using a decomposition of the large minimization function in independent parts. This kind of approach is widely used in complex problems where the large number of parameters makes difficult the minimization.

It is easy to realize that the slope transformation (equation 5.23), and therefore the residuals $\Delta S(x)$ and $\Delta S(y)$, do not depend on any relative translation between MDCs. They only depend on the relative rotation matrix, that is, on the Euler angles which describe the relative rotation between MDCs. Then, we can obtain independently those angles, minimizing the function

$$Q^2 = \sum_{Tracks} \left\{ \frac{1}{W_{S(x)}} [\Delta S(x)]^2 + \frac{1}{W_{S(y)}} [\Delta S(y)]^2 \right\} \tag{5.40}$$

where now $W_{S(x)}$ and $W_{S(y)}$ are the inverses of the transformed slopes variances (again, we use that the correlation between the angular variables is negligible). They can be directly calculated from the variances of the distributions $\Delta S(x)$ and $\Delta S(y)$ in simulations. The parameters which minimize the function 5.40 cannot be found analytically, and their minimization presents the same problems than the general case seen in the previous section.

Let us suppose that we know the relative angles between the modules and therefore the relative rotation matrix and the terms M_{ij} in the expression of the residual variables. Then, let us take them as constants and reduce the search to the parameters of the relative translation between the MDC coordinate systems. The problem reduces to the minimization of the function 5.37 where now all the parameters in expressions 5.39 are constants but the $\vec{V} = (V_0, V_1, V_2)$ vector components. This work can be made analytically; at the minimum, derivatives of $Q^2 = Q^2(V_0, V_1, V_2)$ with respect to V_0, V_1 and V_2 vanish

$$\begin{aligned} \frac{\partial Q^2}{\partial V_0} &= \sum_i \left\{ \frac{-2 \Delta x_i}{W_x} - \frac{2 \Delta S(x)_i}{W_{xS(x)}} - \frac{2 \Delta S(y)_i}{W_{xS(y)}} \right\} = 0 \\ \frac{\partial Q^2}{\partial V_1} &= \sum_i \left\{ \frac{-2 \Delta y_i}{W_y} - \frac{2 \Delta S(y)_i}{W_{yS(y)}} \right\} = 0 \\ \frac{\partial Q^2}{\partial V_2} &= \sum_i \left\{ \frac{2 \Delta x_i \theta_i^x}{W_x} + \frac{2 \Delta y_i \theta_i^y}{W_y} \right. \\ &\quad \left. + \frac{2 \Delta S(x)_i \theta_i^x}{W_{xS(x)}} + \frac{2 \Delta S(y)_i \theta_i^y}{W_{yS(y)}} + \frac{2 \Delta S(y)_i \theta_i^x}{W_{xS(y)}} \right\} = 0 \end{aligned} \quad (5.41)$$

where we short the notation using

$$\begin{aligned} \theta_i^x &= S(x)_B^A = \frac{M_{00} S(x)^A + M_{10} S(y)^A + M_{20}}{M_{02} S(x)^A + M_{12} S(y)^A + M_{22}} \\ \theta_i^y &= S(y)_B^A = \frac{M_{01} S(x)^A + M_{11} S(y)^A + M_{21}}{M_{02} S(x)^A + M_{12} S(y)^A + M_{22}} \end{aligned} \quad (5.42)$$

and where the index i runs over all the pair of compatible *Hits* in the sample. Using the variables

$$\begin{aligned} \Delta x_i^* &= \Delta x_i + V_0 - \theta_i^x V_2 + \frac{W_x}{W_{xSx}} \Delta S(x)_i + \frac{W_x}{W_{xSy}} \Delta S(y)_i \\ \Delta y_i^* &= \Delta y_i + V_1 - \theta_i^y V_2 + \frac{W_y}{W_{ySy}} \Delta S(y)_i \end{aligned} \quad (5.43)$$

then, the linear system in the three parameters results apparent

$$\begin{aligned}
\sum_i \left\{ \frac{1}{W_x} (V_0 - \theta_i^x V_2 - \Delta x_i^*) \right\} &= 0 \\
\sum_i \left\{ \frac{1}{W_y} (V_1 - \theta_i^y V_2 - \Delta y_i^*) \right\} &= 0 \\
\sum_i \left\{ \frac{\theta_i^x}{W_x} \Delta x_i^* + \frac{\theta_i^y}{W_y} \Delta y_i^* + \left(\frac{(\theta_i^x)^2}{W_x} + \frac{(\theta_i^y)^2}{W_y} \right) V_2 - \frac{\theta_i^x}{W_x} V_0 - \frac{\theta_i^y}{W_y} V_1 \right\} &= 0
\end{aligned} \tag{5.44}$$

Using the Cramer formulation, the following three equations return the translation vector $\vec{V} = (V_0, V_1, V_2)$ in the relative transformation (equation 5.3) between points in the MDCs

$$V_0 = \frac{D_a}{D} \quad V_1 = \frac{D_b}{D} \quad V_2 = \frac{D_c}{D} \tag{5.45}$$

where D is the determinant

$$D = \begin{vmatrix} \sum_i \frac{1}{W_x} & 0 & -\sum_i \frac{\theta_i^x}{W_x} \\ 0 & \sum_i \frac{1}{W_y} & -\sum_i \frac{\theta_i^y}{W_y} \\ -\sum_i \frac{\theta_i^x}{W_x} & -\sum_i \frac{\theta_i^y}{W_y} & \sum_i \left\{ \frac{(\theta_i^x)^2}{W_x} + \frac{(\theta_i^y)^2}{W_y} \right\} \end{vmatrix}$$

and

$$\begin{aligned}
D_a &= \begin{vmatrix} \sum_i \frac{\Delta x_i^*}{W_x} & 0 & -\sum_i \frac{\theta_i^x}{W_x} \\ \sum_i \frac{\Delta y_i^*}{W_y} & \sum_i \frac{1}{W_y} & -\sum_i \frac{\theta_i^y}{W_y} \\ -\sum_i \left\{ \frac{\theta_i^x \Delta x_i^*}{W_x} + \frac{\theta_i^y \Delta y_i^*}{W_y} \right\} & -\sum_i \frac{\theta_i^y}{W_y} & \sum_i \left\{ \frac{(\theta_i^x)^2}{W_x} + \frac{(\theta_i^y)^2}{W_y} \right\} \end{vmatrix} \\
D_b &= \begin{vmatrix} \sum_i \frac{1}{W_x} & \sum_i \frac{\Delta x_i^*}{W_x} & -\sum_i \frac{\theta_i^x}{W_x} \\ 0 & \sum_i \frac{\Delta y_i^*}{W_y} & -\sum_i \frac{\theta_i^y}{W_y} \\ -\sum_i \frac{\theta_i^x}{W_x} & -\sum_i \left\{ \frac{\theta_i^x \Delta x_i^*}{W_x} + \frac{\theta_i^y \Delta y_i^*}{W_y} \right\} & \sum_i \left\{ \frac{(\theta_i^x)^2}{W_x} + \frac{(\theta_i^y)^2}{W_y} \right\} \end{vmatrix} \\
D_c &= \begin{vmatrix} \sum_i \frac{1}{W_x} & 0 & \sum_i \frac{\Delta x_i^*}{W_x} \\ 0 & \sum_i \frac{1}{W_y} & \sum_i \frac{\Delta y_i^*}{W_y} \\ -\sum_i \frac{\theta_i^x}{W_x} & -\sum_i \frac{\theta_i^y}{W_y} & -\sum_i \left\{ \frac{\theta_i^x \Delta x_i^*}{W_x} + \frac{\theta_i^y \Delta y_i^*}{W_y} \right\} \end{vmatrix}
\end{aligned} \tag{5.46}$$

The least square estimate is consistent: the estimate converge toward the true value of the parameters as the number of observations increases.

Due to the sample selection scheme, seen in section 5.3.2, the method should be used iteratively; the residuals distributions obtained from the initial parameters can be largely distorted and cut. The estimates returned by the minimization, closer to the true values, are used in the calculation of new residuals as an input for a new sample selection. This is mainly necessary when the initial alignment parameters (our best initial estimates) are far from the true parameters. The iterative method stops when the parameters obtained in two consecutive iterations differ in less than a fixed quantity.

To check the results, let us simulate a misalignment in the relative transformation between two modules. The parameters introduced in the calculations of the residuals (our initial estimates, in a real case) are different from those used in the calculation of the *Hits* in the modules in the HGeant simulation (the true relative parameters). The results shown below correspond to the study of the tracks produced in 10^5 Carbon on Carbon collisions. The tracks produce the *Hits* on the modules, including the gaussian smearing in their coordinates given by the approximate experimental resolution ($\sigma_x = 160 \mu m$ and $\sigma_y = 80 \mu m$). Four different sets of random displacements, gaussian distributed with $\sigma = 10 mm$, has been added to the true values as initial estimates, in the three coordinates, to check the simultaneous convergence of the parameters to their true values. The relative translation between the modules does not match the parameters used during the analysis of the data, and therefore the position residuals distributions are not centered at zero (and also are skewed, see figure 5.13).

The first application of the analytical minimization returns a translation estimate which is a better approximation to the true translation. The iterative application of the minimization to the position residuals distributions obtained after a previous analytical minimization step converge fastly toward the true translation vector. Figure 5.12 shows the results of the minimization after n iterations, for four different initial misalignments. The position of the *Hits* reconstructed in the module II and the target position are used to create the track estimate and extrapolate to the other modules. The picture shows the differences between the translation parameters, resulting after n iterations, and their true value. The minimization converges faster toward the true value for V_0 (along the direction X_{MDC} in the local MDC coordinate system of the modules) and V_1 (direction Y_{MDC}). It also depends on the modules under analysis: the alignment parameters of module I, closer to module II and located between the module and the target, converge faster to the right ones than for the

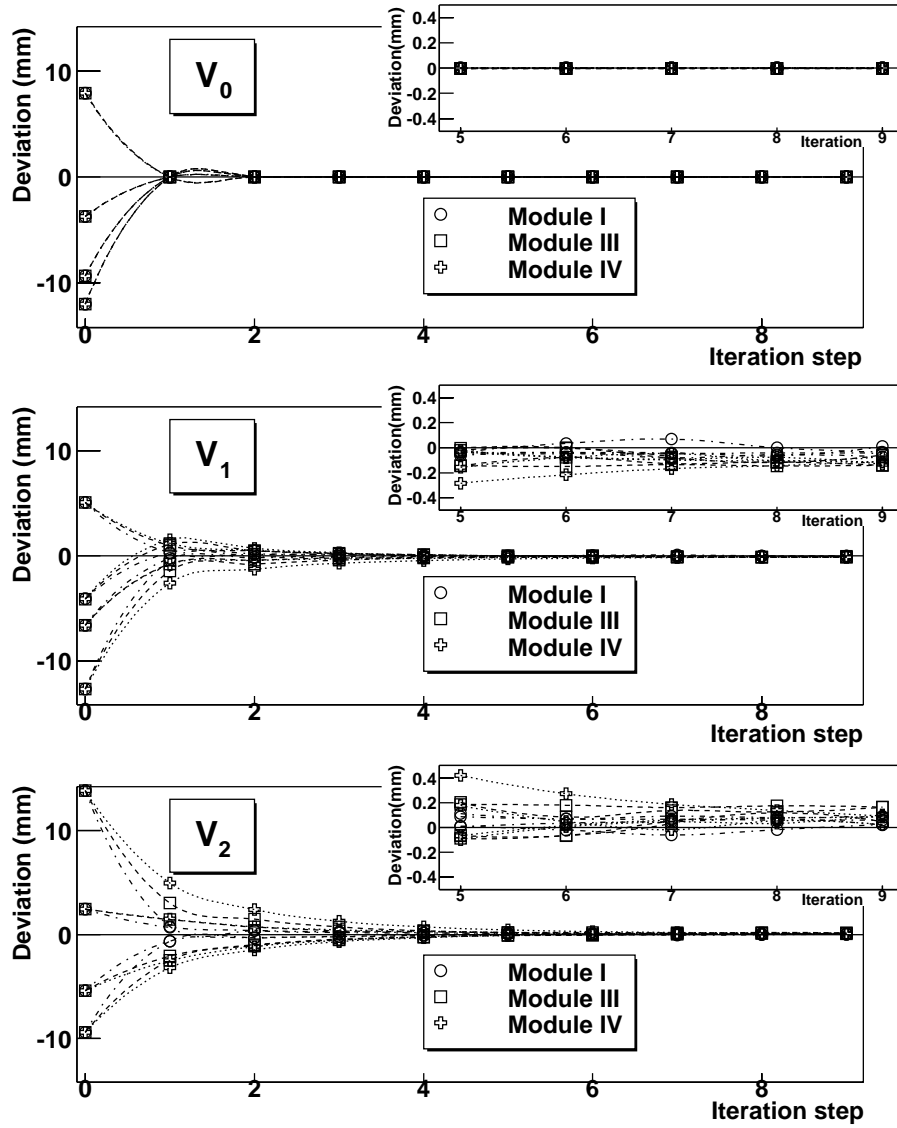


Figure 5.12: Analytical minimization results after several iterations. Four different sets of random gaussian ($\sigma = 10$ mm) numbers have been added to the initial estimates of the modules relative alignment parameters with respect to module II. The plot shows the differences ($\Delta V_0, \Delta V_1, \Delta V_2$), between the real values of the translation vector (V_0, V_1, V_2) and the minimization result after n iterations (initial values for the zero iteration) for each module separately.

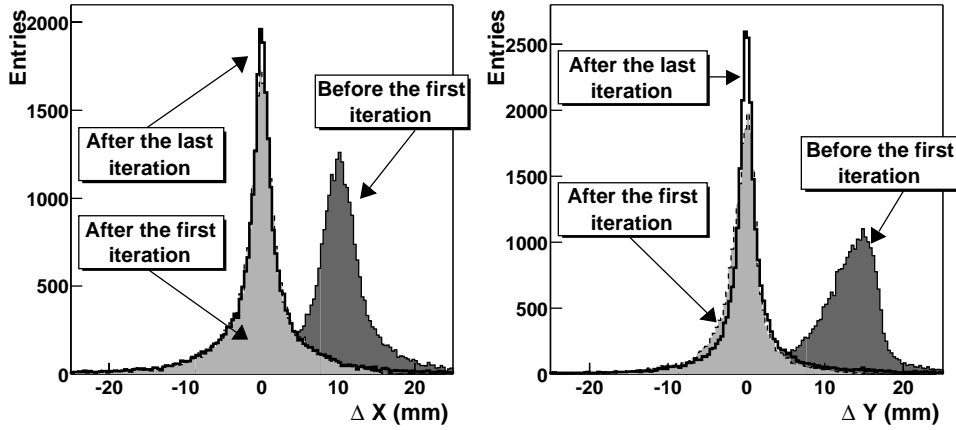


Figure 5.13: Residuals distributions before and after the first iteration and after the complete iterative application of the translation analytical minimization.

other external modules. After the first iteration, in the case of V_0 , the fifth for V_1 , and the seventh for V_2 , the results are stable within $50 \mu m$. The final differences between the minimization outcome and the true values are below $30 \mu m$ for V_0 , $50 \mu m$ for V_1 and $100 \mu m$ for V_2 , for this particular simulation.

5.3.5 Rotations

The analytic minimization presented in the previous section returns the true translation between the modules when the terms of their relative rotation matrix (taken as constants and not as parameters) are correct. In case that the rotation between the modules is not known, the previous method only returns a relative position which minimizes the residuals. An initial value of the relative angles, given by the design values, is normally a good starting point for the calculation of the translation vector between the modules; an additional correction is needed to improve the first estimate.

This section describes a method to improve the estimation of the rotation matrix between the modules. The method is based on the study of the geometrical relations of the residuals in several zones of the module, as a function of the distance to the rotation axis. In this section the corrections in each angle are studied individually and independent of the translations (the translation vector is the correct one along the calculations).

The entry point is an initial approximation to the modules relative ro-

tation, for instance, that given by the design values of the rotation (or any better value obtained by other methods). First, the straight line estimate of the charged particle obtained from each *Hit* in MDC *A* (using the *Hit* parameters or the *Hit* coordinates and the target estimate) is extrapolated and the cross point with the MDC *B* calculated, as shown in section 5.3.1. Following an equivalent notation than in previous sections, the coordinates of the extrapolation cross point in the MDC *B* coordinate system are (x_p, y_p) , while the coordinates of the MDC *B* *Hit* (originated from the same track) are (x^B, y^B) . After a correction on the relative rotation, the coordinates of the extrapolation are (\hat{x}_p, \hat{y}_p) , being the coordinates of the local (MDC *B*) *Hit* unchanged. The correction angle is obtained by requiring the transformation to a new coordinate system where the extrapolated point and the local *Hit* position are identical. To derive the mathematical expressions, let us consider the tracks as perfect straight lines. Then, the extrapolation and the local *Hit* position should coincide for a system perfectly aligned.

In a simple approximation, we are going to divide the problem in three independent rotations around the main MDC axis. First, the rotation around the *Z* axis is studied, and the angle will be notated θ_1 . Then, the other two angles θ_2 and θ_3 are analyzed, representing the rotation around *X* and *Y* axes, and being their mathematical formulation identical. The simulation studies have proved that an iterative determination of the three angles converges to the right values.

Rotation "in plane"

After a rotation of the module coordinate system around the *Z* axis ("in plane rotation") by an angle θ_1 , the coordinates of a point (x, y) are transformed according to

$$\begin{aligned}x' &= x \cos \theta_1 + y \sin \theta_1 \\y' &= -x \sin \theta_1 + y \cos \theta_1\end{aligned}\tag{5.47}$$

where (x', y') are the coordinate of the point (x, y) after the rotation. Let us suppose that this rotation corrects the misalignment. After the rotation applied to the MDC *B*, the points obtained from the extrapolation of the MDC *A* *Hits* transform following equation 5.47, while the local MDC *B* *Hits* does not change (see the right top pad in figure 5.14; by rotating the proper angle the situation in the top left scheme is recovered). Then,

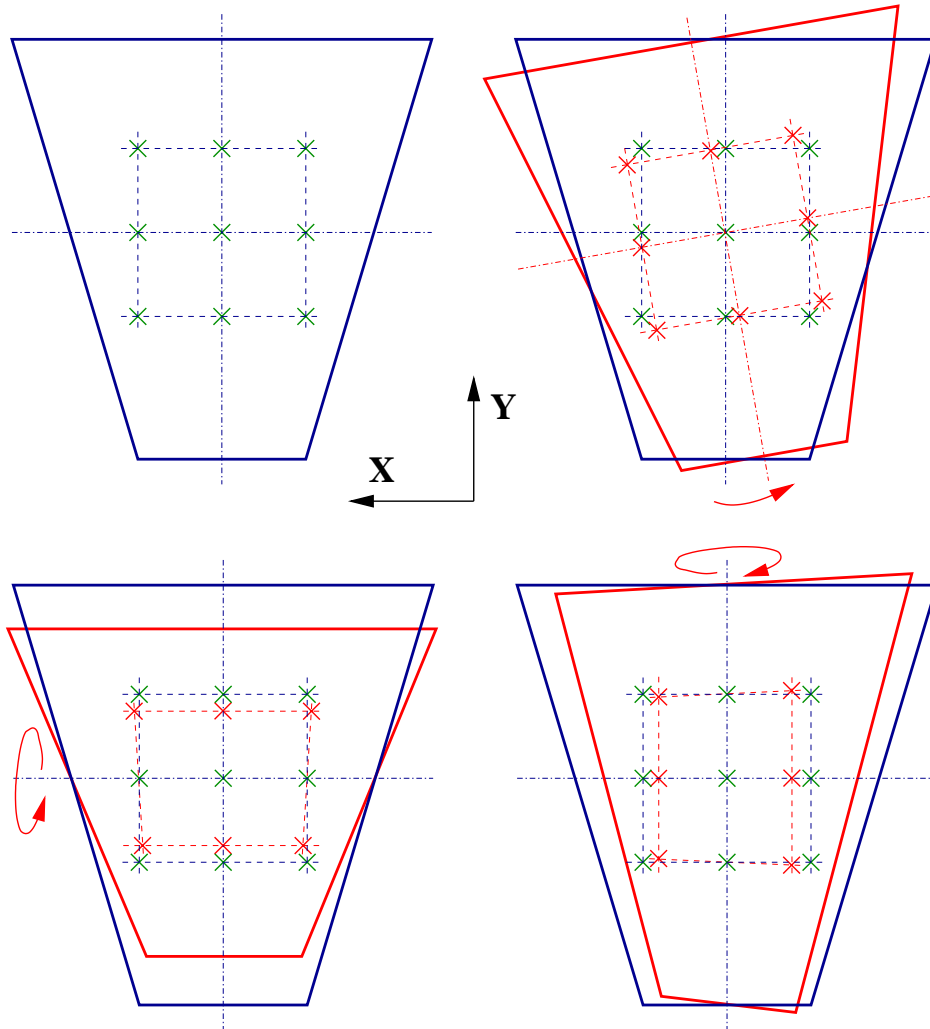


Figure 5.14: Position of the projections and local Hits for nine pairs (or the mean value of a sample in nine zones) after a rotation around the module main axis. In blue, our initial estimation of the module position where the projections are calculated, and in red the real position of the module. The green crosses represent the projection on the module of the track estimate, while the red crosses are the local Hits. **Top left:** ideal position, where the projections and the local Hits positions coincides. **Top right:** module rotated around the local Z axis ("in plane") **Bottom:** rotation "out of plane" (around X and Y in the left and right schemes, respectively). See the text for the definition of the projections from other modules.

equating the coordinates of the MDC B *Hit* to the projections

$$\begin{aligned}x^B &= \hat{x}_p = \cos \theta_1 x_p + \sin \theta_1 y_p \\y^B &= \hat{y}_p = -\sin \theta_1 x_p + \cos \theta_1 y_p\end{aligned}\quad (5.48)$$

By multiplying the first equation by x_p and the second by y_p and adding the results, the cosine of the searched angle is obtained. Also the sine is obtained multiplying the first equation by y_p and the second by x_p and subtracting the results

$$\begin{aligned}\cos \theta_1 &= \frac{x^B x_p + y^B y_p}{x_p^2 + y_p^2} \\ \sin \theta_1 &= \frac{x^B y_p - y^B x_p}{x_p^2 + y_p^2}\end{aligned}\quad (5.49)$$

Rotation "out of plane"

When the correction to a previous estimate of the relative rotation matrix requires a rotation around Y or X axes, the MDC B plane where the extrapolation of the track estimate is calculated changes, and then the cross point between the extrapolated track and the plane should be recalculated.

The two lower pads in figure 5.14 represent a rotation around X and Y axes. By rotating the proper angle, the recalculated projection of the track estimate for the new angle and the local *Hit* coincide. The correct angle can be obtained using a pure geometrical approximation, explained in appendix H. Another solution to the problem is the minimization of the difference between the projection of the track estimate and the local *Hit*. Both the X and Y components of the difference presents a parabolic minimum around the correcting angle. Then, a simple determination of the angle can be obtained by fitting to a second order polynomial the zone of the minimum of the weighted sum of both position residuals. The same procedure could also be applied to "in plane" rotations, but the simplicity of the geometrical solution is preferable in this case. The minimum of the residuals parabolic fit and the calculation of the angle from the geometrical approximation return similar results.

The correction in the relative rotation between modules can be obtained using the complete set of *Hit* pairs (actually the local *Hit* and the estimate of the track from the *Hit* in the other module) returning a value of the angle for each pair. The differences between the angle values for each pair and the real correction depends on the module resolution and on the track scattering between the modules. The distribution of the solutions for each

pair presents a peak centered in the correct value, which is determined using a gaussian fit. An example of the angle determination for an “out of plane” rotation is shown in appendix H.

It is also possible to apply the methods to a set of *Hit* pairs lying in selected zones of the module, defining the zone by requiring the local *Hits* to be close to a point (the center of the zone) of the module. The distribution of the position residuals for the pairs in each zone can be fitted to obtain the mean value of the differences between the projections and the local *Hits*. Then, using the mean values for each zone, it is obtained a reduced set of angle values, as many as zones. In particular, a symmetrical situation of nine points (one in the center and eight in the middle of the sides of a square and in the vertex, as shown in figure 5.14), has been tested. The use of only those pairs with a local *Hit* lying inside a zone reduces the number of pairs contributing to the estimate of the angle correction. The benefits of this approach are the easy interpretation of the graphical output and the possibility to evaluate the rotation of the module considering only defined *Hits* around localized positions. In the first steps of the module features analysis, where the calibration is still far from the expected results, such an approximation has proved to be safe, avoiding the use of *Hits* lying in the extreme of the modules with a large incidence angle.

After the determination of the rotation around each axis, the rotation matrix is corrected before resuming the search of another rotation or a translation determination iteration. For instance, after a rotation θ_2 around the X axis, the new rotation M_{new} between the modules is

$$M_{new} = M * C \quad (5.50)$$

where

$$C = \begin{pmatrix} 1 & 0 & 0 \\ 0 & \cos \theta_2 & \sin \theta_2 \\ 0 & \sin \theta_2 & \cos \theta_2 \end{pmatrix} \quad (5.51)$$

Rotation correction results

The methods for the correction of the module relative rotation has been tested under the same simulation used previously: 10^5 Carbon on Carbon collisions produce the charged particles propagated through one sector of the spectrometer, including their interaction with matter. The tracks are detected by the drift modules, and the position of the constructed *Hits* is (gaussian) smeared according to the approximate experimental resolution ($\sigma_x = 160 \mu m$ and $(\sigma_y = 80 \mu m)$).

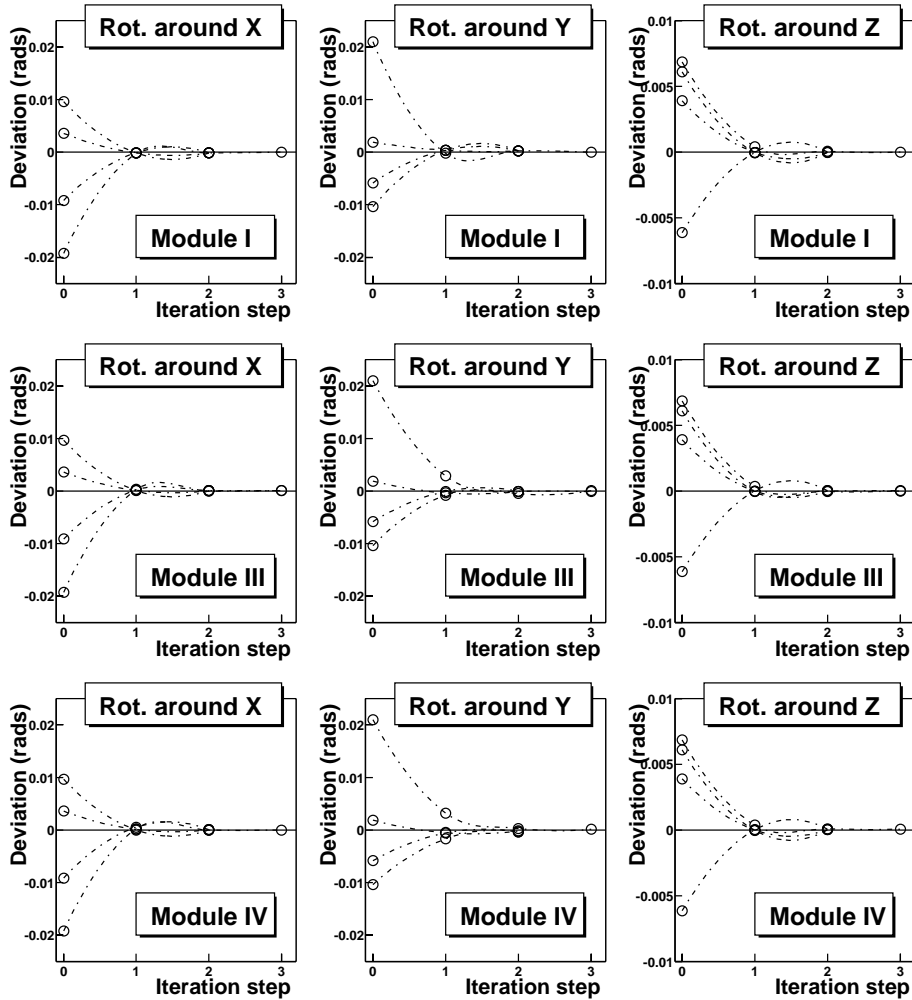


Figure 5.15: Difference between the rotation angles (around the main axis) in the relative transformation between module II and any other module. The plots show the differences after 3 iterations (initial differences for iteration zero) for each rotation and module.

Four different sets of random gaussian distributed numbers has been added to the true rotation angles between the modules, while the translation is fixed in the right values. The correction is calculated first for the “in plane” rotations or rotations around the Z axis, being the easier calculation and less prone to errors. Then, the corrections to the rotation around the module X axis are obtained, producing the larger differences

between the projections and the local *Hits*, due simply to the module geometry. After each angle correction determination, the rotation matrix is recalculated, before continuing with the next rotation. An iteration is completed after the three correcting angles are obtained: the new relative transformation is compared with the transformation in the previous iteration. The iterative process stops when the difference between consecutive transformations is below a constant parameter.

Figure 5.15 shows the results after a few iterations for four different initial misalignment. In all cases, the translation is fixed in the design values, while the relative rotation is modified randomly according to a normal distribution of mean zero and $\sigma = 1^\circ$ ($\sigma = 0.01745 \text{ rad}$). The rows display the results for different modules, being always the relative transformation calculated with respect to a module II (the initial change in the relative rotation matrix is the same for the different modules). The columns show the results of the iterative procedure for the three angles. A good approximation to the correct value of the rotations (all below 0.0002 rad in the figure) are obtained after two or a maximum of three iterations, being the distance to the design values and the number of iterations dependent on the constant parameter which define the end of the iterative procedure.

5.3.6 Results for a random misalignment

The algorithms already presented for the translation and rotation determination has probed to restore the true geometrical parameters under moderate relative misalignments of the translations or rotations, respectively. In a general case, both the relative rotation and translation between modules differ from the initial estimates or design values simultaneously.

The previous methods can be alternatively used to obtain the right parameters. After each step (translation or rotation corrections) the residuals are recalculated and the sample filtered for a new iteration. Each correction should lead to a new configuration closer to the true relative transformation. Then, for a small initial misalignment, it is expected a convergence to the right parameters after a reasonable number of iterations.

The translation finder and rotation correction algorithms can be used in different order to correct the initial transformation estimates. It has been obtained a good result by using the iterative analytical translation finder initially, to obtain a first correction to the translation vector between the modules. If the rotation is not the correct one, the algorithm can return a wrong translation vector, and possibly a worse approximation to the true translation vector than the initial values. But it returns a relative position

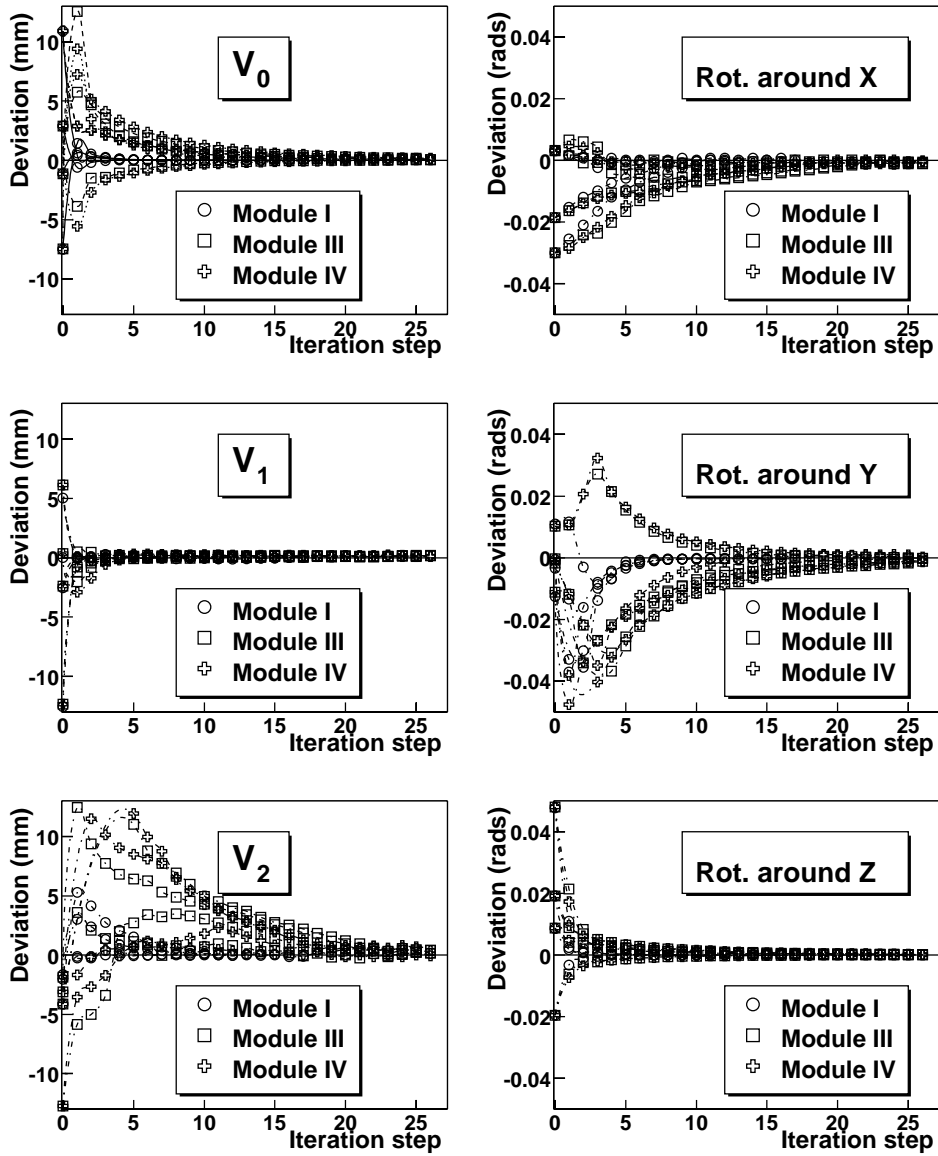


Figure 5.16: Difference between the relative translation vector components and rotation angles (around the main axis) in the relative transformation between module II and any other module. The plots show the differences after 25 iterations (initial differences for iteration zero) for each module.

which minimizes the residuals, presenting a better initial position for the rotation correction algorithm.

To check the behavior of the complete translation finder and rotation correction, a random change has been introduced in all initial parameters of the (already seen) simulation. The components of the relative translation between modules are modified by a random gaussian value obtained from a distribution of mean zero and $\sigma = 10 \text{ mm}$. The angles in the relative rotation are modified by a random gaussian of $\sigma = 1^\circ$ ($\sigma = 0.01745 \text{ rad}$). The results are shown in figure 5.16. After a few initial iterations, the difference between the obtained relative transformation parameters and the true ones is continuously diminishing. Stable results are obtained after around 20-30 iterations for all parameters. The differences are below the $125 \mu\text{m}$ for the translation vector components (in particular below $80 \mu\text{m}$ for V_1 , which correspond to the direction Y_{MDC}) and 0.0002 rad for the rotations around the module main axis, after the last iteration, and for all the modules.

It is important to point out that for larger misalignment has been observed cases where the results does not converge to the right alignment parameters between modules. In particular, combinations of modifications in the parameters including large differences in the relative rotation around the Y_{MDC} module axis leads to large differences in the translation vector, which are difficult to correct in later iterations. In this case, and as a general rule in all the analysis, it is necessary to check both the residuals distributions and the solutions of the geometrical rotation correction (see appendix H for an example) after each iteration step.

5.4 Relative alignment for 3 MDCs

The relative alignment of three modules can be performed by requesting the construction of straight lines from the spatial coordinates of the *Hits* reconstructed in the drift modules.

The aim of the approximation is to obtain a real module alignment algorithm, independent of the target position. The target position estimate represents a mean interaction point between the beam profile and the target volume, while the tracks are originated from different points in the volume of the target or even outside the target. The alternative use of the angular information of the *Hit* (instead target position plus *Hits* position) to obtain a estimate of the track slopes is not adequate, mainly due to their low precision. Then, it was searched an algorithm independent of the target position and, to the maximum extent, also independent of the *Hit*

slopes. Unfortunately, the slope dependence was not completely removed, but the method offers a comparative study of the slopes in several modules.

Several approximations have been tested to obtain the relative transformation between modules. The better results have been obtained minimizing the angle between the straight lines constructed from pairs of modules.

Let us consider three modules, A , B and C , ordered from their distance to the target. The *Hit* coordinates in the modules are represented by the pairs (x^A, y^A) , (x^B, y^B) and (x^C, y^C) , respectively, in their own coordinate systems. Let us use the coordinate system of module B to express the *Hit* coordinates, namely (x_B^A, y_B^A, z_B^A) , (x^B, y^B) and (x_B^C, y_B^C, z_B^C) , using the transformation 5.3. The transformation depends on twelve independent parameters, six for each module. After the selection of those sets of *Hits* in the three modules coming from the same track, as shown in section 5.3.2, two track estimates (straight lines) can be constructed from the positions in modules A and B and in modules B and C . Both estimates contains a common point, (x^B, y^B) and, therefore, it results quite simple to define an angle ϵ between the straight lines. Calling

$$\begin{aligned}\vec{a} &= (a_x, a_y, a_z) = (x_B^A - x^B, y_B^A - y^B, z_B^A) \\ \vec{b} &= (b_x, b_y, b_z) = (x_B^C - x^B, y_B^C - y^B, z_B^C)\end{aligned}\quad (5.52)$$

to the director vectors of both lines, then the angle between them is obtained from the definition of the vector product

$$\sin \epsilon = \frac{|\vec{a} \times \vec{b}|}{|\vec{a}||\vec{b}|}\quad (5.53)$$

In absence of the effects of angular straggling and for a perfect resolution in the modules, the angle ϵ should be π for the set of twelve parameters which correspond to the true modules position. Including the modules resolution and the angular straggling in the air and the modules matter, the angle ϵ takes values randomly distributed around π . The correct alignment parameters would minimize the sum of the sinus of the angle ϵ for all the tracks reconstructed in the three modules. The function to minimize³ is

$$Q = \sum_{Tracks} \frac{(\sin^2 \epsilon)^2}{\sigma^2(\sin^2 \epsilon)}\quad (5.54)$$

³The function is not a χ^2 function, because the $\sin^2 \epsilon$ is not normally (nor gaussian) distributed around zero.

From the expression 5.52 and 5.53, the error in the function $\sin^2(\epsilon)$ is

$$\begin{aligned} \sigma^2(\sin^2 \epsilon) = & \left(\frac{\partial \sin^2 \epsilon}{\partial x^A} \right)^2 \sigma^2(x^A) + \left(\frac{\partial \sin^2 \epsilon}{\partial y^A} \right)^2 \sigma^2(y^A) + \left(\frac{\partial \sin^2 \epsilon}{\partial x^B} \right)^2 \sigma^2(x^B) + \\ & \left(\frac{\partial \sin^2 \epsilon}{\partial y^B} \right)^2 \sigma^2(y^B) + \left(\frac{\partial \sin^2 \epsilon}{\partial x^C} \right)^2 \sigma^2(x^C) + \left(\frac{\partial \sin^2 \epsilon}{\partial y^C} \right)^2 \sigma^2(y^C) \end{aligned} \quad (5.55)$$

where the partial derivatives take the form

$$\begin{aligned} \frac{\partial \sin^2 \epsilon}{\partial x^A} = & \frac{2}{|\vec{a}|^4 |\vec{b}|^4} \left\{ \left((\vec{a} \times \vec{b})_x (M_{01}^A b_z - M_{02}^A b_y) + (\vec{a} \times \vec{b})_y (M_{02}^A b_x - M_{00}^A b_z) + \right. \right. \\ & \left. \left. (\vec{a} \times \vec{b})_z (M_{00}^A b_y - M_{01}^A b_x) \right) |\vec{a}|^2 |\vec{b}|^2 - \right. \\ & \left. |\vec{b}|^2 \left(a_x M_{00}^A + a_y M_{01}^A + a_z M_{02}^A \right) |\vec{a} \times \vec{b}|^2 \right\} \end{aligned} \quad (5.56)$$

The other partial derivatives are obtained in an equivalent way.

The minimization with respect to the twelve parameters is performed using MINUIT (MIGRAD); initially it has been tried the convergence minimizing with respect to the twelve parameters simultaneously. Unfortunately, the solution which minimizes the function is not unique. There is a continuous set of pairs of module positions for which the function returns a similar value. A few examples of the set of positions are shown in figure 5.17. The MDCs I, II and III are plotted in the design positions (thick lines, not to scale). The *Hits* in the modules (crosses) compose straight lines, and the function defined in equation 5.54 takes a minimum value. But the same *Hits* form straight lines for other pairs of module positions, denoted by the Latin letters a, b and c in the scheme; then, the value of the function is practically the same for these pairs. The set of pairs of positions conforms a valley in the twelve parameters function. The MINUIT program checks the values of the function 5.54 along the valley and stops randomly (predominantly when the three modules are in the same plane, and the lines from the *Hits* lie in the same plane).

There is an alternative procedure to determine the parameters. In simulation has been checked that fixing initially in its correct value the distance between the modules center or the relative angle⁴ between two

⁴The relative distance is the only parameter one could fix, if the three modules are parallel

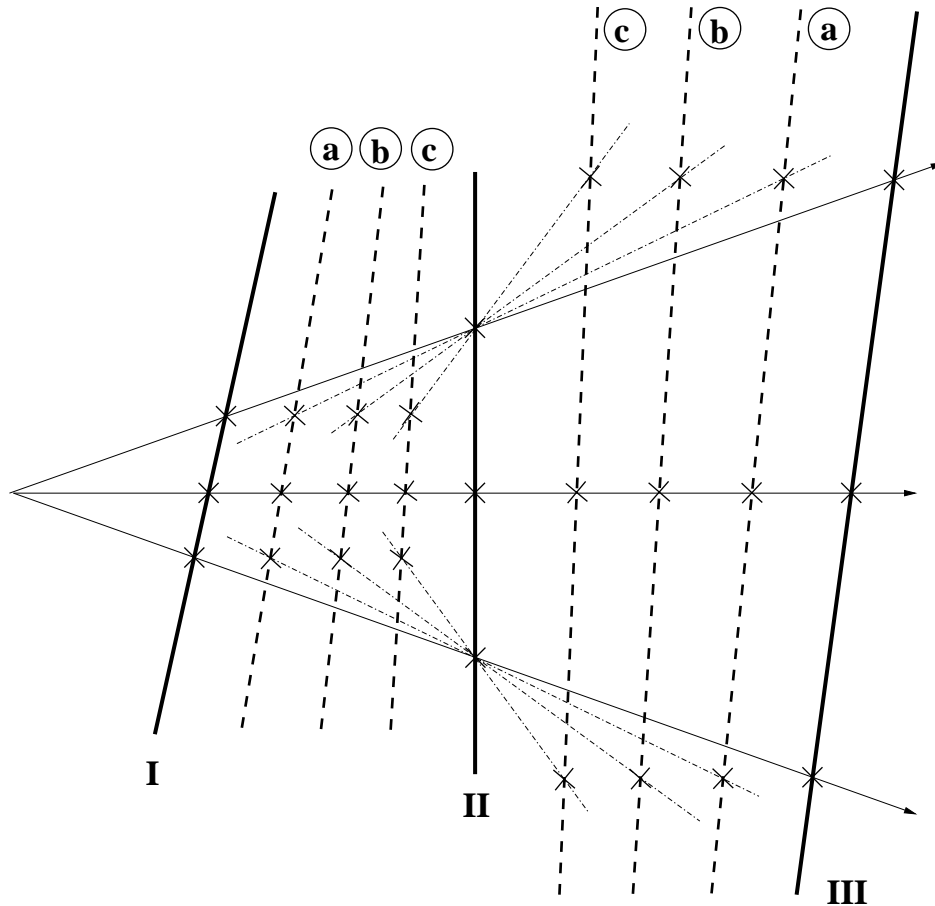


Figure 5.17: Example values of the relative position of the modules from which a minimum value of the minimization function is obtained. The thick lines represent the modules in their true positions. Three tracks (arrows) are represented, and the corresponding Hits in each module (crosses). The same module Hits construct straight lines when the modules are in the positions labeled *a*, *b* and *c*.

modules of the three under study, the other eleven parameters converge to the correct values. This relative angle is the second Euler parameter in the transformation between the modules (θ in the usual notation along this chapter), which is approximately the angle around the local X_{MDC} axis. Then, we have only to determine “a priori” one parameter, or evaluate from the results which value of the fixed parameter is the best from a set of possible values (“sweeping” the parameter and checking control

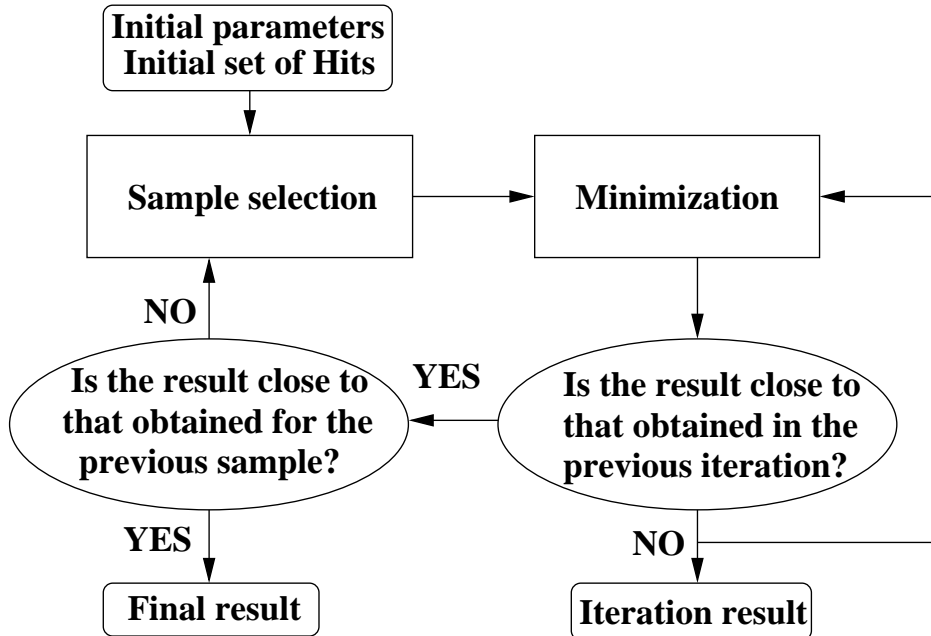


Figure 5.18: Scheme of the double iterative procedure to find the result from the minimization of equation 5.54.

histograms). First, the convergence of the eleven parameters is demonstrated once the relative angle θ between the two first modules is fixed. A secure iterative procedure has been designed to obtain a good convergence independently of the initial relative position. Second, the results for the selection in the angle sweeping are shown.

5.4.1 Convergence for a fixed parameter

The minimization is performed following a double iterative procedure, as it is shown in figure 5.18. In a first inner minimization loop, and for the initial parameters (those best guess values or the outcome from another method), the sample selection policy, seen in section 5.3.2, returns a set of *Hits*. The minimization of equation 5.54 is performed using the *Hits* of the sample; the resulting parameters are again introduced as initial values in the first loop of the iterative procedure. The inner loop ends when the parameters returned by two consecutive minimizations differ in less than a fixed quantity. For this solution, the sample selection is again performed, with the result of a new set of *Hits* passing the conditions. Then a new inner loop begins, searching a stable solution (and independent of the

initial values) for the set of *Hits*. The complete procedure (outer loop) stops when the parameters obtained for the set of *Hits* resulting from the previous sample are stable (does not differ from those used to select the sample more than a fixed quantity).

The procedure has been tested under the simulated sample of tracks coming from 10^5 Carbon on Carbon collisions, propagated through the spectrometer including the multiple scattering (angular straggling) and secondary production. A set of random gaussian ($\sigma = 10$ mm) displacements has been introduced in the relative translation vectors between the modules (a different value for each vector component). The angles in the relative rotation are modified by a random gaussian of $\sigma = 1^\circ$ ($\sigma = 0.01745$ rad), with the exception of that between second Euler angle between module I and II (θ_{I-II} where the subindex indicate the modules the parameter belong to), which is approximately the relative rotation between the modules coordinate systems around the common X_{MDC} direction, which is fixed in the minimization in its design value. The figure 5.19 shows the differences between the real value of the twelve parameters and the outcome from each iteration (the outcome is taken at the end of the inner iterative loop, before a new sample of *Hits* is calculated for the next outer iteration). The figure is divided in six pads, one for each parameter, showing the relative parameters for both modules (vs. the intermediate module) in the same pad. There are four initial misalignments, and therefore there are eight different lines converging to the true values in each pad. The zero iteration step contains the initial parameter displacements (zero in the case of the rotation around X for module I, which is the fixed parameter).

5.4.2 Sweeping the fixed parameter

The second Euler angle θ between the two inner modules has been fixed in its true value, along the previous study of the convergence to the correct alignment parameters. Now, a procedure for the selection of the right value in the fixed parameter is shown; the value of the fixed parameter θ is swept on a short range and the differences in several control histograms are checked. Up to this point, the *Hit* slopes have not been used, and the complete minimization procedure has simply utilized the *Hit* coordinates. Now, the selection of the correct θ requires the comparison of the track slopes and angles reconstructed individually in each module, and also the track slopes obtained from the coordinates in a pair of modules (the slopes of vectors \vec{a} and \vec{b} in equation 5.52).

The track estimate slopes can be transformed to the coordinate system

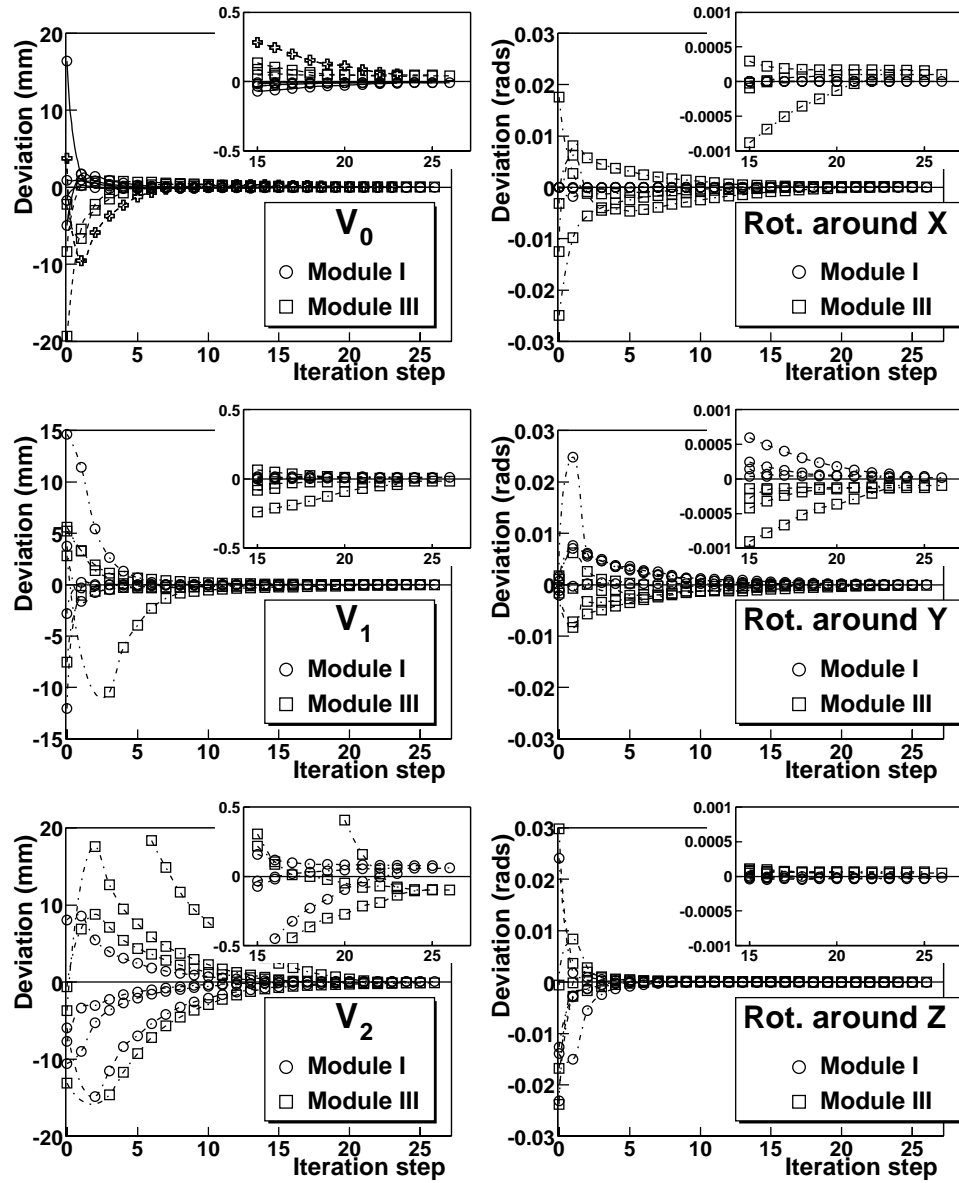


Figure 5.19: Difference between the relative translation vector components and rotation angles (around the main axis) in the relative transformation between module II and the labeled modules. The plots show the differences after 25 iterations (initial differences for iteration zero) for each module.

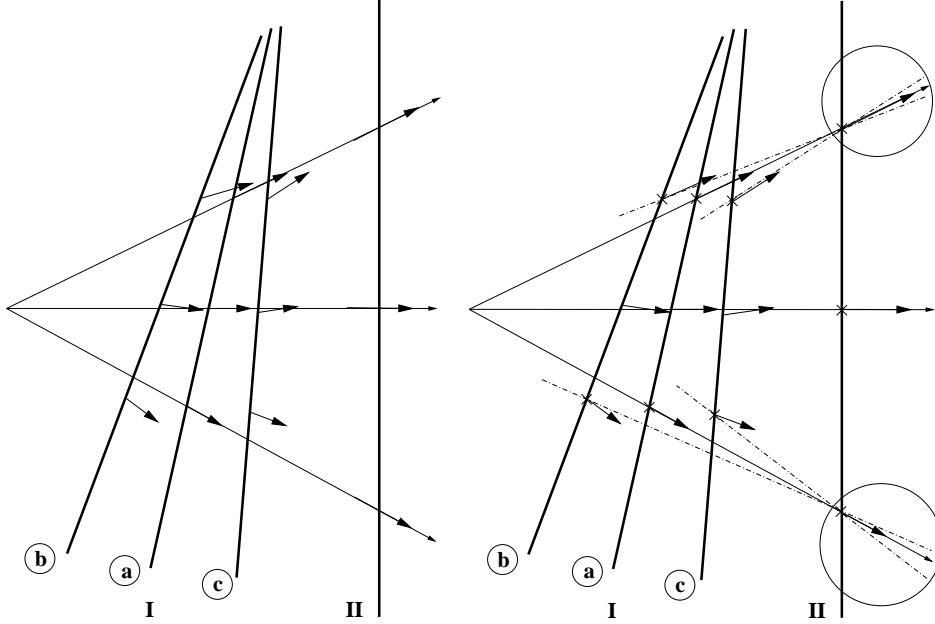


Figure 5.20: *Left: scheme showing the differences between the slopes in the Hits reconstructed in module I and II for the modules in their true relative position (a), and in two neighbor positions, with larger angle θ_{I-II} (b) and with smaller angle (c). The thin long arrows represent charged particles. The differences between the Hit angles in different modules are constant, for a given position. Right: scheme showing the difference between the slopes of the reconstructed Hits in module I and II (arrows) and the slope of the track estimate from the positions of the Hits (dashed lines). In this case, the results depends on the position of the Hit in the module. The circles signal the top and bottom tracks in module II, for their comparison.*

of other modules for comparison, as has been already shown in section 5.3.1. In particular, the differences between the slopes component along the Y_{MDC} coordinate ($\Delta S(y)$, see equation 5.27) of the same track in the two modules related by the fixed angle reflects the difference from the fixed parameter to its true value. In the left part of the figure 5.20 there is an scheme showing the module II and three possible relative positions of the module I. The correct position corresponds to that signaled by the label *a*, while for the label *b* the angle between the modules is larger, and shorter for *c*. The differences between the slopes reconstructed in each module (both slopes expressed in a common coordinate system) nulls only for the correct transformation between coordinates systems; in the other cases,

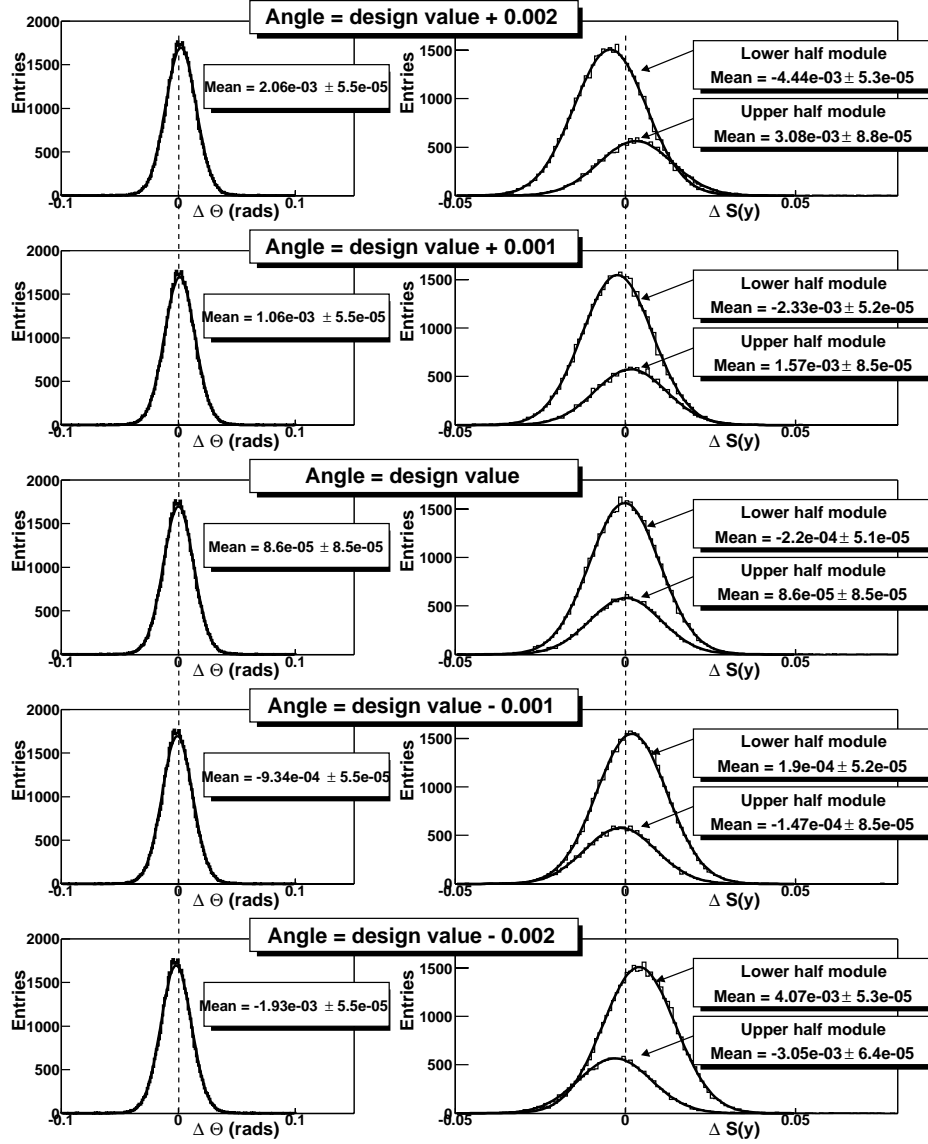


Figure 5.21: Differences in the Hit slopes and angles for several values of the fixed angular parameter θ_{I-II} . In the left column, the differences $\Delta\Theta$ between the angles obtained from the Hit slopes in module II and in module I (transformed to the coordinate system of module II) are displayed. The right column shows the differences between the module I Hit slopes $S(y)_I$ and the slopes reconstructed from the coordinates of the Hits in both modules, for the lower and upper half of the module.

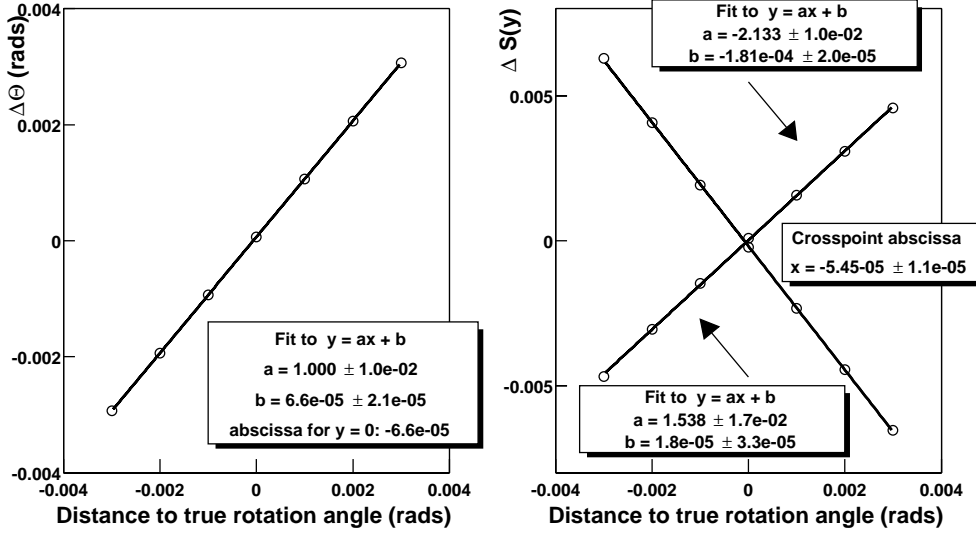


Figure 5.22: Left: Gaussian fit means of the histograms of the Θ differences between modules I and II, for different rotation angles θ_{I-II} fixed in the minimization. From the linear fit to the mean values it is possible to estimate accurately the true rotation angle. Right: Gaussian fit means of the histograms of the differences in a module slopes and that obtained from two modules. The cross point of the straight lines obtained from the points linear fit is an accurate estimate of the true angle θ_{I-II} .

the difference between the relative angle fixed in the minimization and its true value coincides with $E(\Delta\Theta)$, the mean value of the difference between the polar angles reconstructed in the modules

$$E(\Delta\Theta) = E(\Theta_{II} - \Theta_I) = E[\arctan(S(y)_{II}) - \arctan(S(y)_I)] \quad (5.57)$$

The left column in figure 5.21 shows a set of histograms of the difference $\Delta\Theta$ between the angles reconstructed in the modules, along a sequence of values of the fixed angle. The mean of the histograms gaussian fit reproduces nicely (within the errors) the modification introduced in the fixed angle θ_{I-II} in the minimization. The left pad of figure 5.22 displays the values of the mean of the histograms gaussian fit for different modifications introduced in the true θ value fixed in the minimization. The linear fit reproduces perfectly the data, and the value of the abscissa for $y = 0$, that is, the angle θ_{I-II} for which the mean of the histograms gaussian fit is zero, is an accurate estimate of the true angle.

The track slope can be estimated using the *Hit* position in two modules

and their relative position given by the alignment parameters (the slopes of vectors \vec{a} and \vec{b}). Then, the component along the Y_{MDC} direction of the vector slope can be compared with the *Hit* slope $S(y)$ in any of the three module. The right scheme of figure 5.20 represents three relative positions of the modules I and II, solutions of the iterative minimization with different value of θ_{I-II} . When the modules are in the relative position a , where the angle value is correct, the slopes of the reconstructed *Hits* coincides with the slopes given by the *Hit* position in two modules. For the other cases, both estimates differ. The difference between the slopes results to be of different sign in the upper and bottom half of the module. The right part of figure 5.20 shows both cases, framed by a circumference, in the module II. In the upper track, the difference between the *Hit* slope (the arrow) and the slope given by the *Hit* positions in two modules (dashed lines) is positive for b and negative for the position c . For the lower track, the difference is positive for c and negative for b . The right column in figure 5.21 presents the histograms made of the differences between the slopes, separately for the *Hits* in the lower and upper half of the module; the mean value of the histograms gaussian fit is also shown. The mean value of the histograms gaussian fit does not return directly the correction to the fixed angle in this case, but there is an alternative method to determine it. The mean values for both histograms can be plotted versus θ_{I-II} . Then, the correct angle is defined as the abscissa of the crossing point between the straight lines fitting the means of both histograms. The result of this procedure are displayed in the right pad of figure 5.22. The mean value of the two set of histograms gaussian fits are represented versus the distance to the true value of the angle θ_{I-II} . The points fits nicely to straight lines and the abscissa of their cross point results an additional accurate estimate of the true angle.

5.4.3 Estimation of the parameters error

The parameter errors, understood as uncertainties in the best parameter estimates, can be obtained from the shape of the minimization function in some neighborhood of the minimum [4]. In particular, the error on a parameter is defined generically as the change of the parameter which would produce a change of the function value equal to a constant Err . Usually this constant takes the value $Err = 1$, to obtain the usual standard deviation if the function to minimize is a χ^2 -like function. In a linear case, when the function is parabolic at minimum, and for $Err = 1$, the errors correspond to defining the error as the inverse of the second derivative at the minimum. In our case, where a multiparameter fit is performed, MI-

Mods	Par	Δ	σ	$\# \sigma's$	Δ	σ	$\# \sigma's$
II-III	ϕ	1.4×10^{-3}	1.1×10^{-4}	13.4	1.0×10^{-3}	1.5×10^{-4}	6.5
II-III	θ	1.6×10^{-4}	8.7×10^{-5}	1.8	1.8×10^{-4}	7.8×10^{-5}	2.3
II-III	ψ	-1.4×10^{-3}	4.7×10^{-5}	29.1	-9.4×10^{-4}	1.5×10^{-4}	6.2
II-III	V_0	-0.046	0.036	1.3	-0.042	0.051	0.8
II-III	V_1	-0.035	0.025	1.4	-0.011	0.027	0.4
II-III	V_2	0.34	0.16	2.1	0.36	0.14	2.5
I-II	ϕ	-2.1×10^{-4}	4.4×10^{-5}	4.9	-1.1×10^{-4}	7.6×10^{-5}	1.5
I-II	θ	0	0		0	0	
I-II	ψ	1.7×10^{-4}	5.4×10^{-5}	3.2	8.4×10^{-5}	8.0×10^{-5}	1.0
I-II	V_0	0.0076	0.0092	0.8	0.0075	0.014	0.5
I-II	V_1	0.0062	0.0063	1.0	0.0008	0.0067	0.1
I-II	V_2	-0.077	0.043	1.8	-0.084	0.037	2.3

Table 5.3: The table presents the difference (Δ) between the outcome of the minimization procedure and the design value of each parameter, the error returned by MINUIT (σ) and the ratio between both quantities ($\# \sigma's$ or number of sigmas), for each parameter (Par) relating the relative position of the three modules. Two different examples are shown, corresponding to two different initial misalignments.

NUIT returns the error matrix of the parameters as well as the individual parameter errors. The error matrix or covariance matrix is the inverse of the second derivative matrix of the function with respect to the free parameters, usually assumed to be evaluated at the best parameter values (the function minimum). The diagonal elements of the error matrix are the squares of the individual parameter errors, including the effects of the correlations with the other parameters. Actually, the diagonal terms of the second derivative matrix has the diagonal not coupled to other parameters, but the inverse, the error matrix or covariance, contains contributions in the diagonal of the correlations. The effect of the correlation (independently of negative or positive correlation) is always to increase the errors on the other parameters.

When one parameter is exactly known or fixed, the errors of the other parameters decrease, because the row and column elements of the function second derivative with respect to the fixed parameter are zero. Then, the diagonal elements of the inverse matrix are smaller (or, in case of no correlation, equal), because of the effect of the correlation with the fixed parameter.

The use of this scheme requires the use of a normalized minimization

function. If MINUIT is used to perform a fit to some experimental data, the parameter errors will be proportional to the uncertainty in the data, and therefore meaningful parameter errors cannot be obtained unless the measurement errors of the data are known. The function 5.54 is conveniently normalized by dividing by the estimated error of each observation. Actually, if the value of the minimization function would be everywhere multiplied by a constant b , then the errors would decrease by a factor \sqrt{b} , or, in other words, if the data errors are all overestimated by a factor b , then the resulting parameter errors from the fit will be overestimated by the same factor b .

The MIGRAD procedure assumes symmetrical errors, using a stable variation of the Davidon-Fletcher-Powell variable-metric algorithm. This algorithm converges to the correct error matrix as it converges to the function minimum. The errors (σ) returned by the algorithm for two different initial misalignments are displayed in table 5.3. The table shows also the differences between the design values and the outcome of the minimization procedure (Δ) and the ratio between these quantities ($\# \sigma's = \Delta/\sigma$). Note that the difference between the design values and the outcome of the minimization is approximately the same in both examples. This difference or offset is an statistical effect of the limited number of tracks (1×10^5) in the sample. In other words, the sample mean parameters does not coincide with the population mean parameters (the design values). Taken the mean value of the outcome in the four minimizations, performed for different initial misalignments, the individual outcome differs in less than 3σ from the mean in all cases; the errors in the angular parameters are compatible with the standard deviation from the mean, while the errors in the translations seems to be slightly larger.

The error in the determination of the fixed parameter θ contribute to rise the value of the errors returned in the minimization. This effect can be estimated by studying the results fixing the parameter θ one standard deviation above and below its estimate. The resulting parameters differ in less than their own errors returned by the simulation.

Bibliography

- [1] C. Fernández, B. Fuentes, J.A. Garzón, M. Sánchez; *HADES Tracking and Vertex Reconstruction. Status report*. USC/GENP/HADES/00-1, Santiago de Compostela, 2000.
- [2] W.T. Eadie *et al*; *Statistical Methods in Experimental Physics*, North-Holland Publishing Company, Amsterdam, 1971.

- [3] Review of Particle Physics, Physical Review **D54** (1996) 1.
- [4] MINUIT - Function Minimization and Error Analysis, CERN Program Library entry D506.

Chapter 6

Relative Alignment Results

During the so-called November 2001 data taking period (comprising the last week of November and first week of December 2001), a set of approximately 1.9×10^8 collisions of a Carbon beam, at an energy between 1 *AGeV* and 2 *AGeV*, on a Carbon target, has been recorded by the spectrometer. A reduced sample has been taken without magnetic field, divided in two separate sets corresponding to different dates. The second set, containing approximately 2×10^6 valid events and more than 1.8×10^7 *Hits* in 14 modules, has been used along this chapter for the analysis relative position of the modules. The setup includes a total of 14 working modules, including full coverage of MDC II (6 sectors), 5 MDC I (all but sector 1), two MDC III (sectors 1 and 3) and one MDC IV (sector 1).

First, the details concerning the tracking software and the experimental resolution of the modules are explained. The following sections deal with the Target Finder and the alignment methods developed to obtain the relative position of two and three modules. The outcome is evaluated and the errors are estimated for each method.

6.1 Module resolution and tracking features

The common entry point to the different algorithms designed to find out the relative module positions are the *Hits*, that is, the elaborated estimates of the charged particles trajectories in their path along the module, as defined in the section D.1 of appendix D. The raw information from the sense wires in each plane (hit wires and corresponding TDC times) is filtered and calibrated in several steps, in an iterative procedure. The aim of the calibration is to provide the tracking codes (see appendix D) with the required input: the impinged wires and the drift times (or distances calcu-

lated from the drift velocities) in each cell. The path from TDC channels to final drift times involves large difficulties, including non-linear behavior of the drift velocity, temperature dependence... The calibrated data, hit wires and drift times (or distances), are used by the tracking codes to determine the track parameters (see D.2 and D.3).

The data calibration procedures are in progress, but the convergence to a final satisfactory status requires the analysis of large amounts of data and the identification of the specific features in each module. Both debugging and error evaluation tools, for all the calibration steps, are under development, basically based on the results of the tracking codes. The tracking codes are also under development. In particular, for the Santiago tracking, the implementation of the time offset correction for each particle is under investigation. The correction due to the incident angle of the particle (see D.4) has not yet been introduced for the real data. At its present stage, the global time offset correction removes just the time-of-flight of the fastest particles in the calibration procedure; then, for most of the slow particles (hadrons) the assigned drift time and drift distance are too large. The slope correction increases the drift distances to account for the differences between the wire distances to the cross point of the track and the wire plane and the wire distance to the closest point of the track. So, applying the slope correction to drift distances which are already larger than should be, leads to a large increase in the track estimate resolution (or even worse systematic bias).

For the simulation works described in the previous chapter, the tracking input has been carefully checked and the time-of-flight of the particles removed. The tracking software can run under ideal conditions and the slope correction can be introduced. But, for real data, the absence of the correcting terms in the tracking introduces important errors. The poor resolution of the available tracking software is affecting strongly the quality of the alignment.

In this chapter, the results using both tracking methods are analyzed to obtain the alignment parameters. In the following, the tracking method used to obtain particular results or graphics is indicated.

6.2 Target Finder Results

In the next analysis of real events, it is assumed a perfect relative positioning between the modules II in the different sectors. The Santiago tracking results have been used along this section. The estimated error (see section 5.2) is rose up to the value $e = 18.1$, which corresponds to

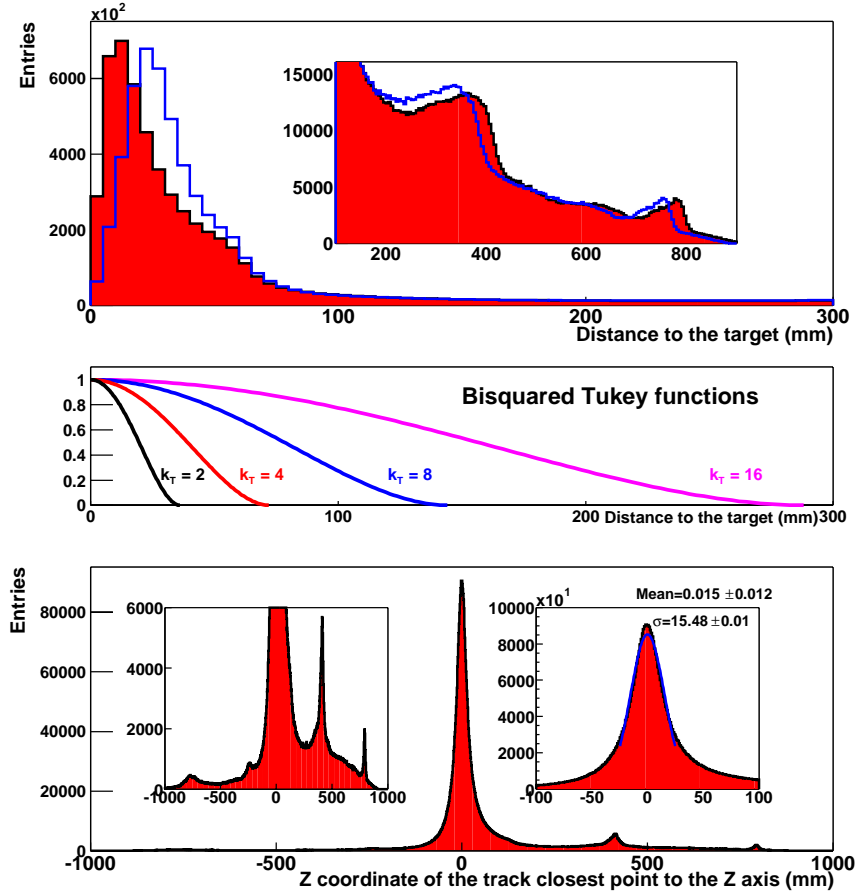


Figure 6.1: Target Finder results from the (Santiago tracking) Hits in all (MDC II) modules. The top pad displays the distance from track to target, first for the target at the design position (blue) and for the resulting target estimate (filled red). For comparison, the Tukey function is shown below. In the bottom pad, the Z coordinate of the track closest point to the Z axis is represented. The coordinate system has been corrected to center the resulting target estimate.

a difference between the reconstructed and original track angle of about 1° . This increase in the estimated error is made to take into account both the difference between the angles of reconstructed and original tracks and the distribution of the distance between the track and the target estimate. This distribution is shown in the top pad of figure 6.1. The blue histogram represents the distribution for the target in the design position, while the red filled histogram shows the distance distribution to the obtained target

k_T	Entries	x_t	y_t	z_t
	6844281	-2.685	-1.110	71.881
8	5121834	-2.987	-0.478	-23.626
4	4583928	-3.367	-0.546	-26.277
2	3346647	-3.415	-0.539	-27.284
1	1992210	-3.521	-0.495	-27.429

Table 6.1: Results of the Target Finder algorithm on November (day 340) data, for different Tukey weights. The first row includes the result for all Hits (without weights).

estimate. The bottom pad shows the the Z coordinate of the track closest point to the Z axis, for all tracks in the six modules. Here, the modules has been relatively displaced according to the new target estimate. The numerical results are presented in table 6.1. The target position estimate for $k_T = 2$, the optimal value determined during simulation, is going to be used in the next section, on the relative positioning of sectors with two modules.

Let us estimate the random and systematic errors related with the method result. First, the random errors are evaluated following the procedure used in section 5.2. The *Hit* sample is divided in groups and the target position is estimated for each group. Then, the random error associated to the Target Finder algorithm and the track parameters is estimated from the variance of the results for each group. The average and the square root of the variance of the position average, in each direction are

$$\begin{aligned}
 \bar{x}_t &= -3.450 & \sigma(\bar{x}_t) &= \sqrt{V(\bar{x}_t)} = 0.045 \\
 \bar{y}_t &= -0.589 & \sigma(\bar{y}_t) &= \sqrt{V(\bar{y}_t)} = 0.057 \\
 \bar{z}_t &= -27.312 & \sigma(\bar{z}_t) &= \sqrt{V(\bar{z}_t)} = 0.043
 \end{aligned} \tag{6.1}$$

for the ten first groups of 50000 events, with more than 105000 tracks contributing to each target position determination. The mean value in each direction agrees with the outcome of the method for the complete sample (in table 6.1 for $k_T = 2$), within the errors. From the errors in equation 6.1, calculating the variance of the average under the simple assumption of independence of results from each group, the random error in the Target Finder for the complete sample (3.3×10^6 tracks) results to be of the order of $10 \mu m$, in the three coordinates.

The error in the target position estimation in the real data is more difficult to estimate than in the simulation, because of the contribution of

Sectors	k_T	Entries	x_t	y_t	z_t
All	2	3346647	-3.415	-0.539	-27.284
1 & 4	2	1073652	-3.091	1.247	-27.713
2 & 5	2	1208796	-2.958	-1.993	-27.713
3 & 6	2	1196846	-4.065	-0.418	-26.625
Weighted mean			-3.380	-0.451	-27.339
Square root of the variance			0.499	1.310	0.517

Table 6.2: Target position estimate taking the tracks from two opposite sectors of the plane II. The columns represent the sectors contributing to the estimate, the Tukey constant k_T , the number of tracks and the target position estimate. The last rows show the weighted mean and square root of the variance of the three separated sets.

other systematic errors. The assignment of the nominal design positions to the modules in the *Hit* transformation to a common reference system, is the largest contribution to the error in the target position estimation. The relative module misalignment produces a systematic bias of the target estimate. Let us calculate the bias of the target estimate that produces the misalignment of a module with respect to the other modules.

If the module is displaced a quantity q in a given direction, with respect to the other modules which are all in their relative design position, then, the straight lines constructed from the *Hits* of the displaced module change in the same quantity q , changing the closest point of the straight line and the target estimate, as well as the distance between these two points. The overall effect is a change in the target position estimate in the same direction of the module displacement, and of a magnitude which is a fraction of the module displacement q . The particular fraction depends on the statistical weight of the number of straight lines contributing to the target estimate in the displaced module, with respect to the total number of contributing lines.

Two different approaches have been used to estimate an upper limit for the systematic error introduced in the target position estimate by the relative misalignment of the modules of the same plane. In the first one, the Target Finder algorithm is employed taking the tracks from couples of opposite sectors of the plane II, instead of the six sectors. The symmetry of the opposite sectors ensures that there are no privileged directions with respect to the complete analysis; the same is not true if only one module is used for the target position determination (or two non opposite modules). The results are shown in table 6.2, including the mean and the standard

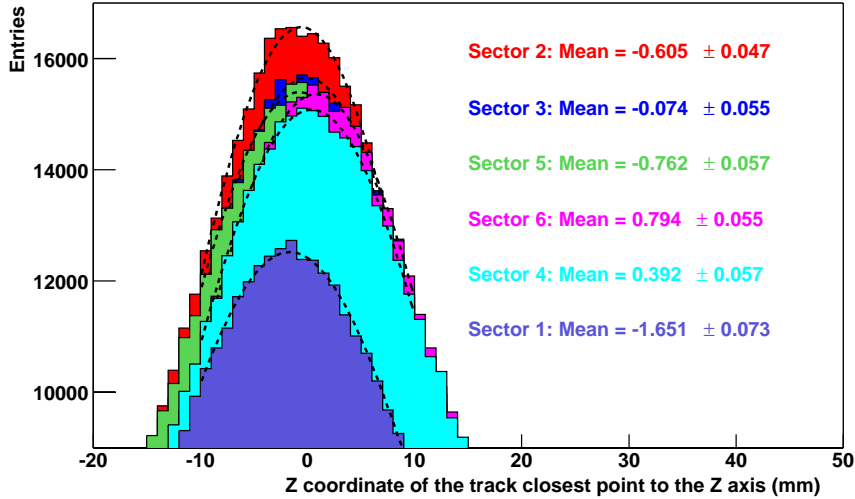


Figure 6.2: Target reconstruction from the *Hits* in each module independently. The gaussian fit mean (defined between $-10 < Z < 10$) is included.

deviation, which is taken as an estimation of the systematic error in each direction.

In the second method, the closest track point to the Z axis is found, but from the *Hits* in the individual modules one by one. Then, the peaks corresponding to the target reconstruction using the *Hits* of each module can be observed separately. Figure 6.2 shows the gaussian fit to the main target region for each module. The dispersion of the gaussian fit means, can be used as a measurement of the systematic error along the Z direction. The square root of the variance is 0.64 mm , in good agreement with the result obtained using the first method.

As a conclusion, the Target Finder method returns an estimate of the target position, allowing both graphical and numerical checks of the method reliability and the estimation of the errors. In particular, the systematic error due to the sectors misalignment has been proven to be the largest error contribution.

6.3 Alignment of sectors with two modules

For those sectors having installed only two modules, the alignment procedure requires the estimation of the target position and the use of the

estimate to construct straight lines with the *Hits* of modules II (those used to obtain the target). The straight lines are then extrapolated to the other module in the sector, to obtain the residuals distributions. Then, the iterative use of the analytical translation minimization and the rotation correction methods, returns the modules relative position.

The first part, the estimation of the target position, has been already explained in section 6.2, for the analyzed data. The residuals distributions constructed from the target position and the *Hits* in module II are fitted to determine the compatibility and select those tracks coming from the target, as shown in section 5.3.2. Then, the iterative procedure, that includes the analytical translation reduction and the geometrical determination of the rotations around the module axis, runs up to the convergence.

Figures 6.3 and 6.4 display the four residuals distributions for the alignment of the module I and II and the module II and III, respectively. The *Hits* has been obtained using the Dubna tracking¹. The dashed histograms represents the residuals for the initial parameters (the design values), while the filled histograms are the residuals when the modules are in the position described by the obtained parameters. The peak of the distributions after the alignment procedure has been fitted to a gaussian, to determine the deviation from zero and the projection resolution. The $S(x)$ and $S(y)$ residuals has been obtained comparing the *Hit* slope (in module I or III) with the target-*Hit* (in the reference module II) line.

The differences between the Δx and Δy distributions are apparent from the histograms. The fitted mean shows the mean deviation of the Δx and Δy residuals in all the module. A large deviation from zero would signal errors in the procedure or the absence of a real convergence. The thickness of the distribution peak, estimated by the gaussian σ , is related to the accuracy of the alignment parameters estimation, but also is related to the resolution of the modules. It is difficult to extract conclusive information, but it is an immediate signal of an erroneous result after the minimization. The results shown in the figures 6.3 and 6.4 are very close to those obtained in simulation, when it is introduced a resolution of around $\sigma(x) = 500 \mu m$ and $\sigma(y) = 350 \mu m$, with all the modules located in their design positions.

The results of the rotation correction can be evaluated by displaying the Δx and Δy residuals distributions in different zones. The top pads in figures 6.5 and 6.6 show a complex two-dimensional representation of the residuals before and after the relative alignment, for the module I and III respectively. The histogram display nine separated zones where

¹The Santiago tracking has been checked as well but, by the time being, the lack of the time-of-flight offset and incidence angle corrections, produces larger errors.

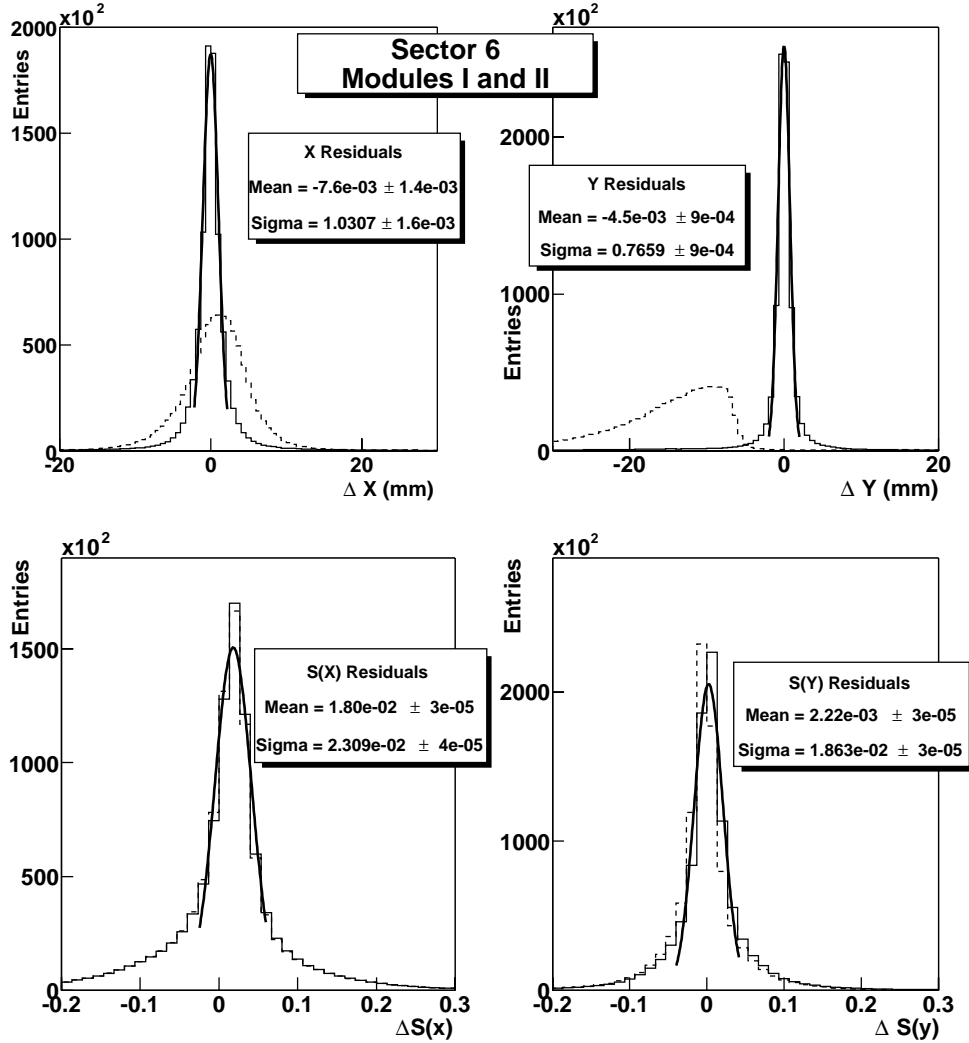


Figure 6.3: Residuals distributions before (dashed line) and after (filled line) the modules alignment. The residuals correspond to the projection of target-module II Hits on module I, for sector 6. The distributions after the alignment has been fitted to a gaussian, whose parameters are shown in each pad.

the residuals are studied independently. The center of this zones in the modules correspond to the reading of the axis in *cm* and are signaled by the red dashed lines. A two dimensional histogram is included in each zone, representing the joint $(\Delta x, \Delta y)$ distribution. To allow the study of

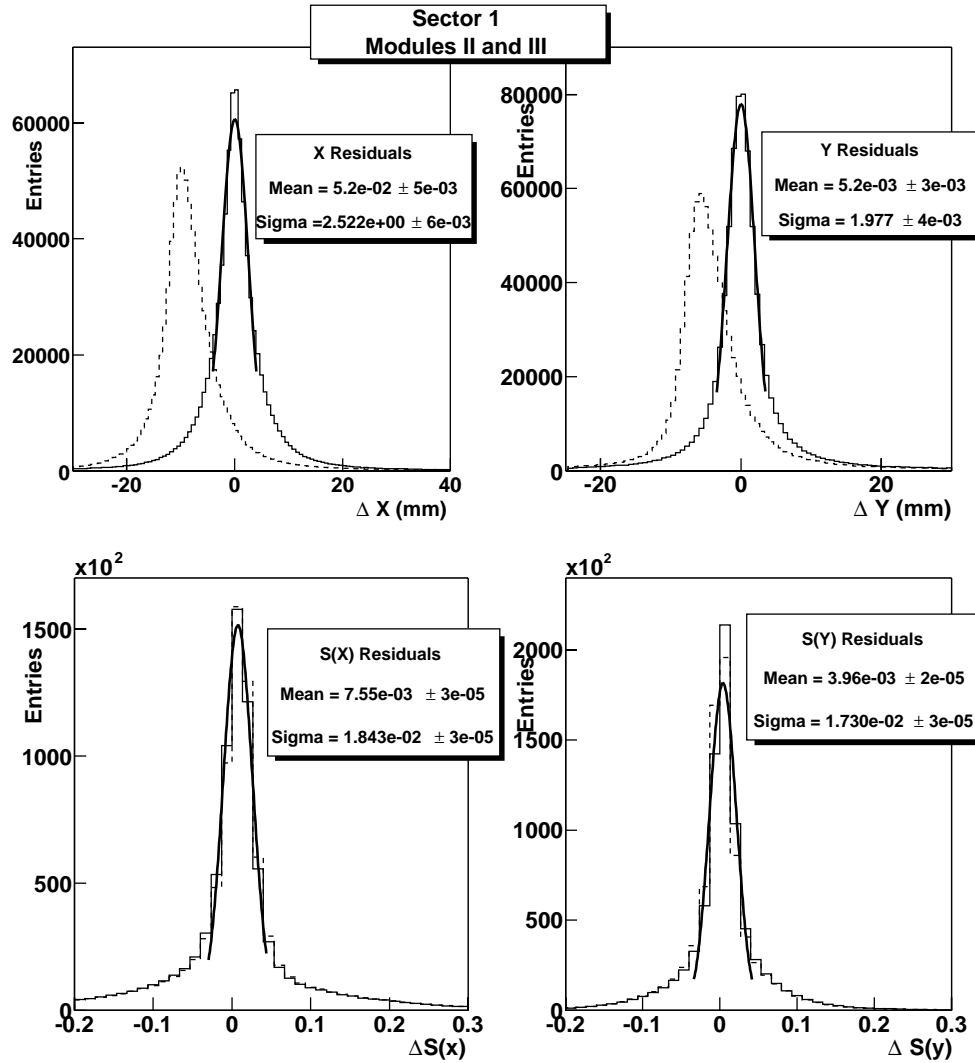


Figure 6.4: Residuals distributions before (dashed line) and after (filled line) the modules alignment. The residuals correspond to the projection of target-module II Hits on module III, for sector 1. The distributions after the alignment has been fitted to a gaussian, whose parameters are shown in each pad.

the residuals for all zones simultaneously, the two dimensional residuals are zoomed a factor 10, and therefore the deviation from the center is obtained by reading the scale in *mm* (and also taken into account that the center of most zones is not at zero, at least in one of the two dimensions). This

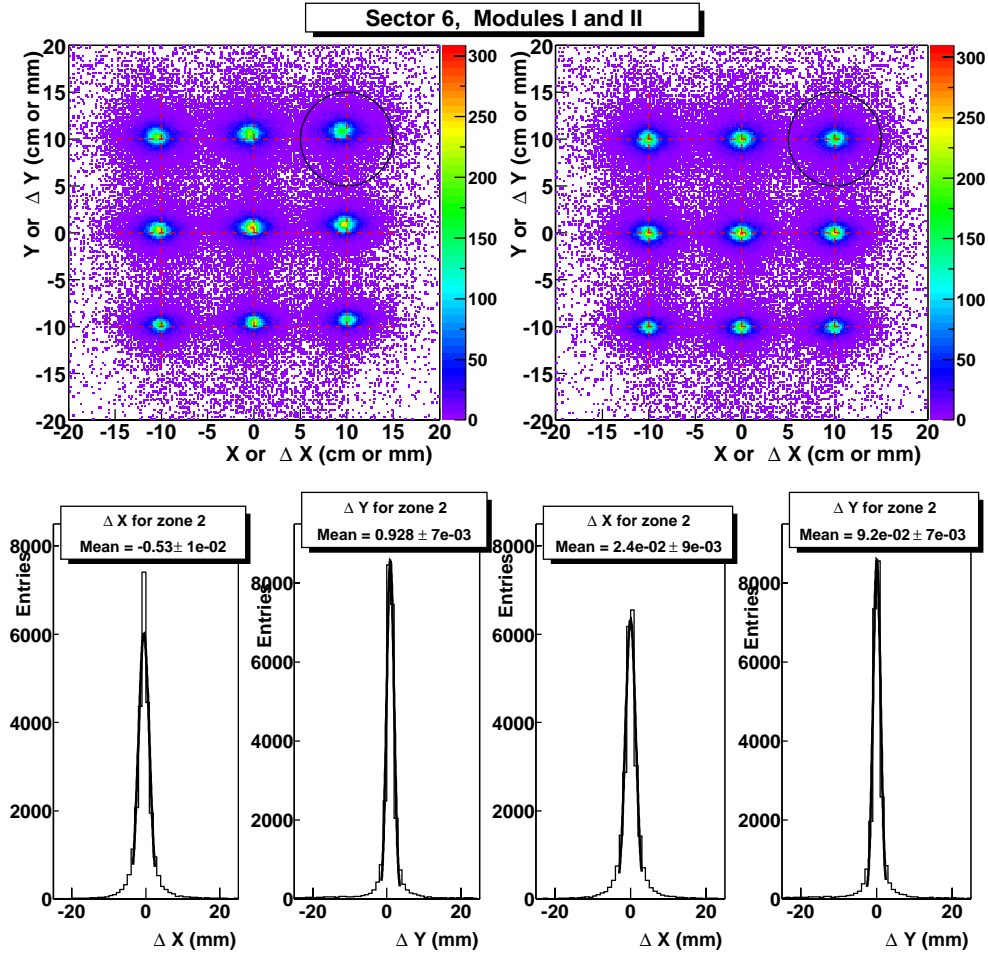


Figure 6.5: Top: two dimensional histograms where the $(\Delta x, \Delta y)$ distributions are shown for nine different zones, before (left) and after (right) the alignment of the modules I and II. See in the text the interpretation of this histogram. Bottom: Δx and Δy distributions for the zone signaled by the circumference in the immediate superior histogram. The mean of the gaussian fit of the distribution peak is shown.

representation permits the immediate observation of the rotation, and the comparison with the analysis given in figure 5.14.

The two dimensional distributions in each zone can be projected onto the axis to obtain the usual Δx and Δy distributions. Those distributions are shown for the so-called zone 2, signaled by a black circumference on

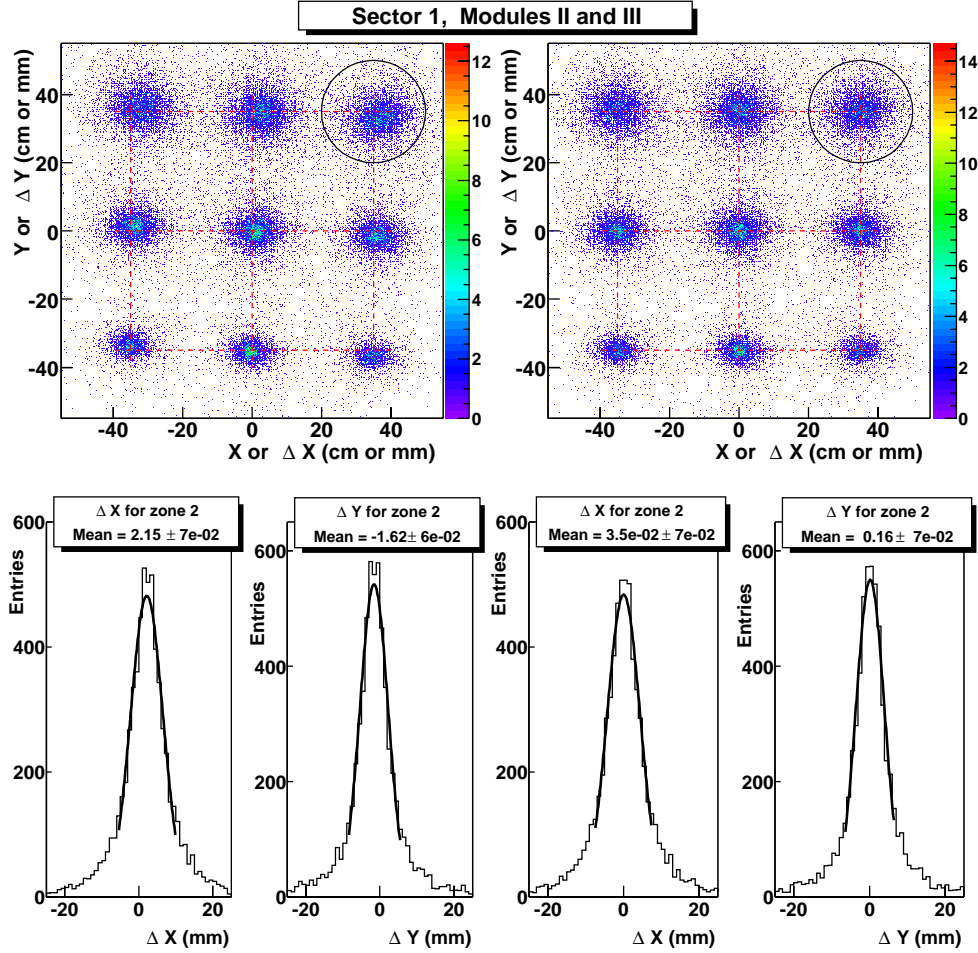


Figure 6.6: Top: two dimensional histograms where the $(\Delta x, \Delta y)$ distributions are shown for nine different zones, before (left) and after (right) the alignment of the modules II and III. See in the text the interpretation of this histogram. Bottom: Δx and Δy distributions for the zone signaled by the circumference in the immediate superior histogram. The mean of the gaussian fit of the distribution peak is shown.

the top histograms², in the pads below each two-dimension histogram.

The random errors in the parameters cannot be directly extracted from the procedure, but they can be obtained indirectly from the error in the determination of the mean of the residuals distributions, for all the avail-

²Zones are enumerated in the code from 0 to 8, from left to right and from the top to bottom one.

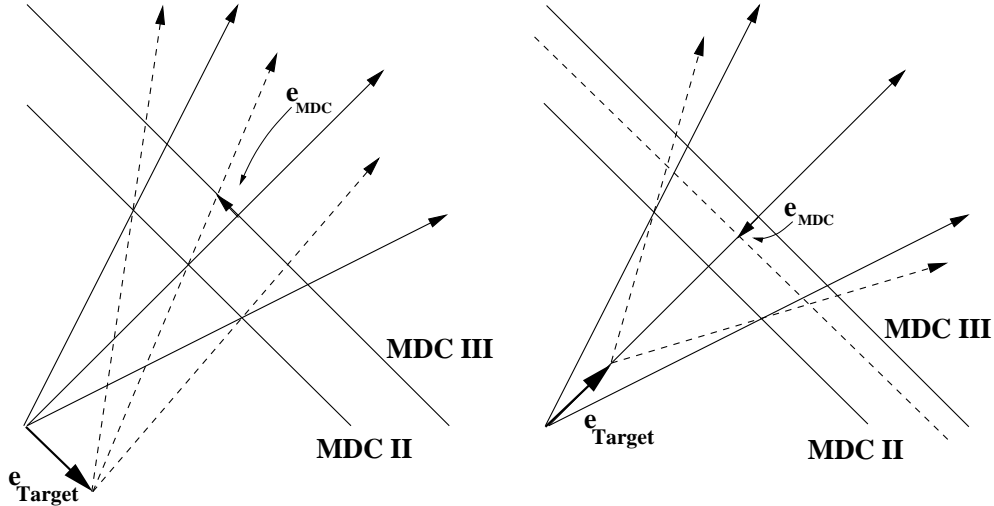


Figure 6.7: Scheme of the propagation of the target systematic error (e_{Target} in the scheme) to a systematic error on the modules position (e_{MDC}). The left picture shows an example where the systematic deviation is perpendicular to the axis target-modules, while in the right side is parallel.

able sectors. In particular, the departure of the fitted mean value of the Δx and Δy residuals from zero in the different zones and sectors indicates the random error in the parameters V_0 and V_1 (parallel to the coordinates X_{MDC} and Y_{MDC} , respectively). For the distribution Δy , the mean values of the fitted peaks are narrowly distributed, with a width below $100 \mu m$, while for Δx is below $150 \mu m$.

From the fitted means of the projections of the two dimensional histograms in the different (well separated) zones on the module planes, it is possible to find out a limit for the random errors in the angular parameters. Taken again the data over all sectors, the random errors are below $0.5 mrad$ in the rotation around the module X_{MDC} and Y_{MDC} axis, and less than $0.2 mrad$ in the rotation around the z axis.

The large systematic errors produced by the target position estimate uncertainties are the dominant effect. The systematic errors in the parameters V_0 and V_1 , following the X_{MDC} and Y_{MDC} directions, are approximately propagated as the ratio of the distance from the reference module to the target and the distance from the reference module to the plane where the *Hits* are projected (see figure 6.7). For the alignment of modules I and II, that are quite close, the ratio takes the value 0.25. Then, the

systematic errors³ on V_0 and V_1 are expected to be below 0.13 *mm* and 0.35 *mm*. For the modules II and III, the ratio takes the value 0.9, and the systematic errors are below 0.45 *mm* and 0.90 *mm*. The systematic error in the parameter V_2 (mainly, the distance between modules) follows approximately the same rule for small errors in the target position, as it is shown in the right graph of 6.7. Then, the V_2 systematic errors can be limited by 0.15 *mm* and 0.47 *mm* for the alignment of modules I - II and II - III, respectively.

The alignment procedure for sectors with two modules has been used successfully to estimate both the position parameters of the modules and their errors. In particular, the random errors has been found to be slightly larger than those obtained in simulation, an expected result due to the tracking lacks. The large value of the systematic error in the target position estimate introduces large systematic errors in the alignment parameters. The method provides visual tools for the evaluation of the results.

6.4 Alignment of sectors with three modules

For those sectors where three modules were operative during the data taking period, the advantageous alignment method for three modules, introduced in section 5.4, can be used.

The *Hits* in the three modules are selected to ensure that they are generated by the same particle track. The coordinate system of the intermediate module is taken as the reference system, and their *Hits* are extrapolated to the external module, searching for a partner *Hit*. If the trivial selection is fulfilled (one and only one *Hit* found in a square window around the extrapolated point, see subsection 5.3.2), the selected pair of *Hits* is trivially combined to obtain a straight line which is extrapolated on the third inner module. The third *Hit* is selected if it is the only one found in a window around the extrapolation. The residuals distribution obtained from the last extrapolation a fitted and filtered according to the 4-dimensional probability surfaces described in subsection 5.3.2. The selected *Hit* combinations are then used as input in the three modules alignment method described in section 5.4. This arrangement has been selected for simplicity and robustness in the analysis of the data tested up to now. The order in which the projection is performed and the reference system chosen is completely selectable during the analysis.

This section deals with the results of the previous scheme applied to the *Hits* obtained in modules MDC I-MDC II-MDC III in sector 3, using

³The results of table 6.2 has been taken into account in this error estimation.

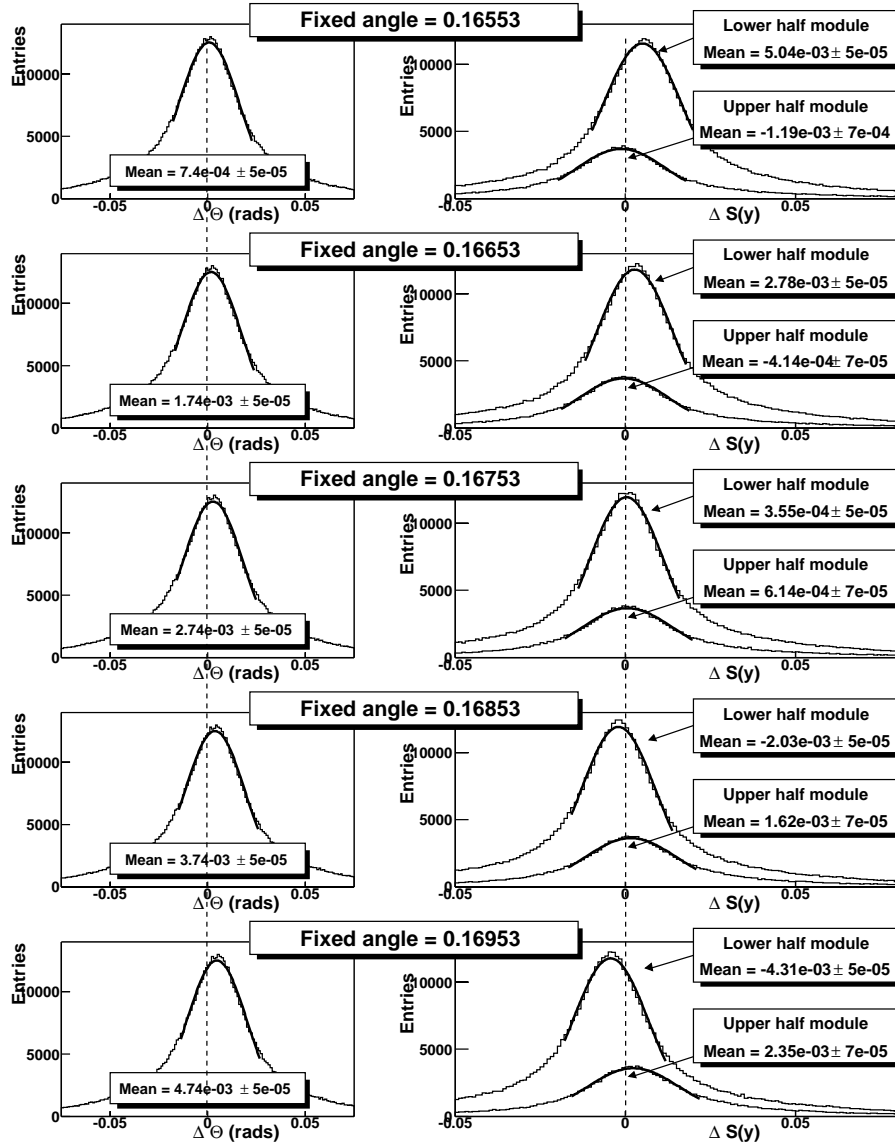


Figure 6.8: Differences in the Hit slopes and angles for several values of the fixed angle θ_{I-II} . In the left column, the differences $\Delta\Theta$ between the angles obtained from the Hit slopes in module II and in module I (transformed to the coordinate system of module II) are displayed. The right column shows the differences between the module I Hit slopes $S(y)_I$ and the slopes reconstructed from the coordinates of the Hits in both modules, for the lower and upper half of the module.

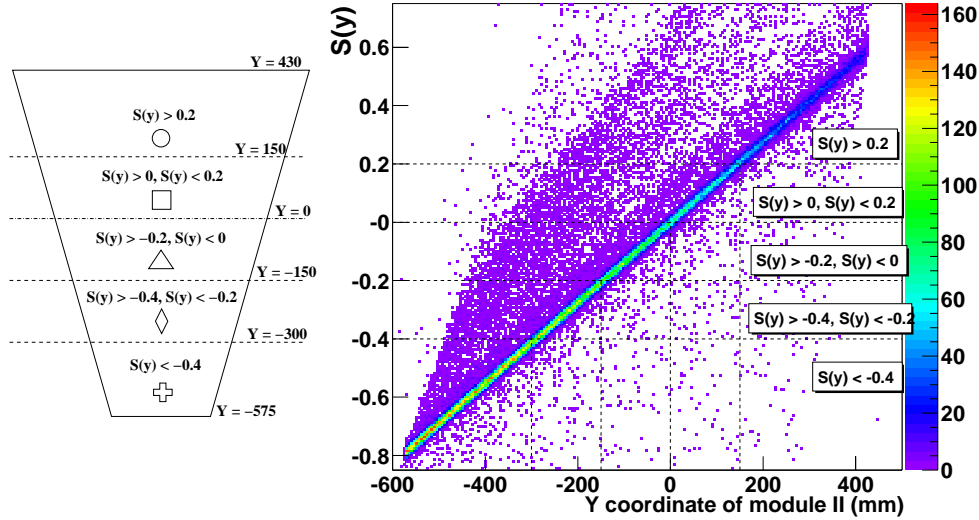


Figure 6.9: Right: slope component along the Y_{MDC} direction ($S(y)$) vs the coordinate Y_{MDC} along the module. A set of bands limited by the value $S(y)$ are bounded by dashed lines. The data correspond to the simulation used in the previous chapter in the three modules alignment section. Left: approximate Y_{MDC} coordinate of the bands boundary, for the linear part of the right histogram. The icons representing each band are going to be used in the next figures.

November 2001 data and the Dubna tracking. To get started, the initial relative transformations between the modules are fixed in their “design” values. The minimization is performed fixing the second Euler angle in the transformation between the inner modules θ_{I-II} , repeating the procedure shown in simulation. To select the best value, θ_{I-II} steps along a suitable range, obtaining a different minimization result for each value. Then, the slopes of the *Hits* produced by the same track in different modules are compared, in analogy with the analysis of section 5.4.2.

The histograms displaying the differences between the *Hit* slopes given by two modules are filled, and the mean values of the peaks are obtained by fitting to a gaussian. Figure 6.8 shows the differences in the *Hit* slopes and angles for several values of the fixed angular parameter (the design value for the second Euler angle between MDC I and MDC II is $\theta_{I-II} = 0.1710 \text{ rad}$). The figure should be compared with figure 5.21, that was done for the simulated data. The value of the angle θ_{I-II} , can be obtained from each column of histograms, as it was explained in section 5.4.2.

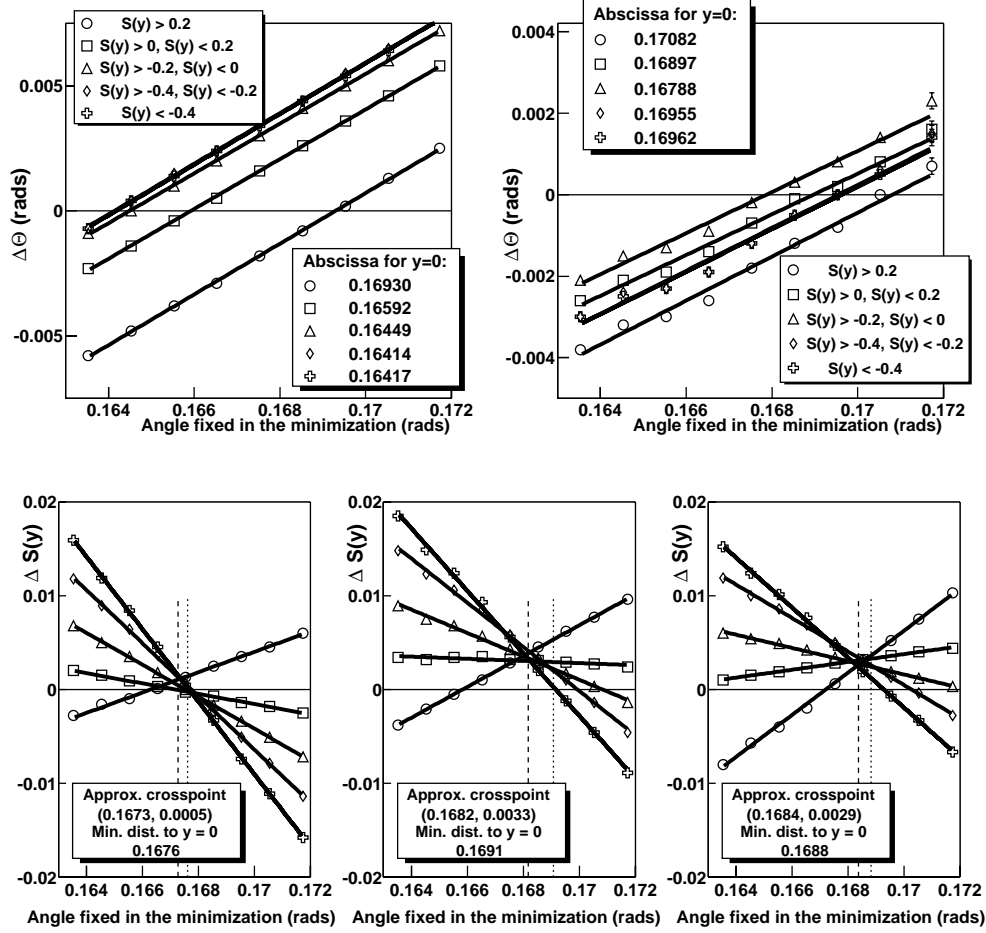


Figure 6.10: *Top: differences between the angle Θ reconstructed in modules I and II (left) and modules II and III (right) vs. the values of the fixed angle in the minimization θ_{I-II} and for each slope band. Bottom: differences between the slope component $S(y)$ of the Hits in a module and the slope from the straight line passing through the Hits. From left to right, Hits from module I, II and III are compared. In all pads, the points represent the mean value of a gaussian fit to the differences in the angle Θ or slope $S(y)$, for each band. Each straight line is a fit to the points in the respective band.*

For the analysis of real data, the two criteria used to determine the angle θ_{I-II} return a significantly different value. Comparing the differences $\Delta\Theta$ (see the definition in the equation 5.57, section 5.4.2) between the inner modules (left histograms in 6.8), it is obtained an angle of $\theta_{I-II} =$

0.16476 *rad*, whereas the comparison of the slopes in the lower and upper part of module I with the slopes given by the reconstructed straight lines (\vec{a} , defined in equation 5.52) indicates a cross point for an angle of $\theta_{I-II} = 0.16748$ *rad*. Moreover, the comparison of the differences $\Delta\Theta$ between the outer modules (MDC II and MDC III), that are not shown in the figure, returns a different value, even larger, of $\theta_{I-II} = 0.16943$ *rad*.

In order to obtain more information, the comparison between the slopes has been performed separately for five different chamber portions (bands), as shown in figure 6.9. The right histogram displays the linear relation between $S(y)$ (the slope component of the incident particle along the Y_{MDC} direction) and the coordinate Y_{MDC} for module II; the *Hits* are ranged by their $S(y)$ value (horizontal dashed lines) and the approximate Y_{MDC} cuts are also shown (vertical dashed lines). The left part shows the approximate portions defined for module II, and the icon which is going to be used in the following figures to identify each band.

For all the *Hits* inside a band, the differences of the angles reconstructed by modules I and II are histogrammed. The peak position of each histogram is fitted to a gaussian. From the five fits, five mean values are obtained, for a given θ_{I-II} . The top left pad in figure 6.10 shows the means as a function of the θ_{I-II} angle, for the *Hits* obtained using the Dubna *Hit* finder. The same procedure is used to produce the graph in the top right pad, for the angles reconstructed by modules II and III. The results for each band are separately fitted to a straight line.

For each straight line, the value of the abscissa for $\Delta\Theta = 0$ is the estimate of the optimal angle θ_{I-II} in the band and the fitted mean value of the difference between the *Hits* direction is zero. The value of the optimal angle differs significantly from band to band inside each graph. The comparison of the optimal angles obtained in the inner modules (left) and in the outer modules (right) do not match either. Fixing a θ_{I-II} value which results satisfactory for a given band will deliver a set of parameters after the minimization which does not lead to a matching between the *Hits* directions in other bands. These differences in the *Hit* directions in each band can be schematically shown in the lower picture of figure 6.11. The value $\theta_{I-II} = 0.168$ has been chosen in the picture, and the arrows in each module and band represents the approximate mean value of the difference between the *Hits* directions. The numbers in the arrows are the angle (in *mrad*) between the fitted means, extracted from the top histograms of figure 6.10.

The second criterion compares the slopes of the *Hits* in different bands with the slopes of the straight lines (\vec{a}) constructed using the *Hit* position

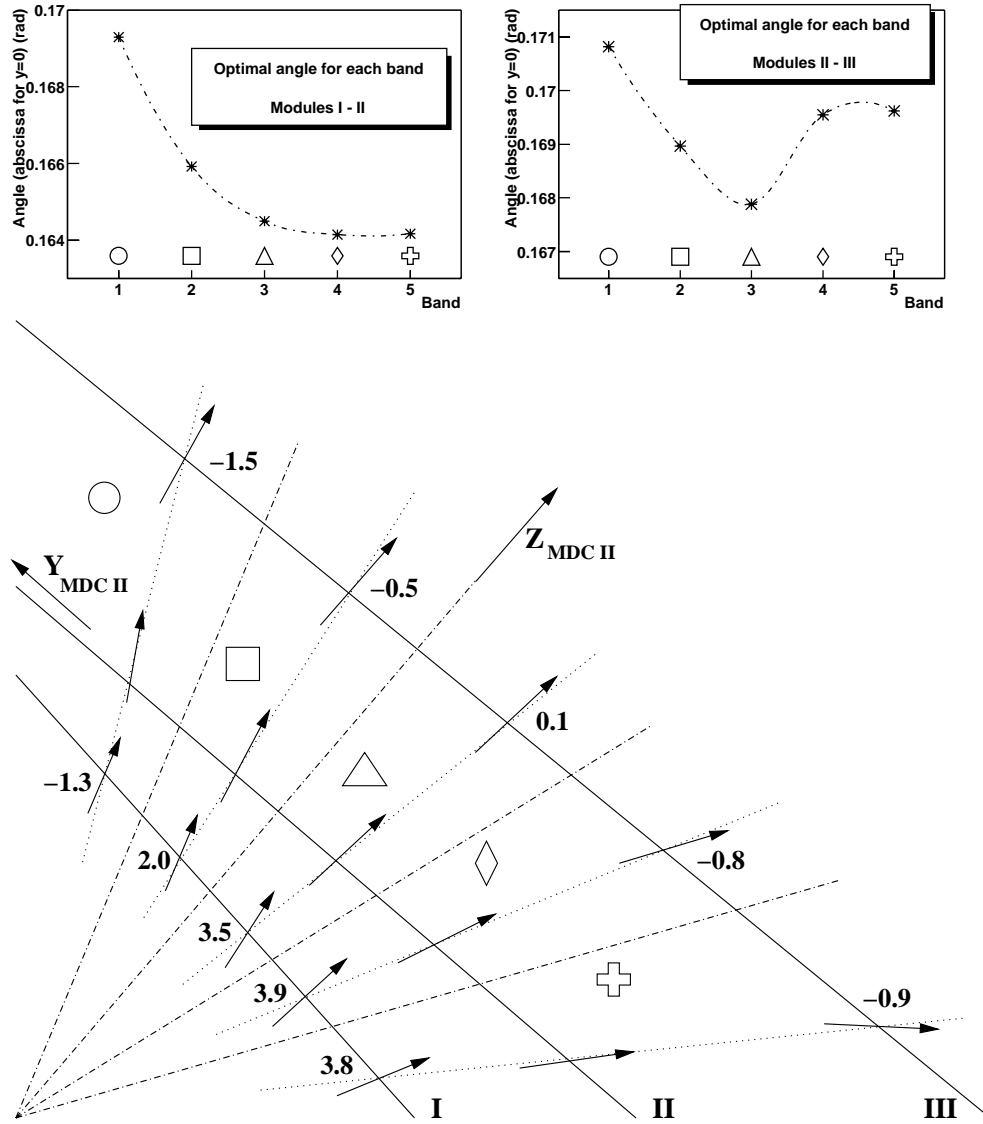


Figure 6.11: Top: value of the optimal angle θ_{I-II} for the different bands (labeled by their icon), for the comparisons between modules I and II (left) and II and III (right). Bottom: schema of the mean differences in the Hit directions (arrows) for each band (labeled by their icon) and for the value $\theta_{I-II} = 0.168$. The numbers in the arrows correspond to the angle (in mrad) between the fitted means, extracted from the top histograms in figure 6.10.

in the modules. The points in the lower pads of figure 6.8 represent the fitted mean of the differences of slopes for the bands, in resemblance with the analysis of section 5.4.2 (right part of figure 5.22, where it is made only for the upper and lower halves of the module). The three pads represent, from left to right, the comparison with the *Hits* in module I, II and III, respectively. The points of each band fits nicely to a straight line. In simulation, the straight lines cross in a point of the plane; its abscissa is the true value of the angle θ_{I-II} while the ordinate should be zero, because the slopes of the *Hits* and the slope of the vector \vec{a} made from the *Hits* coincides for all bands, in mean.

Two approximations has been used to define the cross-point between the lines in figure 6.8: the point of minimum distance to the straight lines (referenced as “Approx. crosspoint” in the figure) and the abscissa which returns a minimum distance between the line $y = 0$ and the set of straight lines. The first approximation is a point, whose abscissa correspond to the angle θ_{I-II} for which the *Hit* slopes in all bands differ in the same quantity from the slopes of \vec{a} , in mean. The ordinate returns the mean difference, common to all bands. From the figure, the ordinate of the cross point is practically zero for the first module, but is quite large for the second and third modules. The second approximation returns the angle θ_{I-II} for which the *Hit* slopes differ less from the \vec{a} slopes, in mean.

The differences of the values of the angles using our criteria makes difficult to fix an angle θ_{I-II} in the minimization and return a set of alignment parameters. A rational option is to use the mean of the values given for the criteria in the three modules as an estimate of the angle. The parameters obtained fixing the angle θ_{I-II} at a standard deviation from the mean could serve as an estimate of the uncertainty on the parameters. Table 6.3 contains the parameters obtained for the minimization in the three cases: the mean value $E(\theta_{I-II}) = 0.16823$, and $E(\theta_{I-II}) \pm \sigma(\theta_{I-II})$.

The results show a stable behavior of the minimization for the three angles. As described during the algorithm explanation in section 5.4, the change in the angle produces the expansion (when θ_{I-II} increases) or collapse of the three modules system. The parameter V_2 , which represents basically the distance between the modules, is then strongly affected by the change in the fixed angle θ_{I-II} . Other parameters (V_1 in both transformations) drift slowly, slightly above the value of their random errors. The parameter V_0 and the relative rotation between the modules remains stable within the minimization random errors.

To prove the independence of the results on the election of the second Euler angle as the fixed parameter in the minimization, the same procedure

Transformation parameters between modules I - II			
	Mean+sigma	Mean	Mean - sigma
ϕ	-1.5725 ± 0.0001	-1.5726 ± 0.0002	-1.5723 ± 0.0003
θ	0.16886	0.16823	0.16760
ψ	1.5735 ± 0.0001	1.5735 ± 0.0002	1.5732 ± 0.0003
V_0	0.985 ± 0.018	0.985 ± 0.020	0.978 ± 0.018
V_1	-75.430 ± 0.019	-75.482 ± 0.019	-75.561 ± 0.013
V_2	-182.204 ± 0.087	-182.006 ± 0.082	-181.589 ± 0.042
Transformation parameters between modules II - III			
	Mean+sigma	Mean	Mean - sigma
ϕ	-1.5460 ± 0.0001	-1.5459 ± 0.0007	-1.5467 ± 0.0002
θ	0.0920 ± 0.0002	0.0921 ± 0.0002	$0.0921\pm 8e-05$
ψ	1.5377 ± 0.0001	1.5376 ± 0.0007	1.5383 ± 0.0002
V_0	-10.297 ± 0.065	-10.300 ± 0.069	-10.274 ± 0.063
V_1	-118.118 ± 0.079	-117.986 ± 0.079	-117.717 ± 0.054
V_2	663.07 ± 0.36	662.38 ± 0.34	660.90 ± 0.16

Table 6.3: Relative alignment parameters obtained after the minimization fixing the angle θ_{I-II} in the mean value of the different criteria (see text), and at a standard deviation from the mean. The random errors given by the minimization for each parameter are included. The angles are given in rad and the vector components in mm.

has been performed fixing the distance between the outer modules (V_2 between module II and III, following our usual notation). The results have matched those previously obtained within the random errors of the minimization.

As a conclusion, the alignment procedure for sectors with three modules has proven to deliver more accurate alignment parameters, being independent of the target position. The method returns an estimation of the error and offers the evaluation of the *Hits* direction in different module bands.

6.5 Beam line reconstruction

Making use of the knowledge about the relative positioning of the modules and the target, an approximated picture of the beam line can be obtained. The particular plots of this section has been obtained with *Hits* from the Santiago tracking.

Taken the set of MDC *Hits* which have passed the compatibility criterion, let us construct the tracks (straight lines) from the *Hit* coordinates

in two modules, for all the sectors and for all the sample. Let us represent each straight line using the equations in two projecting planes

$$\begin{aligned}x(z) &= a_x + b_x z \\y(z) &= a_y + b_y z\end{aligned}\tag{6.2}$$

in the laboratory system, including a displacement of the whole set of modules to locate the target at the point $(0, 0, 0)$.

Several relevant quantities can be obtained once the straight line is defined. The line can intersect the theoretical beam line, the Z axis, or simply pass close to the axis at a distance ρ . For the sake of notation, let us call (x_t, y_t, z_t) to the point in the line at a minimum distance of the Z axis, and ρ to that distance. The line between the closest points is normal to both the track estimate and the Z axis, and therefore should lie in a $Z = z_t$ plane. Writing the track estimate, equation 6.2, as

$$\frac{x - a_x}{b_x} = \frac{y - a_y}{b_y} = \frac{z - 0}{1}\tag{6.3}$$

and the equation of the line which joins the closest points in both lines as

$$\frac{x}{l} = \frac{y}{m}\tag{6.4}$$

then, the closest point of the line to the axis Z is

$$\begin{aligned}x_t &= \frac{a_x b_y^2 - a_y b_x b_y}{b_x^2 + b_y^2} \\y_t &= \frac{a_y b_x^2 - a_x b_x b_y}{b_x^2 + b_y^2} \\z_t &= -\frac{a_y b_y + a_x b_x}{b_x^2 + b_y^2}\end{aligned}\tag{6.5}$$

From the first two terms it is possible to determine the distance between the track closest point to the Z axis and the axis

$$\rho = \sqrt{x_t^2 + y_t^2} = \frac{a_y b_x - a_x b_y}{\sqrt{b_x^2 + b_y^2}}\tag{6.6}$$

It is also possible to define the polar and azimuthal track angles with respect to a polar coordinate system centered in (x_t, y_t, z_t) and oriented in

such a way that the axes are parallel to the laboratory axes. The track equation in this system is simply

$$\begin{aligned}x(z) &= b_x z \\y(z) &= b_y z\end{aligned}\tag{6.7}$$

The shortest distance d from the track to the design target position ($x = 0, y = 0, z = 0$) can be easily obtained

$$d^2 = \frac{a_x^2(b_y^2 + 1) + a_y^2(b_x^2 + 1) - 2 a_x a_y b_x b_y}{b_x^2 + b_y^2 + 1}\tag{6.8}$$

Taken $z = 1$ in equation 6.7 and taking the usual spherical coordinates definition, the polar angle θ and the azimuthal angle ϕ are

$$\begin{aligned}\theta &= \text{arctg} \left(\frac{b_y}{b_x} \right) \\ \phi &= \text{arctg} \left(\sqrt{b_x^2 + b_y^2} \right)\end{aligned}\tag{6.9}$$

Figure 6.12 shows the beam line reconstruction. The closest points to the Z axis (equation 6.5) has been obtained for the inner modules in the top pad, and for the modules II and III in the bottom pad. The target has been cut in the histogram in order to zoom in the details. The entry and exit windows of the RICH beam pipe and the Start detector are easily recognized in both histograms. The Veto can only be seen in the bottom histogram, due to the upstream position of the modules. Additional interacting points, as that marked with a question mark, are detected.

The top two-dimensional histograms in figure 6.13 display both the distance ρ to the Z axis for the closest point of the tracks and the polar angle of the tracks. The histograms are made using the *Hits* of module I and II, in sector 4. A complete picture of the target zone is obtained combining the information of the beam line reconstruction and the ρ distance, which informs about the spread of the particles vertex in a coordinate perpendicular to the Z axis. In the lower pads, a zoomed view of the ρ vs Z histogram is shown, centered on the main target region (left) and the RICH exit window (right). The RICH exit window separates the vacuum beam pipe from the atmosphere at normal pressure. The beam interacts with the nucleus of the air gases, producing the continuous line above the window peak.

The histograms in figures 6.12 and 6.13 demonstrate the capability of the inner modules of the spectrometer to separate the vertex origin of the tracks, and select those coming from the reaction target.

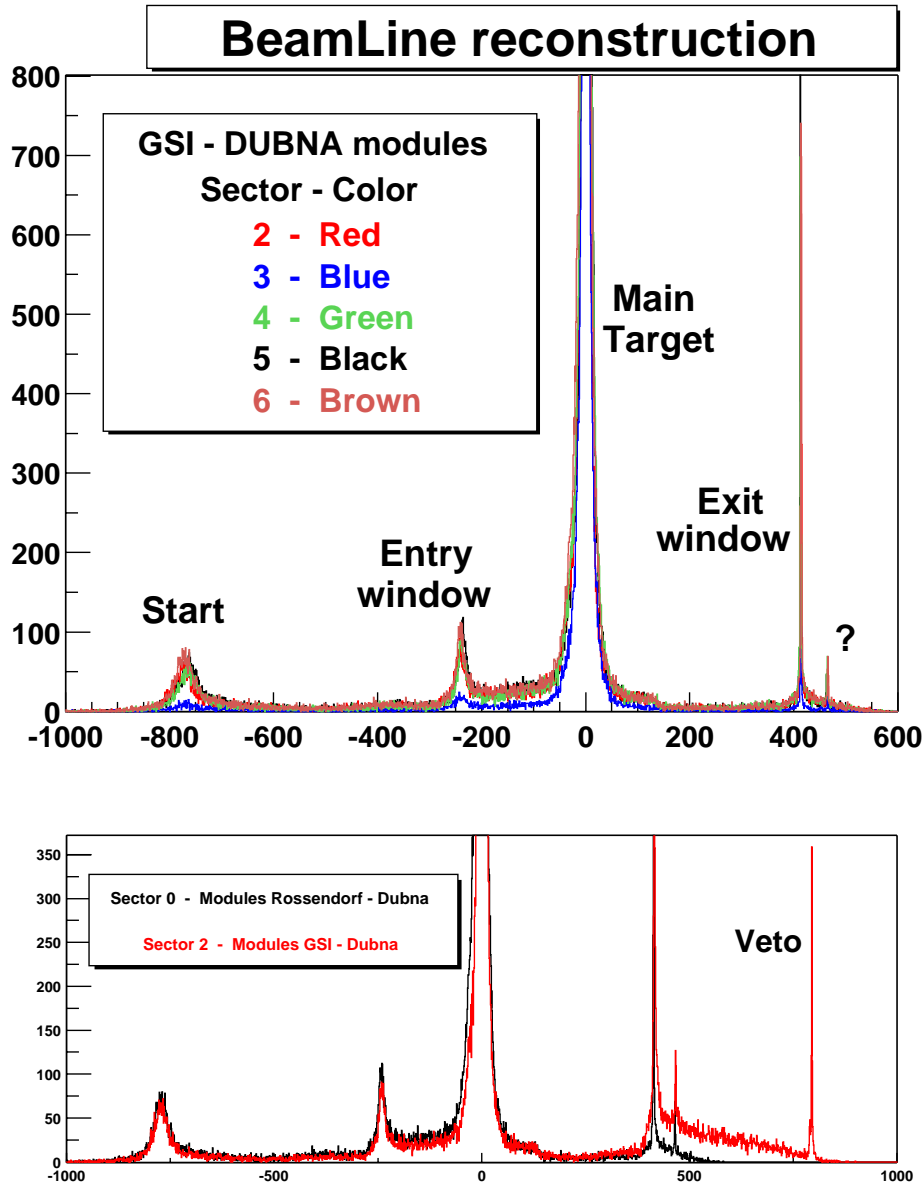


Figure 6.12: Histogram showing the z (laboratory) coordinate of the track point closest to the axis Z (the so-called beam line reconstruction histogram). The top pad represents the reconstruction using all the available sector (5) with modules I and II. In the bottom pad, the reconstruction for the two sector with modules II and III are shown.

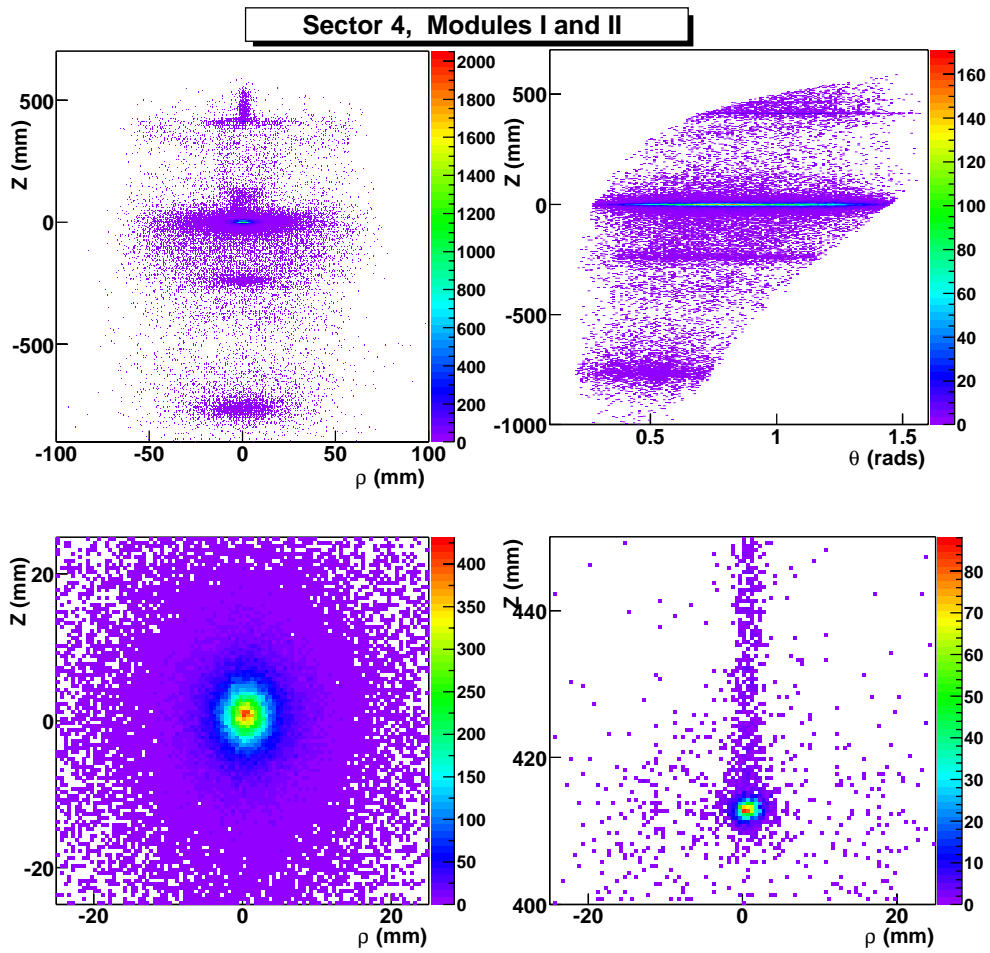


Figure 6.13: Top left: distance ρ to the Z axis vs. the Z coordinate for the closest point of the tracks to the axis Z. Top right: polar angle of the tracks vs. the Z coordinate for the closest point of the tracks to the axis Z. Bottom: zoom of the ρ vs. Z histogram, centered on the main target region (left) and the RICH exit window (right). All histograms are made with the Hits of modules I and II, in sector 4.

Conclusions

In this work, several tools and methods have been developed to obtain the relative alignment of the MultiWire Drift Chambers (MDCs), the main tracking detectors in the HADES spectrometer.

In a first step, the requirements of the different alignment tools and their influence on the resolution in the reconstructed momentum of the positrons and electrons and the invariant mass of the pair, are discussed. These requirements have been explicitly expressed as relative displacements and rotations of the modules with respect to the parameters used in the reconstruction analysis procedures.

As a consequence of the required precise alignment, after the mechanical study of the spectrometer features, it was decided to monitor the relative displacements of the outer MDC modules with respect to the inner ones. A set of RASNIK devices has been considered as optimal candidates for this hardware monitoring and a specific RASNIK configuration has been developed. In particular, the dependence of the light incidence angle onto the camera and of the lens aperture on the resolution have been studied. For test purposes, an experimental setup has been developed, where the optimal values for the parameters has been fixed.

The implementation of the RASNIK devices in the spectrometer has required the design of custom-made pieces. This task has been accomplished from the mechanical design of all pieces up to the final installation in the spectrometer.

The RASNIK setup, just as it was ready for commissioning, has been first tested to check its resolution and stability. The bench-test results have confirmed performances well below the requirements.

A complete monitoring program (RAHAD) has been developed to perform several specific task. In particular it performs a data calibration and transformation, according to the coordinate systems of the MDC modules, as well as the interface with the “HADES Slow Control System”, which is based on EPICS.

Once the RASNIK setup was installed on the spectrometer, the resolu-

tion of the monitors was again measured, confirming performances below the requirements. The RASNIK results have been successfully correlated with temperature changes and with the magnetic field forces acting on the mechanical structures. The outcome of the RASNIK monitoring has been proven to be useful in order to correct the alignment parameters, obtained by software methods.

Regarding the software methods, several iterative algorithms have been developed in order to obtain the relative alignment parameters between modules. For those sectors where only two modules were available, an algorithm based on the analytical minimization of residuals has been adopted, including a correction on the relative rotation of the modules. The use of this algorithm includes the determination of the target position, which is also implemented in the so-called “Target Finder” algorithm. The so-called “three modules algorithm” has been chosen as the main method to obtain the parameters of the relative alignment; the method is based on the minimization of the angle between segments constructed in contiguous MDC modules.

The different algorithms have been first tested under simulation, checking their convergence to the correct parameters. The errors have been estimated and the resolution in the determination of the relative alignment parameters has been proven to fulfill the requirements.

A set of data (Carbon beam at 1 GeV on a Carbon target, November 2001 run) has been analyzed using the alignment algorithm. The application of the methods has allowed the detailed study of several features of the MDCs and served as a check of the track-reconstruction procedures.

Under these circumstances, the alignment parameters have been estimated, including their uncertainty intervals.

Appendix A

Theoretical frame of the HADES Physics

This appendix is included to briefly outline the theoretical frame where the HADES experiment is contained. It is mainly extracted from the works of M. Soyeur and W. Weise [1, 2] in the International School of Heavy Ion Reactions in 1993 in Erice, Italy, and references herein.

A.1 The vector mesons

The ρ and ω mesons have, approximately, the same mass (within less than 2%); while the first is a broad resonance of two pions, the second is a narrow resonance of three pions. The mass seems to be unrelated to their pion content and are mostly of QCD origin.

The Vector Dominance Model (VDM) states that photons couple to hadrons at low energy through intermediate vector mesons [1]. Then, being $g_{\rho\pi\pi}$ and g_ρ the $\pi\pi \rightarrow \rho$ and $\rho \rightarrow e^+e^-$ coupling constants, M_ρ the ρ mass and q the 4-momentum transfer, the pion form factor takes the form

$$F_\pi(q^2) = \frac{g_{\rho\pi\pi}}{2g_\rho} \frac{M_\rho^2}{M_\rho^2 - q^2} \quad (\text{A.1})$$

for all the values of q^2 from $q^2 = M_V^2$ to $q^2 = 0$. The photon-vector meson coupling strengths can be determined from the e^+e^- partial decay widths of the vector mesons, showing a probability an order of magnitude larger for the conversion of the virtual photon in ρ than in ω . This is also the result from a SU(3) quark model calculation, where the photon coupling is proportional to the quark charge. Experimental tests of the model indicate an accuracy of the VDM in the order of the 20%.

ρ^0	$\pi^+\pi^-$	$\sim 100\%$
	$\pi^+\pi^-\gamma$	$(9.9 \pm 1.6) \times 10^{-3}$
	...	
	e^+e^-	$(4.49 \pm 0.22) \times 10^{-5}$
ω	$\pi^+\pi^-\pi^0$	(88.8 ± 0.7)
	$\pi^0\gamma$	(8.5 ± 0.5)
	$\pi^+\pi^-$	(2.21 ± 0.30)
	...	
	$\pi^0e^+e^-$	$(5.9 \pm 1.9) \times 10^{-4}$
	e^+e^-	$(7.07 \pm 0.19) \times 10^{-5}$
ϕ	K^+K^-	(49.2 ± 0.7)
	$K_L^0K_S^0$	(33.8 ± 0.6)
	$\rho\pi +$	
	$\pi^+\pi^-\pi^0$	(15.5 ± 0.6)
	$\eta\gamma$	(1.297 ± 0.033)
	...	
	e^+e^-	$(2.91 \pm 0.07) \times 10^{-4}$

Table A.1: Vector mesons main decay channels. Also it is included the branching ratio for a pair e^+e^- production. Data extracted from [3].

Using the VDM, and the hadronic form factor dependence, which contains a term

$$F(q^2) = \frac{M_V^2}{M_V^2 - q^2} \quad (\text{A.2})$$

as it is shown in equation A.1, one can deduce the production of peaks reflecting the poles corresponding to vector meson masses (smoothed by their widths), and, therefore, such data are very sensitive to changes in the ρ and ω masses.

Different models predict a vector meson mass and width modification with temperature and density. In particular, if one considers the nucleons surrounded by a dense soup of virtual scalar quark-antiquark pairs, the QCD vacuum, the effect is a dropping of vector masses in compressed hadronic matter. The density of quark-antiquark pairs is described by the chiral condensate, with an expectation value ten times larger than the normal nuclear matter. A graphical explanation can be given by taking into account the reduction in the number of quark-antiquark pairs due to the increasing number of nucleons in the same volume. Then, the chiral condensate drops with the increase of the baryon density.

To observe experimentally the changes in the vector meson properties

one should study a decay whose products do not change by strong final-state interactions. This channel exists: the decay into $e^+ - e^-$ (dilepton pair). If the decay is produced in a short time (around $10 \text{ fm}/c$), the vector meson mass can be reconstructed as it was during the dense phase, because the 4-momentum vectors of the leptons are not changed by the strong interaction. The probability of such a decay is very low (see table A.1) and the number of dileptons coming from another sources can obscure the signal. In particular, the Dalitz decay of the π^0 and the η mesons contributes in the region around $100 \text{ MeV}/c$ and between $100 \text{ MeV}/c$ and $400 \text{ MeV}/c$ respectively. The η Dalitz decay is delayed with respect to the vector meson decay and therefore out of the dense phase, due to the larger lifetimes of the pseudo-scalar mesons (when compared with the vector mesons). An accurate measurement of these dilepton sources in the systems under study is required to obtain a clear signal from the vector mesons.

It is worth of mention here that the dilepton mass invariant spectrum is obtained from a combination of dilepton sources, generated at different stages of the reaction. Even the vector meson decays would not correspond to the dense phase, but to $\pi^+\pi^-$ annihilation processes in the expansion phase, where a ρ meson is produced. In the case of ω and ϕ , being their contribution to the dilepton mass invariant spectra weaker than those of ρ , it is expected a pure contribution from the dense phase.

A.2 The chiral symmetry and the quark mass

Let us briefly introduce how the hadron properties can change in dense matter from the point of view of QCD in the low-energy region, where the strength of the interaction prohibits any systematic perturbative approximation scheme. According to broadly used models, hadrons are composed of quarks and gluons and their strong interactions, mediated by the meson fields, change their intrinsic structure in the close vicinity of other nucleons. This effect is expected to increase when a dense phase reduces the mean distance between nucleons (from 1.8 fm at ρ_0 to less than 1.3 fm at $\rho = 3\rho_0$).

Following [2], the QCD Lagrangian with three light quark fields $q = (u, d, s)$, divided into two parts, with and without mass, is given by

$$L_{QCD} = L_{QCD}^{(0)} + \Delta L_{mass} \quad (\text{A.3})$$

with

$$L_{QCD}^{(0)} = \bar{q}i\gamma_\mu(\partial^\mu - igG^\mu)q + \frac{1}{4}F_{\mu\nu}^2 \quad (\text{A.4})$$

$$\Delta L_{mass} = -\bar{u}m_u u - \bar{d}m_d d - \bar{s}m_s s \quad (\text{A.5})$$

where G_μ is the gluon field and the quark masses are introduced in each m_i , the small mass term which can be considered as a perturbation. Let us center on the exact and approximate symmetries of the QCD Lagrangian, from where it is possible to derive part of the low energy dynamics of the hadrons. In particular, the $SU(3)_R \times SU(3)_L \times U(1)_V$ symmetries of QCD and their corresponding conserved currents will establish rules which govern the low energy dynamics of the strongly interacting systems, irrespective of whether their relevant degrees of freedom are elementary quarks and gluons or composite hadrons. The first elemental symmetry of QCD is $SU(3)_{color}$ gauge symmetry. It is also invariant under the $U(1)_V$ group which generates a global phase transformation, giving a conserved current which is the baryon current.

Let us consider the mass-less Lagrangian ($L_{QCD}^{(0)}$). The mass-less quark field can be separated by the projector (covariant spin)

$$q_{R,L} = \frac{1}{2}(1 \pm \gamma_5)q \quad (\text{A.6})$$

into right and left handed fields, which remain decoupled under the gluon fields interaction (as long as they are mass-less). Then, the mass-less Lagrangian is exactly invariant under the chiral flavor group $SU(3)_R \times SU(3)_L$

$$q_{R,L} \rightarrow e^{i\alpha_{R,L}^a \frac{\lambda^a}{2}} q_{R,L} \quad (\text{A.7})$$

Here the transformations are independent of the three left and right quarks. The λ^a are the ($a = 1, \dots, 8$) independent Gell-Mann unitary matrix. As a consequence of the Noether theorem, eight vector currents

$$V_\mu^a = \bar{q}\gamma_\mu \frac{\lambda^a}{2} q \quad (\text{A.8})$$

and eight axial vector currents

$$A_\mu^a = \bar{q}\gamma_\mu \gamma_5 \frac{\lambda^a}{2} q \quad (\text{A.9})$$

are rigorously conserved, that is

$$\partial^\mu V_\mu^a = \partial^\mu A_\mu^a = 0 \quad (\text{A.10})$$

in the chiral limit with $m_u = m_d = m_s = 0$. The mass-less Lagrangian $L_{QCD}^{(0)}$ is also formally invariant with respect to the axial $U(1)_A$ symmetry (transformation $q \rightarrow e^{i\gamma_5\alpha}q$). In nature, this symmetry is broken, as it is reflected in the large mass of the η' meson. It is called the axial anomaly in QCD.

The ΔL_{mass} term, involving the mass of the quarks, breaks the $SU(3)_R \times SU(3)_L$ chiral symmetry *explicitly*. All the terms in ΔL_{mass} contain a mixing part of the type

$$\bar{q}q = \bar{q}_L q_R + \bar{q}_R q_L \quad (\text{A.11})$$

This part of the Lagrangian can be studied as a perturbation (Chiral Perturbation Theory) due to the low bare quark masses (a few MeV) compared with the nucleon mass ($\sim 1 GeV$).

Chiral symmetry is also *spontaneously broken*. If the symmetry were conserved in nature, one would see a hadron spectra showing degenerate pairs of states with positive and negative parity. Instead, it is observed an octet of pseudo-scalar mesons with small masses, well separated from their massive $J^P = 0^+$ partners.

The spontaneously broken chiral symmetry leads to a finite quark condensate in vacuum [4]:

$$\langle \bar{q}q \rangle_0 \approx \langle \bar{u}u \rangle_0 \approx \langle \bar{d}d \rangle_0 \approx -(245 MeV)^3 \quad (\text{A.12})$$

As the density or the temperature (or both) increases in a hadronic system, the spontaneously broken symmetry is expected to be partially restored and the quark condensate would decrease. At normal nuclear matter density, the condensate is already seen to decrease by $\approx 1/3$. The decrease of quark condensate in medium may lead to reduced hadron masses.

Bibliography

- [1] M. Soyeur; *Vector Mesons in the Nuclear Medium*, in International School of Heavy ion Reactions, 3rd Course, Erice, Italy, October 1993. World Scientific, Singapore, 1994.
- [2] W. Weise; *Chiral Dynamics and Hadrons in Dense Matter*, in International School of Heavy ion Reactions, 3rd Course, Erice, Italy, October 1993. World Scientific, Singapore, 1994.
- [3] Groom *et al.*, Particle Data Group. *Review of Particle Physics*, Eur. Phys. J. C 15, 1-878 (2000).
- [4] C.M. Ko, G.Q. Li; J. Phys.G: Nucl. Part. Phys **22** (1996) 1673-1725.

Appendix B

Previous dilepton studies

HADES is not the first attempt to deal with the leptonic decay of short lived resonances. Regarding the collision energy, two lines are separated: medium energy studies performed at LBLN by DLS and ultra-relativistic energies at CERN by CERES, HELIOS1-3 and NA38-50-51. In two separate periods, from 1987 to 1989 and from 1990 to 1993, the DLS spectrometer at Lawrence Berkeley National Laboratory (LBNL) was the first detector able to obtain information in the medium energy range, despite of its low resolution and reduced acceptance.

B.1 The DLS results

The DLS (DiLepton Spectrometer) collaboration [1, 2] carried out a systematic study of e^+e^- production as a function of mass and energy, for p-p, p-nucleus and nucleus-nucleus collisions (Nb on Nb was the heaviest) at energies between 1.0 and 4.9 $AGeV$. During their working time, DLS system collected about 30000 lepton pairs.

The detector consisted of a two arm magnetic spectrometer, with a magnetic field supplied by two-arm's dipole magnet to analyze the particle momentum from their bent track, in the nearly uniform vertical magnetic field of about 1.5 kG . Two gas filled Cherenkov detector arrays allow electron identification. Also, two set of plastic scintillator form a hodoscope array located directly behind each of the Cherenkov arrays. The hodoscope arrays provide a greater segmentation than could be obtained in the Cherenkov systems and improve the capability of detection of charged particles. Finally a set of drift chambers, made of seven drift planes, supply both x and y information of the particle's passage through the spectrometer. This information is used for the track reconstruction.

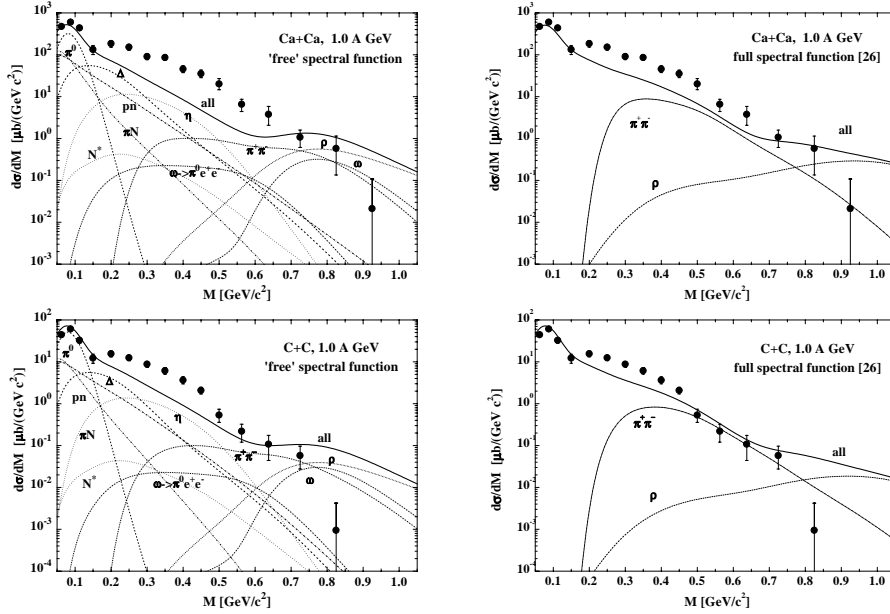


Figure B.1: Comparison between the differential cross section for di-electron production in DLS [2] and the BUU transport calculations [3]. In the left part, the ρ free spectral function is used. In the right part the full in-medium spectral function of ρ is used in the calculation of the decay yields and $\pi^+\pi^-$ annihilation. The thin lines indicate the individual contributions from the different production channels: starting from low masses, Dalitz decay $\pi^0 \rightarrow \gamma e^+ e^-$ (dashed line), $\eta \rightarrow \gamma e^+ e^-$ (dotted line), $\Delta \rightarrow N e^+ e^-$ (dashed line), $\omega \rightarrow \pi^0 e^+ e^-$ (dot-dashed line), $N^* \rightarrow N e^+ e^-$ (dotted line), proton-neutron bremsstrahlung (dot-dashed line), πN bremsstrahlung (dot-dot-dashed line); around masses of 0.8 GeV: $\rho^0 \rightarrow e^+ e^-$ (dashed line), $\omega \rightarrow e^+ e^-$ (dot-dashed line) $\pi^+\pi^- \rightarrow \rho^0 \rightarrow e^+ e^-$ (dot-dashed line). Taken from [3].

The main handicaps of the DLS spectrometer were a reduced acceptance (0.5-1%) and its limited mass resolution.

In the first set of runs the collision system Ca+Ca at 1.0 and 2.0 AGeV incident energy was studied. Within the given experimental error bars the extracted e^+e^- invariant mass spectra could be well reproduced in transport model calculations by an incoherent sum of dilepton yields from pn bremsstrahlung and free hadron decays. Hints at significant medium modifications of hadron properties could not be observed, although there was a limited event statistics and invariant mass resolution. The Ca+Ca collision system was revisited together with light systems (C+C, d+Ca,

He+Ca) in a second round of measurements with an improved experimental setup, better event statistics, and a more sophisticated data analysis [2]. As compared to the earlier measurements the new data had considerably smaller error bars and lead to a dilepton production cross section which is up to a factor 7 larger than predicted by conventional models. This time the discrepancy between the theoretical predictions and the experimental results were clear, mainly in the medium invariant mass range $200\text{MeV}/c^2 < M_{inv} < 600\text{MeV}/c^2$. The theoretical predictions [3] are obtained mixing the expected dilepton sources; such a “cocktail” can be made considering the free hadronic sources of the pairs or the in-medium spectral function of the vector mesons (mainly the in-medium effects for ρ meson). In the last case, the discrepancy is reduced but not enough to account for the complete excess. A simple dropping η mass scheme together with the full ρ spectral function can lead to dilepton spectra that are in good agreement with the data. However, the m_T scaling of pion’s and η ’s observed previously (by TAPS collaboration at GSI) cannot be reproduced within this dropping η mass scenario, which is also incompatible with the η photo-production data on nuclei. Up to now the discrepancy between data and transport calculations with many different assumptions could not be satisfactorily solved. The dilepton enhancement already seen in light ion collisions might eventually be a first hint at unexpected medium modifications.

B.2 CERES results

The CERES (Cherenkov Ring Electron Spectrometer) experiment studies the production of medium mass (between 0.2 and 1.5 GeV/c^2) e^+e^- pairs in p-p, p-nucleus and nucleus-nucleus collisions, at the CERN SPS energies. It was installed in 1990 at the H8 beamline of the CERN SPS North Area. Their beam schedule has included proton on Beryllium and Gold, Sulphur on Gold at 200 AGeV and more recently Lead on Gold at 160 AGeV .

The CERES detector consists of two azimuthally symmetric RICH (Ring Imaging Cherenkov) detectors, before and after a double superconducting solenoid. A pair of cylindrical silicon drift detectors before the first RICH allows particle tracking to the interaction point. The RICH detectors are virtually hadron-blind, while essentially all electrons create Cherenkov rings of asymptotic radius. In the last upgrade, a large TPC is added for particle tracking and improved mass resolution. A magnetic field, provided by a double superconducting solenoid, is introduced between the RICHs for momentum determination. A set of correction coils

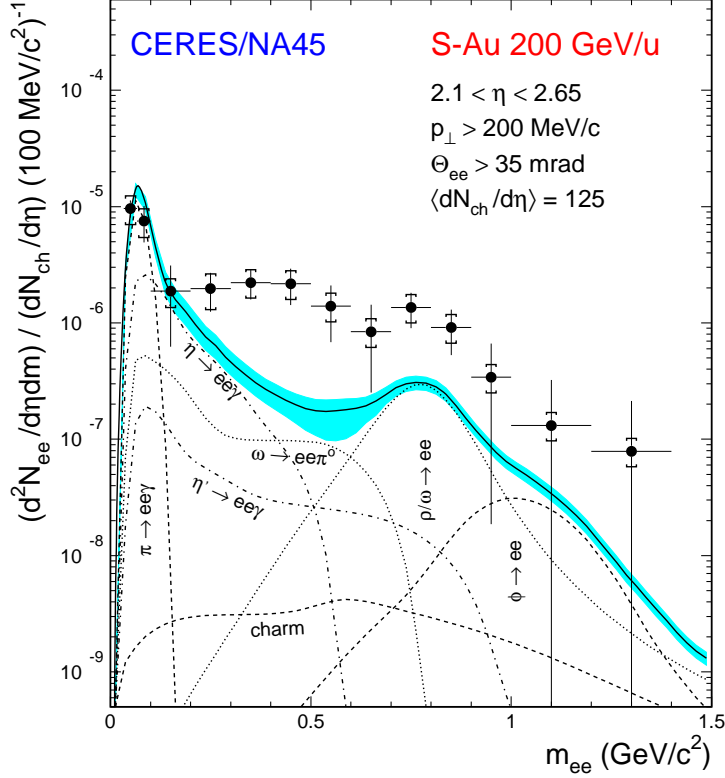


Figure B.2: CERES results. The data points correspond to the experimental data, including the statistical error bars and the systematic errors (brackets). The individual contributions to the theoretical predictions are quoted in the graph. The dilepton enhancement is clearly visible for medium masses (above $0.2 \text{ GeV}/c^2$). From [6].

are introduced to eliminate the magnetic field in the first RICH and the TPC. The acceptance covers the central rapidity region, with an azimuthal 2π symmetry.

The physical results can be separated into two groups: the proton on nucleus data and the nucleus on nucleus data. The first group [4] comprises Beryllium and Gold targets, with proton energies of 450 GeV . The obtained dilepton invariant mass spectra is quite well described by the GENESIS Montecarlo, which represents the output of the conventional hadron sources, including the expected branching ratios, scaling vs. the number of charged particles and a final normalization to reproduce the charge particle density within the acceptance. The second group [5–8]

comprises the Sulfur on Gold and Lead on Gold data at 200 $AGeV$ and 160 $AGeV$. The dilepton invariant mass spectra cannot be described in this case by the conventional hadronic sources, presenting an “enhancement” in the mass region between 0.2 and 1.5 GeV/c^2 (see figure B.2). The value of the enhancement depends on the collision systems and on the mass region, but from the Lead on Gold data sample it results a larger enhancement for central collisions.

Bibliography

- [1] G.Roche *et al.*; Phys. Lett **B226** (1989) 228.
- [2] R.J. Porter *et al.*; Phys. Rev. Lett. **79** (1997) 1229.
- [3] E.L. Bratkovskaya, W. Cassing, R. Rapp, J. Wambach; Nucl. Phys. **A634** (1998) and references herein.
- [4] G.Agakichiev *et al.*; Eur. Phys. J **C4** (1998) 231.
- [5] G.Agakichiev *et al.*; Nucl. Phys. **A590** (1995) 103c.
- [6] G.Agakichiev *et al.*; Phys. Rev. Lett. **75** (1995) 1272.
- [7] G.Agakichiev *et al.*; Nucl. Phys. **A610** (1996) 317c.
- [8] G.Agakichiev *et al.*; Nucl. Phys. **A638** (1998) 3159c.

Appendix C

Limits to the drift chamber resolution

The discrete nature of ionization is relevant in the determination of the fundamental limits of the detector accuracy. If different technical aspects of a drift chamber operation, as wire position, drift velocity, field mapping, electronics are under control with sufficient accuracy, then the statistical fluctuations of the finite number of electrons involved in the measurement are relevant. The fluctuations are strongly influenced by the clustering of the ionization processes; the coordinate measurement will be finally limited by the presence of mechanisms which spread the ionization cloud as it reaches the wire. In this appendix, the statistical limits are reviewed for the geometry of the HADES drift chambers cells. The procedure is based on the derivation from Brum and Rolandi for a drift zone with parallel electric field lines [1].

First, one can calculate quantities of one electron for a single wire. Let us study a simple system, with infinite sense wires along the x axis separated by a distance b in a square cell. The sense wire under study passes through $y = z = 0$. The drift of the electrons produces along the z_i direction, obtained by a different rotation α_i of the initial coordinates in the drift plane for each electron (see left pad of figure C.1). A track crossing the drift gas is defined parallel to the $y-z$ plane. The accuracy will be limited by the differences in the path length among electrons drifting from different ionizations points (different $|z_i|$). The drift chamber spatial resolution also depends on the electron diffusion in its drift. The diffusion root mean square in a given direction (longitudinal or transverse to the drift path) is $\sigma(x) = \sqrt{2Dt}$, being D the diffusion coefficient in that direction and t the time suffering the diffusion.

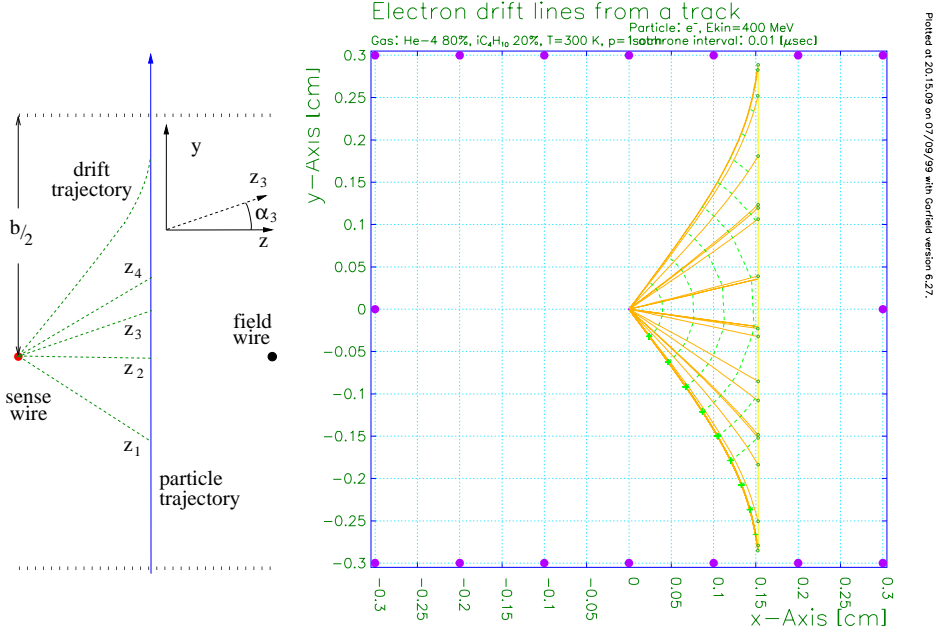


Figure C.1: Ionization electron drift paths in an approximation to the MDC II cell geometry. The left pad schematizes the geometry. The right pad shows the results of the drift simulation performed for a 400 MeV electron track crossing the cell at 1.5 mm from the sense wire. A 80% Helium-20% Isobutane gas mixture was used. The dashed lines represent isochrone intervals of $0.01 \mu\text{s}$. Taken from [2].

Let us consider a track following the y direction at a distance z_0 of the wire, without any loss of generality, due to the cylindrical symmetry of most part of the cell. Our main interest consists in the determination of the resolution in the distance between track and sense wire, obtained from the drift time of the electrons; it is not included any tilt in the trajectory which leads to dispersion along the wire. The frequency distribution $F(t)$ of the time $t = z_i/u$ of the electrons at the entrance of the wire region is determined by the trajectory of the fast particle and by the random diffusion of the drifting electron in the drift region. For a particle produced at a coordinate y along the track, the arrival position can be obtained after a gaussian distributed diffusion is applied around the mean drift value. Let us take as origin values for the ionization $E(x) = x_0$, $E(y) = y$, $E(z) = z_0$, which, converted to the coordinate system (y_i, z_i) (where the drift electrons follow the z_i direction), are $E(x) = x_0$, $E(z_i) = \sqrt{y^2 + z_0^2} = uE(t)$ and $E(y_i) = 0$. The diffusion root mean square is $\sigma_t = \sigma_{long}/u$ (longitudinal),

with u the drift velocity along z_i . Then, the time diffusion along the drift path z_i is

$$G(t_i) = \frac{1}{\sqrt{2\pi}\sigma_t} \exp -\frac{1}{u^2} \frac{(u t_i - \sqrt{y^2 + z_0^2} + z_w)^2}{2\sigma_t^2} \quad (\text{C.1})$$

The frequency distribution of the time at the entrance window of the wire region is then

$$F(t, \pi) d\pi dt = \frac{d\pi dt}{R} \int_{-R/2}^{+R/2} G(\pi) G(t) dy \quad (\text{C.2})$$

for just one ionization electron produced along the track segment R , taken large enough to contain all possible created electrons contributing to the same sense wire. $G(\pi)$ represents the transverse diffusion, being represented as a gaussian with transverse diffusion root mean square σ_π .

Let us assume that just one ionization electron is produced along the track segment, in the previous frequency distribution. This electron is collected by the wire if it is produced inside the cell volume. Then, the integral of the distribution in the allowed space for the wire detection ($-b/2 < y < b/2$) is

$$\int_{-\infty}^{\infty} d\pi \int_{-b/2}^{b/2} dy F(x, y, t) = \int_{-\infty}^{\infty} dx \int_{-\infty}^{\infty} dt \int_{-b/2}^{b/2} dy F(x, y, t) = \frac{b}{R} \quad (\text{C.3})$$

that is, equal to the ratio between the part of the track between the planes $y = -b/2$ and $y = b/2$ and the complete track length R , where one electron is created. The interest lie on the measurement of the coordinate along the drift direction, and electrons arriving at different wire positions contribute equally to the same pulse. Integrating the distribution $F(t, \pi)$ in the coordinate along the sense wire (x) and normalizing using equation C.3, it is obtained the probability distribution of the arrival time

$$f(t) dt = \frac{dt}{b} \int_{-R/2}^{R/2} dy G(t) \quad (\text{C.4})$$

The average and the variance of the arrival time at the wire is

$$E(t_i) = \int_{-b/2}^{b/2} dy \int_{-\infty}^{\infty} t f(t) dt \quad (\text{C.5})$$

$$\begin{aligned} V(t_i) &= E(t^2) - E(t)^2 \\ &= \int_{-b/2}^{b/2} dy \int_{-\infty}^{\infty} t^2 f(t) dt - \left(\int_{-b/2}^{b/2} dy \int_{-\infty}^{\infty} t f(t) dt \right)^2 \end{aligned} \quad (\text{C.6})$$

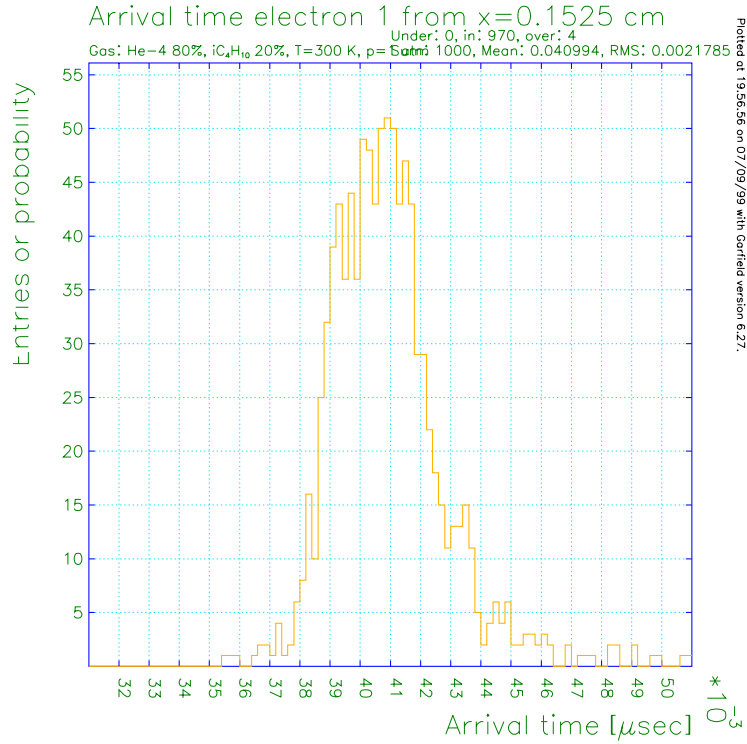


Figure C.2: Arriving time distribution for the first electrons coming to the sense wire. The distribution corresponds to the ionization produced by the electron path of figure C.1. Taken from [2].

Note that these are quantities calculated for only one ionization in the trajectory along the cell volume. The charge along a track is created in discrete clusters that can vary largely in size and the cluster fluctuations influence the resolution in the drift direction, reducing the variance of the coordinate measurement. The main contribution to the fluctuations comes from the electrons following the longest path to reach the wire, effect which is largely dependent on the cell geometry. It is possible to use a fixed-threshold discriminator to define the time signal in the wire by the M th electron arriving at the wire. Then, the influence of the drift path variations in the time resolution is reduced, while the positive effect of the clustering is partially removed. The determination of the threshold is relevant in those cases when both contributions to the variance are of similar importance.

Figure C.1 shows an example of ionizing electron paths in the cell geom-

etry implemented in the simulation of the drift properties¹. The incident particle (a 400 MeV electron) ionizes the gas molecules, releasing electron clusters in different points along the track. In the figure, 20 electron clusters have been created. The histogram in figure C.2 shows the arrival time distribution for the drifting electron coming from the nearest ionization to the sense wire.

Bibliography

- [1] W. Blum, L. Rolandi; *Particle Detection with Drift Chambers*, Springer Verlag, Berlin, 1994.
- [2] M.A. Rozas Pichel; *Estudio dos Parámetros de deriva nas câmaras MDC do espectrómetro HADES*. Tesina de Licenciatura, Universidad de Santiago de Compostela, 1999.

¹The size corresponds to a prototype (so-called Prototyp-0); the cathode wires follow the same direction than sense and field wires, while in the final chambers the cathode follows a normal direction to the sense wires. For this simulation, the sense wires diameter is 100 μm and the cathode diameter 25 μm . The voltage in the field and cathode wires is $-2500 V$ and a 80% Helium-20% Isobutane gas mixture was used.

Appendix D

The MDC tracking software

The electronic signals from the drift chambers are used to reconstruct the geometrical parameters of each track in its path through the detectors. The software algorithms used for this task are commonly called “trackers” or tracking software. Their main task is to obtain the maximum information of the particles from the signals in the drift modules, including their geometrical parameters, vertex, hints for further identification or about their origin (closed pairs...).

The HADES collaboration uses two tracking codes, the so-called Dubna and Santiago trackers. In the following subsections the first code is concisely described, while the second, used constantly in other parts of this work, is deeply shown. But first of all the scheme for calibration is briefly commented.

D.1 Data levels

A set of software data levels has been developed to structure the information from the modules and simplify data comparison and conversion between successive calibration steps.

Up to now the description comprises the electronic generation of the signals in the drift modules and their transport to the tapes. This information is written in a fixed format called Raw MDC subevent, which contains the hardware information about where the signal was generated and the channel contents in the corresponding TDC channel. This information is “unpacked” (that is, converted) to a more friendly format for further calibration. After the unpacking, a software data level denoted as **Raw** is filled. This level still contains the hardware address and the TDC raw data in channels, now structured inside the classes scheme of analysis

software package HYDRA.

The next data level is called **Cal1** and is obtained from Raw through a calibration procedure. The first calibration step translates the hardware addresses to module addresses. The information from the TDCs is transformed to drift times using a linear function. The parameters in the linear correspondence are the TDC offset and gain, individually determined and stored as parameters. The gain is determined from the internal calibration procedure in the TDC explained in the previous section. The offset is introduced to remove from the measured time the part that does not correspond to drift time, i.e., a part of the time-of-flight of the particle. The global offset one should remove from the time reported by the TDC corresponds to the time of the fastest particles which passes the cell closest to the wire. These particles define the sharp edge of the time distribution, being all the other drift times larger (or including in the TDC time information a larger part of the time-of-flight). Technically, this spectrum is integrated and the edge is linearly fitted, as well as the previous integrated background. The cross point of both fitted straight lines determines the offset. The method reports the same offset for all tracks detected in a cell. Up to this point, there is no identification of the particles producing the signal or about their momenta so there is no way to refine the method discriminating tracks. For instance, if the offset is determined by light particles ionizing the gas close to the wire, then the offset should be increased for heavier particles. As heavy particles with lower velocities will cross the modules later than lighters, the common offset will not remove for these particles the complete time-of-flight. This can be corrected in the *Hit* finder as will be shown later.

One step further, the data level called **Cal2** stores the distance to the sense wire. The drift distance can be obtained from the drift time once it is known the drift velocity along the ionization electrons path toward the sense wire. As a first approximation, the drift velocity can be taken as constant (for a MDC II with a mixture 60% Helium and 40% Isobutane at a voltage of -2 kV in cathode and field wires, it was determined a mean drift velocity $v_d = 0.042$ mm/ns, constant in around 80% of the cell [1,2]). In a more sophisticate approximation, the transformation from drift time to drift distance takes into account the dependence of the drift velocity with the track angle and, more important, with the distance to the sense wire. The required parameters for this calibration are obtained from the analysis of the data as well as simulations of the drift on our specific cell geometry.

The **Hit** data level is filled by the tracking codes after the fit of the

calibrated data. A *Hit* is the estimation of the geometrical parameters of the track in its path through the module. A *Hit* contains the position of the estimated cross point of the track with the plane $Z_{MDC} = 0$ of the module coordinate system and the components along the directions X_{MDC} and Y_{MDC} of the unit vector along the direction of the track. It contains also information about the fit quality and the offset¹ for each estimate as well as the references to the impinged cells contributing to the *Hit*. The *Hit* is the last data abstraction inside a module and will be massively used in the software alignment algorithms along this work.

From two *Hits* or directly from the calibrated information in two modules it is possible to construct the next data level, called **Segment**. A segment contains the best estimate to the straight line path in a "lever arm" before or after the magnetic field area.

D.2 The Dubna Hit finder and fitting

The working scheme of the so-called Dubna tracking software is divided in two parts, a *Hit* finder and a *Hit* fitter. The first one determines the candidates or cluster candidates using the hit cells, without time information. To determine the candidates, the hit cells of one or two neighbor modules are projected in a common plane (Hough transformation), using an external point as projection focus [3]. For the inner modules the target is the common external point from where the projection can be performed. A two dimensional histogram is filled with entries in those bins containing a part of the projection. The candidates can be seen as peaks in the histogram. For the external modules behind the magnet there is not a common origin for the tracks. Instead one can try, as projection point, the cross point between the *Hits* found in the inner modules and the Kickplane².

Once the candidates are determined, the drift times in the cells corresponding to the candidates are taken in account. The solution is obtained from the minimization of a complex functional

$$\mathcal{L} = \sum_i (t_i - f_i(xV, yV, zV, xP, yP, v_p))^2 * w_i \quad (\text{D.1})$$

where the t_i are the measured TDC times, (xV, yV, zV) are the target

¹Here, the offset is a common time (or distance) which, subtracted from all the cells contributing to a *Hit*, improves the fit (see figure D.1). The offset is, therefore, the correction to the global offset in the Cal1 to Cal2 calibration due to the track particularities, applied individually to those contributing to a particular *Hit*.

²The Kickplane is a geometrical surface obtained from the cross points of the asymptotic branches of the tracks, behind and after the magnetic field.

coordinates, (xP, yP) the track coordinates in a plane perpendicular to the beam axis, v_p is the particle velocity and w_i are weights, composed of a bi-square Tukey component (see section 5.2 for its expression) multiplied by the inverse of the number of hits per layer [4]. The minimization can be performed on the cells of a MDC or the cells of several MDCs contributing to the same candidate.

D.3 The Santiago Hit finder and fitting

This tracking method has been developed³ at the University of Santiago de Compostela [5]. The tracking comprises the finding of *Hits* in each MDC module, the construction of Segments as combinations of two *Hits* from the two inner or outer MDCs, the selection of good combinations of two segments between those found before and after the magnet and the fitting of the momentum track. In the following paragraphs the finding and fitting of *Hits* in one MDC module is described, being the most relevant part in the development of an alignment software.

The *Hit* finder and fitting takes as input the distances to the Cal2 data level, which contains basically the distance from the wire to the closest point of the ionizing particle. The Cal2 data, just a distance from a wire, is converted to an *impact coordinate* in a plane. For each sense wire plane, the relevant *impact coordinate* is the distance to a reference wire in the plane. Due to the left-right ambiguity of the drift chamber wire planes, each Cal2 will produce two *impact coordinate* or *impacts* in the plane, symmetrically disposed with respect to the sense wire. This is the entry point for the combinatorials, taken an *impact coordinate* for each plane involved in the calculations. The algorithm first searches for *Hits* with six impacts and with the remaining impacts, searches for *Hits* with five impacts. The procedure for six impacts is the following:

- Each combination of four impacts in four different layers defines a straight line. Due to the better straight line geometrical definition and the convenience of interpolate instead of extrapolate, impacts from the external planes are used in the fit. The obtained straight line is tested to be between adequate limits in position and slope, to avoid impossible combinations. For the inner MDCs it is also tested if the straight line points approximately to the target area.
- The straight line is extrapolated to the two remaining layers and their cross points determined. A road or interval in the plane is

³This section refers to the Thesis work of Beatriz Fuentes.

scanned around each cross point. If there are impacts in a given road around the line in these two layers, a straight line is fitted with the six impacts. The *Hit* must fulfill a maximum chi-square test before continuing.

- The *Hit* is tested versus the other already found *Hits*. If they share too much impacts with another *Hit*, only the one with the best χ^2 is kept.
- Once all *Hits* with six impacts have been found, the used impacts are flagged. To assure that they will not be used later, these impacts and their symmetrical partners are deleted from the list of available impacts for the construction of *Hits* with five impacts.
- If five impact *Hits* are searched for, a new procedure begins for the remaining *Hits*. The combinations of four impacts are extrapolated to the fifth layer, if the straight line obtained after the fit passes the test. The line is fitted and kept if the fifth impact is found within the road, the obtained χ^2 is good enough and the number of common impacts with other *Hits* made of five impacts is below a parameter. All combinations of five layers are scanned and the used impacts are flagged as used; they and their symmetric impacts are deleted from the list of available impacts for next steps, if any.

The algorithm works for any number of parallel layers and it can be used to build straight lines with the 12 parallel layers of the outer modules.

Along the previous steps has been shown that a large set of parameters should be used to obtain the *Hits*. This parameter set comprises the minimum number of impacts in the *Hit* (5 or 6), the size of the road, the maximum χ^2 for accepted *Hits*, the maximum number of common impacts between *Hits* and the geometrical constraints of the fitted straight line. The selection of these parameters results of crucial importance to obtain a good reconstruction efficiency without enlarging the sample with fake impact combinations (fake *Hits*).

D.4 Slope correction to the tracking software

The fit performed inside the Santiago tracking software to obtain the track estimates requires the distances to the hit wires in each sense wire plane. The transformation from Cal2 to a coordinate in plane cannot be exactly done without the information of the slopes of the track. Once the *Hit* is found and a first fit has been performed, a correction in slope must be

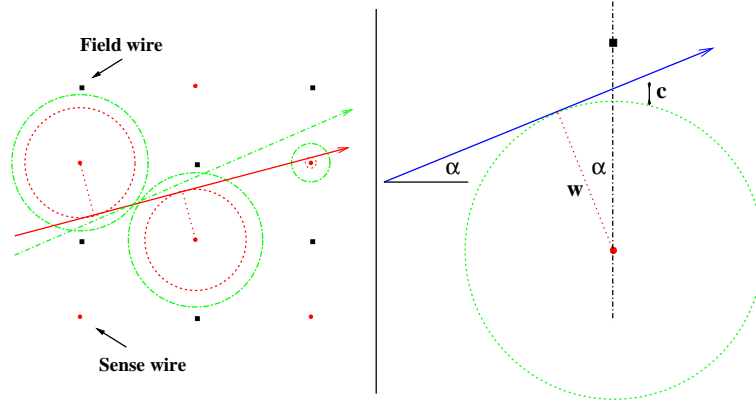


Figure D.1: *Left: An (staggered pitch) disposition of three sense and field wires, to show the effect of the offsets in the track fit. See the explanation in the text. Right: Study of the geometrical correction due to the track inclination in the cell.*

applied to their impacts, improving then the accuracy of the fit parameters and the quality of the fit in successive steps. The individual track offset can also be determined and the impact coordinates corrected for this offset. To determine the offset in the Santiago tracking scheme, the fit function is called for the final set of obtained *Hits*, with different offsets in each call. The left pad of figure D.1 shows the fit for two different offsets in a simplified cell structure with three sense and field wires in the same direction (cathodes are not shown). The inner rings (dashed lines), where an offset is applied to the impact coordinates in each wire, fits nicely a track⁴. The outer rings, without offset correction fits to a different track, with larger residuals and therefore larger χ^2 . The χ^2 obtained in each fit is plotted versus the respective offset and fitted to a polynomial function. The offset given the minimum of the function is selected.

The distance obtained in each wire after calibration is converted to a coordinate in the wire plane. But, if the track crosses the cell inclined an angle α , the closest point between the track and the wire does not lie in the plane. From the right pad of figure D.1 it is immediate to obtain the expression for the correction c of the track impact coordinate in the plane

$$c = \frac{w}{\cos \alpha} - w \quad (\text{D.2})$$

where w is the original impact coordinate. The correction is always posi-

⁴The described case is present mainly for slow particles, when the global offset for all impinging wires is determined using a method which involves fast particles.

tive, increasing slightly the impact coordinate for all cells. To apply this correction it is necessary to know previously the angle α . An estimation of the angle is obtained from a previous track fit, where the transformation is performed without any correction. This iterative approximation converges very fast (one or two steps) for most tracks.

Bibliography

- [1] C. Müntz; Nuclear Physics B **78**, (1999), 139-144.
- [2] C. Müntz; *Results from MDC Prototype-1 Analysis - Test Beam April'97*, MDC Internal report, October 1997.
- [3] V. Pechenov; *Algorithms for track finding*, HADES Collaboration Meeting VIII, 1998, GSI, Darmstadt.
- [4] G. Agakichiev, V. Pechenov; *HADES MDC12 Track Finder*, HADES Collaboration Meeting IX, 1999, Santiago de Compostela.
- [5] C. Fernández, B. Fuentes, J.A. Garzón, M. Sánchez; *HADES Tracking and Vertex Reconstruction. Status report*. USC/GENP/HADES/00-1, Santiago de Compostela, 2000.

Appendix E

Euler transformations

The rotation of a rigid solid is described by three independent parameters. Browsing the literature, several parameters sets are available, while the most used and standardized are the Euler angles. The next lines are devoted to the description of the Euler angles and the calculation of the orthogonal transformation matrices.

The transformation from an initial coordinate system (X, Y, Z) to the final one (X', Y', Z') can be performed using three rotations in a fixed sequence. The Euler angles are defined as the angles used in the successive steps defined in this fixed sequence. Being the order of the rotations arbitrary, there are several alternative conventions, which normally differs in the second of the rotations to be performed on the original system. According to the normal use in the HADES collaboration [1], we adopt here the so-called *Y medium Euler angles system* [2], where the second rotation is realized around this particular axis. The angles are defined according to the following criteria (observe figure E.1).

1. First, we rotate the initial system (X, Y, Z) an angle ϕ around Z axis, anti-clockwise. The obtained auxiliary axis system will be notated as (ξ, η, ζ) (with $\zeta = Z$). The angle ϕ is chosen in such a way that the projection of Z' , the third axis of the final coordinate system, on the plane (X, Y) results ξ .
2. Second, we rotate the (first) auxiliary system (ξ, η, ζ) an angle θ around the η axis, anticlockwise. The new coordinate system obtained after the rotation will be notated (ξ', η', ζ') . The value of the rotation angle θ is chosen in such a way that the ζ' axis, obtained after the rotation, coincides with the final axis Z'
3. Finally, the (second) auxiliary system (ξ', η', ζ') are rotated and angle

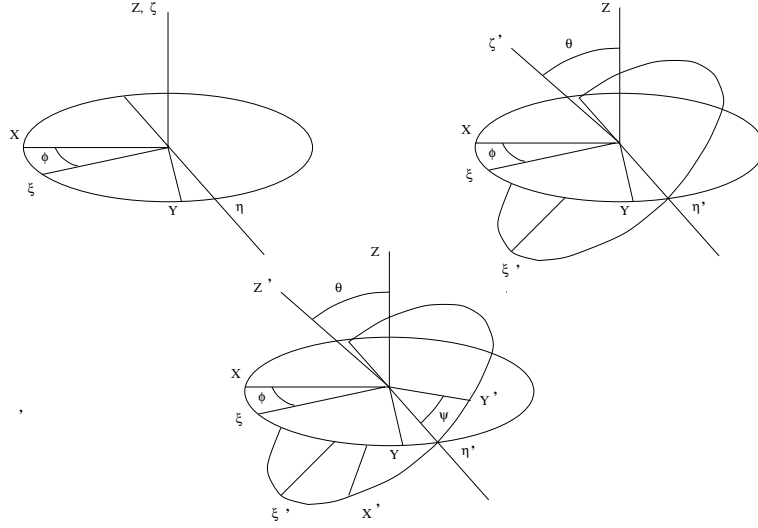


Figure E.1: Rotations performed to define the Euler angles.

ψ around the ζ' axis, anti-clockwise. The rotation angle ψ is selected to obtain from the rotation the final coordinate system (X', Y', Z') .

Once these angles are defined, it is immediate to define the rotation matrix R transforming the coordinates of a vector or a point from the initial (X, Y, Z) system to the final one (X', Y', Z') . This matrix is just the product of the three individual rotations previously mentioned in the correct order. The first rotation around the (original coordinate system) Z axis is represented by the rotation matrix

$$\begin{pmatrix} \xi \\ \eta \\ \zeta \end{pmatrix} = \begin{pmatrix} \cos \phi & \sin \phi & 0 \\ -\sin \phi & \cos \phi & 0 \\ 0 & 0 & 1 \end{pmatrix} \begin{pmatrix} X \\ Y \\ Z \end{pmatrix}$$

The transformation from $\xi\eta\zeta$ to $\xi'\eta'\zeta'$ can be described using the following equation

$$\begin{pmatrix} \xi' \\ \eta' \\ \zeta' \end{pmatrix} = \begin{pmatrix} \cos \theta & 0 & -\sin \theta \\ 0 & 1 & 0 \\ \sin \theta & 0 & \cos \theta \end{pmatrix} \begin{pmatrix} \xi \\ \eta \\ \zeta \end{pmatrix}$$

and the third rotation to the final system (X', Y', Z') is described by

$$\begin{pmatrix} X' \\ Y' \\ Z' \end{pmatrix} = \begin{pmatrix} \cos \psi & \sin \psi & 0 \\ -\sin \psi & \cos \psi & 0 \\ 0 & 0 & 1 \end{pmatrix} \begin{pmatrix} \xi' \\ \eta' \\ \zeta' \end{pmatrix}$$

The matrix which describes the complete transformation is obtained from the individual ones

$$\begin{pmatrix} X' \\ Y' \\ Z' \end{pmatrix} = \begin{pmatrix} \cos \psi \cos \theta \cos \phi - \sin \psi \sin \phi & \cos \psi \cos \theta \sin \phi + \sin \psi \cos \phi & -\cos \psi \sin \theta \\ -\sin \psi \cos \theta \cos \phi - \cos \psi \sin \phi & -\sin \psi \cos \theta \sin \phi + \cos \psi \cos \phi & \sin \psi \sin \theta \\ \sin \theta \cos \phi & \sin \theta \sin \phi & \cos \theta \end{pmatrix} \begin{pmatrix} X \\ Y \\ Z \end{pmatrix}$$

The inverse transformation, to obtain the coordinates of a point or vector in the (X, Y, Z) system from those given in the (X', Y', Z') one, is given by the R transpose matrix, \tilde{R} .

$$\begin{pmatrix} X \\ Y \\ Z \end{pmatrix} = \begin{pmatrix} \cos \psi \cos \theta \cos \phi - \sin \psi \sin \phi & -\sin \psi \cos \theta \cos \phi - \cos \psi \sin \phi & \sin \theta \cos \phi \\ \cos \psi \cos \theta \sin \phi + \sin \psi \cos \phi & -\sin \psi \cos \theta \sin \phi + \cos \psi \cos \phi & \sin \theta \sin \phi \\ -\cos \psi \sin \theta & \sin \psi \sin \theta & \cos \theta \end{pmatrix} \begin{pmatrix} X' \\ Y' \\ Z' \end{pmatrix}$$

The Euler angles ϕ , θ y ψ determine unequivocally the axis orientation of the final system with respect to the original one.

Bibliography

- [1] M. Dahlinger; *HADES Geometry and Database*
(<http://depc14.gsi.de/hades/Geometry.htm>).
- [2] H. Goldstein; *Mecánica Clásica, segunda edición* (Editorial Reverte, Barcelona, 1990).

Appendix F

Coordinate system transformation using the Euler angles

The transformation between coordinate systems seen in section 4.5 can be performed using the Euler angles. The explanation and definition of the Euler transformations and angles is included in the appendix E.

The transformation between the base coordinates and the drift module coordinates is that corresponding to the Euler angles $\phi = \frac{\pi}{2}$, $\theta = \beta$ and $\psi = \frac{-\pi}{2}$, where the notation and angle order correspond to the appendix E criteria. Then, the matrix equation relating the coordinates in both systems is

$$\begin{pmatrix} X_{MDC} \\ Y_{MDC} \\ Z_{MDC} \end{pmatrix} = M \begin{pmatrix} X \\ Y \\ Z \end{pmatrix}$$

with

$$M = \begin{pmatrix} \cos \frac{-\pi}{2} \cos \beta \cos \frac{\pi}{2} - \sin \frac{-\pi}{2} \sin \frac{\pi}{2} & \cos \frac{-\pi}{2} \cos \beta \sin \frac{\pi}{2} + \sin \frac{-\pi}{2} \cos \frac{\pi}{2} & -\cos \frac{-\pi}{2} \sin \beta \\ -\sin \frac{-\pi}{2} \cos \beta \cos \frac{\pi}{2} - \cos \frac{-\pi}{2} \sin \frac{\pi}{2} & -\sin \frac{-\pi}{2} \cos \beta \sin \frac{\pi}{2} + \cos \frac{-\pi}{2} \cos \frac{\pi}{2} & \sin \frac{-\pi}{2} \sin \beta \\ \sin \beta \cos \frac{\pi}{2} & \sin \beta \sin \frac{\pi}{2} & \cos \beta \end{pmatrix}$$

Simplifying the terms in the rotation matrix

$$\begin{pmatrix} X_{MDC} \\ Y_{MDC} \\ Z_{MDC} \end{pmatrix} = \begin{pmatrix} 1 & 0 & 0 \\ 0 & \cos \beta & -\sin \beta \\ 0 & \sin \beta & \cos \beta \end{pmatrix} \begin{pmatrix} X \\ Y \\ Z \end{pmatrix} \quad (\text{F.3})$$

Observe that the previous rotation matrix is the same as that found in section 4.5 (equation 4.9).

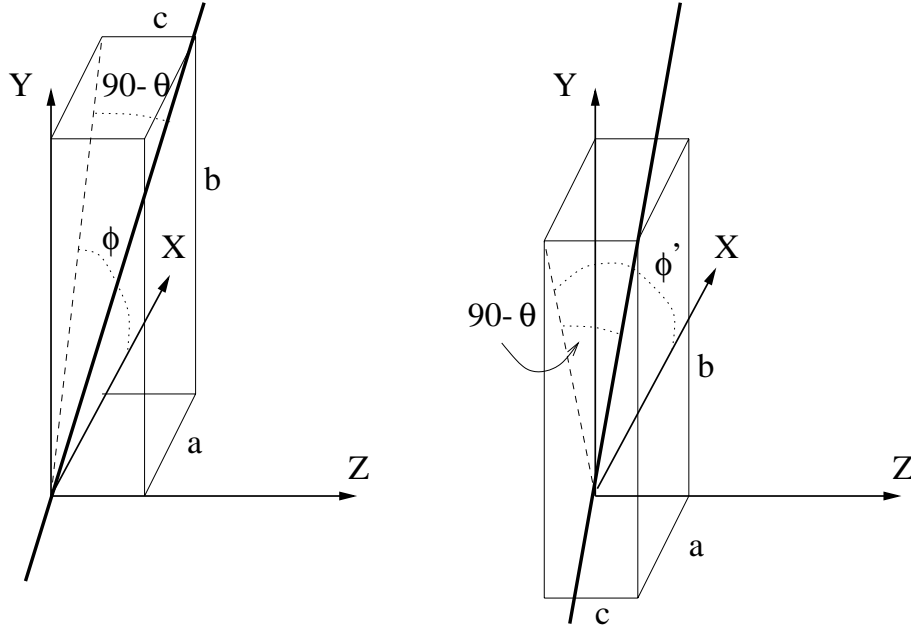


Figure F.1: Projections and relative angles of the RASNIK optical axis. To the left, the positive X light path is shown.

The transformation between the laboratory coordinate system and the RASNIK channel coordinate system requires some previous geometrical calculations. From the components (a, b, c) in the laboratory coordinates of a vector in the direction of the optical axis (Z_R) and from the angles shown in figure F.1, the following relations stand

$$\begin{aligned} \cos \phi &= \frac{a}{\sqrt{a^2 + b^2}} & \cos \phi' &= \frac{-a}{\sqrt{a^2 + b^2}} \\ \sin \phi &= \frac{b}{\sqrt{a^2 + b^2}} & \sin \phi' &= \frac{b}{\sqrt{a^2 + b^2}} \end{aligned} \quad (\text{F.4})$$

The first Euler rotation (see figure F.2) introduces an anti-clockwise rotation around Z , in such a way the new axis ξ (transformed from X in the rotation) coincides with the Z' projection on the plane XY . Previously, it has been calculated (see equation G.4) the unitary vector in the optical axis direction, $\vec{U}(Z_R)$. This direction coincides with the $Z' = Z_R$ axis and, therefore, to know the first Euler angle value it is required the calculation of their projection on the plane XY . Using the equations F.4 and identifying the terms inside $(a, b, c) = (\sin \alpha, \cos \omega \cos \alpha, \sin \omega \cos \alpha)$ as the components of the unitary vector $\vec{U}(Z_R)$, the first Euler angle ϕ (or ϕ' for

the RASNIK channel with negative α) is obtained. Considering, as in the previous point, that the α angle takes a positive value when the channel optical axis crosses the $X > 0$, $Y > 0$ and $Z > 0$ octant (as shown in the left pad of figure F.1) and negative in the opposite case, then one can use the left pair of expression in the equations set F.4 to describe both cases, using the correct α sign for each channel

$$\cos \phi = \frac{\sin \alpha}{\sqrt{\sin^2 \alpha + \cos^2 \omega \cos^2 \alpha}} \quad (\text{F.5})$$

$$\sin \phi = \frac{\cos \omega \cos \alpha}{\sqrt{\sin^2 \alpha + \cos^2 \omega \cos^2 \alpha}} \quad (\text{F.6})$$

Observe that, for a positive α angle (left pad in figure F.1), the unitary vector in the optical axis direction $\vec{U}(Z_R)$ has the first component positive, while is simply the opposite for a negative angle α . Also the ϕ angle is correct, because for $\alpha > 0$ then $0 < \phi < \frac{\pi}{2}$, while for $\alpha < 0$ then $\sin \alpha < 0$ in equation F.5 and therefore $\frac{\pi}{2} < \phi < \pi$. The axes (ξ, η, ζ) will stand for the system obtained after this first rotation, following the appendix E notation (see first pad in figure F.2).

The second Euler transformation is the rotation of this auxiliary axis around η anti-clockwise. The second Euler angle is that which transforms ζ in the final Z_R . Looking at figure F.1, one can see the identities

$$\cos(90 - \theta) = \sin \theta = \frac{\sqrt{a^2 + b^2}}{\sqrt{a^2 + b^2 + c^2}} \quad (\text{F.7})$$

$$\sin(90 - \theta) = \cos \theta = \frac{c}{\sqrt{a^2 + b^2 + c^2}} \quad (\text{F.8})$$

After the substitution in the previous equation of $(a, b, c) = \vec{U}(Z_R)$ by its decomposition in the base coordinates,

$$\sin \theta = \sqrt{\sin^2 \alpha + \cos^2 \omega \cos^2 \alpha} \quad (\text{F.9})$$

$$\cos \theta = \sin \omega \cos \alpha \quad (\text{F.10})$$

which defines the second Euler angle. The angle θ belongs to the interval $(0 < \theta < \frac{\pi}{2})$ and the rotation results anti-clockwise, as needed in our convention. After this rotation, the resultant axes are denoted (ξ', η', ζ') , and are displayed in the second pad of figure F.2.

The third rotation corresponds to an angle ψ (anti-clockwise) around $\zeta' = Z_R$, to obtain the final system (X_R, Y_R, Z_R) , as shown in the third pad of figure F.2. Observe that, with the two simple rotations as performed in section 4.5, the Y_R axis lies in the $X = 0$ plane and its decomposition

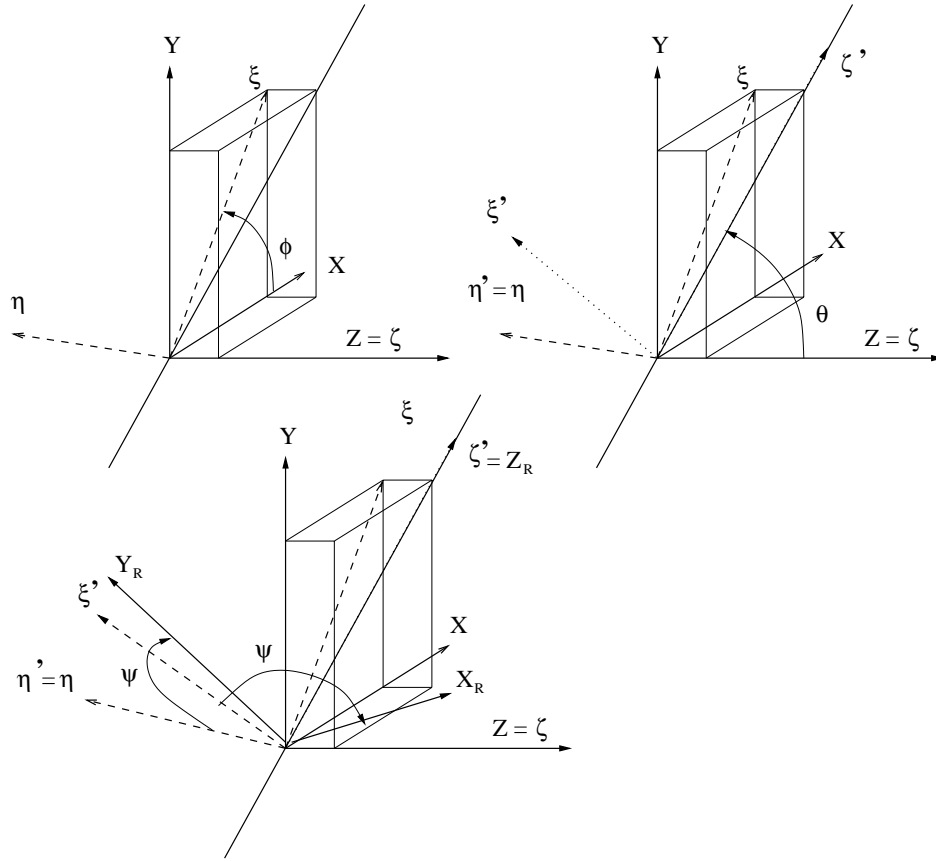


Figure F.2: Euler transformation from the laboratory to the RASNIK coordinate systems. The Euler angles and the intermediate coordinate system are displayed. The pads show sequentially the Euler rotations.

in the base coordinate system is $(0, \sin \omega, -\cos \omega)$. From F.1, may be observed that an unitary vector following the direction of $\eta' = \eta$ can be decomposed in the base coordinates $(-b, a, 0) = (-\cos \omega \cos \alpha, \sin \alpha, 0)$. The third Euler angle is no more than the angle between these two axes

$$\cos(-\psi) = \cos \psi = \frac{\sin \alpha \sin \omega}{\sqrt{\cos^2 \omega \cos^2 \alpha + \sin^2 \alpha}} \quad (\text{F.11})$$

$$\sin(-\psi) = -\sin \psi = \frac{\cos \omega}{\sqrt{\cos^2 \omega \cos^2 \alpha + \sin^2 \alpha}} \quad (\text{F.12})$$

The angle obtained from the previous vector and scalar products corresponds to a clockwise rotation. Then, for the angle ψ a minus sign is added.

Given the three Euler angles, the transformation matrix is immediate

$$\begin{pmatrix} X_R \\ Y_R \\ Z_R \end{pmatrix} = \begin{pmatrix} E_{00} & E_{01} & E_{02} \\ E_{10} & E_{11} & E_{12} \\ E_{20} & E_{21} & E_{22} \end{pmatrix} \begin{pmatrix} X \\ Y \\ Z \end{pmatrix} \quad (\text{F.13})$$

where

$$E_{00} = \cos \psi \cos \theta \cos \phi - \sin \psi \sin \phi = \cos \alpha \frac{\sin^2 \alpha \sin^2 \omega - \cos^2 \omega}{\sin^2 \alpha + \cos^2 \omega \cos^2 \alpha} = \cos \alpha$$

$$\begin{aligned} E_{01} &= \cos \psi \cos \theta \sin \phi + \sin \psi \cos \phi \\ &= \frac{\sin \alpha \cos \omega (\sin^2 \omega \cos^2 \alpha - 1)}{\sin^2 \alpha + \cos^2 \omega \cos^2 \alpha} = -\sin \alpha \cos \omega \end{aligned}$$

$$E_{02} = -\cos \psi \sin \theta = \frac{-\sin \alpha \sin \omega \sqrt{\sin^2 \alpha + \cos^2 \omega \cos^2 \alpha}}{\sqrt{\sin^2 \alpha + \cos^2 \omega \cos^2 \alpha}} = -\sin \alpha \sin \omega$$

$$\begin{aligned} E_{10} &= -\sin \psi \cos \theta \cos \phi - \cos \psi \sin \phi \\ &= \frac{\cos \omega \sin \omega \cos \alpha \sin \alpha - \cos \omega \sin \omega \cos \alpha \sin \alpha}{\sin^2 \alpha + \cos^2 \omega \cos^2 \alpha} = 0 \end{aligned}$$

$$E_{11} = -\sin \psi \cos \theta \sin \phi + \cos \psi \cos \phi = \sin \omega \frac{\cos^2 \omega \cos^2 \alpha + \sin^2 \alpha}{\sin^2 \alpha + \cos^2 \omega \cos^2 \alpha} = \sin \omega$$

$$E_{12} = \sin \psi \sin \theta = \frac{-\cos \omega \sqrt{\sin^2 \alpha + \cos^2 \omega \cos^2 \alpha}}{\sqrt{\sin^2 \alpha + \cos^2 \omega \cos^2 \alpha}} = -\cos \omega$$

$$E_{20} = \sin \theta \cos \phi = \frac{\sin \alpha \sqrt{\sin^2 \alpha + \cos^2 \omega \cos^2 \alpha}}{\sqrt{\sin^2 \alpha + \cos^2 \omega \cos^2 \alpha}} = \sin \alpha$$

$$E_{21} = \sin \theta \sin \phi = \frac{\cos \omega \cos \alpha \sqrt{\sin^2 \alpha + \cos^2 \omega \cos^2 \alpha}}{\sqrt{\sin^2 \alpha + \cos^2 \omega \cos^2 \alpha}} = \cos \omega \cos \alpha$$

$$E_{22} = \cos \theta = \sin \omega \cos \alpha \quad (\text{F.14})$$

The rotation matrix coincides with that calculated in section 4.5.

Appendix G

Geometry of the mask support pieces

The support pieces for the mask and the light emitter should lie on the upper external frame of each MDC III. Their shape and location are constrained by the incidence of the emitted light on the camera aperture. The LEDs light should be emitted following the symmetry axis defined by the center of the lens and the camera sensor. Previously it was used the notation Z_R for this symmetry axis. For an optimal behavior of the hardware, the normal directions to this axis (Y_R and X_R) defined by the main directions of the mask pattern, should coincide with the main directions of the camera pixel array. A small relative rotation in the plane $Z_R = 0$ between the directions of the mask black-white transitions and the camera pixels is allowed and recognized in the RASNIK analysis software. Nevertheless, a large relative rotation can be misinterpreted by the code and lead to errors. The pieces have been designed for a perfect matching of these directions, as is shown below; the imperfections in the machining and the mounting are the only deviation that the analysis software should correct.

According to figure G.1, there are three angles characterizing the position and the shape of the support piece. The first angle, that is called χ , corresponds to a rotation around Z_{MDC} , an inclination of the piece on the surface¹. The angle χ is the tilt angle between the larger axis of the support piece base, where the holes for the screws are, and the X_{MDC} axis; the angle between the screw threads at the MDC III and the frame border is χ . The second angle, denoted as γ , is the angle between the two basic surfaces of the piece, that is, the angle between the surface lying on the MDC III frame (or the frame itself) and the surface where the mask is

¹Along this appendix MDC stands for MDC III as subindex, shorting the notation

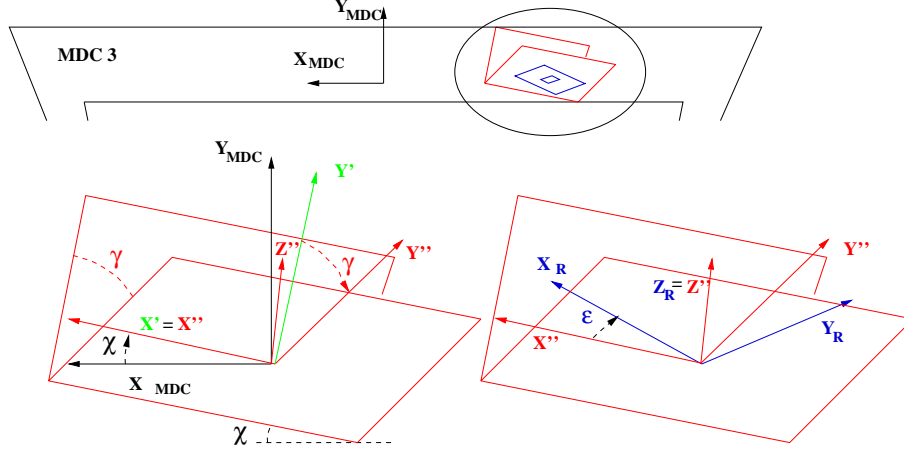


Figure G.1: Angles among the coordinate system axes. The upper drawing schematizes the upper MDC III frame, where the mask and LEDs support is attached. The lower schemes represent the planes of the MDC frame ($X_{MDC}Y_{MDC}$ plane) and the plane normal to the RASNIK optical axis ($X_R Y_R$). All the coordinate systems are represented on the same origin for a simple angle determination. See the text for an explanation.

fixed (or the mask surface itself). The third angle, denoted as ϵ , represents the mask tilt on the surface which supports the mask, to align the main mask directions with the main directions in the camera pixel pattern.

The angle γ can be obtained using the known transformation to the laboratory coordinate system. The Z_{MDC} unit vector expressed in the laboratory system is

$$\vec{U}(Z_{MDC}) = (0, \sin \beta, \cos \beta) \quad (\text{G.1})$$

where β represents the angle between the normal vector to the MDC wire planes and the laboratory system Z axis, as shown in figure 4.11.

The Z_R decomposition in laboratory coordinates requires the combination of two rotations around the angles shown in figure G.2 (compare with figure 4.11 to identify the elements). The angle α stands between the *binocular* piece symmetry plane and the Z_R axis, and ω represents the *binocular* piece tilt angle with respect to the vertical.

With the help of an auxiliary coordinate system defined by the rotation of a positive ω angle around X axis, the unitary vector in the direction of Z_R can be expressed, in the auxiliary system, as

$$[\vec{U}(Z_R)]_{AUX} = (\sin \alpha, \cos \alpha, 0) \quad (\text{G.2})$$

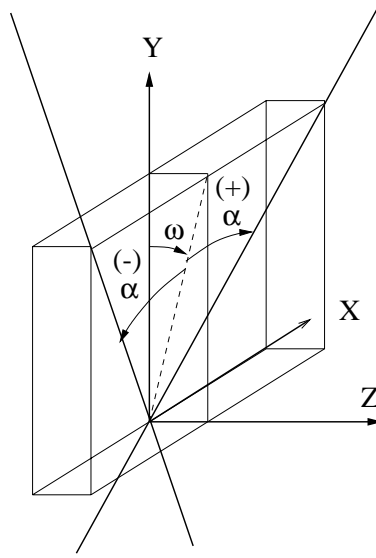


Figure G.2: Relationship between the laboratory coordinate system and the RASNIK optical axis. The optical axis of both RASNIK channels determines the symmetry plane of the binocular piece, tilted an angle ω with respect to the XY plane. The α angle is positive or negative for each channel (see the text for the convention). The (+) sign shows a positive rotation ($\alpha > 0$) and vice versa.

The expression of the auxiliary system in laboratory coordinates is

$$\begin{pmatrix} X \\ Y \\ Z \end{pmatrix} = \begin{pmatrix} 1 & 0 & 0 \\ 0 & \cos \omega & -\sin \omega \\ 0 & \sin \omega & \cos \omega \end{pmatrix} \begin{pmatrix} X_{AUX} \\ Y_{AUX} \\ Z_{AUX} \end{pmatrix}$$

The unit vector in the direction and sense of Z_R , in the laboratory coordinates, is

$$\vec{U}(Z_R) = (\sin \alpha, \cos \omega \cos \alpha, \sin \omega \cos \alpha) \quad (\text{G.4})$$

Finally, the angle between Z_R and Z_{MDC} axes is

$$\gamma = \arccos(\cos \alpha(\sin \beta \cos \omega + \cos \beta \sin \omega)) \quad (\text{G.5})$$

or simplified:

$$\gamma = \arccos(\cos \alpha \sin(\beta + \omega)) \quad (\text{G.6})$$

For the design values of the angles, $\alpha = 25^\circ$, $\omega = 7^\circ$ and $\beta = 49.10^\circ$, it is found an angle $\gamma = 41.2^\circ$.

To obtain the other angles, let us apply rotations on the coordinate systems and require the fulfilling of identities obtained in the previous section. Figure G.1 shows the coordinate transformation and the angles that have to be determined. Beginning with the MDC coordinate system, and after a rotation of an angle χ around Z_{MDC} , the system (X', Y', Z') is obtained, where $Z' = Z_{MDC}$. The second rotation transforms the prime ($'$) system into the double prime ($''$) system (X'', Y'', Z'') , after a rotation around X' of an angle γ . The third rotation, of an angle ϵ around Z'' , transforms the double prime system into the RASNIK coordinate system.

The matrices associated to each rotation are

$$\begin{pmatrix} X' \\ Y' \\ Z' \end{pmatrix} = \begin{pmatrix} \cos \chi & \sin \chi & 0 \\ -\sin \chi & \cos \chi & 0 \\ 0 & 0 & 1 \end{pmatrix} \begin{pmatrix} X_{MDC} \\ Y_{MDC} \\ Z_{MDC} \end{pmatrix} \quad (\text{G.7})$$

and

$$\begin{pmatrix} X'' \\ Y'' \\ Z'' \end{pmatrix} = \begin{pmatrix} 1 & 0 & 0 \\ 0 & \cos \gamma & \sin \gamma \\ 0 & -\sin \gamma & \cos \gamma \end{pmatrix} \begin{pmatrix} X' \\ Y' \\ Z' \end{pmatrix} \quad (\text{G.8})$$

and therefore

$$\begin{pmatrix} X'' \\ Y'' \\ Z'' \end{pmatrix} = \begin{pmatrix} \cos \chi & \sin \chi & 0 \\ -\cos \gamma \sin \chi & \cos \gamma \cos \chi & \sin \gamma \\ \sin \gamma \sin \chi & -\sin \gamma \cos \chi & \cos \gamma \end{pmatrix} \begin{pmatrix} X_{MDC} \\ Y_{MDC} \\ Z_{MDC} \end{pmatrix} \quad (\text{G.9})$$

As shown in G.6, the angle between Z_R and Z_{MDC} is:

$$\gamma = \arccos[\cos \alpha \sin(\omega + \beta)] \quad (\text{G.10})$$

The sign of γ is negative ($-\frac{\pi}{2} < \gamma < 0$), as is expected, being γ clockwise, as can be seen in the lower left pad of figure G.1.

The angle χ is obtained when one requires that $Z'' = Z_R$ after the rotation induced by this angle. There are two possibilities, corresponding to the optical axis with $\alpha > 0$ or $\alpha < 0$. For the first case, ($\alpha > 0$) with the light emitter located at $X > 0$, the χ angle is negative (clockwise). In the second case, ($\alpha < 0$), corresponding to the support shown in figure G.1 in the $X_{MDC} < 0$ hemisphere, the angle χ is positive (anti-clockwise). The unitary vectors in the direction of these axes can be decomposed in the MDC III coordinate system $(X_{MDC}, Y_{MDC}, Z_{MDC})$

$$[U(Z'')]_{MDC} = (\sin \gamma \sin \chi, -\sin \gamma \cos \chi, \cos \gamma) \quad (\text{G.11})$$

$$[U(Z_R)]_{MDC} = (\sin \alpha, \cos \alpha \cos(\omega + \beta), \cos \alpha \sin(\omega + \beta)) \quad (\text{G.12})$$

From these expressions, comparing term by term,

$$\sin \chi = \frac{\sin \alpha}{\sin \gamma} \quad (\text{G.13})$$

$$\cos \chi = -\frac{\cos \alpha \cos(\omega + \beta)}{\sin \gamma} \quad (\text{G.14})$$

For $\alpha < 0$, then $0 < \chi < \frac{\pi}{2}$ while for $\alpha > 0$, the results is $\frac{-\pi}{2} < \chi < 0$, because γ is negative in both cases.

To find the third angle ϵ , it is necessary to calculate the transformation matrix generated by the angle and compare term by term with the transformation matrix 4.11 in section 4.5. The effect of the third rotation is described by

$$\begin{pmatrix} X_R \\ Y_R \\ Z_R \end{pmatrix} = \begin{pmatrix} \cos \epsilon & \sin \epsilon & 0 \\ -\sin \epsilon & \cos \epsilon & 0 \\ 0 & 0 & 1 \end{pmatrix} \begin{pmatrix} X'' \\ Y'' \\ Z'' \end{pmatrix}$$

and the combined effect of the three rotations is

$$\begin{pmatrix} X_{MDC} \\ Y_{MDC} \\ Z_{MDC} \end{pmatrix} = \begin{pmatrix} \cos \chi & -\cos \gamma \sin \chi & \sin \gamma \sin \chi \\ \sin \chi & \cos \gamma \cos \chi & -\sin \gamma \cos \chi \\ 0 & \sin \gamma & \cos \gamma \end{pmatrix} \begin{pmatrix} \cos \epsilon & -\sin \epsilon & 0 \\ \sin \epsilon & \cos \epsilon & 0 \\ 0 & 0 & 1 \end{pmatrix} \begin{pmatrix} X_R \\ Y_R \\ Z_R \end{pmatrix} \quad (\text{G.16})$$

or simplifying

$$\begin{pmatrix} X_{MDC} \\ Y_{MDC} \\ Z_{MDC} \end{pmatrix} = \begin{pmatrix} R_{00} & R_{01} & R_{02} \\ R_{10} & R_{11} & R_{12} \\ R_{20} & R_{21} & R_{22} \end{pmatrix} \begin{pmatrix} X_R \\ Y_R \\ Z_R \end{pmatrix} \quad (\text{G.17})$$

with

$$\begin{aligned} R_{00} &= \cos \chi \cos \epsilon - \cos \gamma \sin \chi \sin \epsilon \\ R_{01} &= -\cos \chi \sin \epsilon - \cos \gamma \sin \chi \cos \epsilon \\ R_{02} &= \sin \gamma \sin \chi \\ R_{10} &= \sin \chi \cos \epsilon + \cos \gamma \cos \chi \sin \epsilon \\ R_{11} &= -\sin \chi \sin \epsilon + \cos \gamma \cos \chi \cos \epsilon \\ R_{12} &= -\sin \gamma \cos \chi \\ R_{20} &= \sin \gamma \sin \epsilon \\ R_{21} &= \sin \gamma \cos \epsilon \\ R_{22} &= \cos \gamma \end{aligned} \quad (\text{G.18})$$

Comparing term by term the transformation matrix G.17 and the transpose matrix of that in 4.11,

$$-\sin \alpha \sin(\omega + \beta) = \sin \gamma \sin \epsilon \quad (\text{G.19})$$

$$-\cos(\omega + \beta) = \sin \gamma \cos \epsilon \quad (\text{G.20})$$

and, therefore, the third rotation angle is

$$\sin \epsilon = -\frac{\sin \alpha \sin(\omega + \beta)}{\sin \gamma} \quad (\text{G.21})$$

$$\cos \epsilon = -\frac{\cos(\omega + \beta)}{\sin \gamma} \quad (\text{G.22})$$

Observe that, for negative α , then $-\frac{\pi}{2} < \epsilon < 0$. Then, ϵ corresponds to a clockwise rotation. For a positive α , then $0 > \epsilon > \frac{\pi}{2}$.

Using the designed numerical values for the angles, $\alpha = 25^\circ$, $\omega = 7^\circ$ and $\beta = 49.1^\circ$, the angles in the support pieces are $\gamma = -41.2^\circ$ (clockwise), $\chi = -39.9^\circ$ (clockwise) and $\epsilon = 32.2^\circ$ (anti-clockwise). For $\alpha = -25^\circ$ (right pad in figure F.1 and the only support schematized in figure G.1), χ is positive (anti-clockwise) and ϵ negative (clockwise).

Appendix H

Geometrical solution to the “out of plane” rotation

When the correction to a previous estimate of the relative rotation matrix requires a rotation around Y or X axes, the MDC B plane where the extrapolation of the track estimate is calculated changes, and then the cross point between the extrapolated straight line generated by the MDC A *Hit* (and maybe the target) and the plane should be recalculated. Let us exemplify the calculations introducing a correction to the rotation around the Y axis. The rotation around the X axis can be obtained by a symmetrical change of the coordinates x and y in the expressions (and the sign if necessary). The notation of this appendix corresponds to that used in section 5.3.5, where the following calculations are framed.

The transformation between coordinate systems related by a rotation around the $Y = Y'$ axis is (see figure H.1)

$$\begin{aligned}x' &= x \cos \theta_2 + z \sin \theta_2 \\y' &= y \\z' &= -x \sin \theta_2 + z \cos \theta_2\end{aligned}\tag{H.1}$$

where the (x', y', z') are the coordinates of the point (x, y, z) in the new coordinate system after the rotation. The plane $Z' = 0$ obtained after the transformation can be expressed in the initial coordinates by the expression

$$z = \tan \theta_2 x\tag{H.2}$$

Now, it is possible to calculate the new cross point between the track estimate and the plane $Z' = 0$. The straight line defined from the MDC A

Hit can be written as

$$\frac{x - x_p}{x_p - x_t} = \frac{y - y_p}{y_p - y_t} = \frac{z}{-z_t} \quad (\text{H.3})$$

In case the target is not being used, the equation is still valid using x_B^A, y_B^A, z_B^A (see equation 5.24) instead of x_t, y_t, z_t , calculated for the initial transformation between the modules. The cross points between the plane H.2 and the straight lines H.3 are

$$\begin{aligned} x &= \frac{z_t x_p}{(x_p - x_t) \tan \theta_2 + z_t} \\ y &= y_p - (y_p - y_t) \frac{x_p \tan \theta_2}{(x_p - x_t) \tan \theta_2 + z_t} \\ z &= \frac{z_t x_p \tan \theta_2}{(x_p - x_t) \tan \theta_2 + z_t} \end{aligned} \quad (\text{H.4})$$

If the misalignment is corrected after the rotation around Y , then the angle θ_2 can be obtained equaling the local (MDC B) *Hit*, (x^B, y^B) , and the cross point between the extrapolation and the $Z' = 0$ plane (point (\hat{x}_p, \hat{y}_p) , given by equation H.4), both expressed in the (X', Y', Z') system. Using the equation H.1, the three components lead to three independent equations

$$\begin{aligned} x^B = \hat{x}_p &= \frac{z_t x_p \cos \theta_2 + z_t x_p \frac{\sin^2 \theta_2}{\cos \theta_2}}{(x_p - x_t) \tan \theta_2 + z_t} \\ y^B = \hat{y}_p &= y_p - (y_p - y_t) \frac{x_p \tan \theta_2}{(x_p - x_t) \tan \theta_2 + z_t} \\ z^B &= \frac{-z_t x_p \sin \theta_2 + z_t x_p \sin \theta_2}{(x_p - x_t) \tan \theta_2 + z_t} = 0 \end{aligned} \quad (\text{H.5})$$

The third equation simply certifies that the cross point is on the plane $Z' = 0$ (the z component of a local *Hit* is always zero).

The angle θ_2 , solution to the equations H.5, can be obtained directly from any of the two equations; from the first, after some elaboration

$$\cos \theta_2 + \frac{x_p - x_t}{z_t} \sin \theta_2 = \frac{x_p}{x^B} \quad (\text{H.6})$$

or

$$\sin^2 \theta_2 \left[1 + \left(\frac{x_p - x_t}{z_t} \right)^2 \right] + \sin \theta_2 \left[-2 \frac{x_p (x_p - x_t)}{z_t x^B} \right] + \left(\frac{x_p}{x^B} \right)^2 - 1 = 0 \quad (\text{H.7})$$

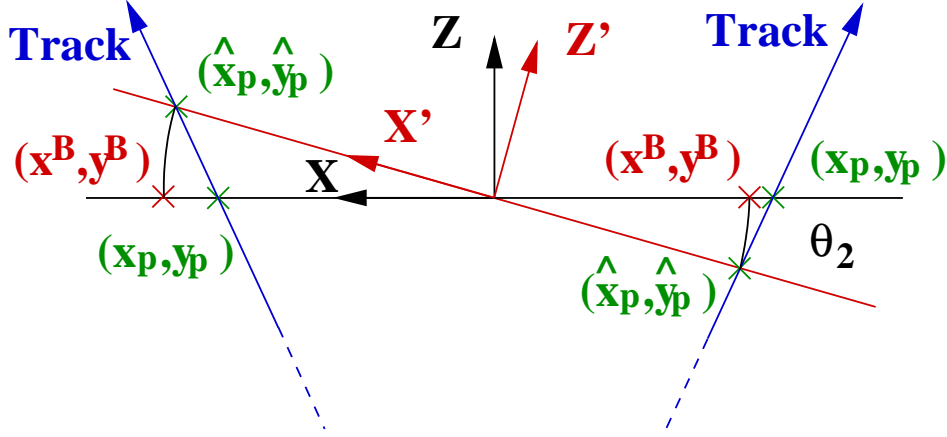


Figure H.1: Position of the projection of the tracks estimates and the local Hits in a module before (system (X, Z)) and after (system (X', Z')) a correcting rotation around the Y axis. The tracks (blue arrows) crosses the module leaving the Hit in the coordinates (x^B, y^B) ; the projections of the track estimates given by another module coincide with the Hits only if the relative rotation is correct (after the correcting rotation, system (X', Z')). In any other case, the projection and the Hit coordinates do not coincide for all Hits.

This second order equation could have one, two or even no real solution, for different values of the projection point (x_p, y_p) and the Hit position (x^B, y^B) . Graphically, the possible solutions to the problem are shown in figure H.2. Numerically, the solutions are

$$\sin \theta_2 = \frac{1}{1 + \left(\frac{x_p - x_t}{z_t}\right)^2} \left[\frac{x_p(x_p - x_t)}{x^B z_p} \pm \sqrt{1 + \left(\frac{x_p - x_t}{z_t}\right)^2 - \left(\frac{x_p}{x^B}\right)^2} \right] \quad (\text{H.8})$$

Considering perfect straight lines and reconstruction, there are two solutions (except for the unusual case when the track is tangent to the circle, as shown in the second track of figure H.2). It is impossible to determine individually which angle is the correct one, and only the comparison between results of different tracks show the correct one. In a real case, where the charged particles path suffers angular straggling and the resolution of the modules smears both the position of the local *Hit* and the extrapolation of the track estimate, there is no real solution for a considerable number of combinations (as it is shown for the left track of figure H.2). If the solution exist, the difference between the two solutions is small for a large number of tracks, making difficult the selection of the correct angle.

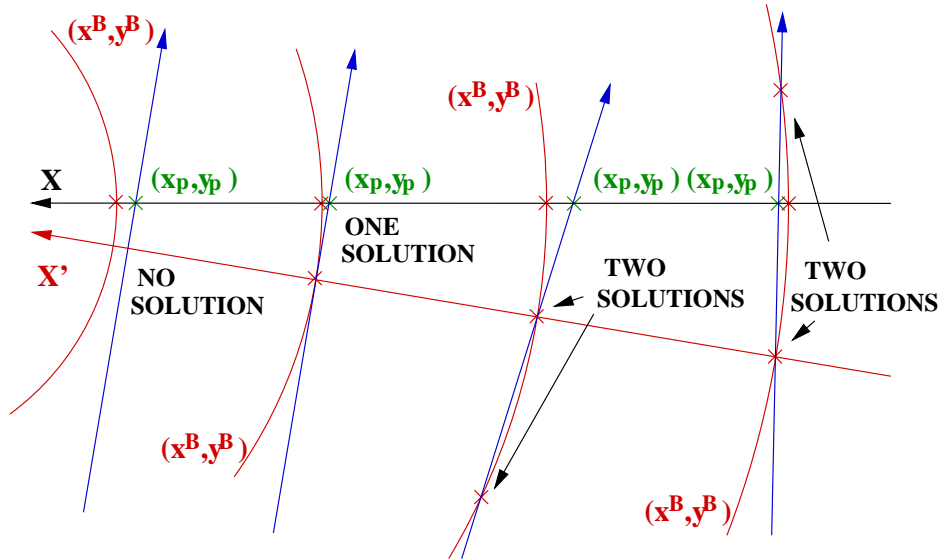


Figure H.2: Graphical representation of the solutions of the equation H.5. The red circle arcs (and the red crosses for the two fixed axis) represents the position of the local MDC Hit. The green points (x_p, y_p) are the crossing points between the track estimate, obtained externally to the module, and the module plane. The cross points between the track estimate and the the circle are solutions to the equation.

Figure H.3 shows both the positive and the negative solutions for a set of *Hit* pairs from the same track. The tracks come from 50000 events in a C+C simulation, including multiple scattering and setting the design resolution in the drift modules. The plot shows the results of the calculation for rotations around the X axis in the relative transformation between a module I and a module II. Both the negative and the positive solutions are plotted in independent histograms. Both present common features: a continuum of solutions is visible for large values of the angle, positive for the positive sign solutions and negative for negative sign solutions. There is a central peak, corresponding to the right solutions which is common to both solutions. The continuum part of the histograms correspond to wrong election of the sign in the solution. For each entry in the continuum, there is an entry in the main peak of the solution with opposite sign. The pad in the top right corner shows selected right solutions from both histograms. Fitting to a gaussian the central part of the resulting histogram (in particular, the plot shows a fit defined in an interval $1.64 \times \sigma$ around the histogram mean), the correcting angle can be obtained as well as an

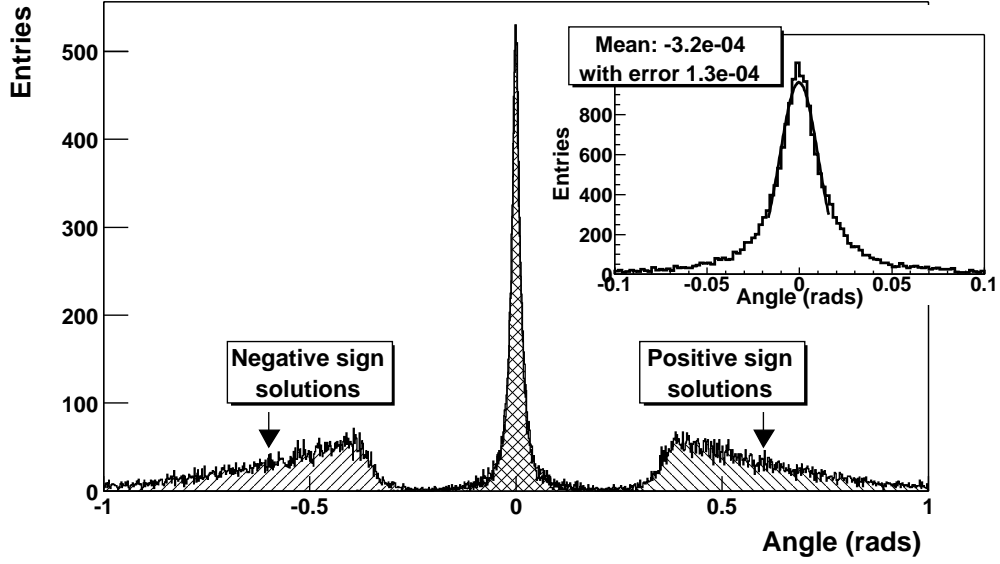


Figure H.3: Positive and negative sign solutions of equation H.8, calculated for all the Hits in a C+C simulation. Both solutions present a continuum and a peak centered in the true correcting angle. In the small pad, the solutions corresponding to the right angle are fitted to a gaussian defined in $1.64 \times \sigma$ around the mean. The correcting angle are obtained from the mean of the fit as well as the error estimate.

estimate of their error.

The solution to the second equation in H.5 is

$$\tan \theta_2 = \frac{z_t(y^B - y_p)}{(x_p - x_t)(y_p - y^B) - (y_p - y_t)x_p} \quad (\text{H.9})$$

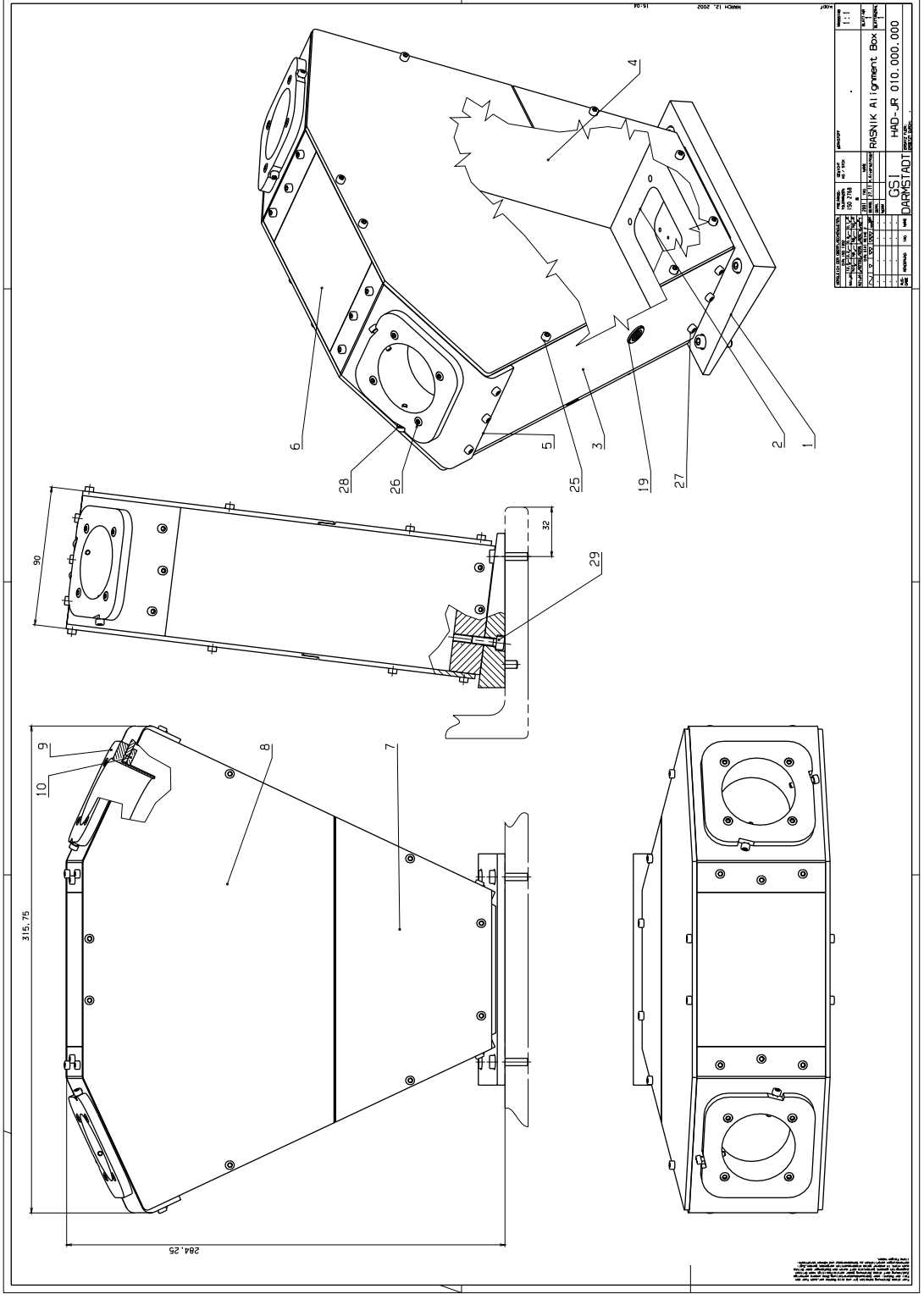
This solution is unique and returns the correct angle provided the track is not contained in the $Y = cte$ plane. In a real case, this solution could be used to determine the angle θ_2 only for tracks with a large slope in the Y direction.

Appendix I

Technical drawings

This appendix include the technical drawings of the pieces designed specifically for the hardware alignment system of the drift chambers of the HADES spectrometer. All the supporting pieces have been designed using CATIA (CATIA-CADAM Solutions Version 4, Dassault Systemes), a CAD/CAM/CAE system for digital design processes. By default, the standard ISO 2768-1 m has been selected, providing a reasonable machining accuracy at a medium price. The identifying numbers in the drawing correspond to the standard naming scheme of the HADES pieces database. The materials and special features are included as well.

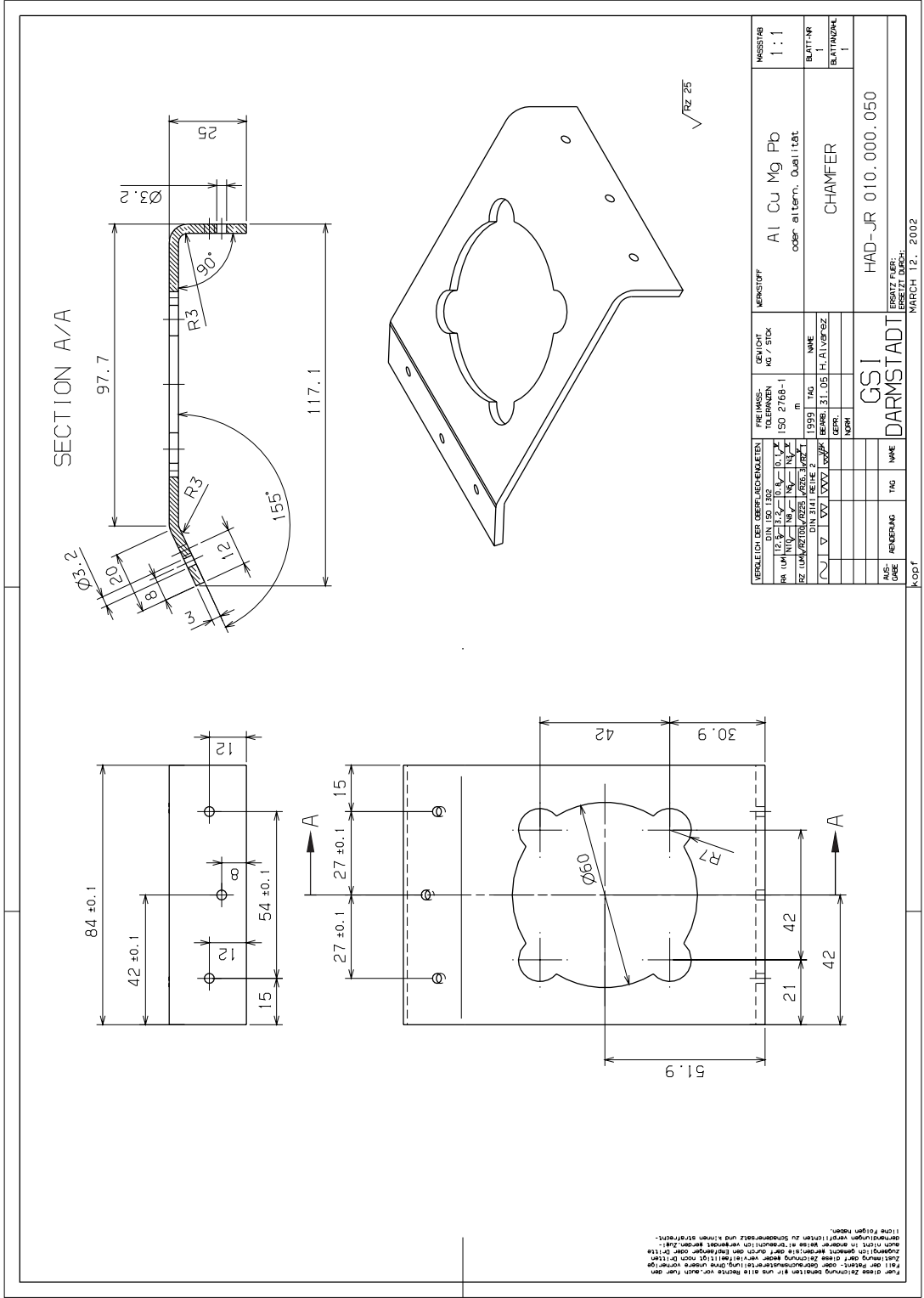
kopf FRAME 1 MARCH 12, 2002 15.04.38



DATE	12.03.2002	SCALE	1:1
DESIGNER		CHECKER	
PROJECT	PRASNIK Alignment Box	WORKSHEET	
NO.	01	DATE	
NAME	CS1	NO.	
ADDRESS	DARSTADT	NO.	
PHONE		NO.	
FAX		NO.	
E-MAIL		NO.	
WWW		NO.	
PROJECT NO.	HAD-JR 010.000.000	NO.	
PROJECT NAME		NO.	
PROJECT ADDRESS		NO.	
PROJECT PHONE		NO.	
PROJECT FAX		NO.	
PROJECT E-MAIL		NO.	
PROJECT WWW		NO.	

1:1
 12.03.2002
 PRASNIK Alignment Box
 CS1
 DARSTADT
 HAD-JR 010.000.000

kopf FRAME 1 MARCH 12, 2002 15.41.47



ERSATZ FÜR: HAD-JR 010.000.050

ERSATZ FÜR: DARMSSTADT

GEWICHT: 150 2768-1

FRÜHERES: 150 2768-1

MARKSTOFF: Al Cu Mg Pb

MESSSTAB: 1:1

BLATT-NR: 1

BLATTANZAHL: 1

CHAMFER

HAD-JR 010.000.050

DARMSSTADT

150 2768-1

150 2768-1

Al Cu Mg Pb

1:1

1

1

CHAMFER

HAD-JR 010.000.050

DARMSSTADT

150 2768-1

150 2768-1

Al Cu Mg Pb

1:1

1

1

CHAMFER

HAD-JR 010.000.050

DARMSSTADT

150 2768-1

150 2768-1

Al Cu Mg Pb

1:1

1

1

CHAMFER

HAD-JR 010.000.050

DARMSSTADT

150 2768-1

150 2768-1

Al Cu Mg Pb

1:1

1

1

CHAMFER

HAD-JR 010.000.050

DARMSSTADT

150 2768-1

150 2768-1

Al Cu Mg Pb

1:1

1

1

CHAMFER

HAD-JR 010.000.050

DARMSSTADT

150 2768-1

150 2768-1

Al Cu Mg Pb

1:1

1

1

CHAMFER

HAD-JR 010.000.050

DARMSSTADT

150 2768-1

150 2768-1

Al Cu Mg Pb

1:1

1

1

CHAMFER

HAD-JR 010.000.050

DARMSSTADT

150 2768-1

150 2768-1

Al Cu Mg Pb

1:1

1

1

CHAMFER

HAD-JR 010.000.050

DARMSSTADT

150 2768-1

150 2768-1

Al Cu Mg Pb

1:1

1

1

CHAMFER

HAD-JR 010.000.050

DARMSSTADT

150 2768-1

150 2768-1

Al Cu Mg Pb

1:1

1

1

CHAMFER

HAD-JR 010.000.050

DARMSSTADT

150 2768-1

150 2768-1

Al Cu Mg Pb

1:1

1

1

CHAMFER

HAD-JR 010.000.050

DARMSSTADT

150 2768-1

150 2768-1

Al Cu Mg Pb

1:1

1

1

CHAMFER

HAD-JR 010.000.050

DARMSSTADT

150 2768-1

150 2768-1

Al Cu Mg Pb

1:1

1

1

CHAMFER

HAD-JR 010.000.050

DARMSSTADT

150 2768-1

150 2768-1

Al Cu Mg Pb

1:1

1

1

CHAMFER

HAD-JR 010.000.050

DARMSSTADT

150 2768-1

150 2768-1

Al Cu Mg Pb

1:1

1

1

CHAMFER

HAD-JR 010.000.050

DARMSSTADT

150 2768-1

150 2768-1

Al Cu Mg Pb

1:1

1

1

CHAMFER

HAD-JR 010.000.050

DARMSSTADT

150 2768-1

150 2768-1

Al Cu Mg Pb

1:1

1

1

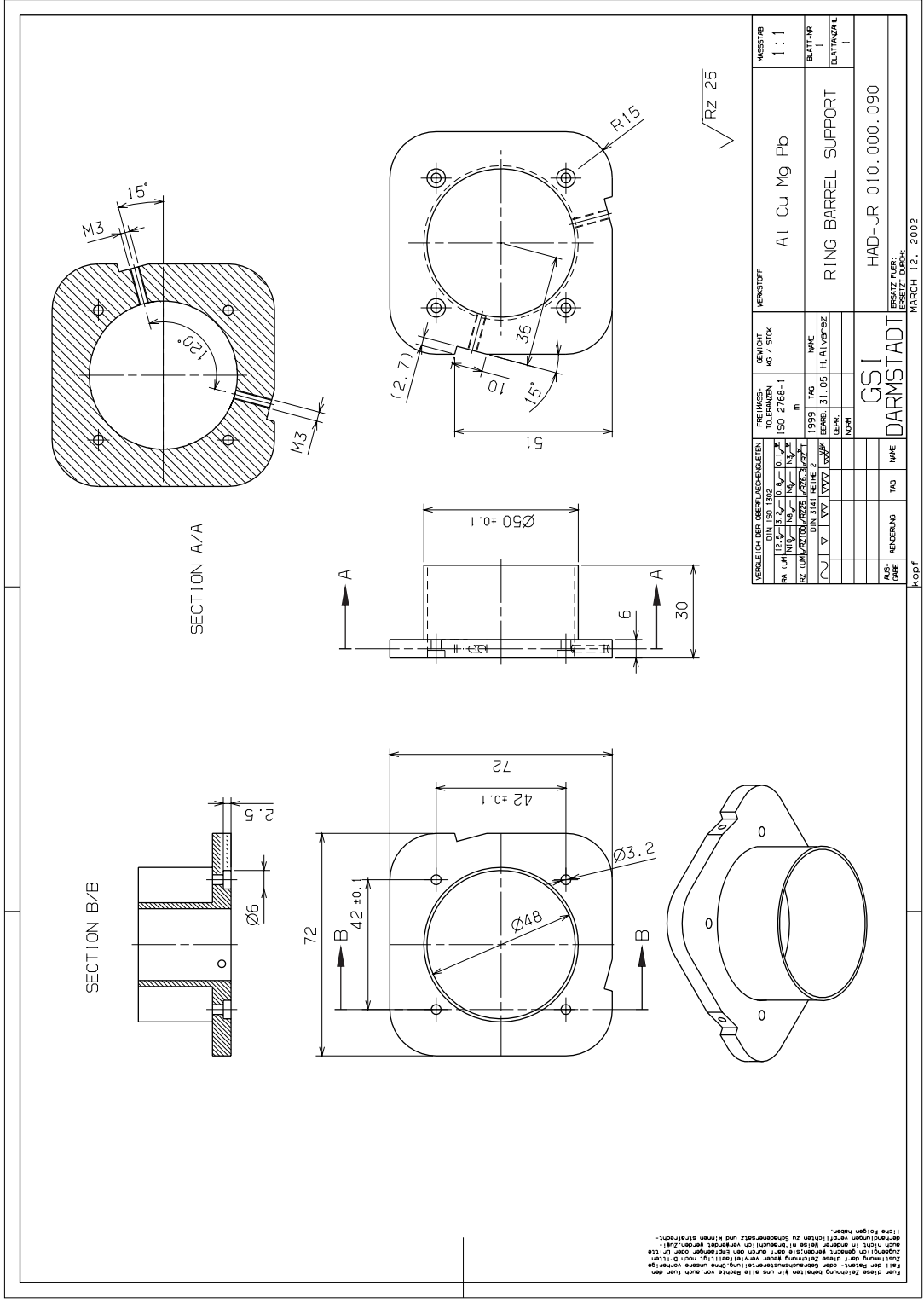
CHAMFER

HAD-JR 010.000.050

DARMSSTADT

150 2768-1

150 2768-1



Alle Rechte vorbehalten. Nachdruck, Vervielfältigung und Verbreitung, auch auszugsweise, ist ohne schriftliche Genehmigung der GSI Darmstadt. Die Verantwortung für die Richtigkeit der Zeichnung übernimmt der Zeichner. Die Haftung für die Richtigkeit der Zeichnung liegt bei dem Auftraggeber. Die Haftung für die Richtigkeit der Zeichnung liegt bei dem Auftraggeber. Die Haftung für die Richtigkeit der Zeichnung liegt bei dem Auftraggeber.

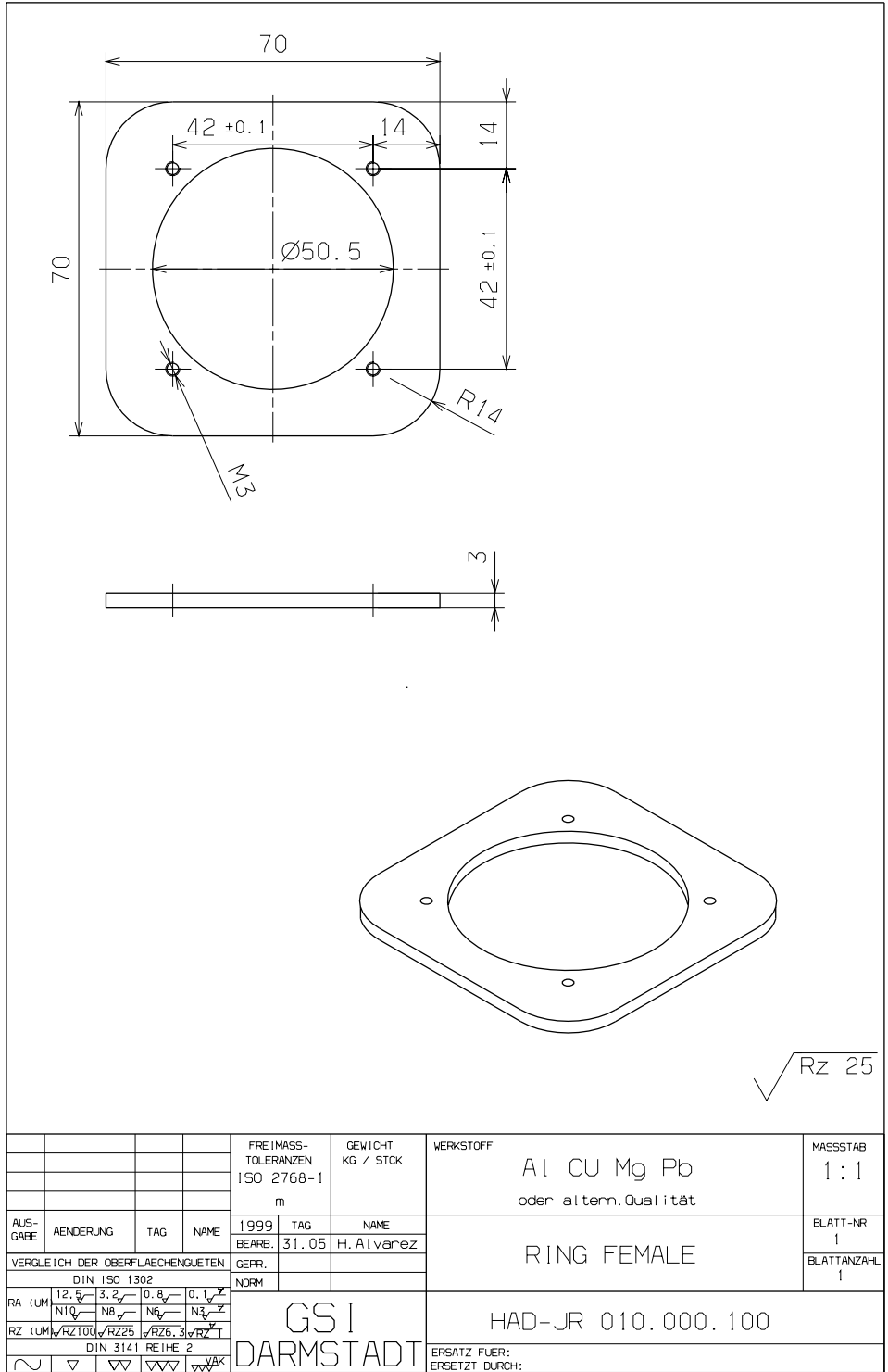
VERGLEICH DER OBERFLÄCHENGEFÜHRE	FREIWAIGE TOLERANZEN	GEWICHT	WÄRMESTOFF	WÄRMESTOFF	WÄRMESTOFF
DIN ISO 1302	ISO 2768-1	KG / STÜCK	AL	Cu	Mg Pb
12.5	m				
13.5					
14.5					
15.5					
16.5					
17.5					
18.5					
19.5					
20.5					
21.5					
22.5					
23.5					
24.5					
25.5					
26.5					
27.5					
28.5					
29.5					
30.5					
31.5					
32.5					
33.5					
34.5					
35.5					
36.5					
37.5					
38.5					
39.5					
40.5					
41.5					
42.5					
43.5					
44.5					
45.5					
46.5					
47.5					
48.5					
49.5					
50.5					
51.5					
52.5					
53.5					
54.5					
55.5					
56.5					
57.5					
58.5					
59.5					
60.5					
61.5					
62.5					
63.5					
64.5					
65.5					
66.5					
67.5					
68.5					
69.5					
70.5					
71.5					
72.5					
73.5					
74.5					
75.5					
76.5					
77.5					
78.5					
79.5					
80.5					
81.5					
82.5					
83.5					
84.5					
85.5					
86.5					
87.5					
88.5					
89.5					
90.5					
91.5					
92.5					
93.5					
94.5					
95.5					
96.5					
97.5					
98.5					
99.5					
100.5					
101.5					
102.5					
103.5					
104.5					
105.5					
106.5					
107.5					
108.5					
109.5					
110.5					
111.5					
112.5					
113.5					
114.5					
115.5					
116.5					
117.5					
118.5					
119.5					
120.5					
121.5					
122.5					
123.5					
124.5					
125.5					
126.5					
127.5					
128.5					
129.5					
130.5					
131.5					
132.5					
133.5					
134.5					
135.5					
136.5					
137.5					
138.5					
139.5					
140.5					
141.5					
142.5					
143.5					
144.5					
145.5					
146.5					
147.5					
148.5					
149.5					
150.5					
151.5					
152.5					
153.5					
154.5					
155.5					
156.5					
157.5					
158.5					
159.5					
160.5					
161.5					
162.5					
163.5					
164.5					
165.5					
166.5					
167.5					
168.5					
169.5					
170.5					
171.5					
172.5					
173.5					
174.5					
175.5					
176.5					
177.5					
178.5					
179.5					
180.5					
181.5					
182.5					
183.5					
184.5					
185.5					
186.5					
187.5					
188.5					
189.5					
190.5					
191.5					
192.5					
193.5					
194.5					
195.5					
196.5					
197.5					
198.5					
199.5					
200.5					

MARCH 12, 2002

KOPF

kopf FRAME 1 MARCH 12, 2002 15.56.16

Für diese Zeichnung behalten wir uns alle Rechte vor, auch für den Fall der Patent- oder Gebrauchsmustererteilung. Ohne unsere vorherige Zustimmung darf diese Zeichnung weder vervielfältigt noch Dritten zugänglich gemacht werden. Es ist ausdrücklich zu erklären, dass wir keine Gewähr für die Richtigkeit der Angaben übernehmen und für die Folgen der nach dem Stand der Technik nicht erkennbaren Verletzungen zu Schadensersatz und künftigen strafrechtlichen Folgen haben.



kopf

MARCH 12, 2002

Conclusiones

Se traducen aquí los puntos principales de las conclusiones presentadas en la sección 6.5.

En este trabajo, se han desarrollado métodos y dispositivos para realizar el alineamiento relativo de las cámaras de deriva multihilos (MDC) del espectrómetro HADES.

Primero se han determinado explícitamente los requisitos de los sistemas de alineamiento, en función de su influencia en la resolución en momento y masa invariante del espectrómetro.

Tras un estudio mecánico de las características del espectrómetro, se han estudiado los sistemas RASNIK como candidatos óptimos para la monitorización de los desplazamientos de las cámaras de deriva internas frente a las externas. Se ha estudiado la dependencia en la resolución del ángulo de incidencia de la imagen sobre la videocámara y de la apertura de la lente en un montaje experimental, obteniendo los valores ideales de funcionamiento.

Se han diseñado piezas específicas para el montaje de los sistemas RASNIK en el espectrómetro, tarea que ha sido realizada desde el diseño preliminar hasta el montaje en posición de medida.

La resolución y la estabilidad del sistema integrado, ya listo para su montaje en el espectrómetro ha sido revisada en un banco óptico, habiendo superado los requisitos.

Se ha realizado un completo programa de monitorización (RAHAD), que incluye la calibración, la transformación de coordenadas y la interfaz con EPICS, el sistema de Slow Control de HADES.

Una vez instalado en el espectrómetro, ha vuelto a comprobarse la alta resolución del sistema RASNIK, y se han correlacionado satisfactoriamente los resultados con los cambios de temperatura y con la intensidad del campo magnético. Los resultados han sido utilizados para corregir los desplazamientos sobre los parámetros encontrados por los algoritmos de alineamiento.

Se han desarrollado algoritmos para obtener, de forma iterativa, los

parámetros de alineamiento de los módulos. El algoritmo de tres módulos es el principal método de alineamiento, basado en la minimización del seno del ángulo entre los vectores que se puede formar con pares de módulos contiguos. En los sectores donde sólo hay dos módulos, se han desarrollado métodos específicos de minimización analítica de residuos, con correcciones por la rotación relativa. Este procedimiento incluye la determinación de la posición del blanco, en el algoritmo denominado “buscador del target”.

Los algoritmos se han comprobado en simulación, especialmente su convergencia a los parámetros correctos. Se ha estimado el error cometido; la resolución en la determinación de los parámetros de alineamiento relativos mediante estos algoritmos es suficiente para cumplir los requisitos.

Se ha analizado una muestra de datos pertenecientes a colisiones de iones de carbono a 1 GeV contra un blanco de carbono, utilizando los algoritmos de alineamiento. Los métodos de alineamiento han permitido un estudio detallado de las características de los módulos y de los procedimientos de tracking. Por último, se han determinado los parámetros del alineamiento, incluyendo sus intervalos de incertidumbre, para los sectores y módulos de los que se disponen datos experimentales.